Investigation of ambient radio-frequency energy harvesting using a rapid prototyping plastronic approach

Xuan Viet Linh Nguyen

▶ To cite this version:

Xuan Viet Linh Nguyen. Investigation of ambient radio-frequency energy harvesting using a rapid prototyping plastronic approach. Electric power. INSA de Lyon, 2023. English. NNT : 2023ISAL0007 . tel-04248664

HAL Id: tel-04248664
https://theses.hal.science/tel-04248664
Submitted on 18 Oct 2023

HAL is a multi-disciplinary open access archive for the deposit and dissemination of scientific research documents, whether they are published or not. The documents may come from teaching and research institutions in France or abroad, or from public or private research centers.

L'archive ouverte pluridisciplinaire **HAL**, est destinée au dépôt et à la diffusion de documents scientifiques de niveau recherche, publiés ou non, émanant des établissements d'enseignement et de recherche français ou étrangers, des laboratoires publics ou privés.

N°d'ordre NNT : 2023ISAL0007

THESE de DOCTORAT DE L'UNIVERSITE DE LYON
opérée au sein de
INSA Lyon

Ecole Doctorale N° 160
Electronique, Electrotechnique, Automatique (EEA)

Spécialité de doctorat : Electronique, Electrotechnique, Automatique
Discipline : Génie Electrique

Soutenue publiquement/à huis clos le 03/02/2023, par :
Xuan Viet Linh NGUYEN

Investigation of Ambient Radio-Frequency Energy Harvesting using a Rapid Prototyping Plastronic Approach

---

Devant le jury composé de :

BENECH, Philippe	Professeur des Universités	UGA Grenoble	Président
VIGNERAS, Valérie	Professeur des Universités	Bordeaux INP	Rapportrice
PRODIC, Aleksandar	Professeur des Universités	University of Toronto	Rapporteur
BECHEVET, Delphine	Associated Professor	HES Genève	Examinatrice
DUCHAMP, Jean-Marc	Maitre de Conférences HDR	UGA Grenoble	Examinateur
ALLARD, Bruno	Professeur des Universités	INSA Lyon	Directeur de thèse
CABRERA, Michel	Chargé de Recherche	INSA Lyon	Co-encadrant
VERDIER, Jacques	Maitre de Conférences	INSA Lyon	Invité

Cette thèse est accessible à l'adresse : https://theses.insa-lyon.fr/publication/2023ISAL0007/these.pdf
© [X.V.L. NGUYEN], [2023], INSA Lyon, tous droits réservés

Cette thèse est accessible à l'adresse : https://theses.insa-lyon.fr/publication/2023ISAL0007/these.pdf
© [X.V.L. NGUYEN], [2023], INSA Lyon, tous droits réservés

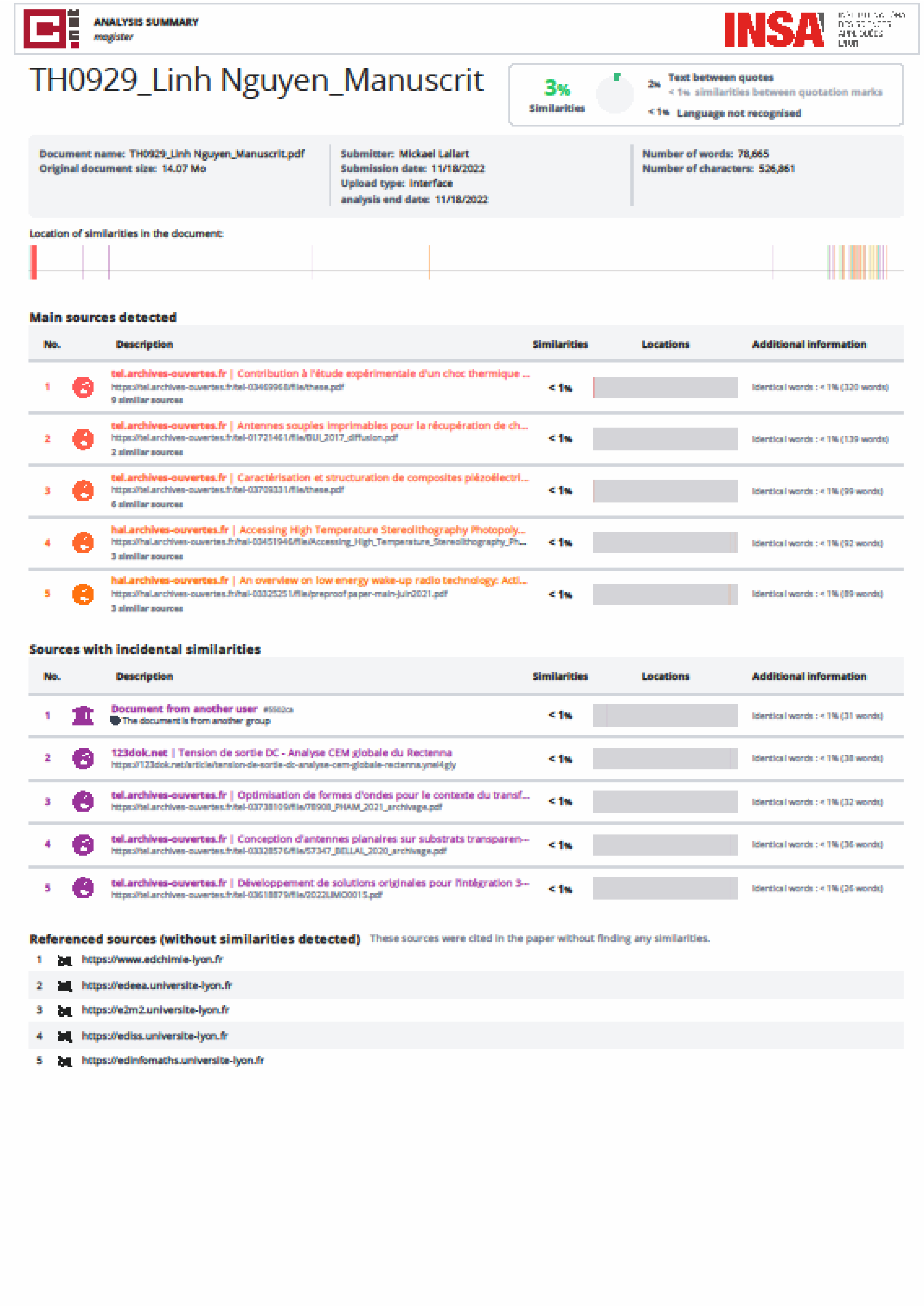

ANALYSIS SUMMARY
magister

TH0929_Linh Nguyen_Manuscrit

3% Similarities

2% Text between quotes
< 1% similarities between quotation marks
< 1% Language not recognised

Document name: TH0929_Linh Nguyen_Manuscrit.pdf
Original document size: 14.07 Mo

Submitter: Mickael Lallart
Submission date: 11/18/2022
Upload type: interface
analysis end date: 11/18/2022

Number of words: 78,665
Number of characters: 526,861

Location of similarities in the document:

Main sources detected

No.	Description	Similarities	Locations	Additional information
1	tel.archives-ouvertes.fr | Contribution à l'étude expérimentale d'un choc thermique ... https://tel.archives-ouvertes.fr/tel-03469968/file/these.pdf 9 similar sources	< 1%		Identical words : < 1% (320 words)
2	tel.archives-ouvertes.fr | Antennes souples imprimables pour la récupération de ch... https://tel.archives-ouvertes.fr/tel-01721461/file/BUI_2017_diffusion.pdf 2 similar sources	< 1%		Identical words : < 1% (139 words)
3	tel.archives-ouvertes.fr | Caractérisation et structuration de composites piézoélectri... https://tel.archives-ouvertes.fr/tel-03709331/file/these.pdf 6 similar sources	< 1%		Identical words : < 1% (99 words)
4	hal.archives-ouvertes.fr | Accessing High Temperature Stereolithography Photopoly... https://hal.archives-ouvertes.fr/hal-03451946/file/Accessing_High_Temperature_Stereolithography_Ph... 3 similar sources	< 1%		Identical words : < 1% (92 words)
5	hal.archives-ouvertes.fr | An overview on low energy wake-up radio technology: Acti... https://hal.archives-ouvertes.fr/hal-03325251/file/preproof paper-main-juin2021.pdf 3 similar sources	< 1%		Identical words : < 1% (89 words)

Sources with incidental similarities

No.	Description	Similarities	Locations	Additional information
1	Document from another user #5582ca The document is from another group	< 1%		Identical words : < 1% (31 words)
2	123dok.net | Tension de sortie DC - Analyse CEM globale du Rectenna https://123dok.net/article/tension-de-sortie-dc-analyse-cem-globale-rectenna.ynel4gly	< 1%		Identical words : < 1% (38 words)
3	tel.archives-ouvertes.fr | Optimisation de formes d'ondes pour le contexte du transf... https://tel.archives-ouvertes.fr/tel-03738109/file/78908_PHAM_2021_archivage.pdf	< 1%		Identical words : < 1% (32 words)
4	tel.archives-ouvertes.fr | Conception d'antennes planaires sur substrats transparen... https://tel.archives-ouvertes.fr/tel-03328576/file/57347_BELLAL_2020_archivage.pdf	< 1%		Identical words : < 1% (36 words)
5	tel.archives-ouvertes.fr | Développement de solutions originales pour l'intégration 3-... https://tel.archives-ouvertes.fr/tel-03618879/file/2022LIMO0015.pdf	< 1%		Identical words : < 1% (26 words)

Referenced sources (without similarities detected)

These sources were cited in the paper without finding any similarities.

1	https://www.edchimie-lyon.fr
2	https://edeea.universite-lyon.fr
3	https://e2m2.universite-lyon.fr
4	https://ediss.universite-lyon.fr
5	https://edinfomaths.universite-lyon.fr

Cette thèse est accessible à l'adresse : https://theses.insa-lyon.fr/publication/2023ISAL0007/these.pdf
© [X.V.L. NGUYEN], [2023], INSA Lyon, tous droits réservés

Cette thèse est accessible à l'adresse : https://theses.insa-lyon.fr/publication/2023ISAL0007/these.pdf
© [X.V.L. NGUYEN], [2023], INSA Lyon, tous droits réservés

Département FEDORA – INSA Lyon – Ecoles Doctorales

SIGLE	ECOLE DOCTORALE	NOM ET COORDONNEES DU RESPONSABLE
CHIMIE	**CHIMIE DE LYON** **https://www.edchimie-lyon.fr** Sec. : Renée EL MELHEM Bât. Blaise Pascal, 3e étage secretariat@edchimine-lyon.fr	**M. Stéphane DANIELE** C2P2-CPE LYON-UMR5265 Bâtiment F308, BP 2077 43 Boulevard du 11 Novembre 1918 69616 Villeurbanne directeur@edchimie-lyon.fr
E.E.A	**ELECTRONIQUE, ELECTROTECHNIQUE, AUTOMATIQUE** **https://edeea.universite-lyon.fr** Sec. : Stéphanie CAUVIN Bâtiment Direction INSA Lyon Tél : 04.72.43.71.70 secretariat.edeea@insa-lyon.fr	**M. Philippe DELACHARTRE** INSA LYON Laboratoire CREATIS Bâtiment Blaise Pascal, 7 avenue Jean Capelle 69621 Villeurbanne CEDEX Tél : 04.72.43.88.63 philippe.delachartre@insa-lyon.fr
E2M2	**EVOLUTION, ECOSYSTEME, MICROBIOLOGIE, MODELISATION** **https://e2m2.universite-lyon.fr** Sec. : Sylvie ROBERJOT Bât. Atrium, UCB Lyon 1 Tél : 04.72.44.83.62 Secretariat.e2m2@univ-lyon1.fr	**M. Philippe NORMAND** Université Claude Bernard Lyon 1 UMR 5557 Lab. d'Ecologie Microbienne Bâtiment Mendel 43, boulevard du 11 Novembre 1918 69622 Villeurbanne CEDEX philippe.normand@univ-lyon1.fr
EDISS	**INTERDISCIPLINAIRE SCIENCES-SANTE** **https://ediss.universite-lyon.fr** Sec. : Sylvie ROBERJOT Bât. Atrium, UCB Lyon 1 Tél : 04.72.44.83.62 Secretariat.e2m2@univ-lyon1.fr	**Mme Sylvie RICARD-BLUM** Institut de Chimie et Biochimie Moléculaire et Supramoléculaires (ICBMS) – UMR 5246 CNRS – Université Lyon 1 Bâtiment Raulin – 2ème étage Nord 43 Boulevard du 11 Novembre 1918 69622 Villeurbanne Cedex Tél : +33(0)4 72 44 82 32 sylvie.ricard-blum@univ-lyon1.fr
INFOMATHS	**INFORMATIQUE ET MATHEMATIQUES** **https://edinfomaths.universite-lyon.fr** Sec. : Renée EL MELHEM Bât. Blaise Pascal, 3e étage Tél : 04.72.43.80.46 infomaths@univ-lyon1.fr	**M. Hamamache KHEDDOUCI** Université Claude Bernard Lyon 1 Bât. Nautibus 43, Boulevard du 11 Novembre 1918 69622 Villeurbanne Cedex France Tél : 04.72.44.83.69 hamamache.kheddouci@univ-lyon1.fr
Matériaux	**MATERIAUX DE LYON** **https://ed34.universite-lyon.fr** Sec. : Yann DE ORDENANA Tél : 04.72.18.62.44 Yann.de-ordenana@ec-lyon.fr	**M. Stéphane BENAYOUN** Ecole Centrale de Lyon Laboratoire LTDS 36 avenue Guy de Collongue 69134 Ecully CEDEX Tél : 04.72.18.64.37 stephane.benayoun@ec-lyon.fr
MEGA	**MECANIQUE, ENERGETIQUE, GENIE CIVIL, ACOUSTIQUE** **https://edmega.universite-lyon.fr** Sec. : Stéphanie CAUVIN Tél : 04.72.43.71.70 Bâtiment Direction INSA Lyon mega@insa-lyon.fr	**M. Jocelyn BONJOUR** INSA Lyon Laboratoire CETHIL Bâtiment Sadi-Carnot 9, rue de la Physique 69621 Villeurbanne CEDEX jocelyn.bonjour@insa-lyon.fr
ScSo	**ScSo*** **https://edsciencessociales.universite-lyon.fr** Sec. : Mélina FAVETON INSA : J. Y. TOUSSAINT Tél : 04.78.69.77.79 melina.faveton@univ-lyon2.fr	**M. Christian MONTES** Université Lumière Lyon 2 86 Rue Pasteur 69365 Lyon CEDEX 07 christian.montes@univ-lyon2.fr

***ScSo : Histoire, Géographie, Aménagement, Urbanisme, Archéologie, Science politique, Sociologie, Anthropologie

Cette thèse est accessible à l'adresse : https://theses.insa-lyon.fr/publication/2023ISAL0007/these.pdf
© [X.V.L. NGUYEN], [2023], INSA Lyon, tous droits réservés

Cette thèse est accessible à l'adresse : https://theses.insa-lyon.fr/publication/2023ISAL0007/these.pdf
© [X.V.L. NGUYEN], [2023], INSA Lyon, tous droits réservés

Acknowledgement

This work has been carried out within the project IPCEI INCA Nano 2022. This thesis has been realized at AMPERE Laboratory of Institut National des Sciences Appliquées (INSA) de Lyon.

First of all, I would like to give my deepest gratitude to my supervisor, Prof. Dr. Bruno ALLARD, professor of Electrical Engineering department of INSA de Lyon, and my advisors, Dr. Michel CABRERA, researcher at Centre National de la Recherche Scientifique (CNRS) and Dr. Jacques VERDIER, associated professor of Electrical Engineering department of INSA de Lyon, for their help, advices and support during my thesis.

I would like to express my sincere appreciation to Prof. Dr. Valérie VIGNERAS, professor of Bordeaux INP and Prof. Dr. Aleksandar PRODIC, professor of University of Toronto, for their acceptation to become reviewers of my thesis and their remarks for my manuscript.

I would like to express many thanks to Prof. Dr. Philippe BENECH, professor of UGA Grenoble, and Dr. Jean-Marc DUCHAMP, associated professor of UGA Grenoble, for their advices and help during my thesis and their acceptation to examine my work, and Dr. Delphine BECHEVET, associated professor of HES Genève, for her acceptation to become examiner of my thesis.

I would like to give my big thanks to my colleagues and friends at Plastronique team of AMPERE Laboratory, Dr. Philippe LOMBARD, Dr. Vincent SEMET, Dr. Tony GERGES, Dr. Simon LAMBERT for their help and Caroline, Camila, Jean-Lynce, Valernst, Thomas, Hugo, Pangsui for their mental support. I am waiting for your Ph.D. defense and your “pot de thèse” and I am willing to call all of you as Doctors.

I would like to give my thanks to my colleagues at AMPERE Laboratory for your help during my Ph.D.

Finally, I would like to send a deep love and gratitude to my family including my Father, my Mother who are always by my side and encourage me in the process of my life, my Brother, my Sister-in-law for their support and especially my beloved nephew Loris for his naivety.

Cette thèse est accessible à l'adresse : https://theses.insa-lyon.fr/publication/2023ISAL0007/these.pdf
© [X.V.L. NGUYEN], [2023], INSA Lyon, tous droits réservés

Cette thèse est accessible à l'adresse : https://theses.insa-lyon.fr/publication/2023ISAL0007/these.pdf
© [X.V.L. NGUYEN], [2023], INSA Lyon, tous droits réservés

Abstract

Internet of Things (IoT) or Internet of Objects is defining a new era of technology, where the electrical devices communicate with each other wirelessly. IoT devices have their applications in many fields in our quotidian life, such as telecommunications, education, health care, industrial domains, etc. A barrier to overcome in the development of these devices is their autonomic energy supply scheme. In the aspect of energy supply scheme, Radio Frequency Energy Harvester (RFEH) is selected among recent energy harvester mechanisms (thermal, mechanical, light, etc.). Another interesting aspect is the possibility of integrating the RFEH onto the surface of polymeric objects, which are often largely unused. This seems impossible with PCB and FLEX-PCB, but Plastronics allows to realize this idea. Therefore, the objective of this work is to demonstrate the feasibility of RFEH with a low cost, versatile Plastronics technology developed in our laboratory, suitable for prototyping. This technology, called Rapid Plastronics, is based on the fabrication of the device substrate by 3D printing, using Stereolithography (SLA), and realizing the conductive traces applying Electroless Deposition (ELD). The objective was not to develop this technology, but to apply it in the RF (which was not done before) and RFEH context.

This thesis is conducted in the following phases.

In the first phase, the studies of materials manufacturing process (Stereolithography (SLA) substrate, ELD copper) in Rapid Plastronics, relative permittivity, loss tangent of the substrate, and resistivity of the conductor are carried out. These parameters have a crucial role in designing the antennas and the RF-DC rectifier.

In the second phase, designs of patch antenna for the energy harvesting (EH) applications are discussed. Firstly, a fundamental linearly polarized patch antenna operating at 2.45 GHz is studied, and the impacts of the SLA substrate and the ELD copper on the performance of the antenna are mentioned. Then, the circularly polarized patch antennas being able to capture all the polarizations in the air are studied.

The third phase is about the RF-DC rectifiers, the proposed Power Management Unit (PMU) as well as the electrical interconnection between the designed antennas, the rectifiers and the PMU. The technique of matching the 50 Ω impedance between the antenna and the rectifier is presented. Moreover, the technique of identifying the optimal load of the rectifier that offers a vision of setting up the impedance interference between the designed rectifier and the PMU will be also introduced.

In the last phase, the performance of the assembling of the PMU, the rectifiers and the antennas will be analyzed.

Keywords: Radio Frequency Energy Harvesting, Antennas, Power Management Unit, Plastronics, Rapid Plastronics, Stereolithography, Electroless Deposition.

Cette thèse est accessible à l'adresse : https://theses.insa-lyon.fr/publication/2023ISAL0007/these.pdf
© [X.V.L. NGUYEN], [2023], INSA Lyon, tous droits réservés

Cette thèse est accessible à l'adresse : https://theses.insa-lyon.fr/publication/2023ISAL0007/these.pdf
© [X.V.L. NGUYEN], [2023], INSA Lyon, tous droits réservés

Résumé

L’Internet of Things (IoT) ou l’Internet des objets définit une nouvelle ère de technologie, où les dispositifs électriques communiquent entre eux sans fil. Les appareils IoT trouvent leurs applications dans de nombreux domaines de notre vie quotidienne, tels que les télécommunications, l’éducation, les soins de santé, les domaines industriels, etc. Un obstacle à surmonter dans le développement de ces dispositifs est leur système d’approvisionnement en énergie autonome. En matière de système d’approvisionnement en énergie, le circuit de récupération d’énergie de radiofréquence (RFEH[1]) est sélectionné parmi les circuits récents de récupération d’énergie (thermique, mécanique, lumière, etc.). Un autre aspect intéressant est la possibilité d’intégrer le RFEH à la surface des objets polymères, qui sont souvent largement inutilisées. Cela semble impossible avec les techniques du PCB et du FLEX-PCB, mais la Plastronique permet de réaliser cette idée. Par conséquent, l’objectif de ce travail est de démontrer la faisabilité de l’intégration d’un RFEH à la surface d’un polymère à l’aide d’une technologie de la Plastronique développée dans notre laboratoire, peu coûteuse et adaptée au prototypage. Cette technologie, appelée Plastronique Rapide, est basée sur la fabrication du substrat de l’appareil par impression 3D, en utilisant la Stéréolithographie (SLA), et la réalisation des traces conductrices en appliquant la métallisation autocatalytique (ELD[2]). L’objectif n’était pas de développer cette technologie mais de l’appliquer dans le contexte RF (ce qui n’était pas fait auparavant) et RFEH.

Cette thèse comporte les phases suivantes.

Dans la première phase, les études du processus de fabrication des circuits de la Plastronique Rapide, de la permittivité relative, de la tangente de perte du substrat et de la résistivité du conducteur sont effectuées. Ces paramètres jouent un rôle important dans la conception des antennes et du redresseur RF-DC.

Dans la deuxième phase, les conceptions d’antennes patch pour les applications de récupération d’énergie sont discutées. Premièrement, une antenne patch de polarisation linéaire fonctionnant à 2,45 GHz et les impacts du substrat SLA et du cuivre ELD sur les performances de l’antenne sont mentionnés. Ensuite, les antennes patch de polarisation circulaire capables de capturer toutes les polarisations dans l’espace sont étudiées.

La troisième phase concerne les redresseurs RF-DC, le circuit de gestion de puissance (PMU[3]) proposé ainsi que l’interconnexion électrique entre les antennes conçues, les redresseurs et le PMU. La technique d’adaptation d’impédance à 50 Ω entre l’antenne et le redresseur est présentée. De plus, la technique d’identification de la charge optimale du redresseur qui donne une vision de la mise en place de l’interférence d’impédance entre le redresseur conçu et le PMU sera également introduite.

Dans la dernière phase, la performance de l’assemblage du PMU, des redresseurs et des antennes seront analysées.

Mots clés : Récupération d’énergie de radiofréquence, Antennes, Circuit de Gestion de Puissance, Plastronique, Plastronique Rapide, Stéréolithographie, Métallisation Autocatalytique

---

[1] RFEH (en anglais) : Radio Frequency Energy Harvester

[2] ELD (en anglais) : Electroless Deposition

[3] PMU (en anglais) : Power Management Unit

Cette thèse est accessible à l'adresse : https://theses.insa-lyon.fr/publication/2023ISAL0007/these.pdf
© [X.V.L. NGUYEN], [2023], INSA Lyon, tous droits réservés

Cette thèse est accessible à l'adresse : https://theses.insa-lyon.fr/publication/2023ISAL0007/these.pdf
© [X.V.L. NGUYEN], [2023], INSA Lyon, tous droits réservés

Table of contents

Cette thèse est accessible à l'adresse : https://theses.insa-lyon.fr/publication/2023ISAL0007/these.pdf
© [X.V.L. NGUYEN], [2023], INSA Lyon, tous droits réservés

Cette thèse est accessible à l'adresse : https://theses.insa-lyon.fr/publication/2023ISAL0007/these.pdf
© [X.V.L. NGUYEN], [2023], INSA Lyon, tous droits réservés

Cette thèse est accessible à l'adresse : https://theses.insa-lyon.fr/publication/2023ISAL0007/these.pdf
© [X.V.L. NGUYEN], [2023], INSA Lyon, tous droits réservés

Cette thèse est accessible à l'adresse : https://theses.insa-lyon.fr/publication/2023ISAL0007/these.pdf
© [X.V.L. NGUYEN], [2023], INSA Lyon, tous droits réservés

List of Figures

Cette thèse est accessible à l'adresse : https://theses.insa-lyon.fr/publication/2023ISAL0007/these.pdf
© [X.V.L. NGUYEN], [2023], INSA Lyon, tous droits réservés

Cette thèse est accessible à l'adresse : https://theses.insa-lyon.fr/publication/2023ISAL0007/these.pdf
© [X.V.L. NGUYEN], [2023], INSA Lyon, tous droits réservés

Cette thèse est accessible à l'adresse : https://theses.insa-lyon.fr/publication/2023ISAL0007/these.pdf
© [X.V.L. NGUYEN], [2023], INSA Lyon, tous droits réservés

Cette thèse est accessible à l'adresse : https://theses.insa-lyon.fr/publication/2023ISAL0007/these.pdf
© [X.V.L. NGUYEN], [2023], INSA Lyon, tous droits réservés

Cette thèse est accessible à l'adresse : https://theses.insa-lyon.fr/publication/2023ISAL0007/these.pdf
© [X.V.L. NGUYEN], [2023], INSA Lyon, tous droits réservés

Cette thèse est accessible à l'adresse : https://theses.insa-lyon.fr/publication/2023ISAL0007/these.pdf
© [X.V.L. NGUYEN], [2023], INSA Lyon, tous droits réservés

List of Tables

Cette thèse est accessible à l'adresse : https://theses.insa-lyon.fr/publication/2023ISAL0007/these.pdf
© [X.V.L. NGUYEN], [2023], INSA Lyon, tous droits réservés

Cette thèse est accessible à l'adresse : https://theses.insa-lyon.fr/publication/2023ISAL0007/these.pdf
© [X.V.L. NGUYEN], [2023], INSA Lyon, tous droits réservés

List of Abbreviations

IoT	Internet Of Things
RF	Radio Frequency
RFEH	Radio Frequency Energy Harvester
EM	Electromagnetic
CP	Circular Polarization
HPBW	Half Power Beamwidth
VNA	Vector Network Analyzer
IC	Integrated Circuit
PMU	Power Management Unit
RFoM	Rectenna Figure of Merit
MPP	Maximum Power Point
MPPT	Maximum Power Point Tracking
ZBR	Zero Bias Resistance
VS	Voltage Supervisor
AO	Armstrong Oscillator
UVLO	Under-Voltage-Lock-Out
PCB	Printed Circuit Board
2K	Two Shot (in Two Shot Injection Molding)
LDS	Laser Direct Structuring
IME	In Mold Electronics
PE	Printed Electronics
FDM	Fused Deposition Modeling
SLA	Stereolithography
UV	Ultraviolet
HT	High Temp
TTL	Two Transmission Lines
ELD	Electroless Deposition
SMD	Surface Mounted Device

Cette thèse est accessible à l'adresse : https://theses.insa-lyon.fr/publication/2023ISAL0007/these.pdf
© [X.V.L. NGUYEN], [2023], INSA Lyon, tous droits réservés

Cette thèse est accessible à l'adresse : https://theses.insa-lyon.fr/publication/2023ISAL0007/these.pdf
© [X.V.L. NGUYEN], [2023], INSA Lyon, tous droits réservés

INTRODUCTION

We are living in a new era of technology, called Internet of Things (IoT) or Internet of Object, where the electrical devices are able to communicate with each other wirelessly. IoT devices find their applications in many fields, like telecommunications, education, health care, industrial domains, etc. [1]. Due to their rapid development, these devices exist everywhere in our daily life in many form-factors from tiny size (i.e. stand-alone sensors), to small size (i.e. mobile phones, headsets, etc.), or even big size such as vehicles, drones, home appliances, factory facilities, etc.

According to Cisco, it is estimated that the number of connected devices will reach 500 billion by 2030, which is about 59 times larger than the world population by that time [2].

A barrier to overcome in the development of the IoT devices is their energy supply scheme. Using batteries to feed those devices is no more a solution. Regular battery maintenance is complicated and up to 78 million batteries of IoT devices are estimated to be thrown away daily by 2025 if nothing is done to improve their lifespan [1]. Most of batteries contain metals and chemicals causing damage to the environment and human health. Therefore, replacing the batteries by other eco-friendly sources might be considered as a way-out to obtain long lifetime devices.

Harvesting ambient energy available in the environment and converting them into DC energy seems a good solution [3]. Many types of energy harvesters are developed to address thermal energy, mechanical energy, light or Radio Frequency (RF) waves. Among them, Radio Frequency Energy Harvester (RFEH) circuits are good candidates when there is no light, no heat or when the objects are not moving.

A RFEH is based on three main blocks. The first block is dedicated to capture the ambient electromagnetic waves with an electromagnetic waves capturer and transfer them to the RF-DC rectifier to transform RF energy into DC energy. The second block Power Management Unit (PMU) contains a DC/DC converter, which controls the flow of energy to a storage device (i.e. a capacitor, a battery, etc.), and a Voltage Supervisor (VS), which transfers the DC energy to the third block – the consumption load – or cut this link when the storage device is too depleted. The consumption load can be the micro-controllers, the sensors, etc.

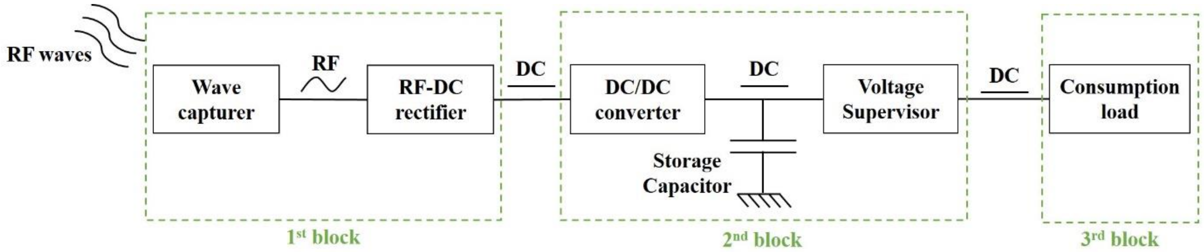

Figure 0.1: Schematic block of a RFEH

Conventional processes for electronic circuits allow fabricating RFEH by assembling 2D rigid Printed Circuit Board (PCB) and/or semi-rigid/flexible circuit board (also called FLEX-PCB) [4], [5], [6] and [7]. As we shall see below, although quite efficient with regard to the capture of RF energy (thanks to the use of patch antennas, for example) and the electronics (efficiency of RF-DC conversion), the possibilities allowed by conventional manufacture of RFEH are limited at a mechanical level, even at most basic geometrical level.

In other respect, a disadvantage of the RFEH in general is the geometric footprint, in particular, as regards the surface of the antenna at low frequency, which is difficult to reduce either for theoretical (ratio between the antenna dimensions and the RF wavelength) and practical reasons (permittivity

Cette thèse est accessible à l'adresse : https://theses.insa-lyon.fr/publication/2023ISAL0007/these.pdf
© [X.V.L. NGUYEN], [2023], INSA Lyon, tous droits réservés

and RF loss of materials). Therefore, new solutions based on the use of multiple rectennas (possibly with different orientations, polarization and even working frequency) may be of interest.

In this work, we want to explore the possibilities to fabricate RFEH with a strategy based on a new technology called Plastronics, which may allow to bypass some limitations imposed by the conventional assembly of PCBs and FLEX-PCBs.

Plastronics is the convergence of Plastics and Electronics domains as shown in Fig. 0.2, in order to create the conductor traces (including antennas) and mount the Surface Mounted Devices (SMDs) on any form of polymer surfaces, from 2D to 3D, from simple to complex.

Figure 0.2: Example of a plastronic device assembling from plastic model (left) and electric circuit (right) [8]

Compared to conventional PCB and FLEX-PCB manufacturing techniques, Plastronics offers specific advantages in order to [8]

- Integrate antennas and SMDs on the polymer casing of electronic devices (as discussed below, most mobile phones already contain plastronic antennas for telecommunications, etc.)
- Combine a wide variety of polymeric materials with electronic circuits (unlike PCBs and FLEX-PCBs, which are limited to a few polymers not used to form such casing)
- Simplify electrical interconnections between the different blocks of a device
- Simplify the assembly process, etc.

Plastronics allows electronics to be integrated onto the surface of polymeric objects, which is often largely unused. Thus, instead of miniaturizing the rectennas of the RFEHs, it would perhaps be advantageous to arrange several RFEHs on the same surface. After all, the number of ambient RF sources, their distances and their orientations to the RFEH are unknown.

There are different processes to elaborate plastronic circuits, which will be discussed below. However, most of them are industrial ones, requiring expensive and complex tooling (e.g., injection mold), not suitable for a research work. Moreover, the existing methods for prototyping plastronic devices are not completely satisfactory (for example, the section about the ProtoPaint process in the thesis of S. Kamotesov [9]).

Therefore, the objective of this work is to demonstrate the feasibility of RFEH with a low cost, versatile Plastronics technology developed in our laboratory, suitable for prototyping. This technology, called Rapid Plastronics, is based on the fabrication of the device substrate by 3D printing, using Stereolithography (SLA), and realizing the conductive traces applying Electroless Deposition (ELD). The objective was not to develop this technology, but to apply it in the RF (which was not done before) and RFEH context.

The contexts of this thesis are:

- Developing a RFEH dedicated to low power/low-consumption sensors for IoT applications.

Cette thèse est accessible à l'adresse : https://theses.insa-lyon.fr/publication/2023ISAL0007/these.pdf
© [X.V.L. NGUYEN], [2023], INSA Lyon, tous droits réservés

- Integrating a rectenna with a discrete Power Management Unit and storage device.
- Demonstrating an autonomous test vehicle manufactured using Rapid Plastronics using resistive loads.

A specific point is that due to the very low level of available ambient energy, the fabrication of RFEH cannot be directly derived from the methods used to obtain plastronic antennas for telecommunications. The connection of the rectifier with the antenna has been carefully designed and realized. In order to realize that, it is necessary to improve our understanding of many questions related to RF, electronics at low power level, material properties and material processing. I have been asked to work on the first two points and to cooperate with material specialists as regards the other two points and use their results. Therefore, it is interesting to classify the difficulties in terms of scientific and technical questions as follows:

Scientific questions

- Electromagnetic properties of polymer over the RF range: relative permittivity, loss tangent.
- Conductor properties: conductivity, deposition thickness, surface roughness.
- Concept of antennas and RF-DC rectifiers for the proposed RFEH.

Technological questions

- Electrical interconnection of components and functions in the circuit:

What are the main parameters?
How to realize the interconnection?

- Types and forms of antennas for the proposed RFEH.
- The methodology of simulation of antennas and RF-DC rectifiers.

This manuscript consists of seven chapters.

In the first chapter, a brief state-of-art on Plastronics is reported. Examples of 3D antennas fabricated using 3D printing methods are also discussed. Several aspects of Rapid Plastronics are reported to motivate this work.

The second chapter gives a review of energy harvester circuits in the literature. The topologies of the rectifier will be presented. The interest of different antennas (patch antenna, dipole antenna, etc.) for RFEH is discussed. In addition, the interaction between the antenna, the rectifier and the PMU will be also mentioned. Some examples of 2D rectennas and 3D rectennas will be introduced.

In the third chapter, the Rapid Plastronics will be described. This includes the substrate manufacturing method, the process for realizing the conductive traces and the method for connecting the SMDs to the traces. The substrate and the conductor always have crucial effects on the performances of the antennas and the RF circuits. Therefore, the steps of extracting the electromagnetic properties of the realized conductor and substrate will be presented. The method of measuring the relative permittivity, the loss tangent of the substrate, Two Transmission Lines method, deployed in this thesis will be also introduced. A comparison between the selected materials and the ones in literature will be given.

Next, in the fourth chapter, the design of the patch antenna is discussed. In fact, it should respect some requirements for energy harvesting applications. The most important requirements are that the desired frequency bandwidth of the antenna, which is chosen to cover the Wi-Fi range (2.45 GHz), with the possibility of capturing all the polarizations around the object. The patch antenna is chosen due to its simplicity of electrical design. The full ground surface of the patch can reduce the impacts of elements placed behind the plane on the radiating performance of the antenna. The configuration of the patch antennas will be studied to satisfy the previous requirements.

Cette thèse est accessible à l'adresse : https://theses.insa-lyon.fr/publication/2023ISAL0007/these.pdf
© [X.V.L. NGUYEN], [2023], INSA Lyon, tous droits réservés

Electromagnetic simulation tools will be used to obtain the most suitable antenna design for the final demonstrator.

A fundamental linearly polarized patch antenna operating at 2.45 GHz is mentioned firstly. The study of the impacts of the substrate and the conductors on the radiating performance of the patch antenna will be also presented. Afterwards, to satisfy the requirements of capturing all the polarizations in the air of the antenna for RFEH, the proposed configuration of circularly polarized patch antennas will be described.

The fifth chapter shows the method of simulating and designing the rectifier for the antennas designed in the previous chapter. The methodology of simulating and designing this circuit for Wi-Fi bands will be mentioned. The PMU is added generally after the rectifier with the purpose of boosting the low rectified voltage to the minimum operating voltage of the load and regulating the boosted output voltage. The electrical interconnection between the antenna, the rectifier and the PMU will be studied.

The technique of matching the 50 Ω impedance between the antenna and the rectifier will be presented. Moreover, this chapter gives an overview of identifying optimal load of the rectifier at different levels of input power. The optimal load of the designed rectifier for the demonstrator will be studied. This offers a vision of setting up the impedance interference between the designed rectifier and the PMU.

The sixth chapter shows the experimental results of RFEHs fabricated using the Rapid Plastronics technology. Firstly, the electrical behavior of the PMU connecting to the designed rectifier is studied in variation of the output load (1 MΩ, 100 kΩ, 80 kΩ and 10 kΩ). Afterwards, the plastronic RFEH with the antenna presented in Chapter 4 will be tested with the purpose of verifying the performance of the whole circuit. A comparison with state-of-art will be also discussed.

Finally, in Conclusion, we summarize the work deployed in this thesis. The suggested improvements and the perspectives concerning the plastronic RFEHs are presented.

Cette thèse est accessible à l'adresse : https://theses.insa-lyon.fr/publication/2023ISAL0007/these.pdf
© [X.V.L. NGUYEN], [2023], INSA Lyon, tous droits réservés

CHAPTER 1: STATE-OF-ART ON PLASTRONICS

Cette thèse est accessible à l'adresse : https://theses.insa-lyon.fr/publication/2023ISAL0007/these.pdf
© [X.V.L. NGUYEN], [2023], INSA Lyon, tous droits réservés

Cette thèse est accessible à l'adresse : https://theses.insa-lyon.fr/publication/2023ISAL0007/these.pdf
© [X.V.L. NGUYEN], [2023], INSA Lyon, tous droits réservés

1. STATE-OF-ART ON PLASTRONICS

As mentioned above, Plastronics is the convergence of Plastics and Electronics domains (Fig. 0.2), in order to create the conductor traces (including antennas) and to mount the Surface Mounted Devices (SMDs) on any form of polymer surfaces, from 2D to 3D, from simple to complex.

In fact, there is not a single process for fabricating plastronic devices, but many ones at different level of maturity. Therefore, the aim of this chapter is to make a short review in order to select which processes are of interest in this work. In addition, it is also necessary compared to Plastronics, with the PCB and FLEX-PCB which constitute the gold standard in Electronics, and other fields such as Printed Electronics (PE).

1.1. PCBs

Conceptually, PCB and FLEX-PCB could be part of Plastronics since the conductive traces are created on polymer substrates. However, these technologies have been in continuous development since the early stage of Electronics and constitute an independent branch. When comparing PCBs and Plastronics, an important point, as regards the nature of the materials (polymer substrate, conductive material), is that PCBs use fewer materials, which have largely optimized, while Plastronics uses a wide variety of materials which are generally not (yet) optimized. This is an important point as RFEH devices have to collect low level of ambient energy that requires careful choices of low loss materials.

Contrary to Plastronics, PCB and FLEX-PCB substrates are always flat during manufacturing. After manufacturing, they remain flat in the case of rigid PCB or can be bent in the case of the FLEX-PCB. This flatness during manufacturing is really a key point since it allows using a combination of spin coating, photolithography and etching for patterning the conductive traces on the substrate. In a very similar manner to Microelectronics (but at a different scale), this principle allows proceeding to the collective fabrication of many devices on flat surfaces with subsequent cost reduction.

The main material to constitute the conductive trace on PCB and FLEX-PCB is most often copper. It is deposited on the polymer substrate by laminating a copper foil. This foil is obtained either by successive cold rolling operations to reduce thickness and extend length starting with a billet of pure copper, or by electrodeposition [10]. Copper is chosen because of its low resistivity (1.68 µΩ.cm at 20 °C for bulk copper), close to the best conducting material, which is silver (1.59 µΩ.cm at 20 °C) but at 1/100 of its cost. However, the important point is that the conductivity of the copper on PCBs is close to the bulk copper. The difference is due to several factors such as the presence of impurities, crystal defects, size of grains, etc.

As regards the nature of the substrate, rigid PCBs are most often made of fiberglass-reinforced polymer sheets, which can be considered as polymer composites. A well-known family of rigid PCB is the so called FR4, which most often is made of fiberglass-reinforced thermoset[4] epoxy-laminated sheets (FR stands for "flame retardant" and "4" is the grade as defined for example in

---

[4] A thermoset, is a polymer that is obtained by hardening ("curing") a liquid prepolymer (resin). Curing is induced by heat, radiation or by means of a chemical, but the important point it induces an irreversible change. Contrary to thermoplastics (extensively used in Plastronics), cured thermosets do not flow under application of heat. Therefore, when FR4 boards are manufactured flat, it is not possible to change their shape.

Cette thèse est accessible à l'adresse : https://theses.insa-lyon.fr/publication/2023ISAL0007/these.pdf
© [X.V.L. NGUYEN], [2023], INSA Lyon, tous droits réservés

the IPC-4101). An important example of rigid PCB, is the Rogers 4003C, more suitable for RF applications. Rogers 4003C is made of a woven glass-reinforced hydrocarbon/ceramic.

As regards FLEX-PCB, the polymer substrate is made of polyester (Mylar) for low cost application or polyimide for high performance. Table 1.1 gives the main properties of PCBs. A subject which is not covered in this review is that it is possible to manufacture PCBs with multiple conductive layers and also the manufacturing of vias. An important point is that the rigid PCBs and polyimide can stand the temperature use for soldering SMDs, which is not the case of polyester PCB.

Table 1.1: Main properties of PCBs

Properties	FR-4	Rogers 4003C
Standard conductor thickness	18 µm 35 µm 55 µm 70 µm	17 µm 35 µm 70 µm
Resistivity of the conductor	1.68 µΩ.cm at 20 °C	1.68 µΩ.cm at 20 °C
Typical standard PCB layer thickness	1.25 mm 1.5 mm 3 mm	0.4 mm 0.8 mm 1.5 mm
Volume resistivity	8×10^7 MΩ.cm	1.7×10^{10} MΩ.cm
Surface resistivity	4.2×10^5 MΩ	4.2×10^9 MΩ
Relative permittivity at 2.5 GHz	4.4	3.55
Loss tangent at 2.5 GHz	0.04	0.0021

1.2. Printed Electronics

Printed Electronics (PE) is the art of patterning conductive traces on flexible films by means of conductive inks [11]. The term “Printing” is used in an appropriate manner, since PE is directly derived from the techniques used in the book printing industry. As for PCBs, PE is a topic close to Plastronics and could be even considered as a kind of 2D Plastronics.

Flexible films may be of different nature: thin glass film, polymer films (paper, polyimide, polyester, polyethylene terephthalate PET, Polycarbonate PC, etc.), Films can be handled in roll form or in plate form. In the first case, the patterning is a roll to roll process, suitable for mass production, with techniques such as gravure, offset printing, flexography, etc. In the second case: the patterning is a basically a sheet to sheet process with techniques such as screen printing [11], ink jet printing [11], syringe deposition [12], pad printing [13], aerosol jet printing [14] and others.

Fig. 1.1 adapted from [11] classifies the patterning techniques in a different manner that is to say in contact printing methods and non-contact printing methods. In the case of contact printing, it is not possible to pattern 3D surfaces except for syringe printing and pad printing. However, syringe printing is slow and pad printing of conductive inks is not yet enough developed. Therefore, the most contact patterning technique is of use if the goal is to pattern directly 2D surfaces.

In the case of non-contact printing, except for aerosol jet printing, an important limitation is that the distance between the substrate and the mean of patterning is small. For example, in the case of ink jet printing (whatever the principle of projection is: piezoelectric, thermal, pressure driven, etc.), the distance between the printing head and the substrate is in the range of 1 mm. As all dimensions of a printing head are in the few cm ranges, it is in general not possible to move an ink

Cette thèse est accessible à l'adresse : https://theses.insa-lyon.fr/publication/2023ISAL0007/these.pdf
© [X.V.L. NGUYEN], [2023], INSA Lyon, tous droits réservés

jet printing on top of a 3D substrate with a 1 mm gap. So, in the case of non-contact printing, in practice, it is not possible to pattern directly 3D surfaces, except for aerosol jet printing.

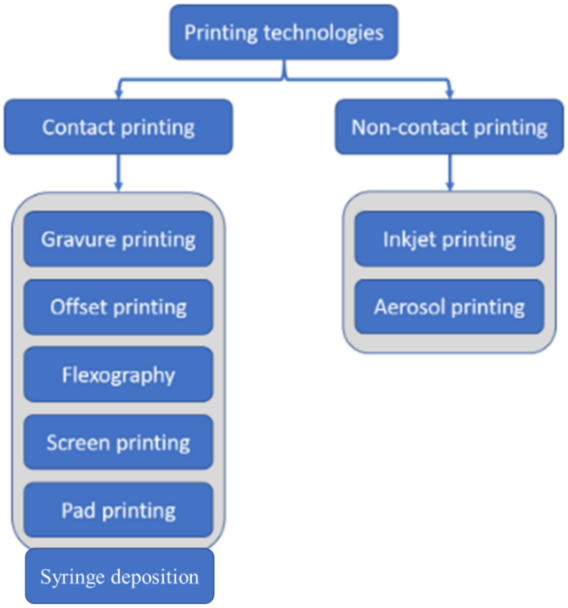

Figure 1.1: Patterning techniques used in PE adapted from [11]

In other respects, it is possible to pattern 2D films with these techniques and to shape them in 3D after patterning. This is notably the case of a plastronic fabrication process named In Mold Electronics (IME), which will be described in Section 1.3.3.3 of this Chapter. IME makes extensive use of screen printing, ink jet printing and syringe deposition on polymer films.

However, another drawback of all these techniques is due to the nature of the conductive inks and their principle of work. Typically, a conductive ink is composed of (Fig. 1.2) [15]

- Conductive powder (silver, gold, copper, graphite…)
- Organic binder
- Solvent
- Miscellaneous (rheology, etc.)

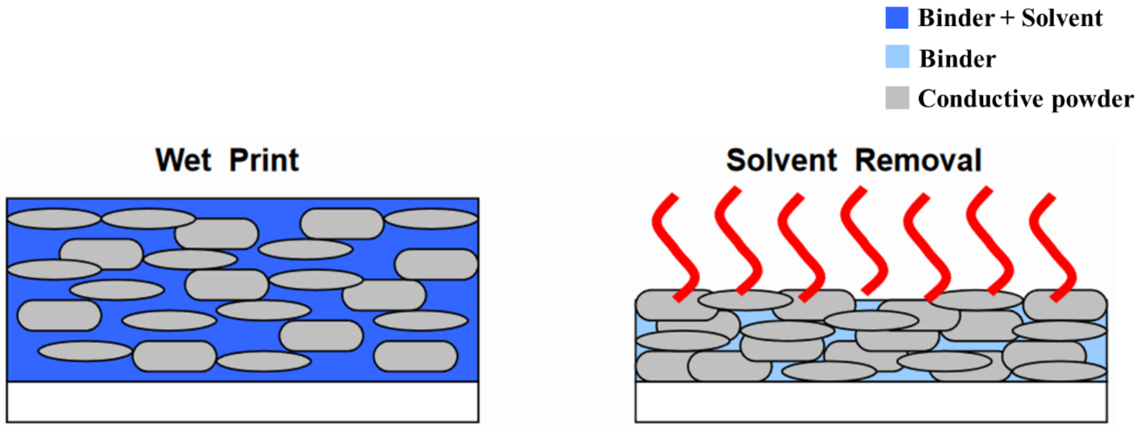

Figure 1.2: How conductive inks work adapted from [15]

Cette thèse est accessible à l'adresse : https://theses.insa-lyon.fr/publication/2023ISAL0007/these.pdf
© [X.V.L. NGUYEN], [2023], INSA Lyon, tous droits réservés

After deposition or projection, the solvent is volatilized, in a natural manner or most often with post-treatment (heat curing, light curing, microwave, etc.). At a certain stage of solvent volatilization, there is a percolation threshold so that a continuous electrically conductive network is created. The conductivity further increases and but reaches a final value due to the presence of the binder. This final value depends on many factors but primarily on the nature, quantity and size (micro, nano) of the powder. The temperature of the film during post-treatment is very important and also duration of post-treatment, etc. The best conductive inks used silver conductive flakes and can reach at best 0.02 μΩ.m of electrical resistivity [16] for non-temperature sensitive substrates (Polymide and glass mainly). For temperature sensitive substrate, the resistivity is significantly higher. The resistivity of different conductive materials is listed in Table 1.2 in Section 1.3.1.2.

There are many other points to consider when using PE (thickness of the conductive layer, adhesion of ink to substrate, etc.). However, one important point is that, on temperature sensitive substrates, it is difficult or even not possible to braze SMDs with conventional technologies. Conductive pastes are used to make the connections. As for conductive inks and for the same reasons, they are less conductive than solders.

The conclusion is that in the field of RFEH, at low levels of ambient energy, the use of conductive inks and conductive past should be avoided when possible. Therefore, as we shall see below, Electroless Deposition (ELD) of copper will be extensively used in this work, as well as conventional soldering.

1.3. 3D Plastronics

1.3.1. Introduction

By analogy with additive manufacturing, we often imagine that 3D Plastronics corresponds to the integration of electronics “into” 3D polymer parts stacking conductive and non-conductive layers. This kind of technology does exist [17] and is a combination of additive manufacturing and ink jet printing with two inks: a conductive one and a non-conductive one [18]. However, it can be considered as an additional way for printing multilayer PCBs, in a more flexible (and expensive) manner than conventional PCB fabrication.

Our conclusion is that due to the existing state of the art in PCB and PE and their long history, it makes sense to reserve the use of the term Plastronics for devices implemented in the 3D surface of polymer substrates. This is the reason why "3D Plastronics” was proposed by the IPC Committee to name this technology.

In other respects, key aspects of 3D Plastronics are listed below and discussed [8] :

- 3D shaping the polymer substrate
- Metallizing the polymer substrate and creating the conductive traces
- Placing and connecting the SMD to the conductive traces.

1.3.2. Key aspects of 3D Plastronics

1.3.2.1. 3D Shaping the polymer substrate

In the field of 3D Plastronics, polymer substrates are shaped in 3D by means conventionally known in the polymer science and industry. These will be briefly reviewed below and include mass production processes as well as prototyping processes, including 3D printing. They are all sequential processes, that is to say non-collective, fabrication processes. This combination of sequential polymer processing and collective electronics is a feature of 3D Plastronics.

Most often, the polymer is of thermoplastic nature since it can be shaped in 3D by the application of heat and pressure on the raw material by means of a tool. Of course, it is possible to use a

Cette thèse est accessible à l'adresse : https://theses.insa-lyon.fr/publication/2023ISAL0007/these.pdf
© [X.V.L. NGUYEN], [2023], INSA Lyon, tous droits réservés

thermoset or even a composite, but this is less usual and will not further discussed (one exception is the photopolymer used in Stereolithography which is a thermoset that will be discussed below).

Fig. 1.3 shows the classification of thermoplastics in the form of a pyramid. The polymers are classified according to their thermal stability and cost with the materials of higher performance on the top. The higher the position in the pyramid, the higher the cost. Therefore, the choice of expensive high-performance polymers is often not relevant.

In other respects, polymers are often mixed with different fillers (talc, silica, etc.) and additives to improve certain properties, for instance, mechanical or thermal properties, fire behavior, etc. The weight ratio varies from less than 1% to 40%. These fillers are sometimes important for RF properties, for example LCP is filled) with glass beads. Of course, the RF properties of a polymer depend also on other factors, such as the chemical nature of the polymer, the polymer/filler interface etc. [19].

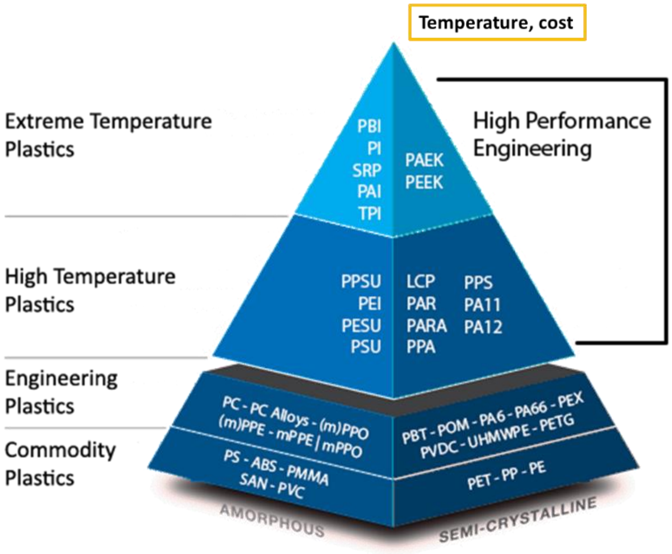

Figure 1.3: Pyramid of thermoplastics adapted from [20]

For the mass-production of 3D substrates, the processes commonly used in 3D Plastronics are injection molding and/or thermoforming. Fig. 1.4 shows the principle of injection molding of thermoplastics pellets inside a cavity mold [21]. Fig. 1.5 shows the principle of thermoforming of a thermoplastic sheet against a tool.

Cette thèse est accessible à l'adresse : https://theses.insa-lyon.fr/publication/2023ISAL0007/these.pdf
© [X.V.L. NGUYEN], [2023], INSA Lyon, tous droits réservés

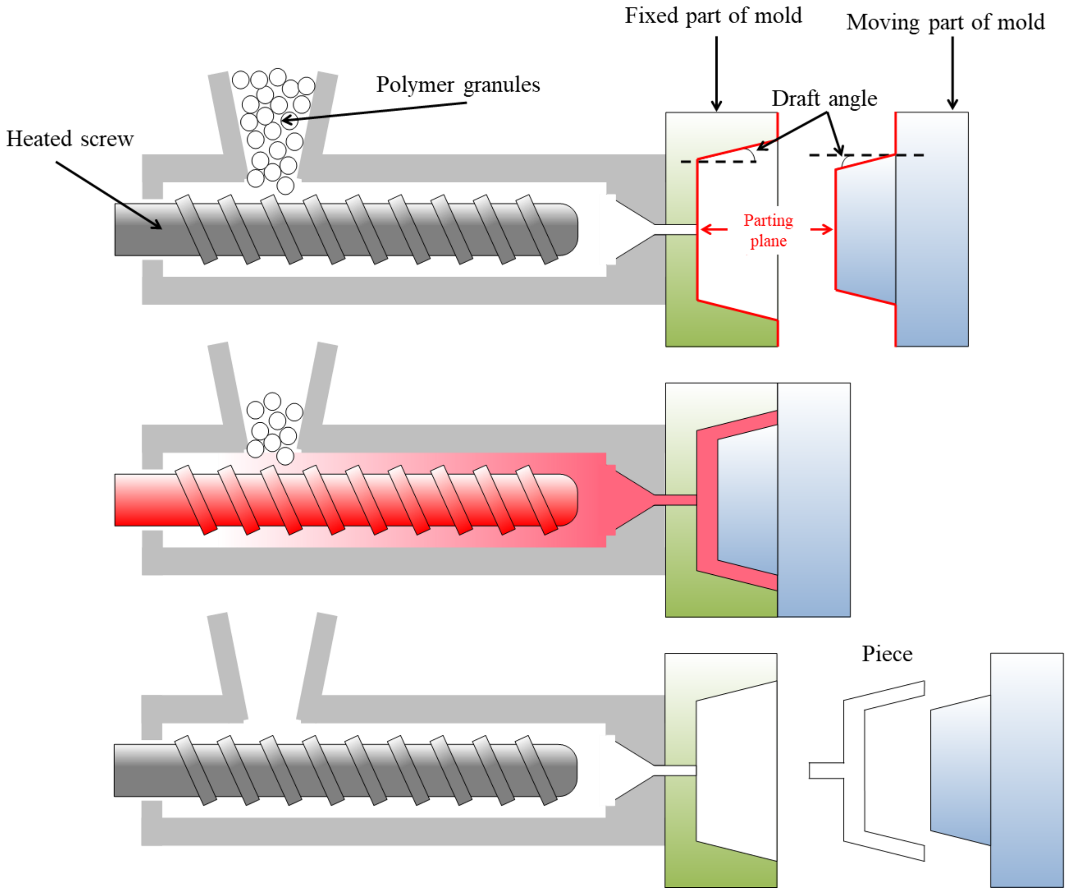

Figure 1.4: Principle of injection molding of thermoplastic pellets [21]

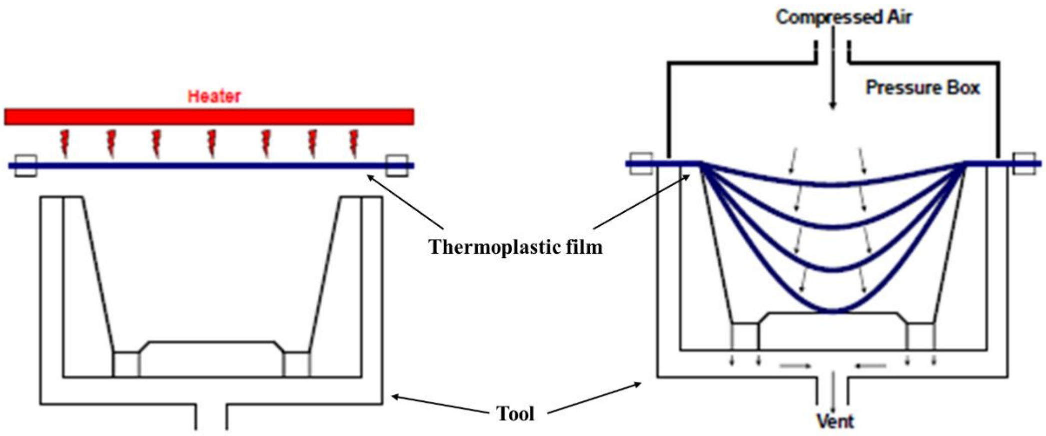

Figure 1.5: Principle of thermoforming of a thermoplastic sheet with heat and pressure

In the case of a complex 3D part, the manufacture of a mold is very expensive and therefore injection molding is often avoided within the framework of a research project. The manufacture of a tool for thermoforming is less expensive, but there are limitations in terms of 3D geometry.

Therefore, for prototyping a few 3D substrates, 3D printing is a convenient solution. An additional advantage of 3D printing is that it is easy to use, which is not the case of injection molding which is very specialized (thermoforming is intermediate). However, it is necessary to select the

Cette thèse est accessible à l'adresse : https://theses.insa-lyon.fr/publication/2023ISAL0007/these.pdf
© [X.V.L. NGUYEN], [2023], INSA Lyon, tous droits réservés

appropriate 3D printing technology for Plastronics. For 3D printing polymers, the main methods are [22]

- Stereolithography (SLA), which consists of curing a liquid photopolymer, layer by layer, by means of light (most often an ultraviolet laser or blue LED) [23]
- Laser sintering, which consists of sintering a thermoplastic powder, layer by layer, by means of an infrared laser [24]
- Fused Deposition Modeling (FDM) which consists of making a 3D with a thermoplastic wire passing through a heated nozzle [25]

Laser sintering and FDM make use of thermoplastics, but for easy processing at a reasonable temperature, they are almost all commodity or engineering plastics (Fig. 1.3). Examples of such polymers are: PolyLactic Acid (PLA), Acrylonitrile Butadiene Styrene (ABS), PolyCarbonate (PC), etc. Due to their limited thermal stability, it is difficult to solder the SMDs on these polymers with repeatable results.

Laser sintering and FDM of high temperature or extreme high temperature thermoplastics (PolyEtherEtherKetone PEEK, PolyEtherImide PEI with trade name ULTEM, etc.) does exist, but make use of expensive printers due to the high temperature to manage. These promising technologies are still under development.

However, for all thermoplastics, FDM and laser sintering have several drawbacks. The parts are porous which leads to poor results during metallization, especially during electroless metallization (see below). Also, the surface roughness is very poor.

The principle of SLA is based on a different process: the photopolymerization (photocuring) of a liquid photopolymer (photosensitive resin). As discussed above the material is a thermoset. However, to the liquid nature of SLA photopolymers before curing, the parts have excellent surface finish and no porosity.

Therefore, AMPERE has extensively developed the use of SLA for prototyping plastronic parts. However, SLA has its own limitations. Most SLA photopolymers do not stand the thermal conditions of brazing but a careful study led to the selection of two resins with acceptable thermal performance. The trade names of the resins are: “High Temp Resin v1”, which was discontinued, and “High Temp Resin v2” from the company Formlabs. There photopolymers have still the disadvantage of being brittle, but this is the case for many SLA photopolymers.

In another respect, it is rather difficult to terminate the curing of SLA photopolymers with the consequence that the properties of the parts change over time (dimensions, distortion due to internal stress, initiation of cracks etc.). After manufacturing in the printer, thermal and light post-processing is applied to stabilize the parts but with non-reproducible results. Therefore, SLA is suitable mostly for prototyping plastronic parts. In a first step, SLA is useful to validate a prototype and perform quickly many changes, but it is wise to use more stable technologies in a second step. Because of the cost and complexity of the molds (injection mold) or tools (thermoforming tool), this can only be considered when design, and especially the mechanical design, of the device is finalized.

1.3.2.2. Metallizing the polymer substrate and creating the conductive traces

A feature of 3D Plastronics is that after fabrication, the polymer substrate is a non-electrically conductive material. Therefore, electrodeposition of metal cannot be directly applied to metallize the polymer surface: the application of a conductive layer (conductive paint, pen with conductive ink, silver lacquer, electroless metallization, metal sputtering, metal thermal evaporation, etc.) is

Cette thèse est accessible à l'adresse : https://theses.insa-lyon.fr/publication/2023ISAL0007/these.pdf
© [X.V.L. NGUYEN], [2023], INSA Lyon, tous droits réservés

necessary. Electrodeposition for 3D Plastronics is discussed in [9] and is mainly used for thickening the thickness of the conductive material when medium to high current is necessary [9] or when high quality inductances are required [26], [27]. We shall see below that electrodeposition is not required for RFEH, since the thickness of electroless copper can easily reach 6-8µm with metal of good conductivity. The idea about the thickness and the conductivity of the conductor will be discussed in Chapter 3.

Another feature of 3D Plastronics is the 3D geometry of the conductive traces onto the polymer surface, which can be obtained either through a subtracting process or an additive process. In the subtractive process, the 3D surface is entirely metallized and the traces are defined by removing the metal either directly (micromilling, laser machining, etc.) or through a mask (for example chemical etching through a mask made of a removal adhesive cut with a plotter). In the additive process, the metallization is directly performed locally. Examples of additive process are: printing with conductive ink, use of adhesive copper foil cut by a plotter, microcontact printing [21], etc.

The most important processes are the printing with conductive ink, which have described below and electroless metallization which is presented below.

The name “electroless metallization” (also called ElectroLess Deposition or ELD) comes from the fact, that contrary to electrodeposition, ELD can metallize non-conductive surfaces, including polymers, ceramics, etc. One of the advantages of ELD is that the thickness of deposited metal is (to some extent) independent of the surface geometry. This is not the case of electrodeposition which depends on current density and vary with the shape of the surface. ELD is considered as homogeneous whilst electrodeposition is heterogeneous and require complex compensation if a constant thickness is required (Fig. 1.6). This is the reason why ELD is also used to deposit metal on top of 3D metallic surfaces. For example, ELD of Nickel-Phosphore or Chromium are extensively used in the industry to apply a new coating on metallic part.

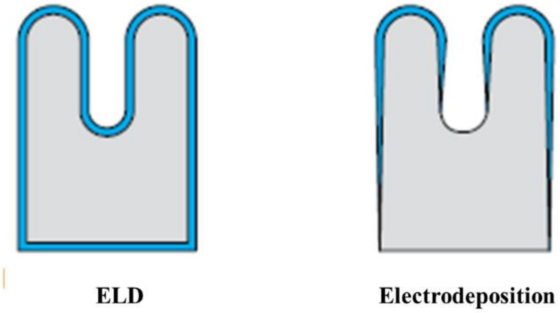

Figure 1.6: Metal thickness in case of ELD (a) and electrodepostion (b).

The ELD takes place in liquid phase. In fact, at least three successive liquid tanks are used:

- One tank for chemical reaction for preparing the surface of the polymer.
- One tank of catalysis for activating the surface of the polymer.
- One tank for the increment of the metal on the pre-activated surface of the polymer.

The first tank is used to prepare the surface of the polymer for the catalysis. Generally, it is a chemical reaction which allows to create the surface roughness of the object and to improve chemical adhesion. The exact nature of the tank, the duration of the reaction, the temperature, etc. can vary in different polymers. Nevertheless, generally, it is a chemical reaction of Chromic Acid and/or Sulfo-Chromic Acid, which are carcinogenic. In fact, for the Rapid Plastronics, these chemical products are not used.

Cette thèse est accessible à l'adresse : https://theses.insa-lyon.fr/publication/2023ISAL0007/these.pdf
© [X.V.L. NGUYEN], [2023], INSA Lyon, tous droits réservés

After washing the object, the second tank allows us to activate the object's surface due to a catalyzer. This catalyzer contains a solution of colloidal Palladium, shown in Fig. 1.7. The core of the colloidal is composed of Pd/Sn covered by the ions of tin. The Palladium is in state of Pd^{2+}, thus non-catalyzer. The counter-ions of chloride ensure the stability of colloidal. After soaking in the tank, the object is washed with the water this modify the pH of the colloidal locally. The palladium transforms from the state Pd^{2+} to Pd^{0}, which enables to trigger the reaction of metallic deposition. This reaction will be explained later in this section.

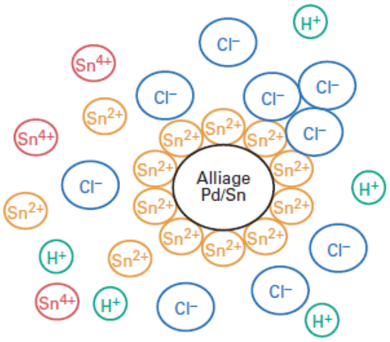

Figure 1.7: Solution of colloidal Palladium (10 nm)

The third tank corresponds to the "electroless" reaction. The principle is based on the reaction of oxydo-reduction between the deposited metallic ions with a reducing agent presented in the solution of the tank. The source of electrons is from the reducer in the solution and the deposition of the metal is "catalyzed" on the surface of the object as shown in Fig. 1.8 [28], [29].

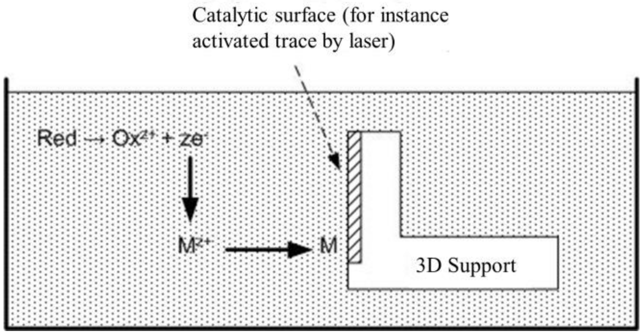

Figure 1.8: Principle of ELD

In fact, the reaction is a controlled metastable equilibrium. In other words, the reduction is possible in the volume of the solution, but it cannot be produced spontaneously. The reduction can only occur with a presence of a catalytic surface on the surface of the object.

After depositing the first layer of the metal, in general, the process stops. However, for certain metals called auto-catalytic, the first layer is catalytic and can be served as a new catalytic surface. This will continue and maintain the reaction. In other words, this metallization reaction is auto-maintained. The auto-catalytic metals are in groups VIII and IB of the table of Mendeleyev, i.e. Fe, Ru, Os, Co, Rh, Ir, Ni, Pd, Pt, Cu, Ag and Au. Among them, we have the copper.

The global reaction can be expressed as

$$M^{Z+}_{solution} + Red_{solution} \xrightarrow{catalyzer} M_{solide} + Ox^{Z+}_{solution}$$

Cette thèse est accessible à l'adresse : https://theses.insa-lyon.fr/publication/2023ISAL0007/these.pdf
© [X.V.L. NGUYEN], [2023], INSA Lyon, tous droits réservés

In case of depositing the copper, the ions of copper (Cu^{2+}) is reduced by the formaldehyde (CH_2O) in an aqueous solution. The global reaction of depositing is given by [30] :

$$Cu^{2+} + CH_2O + H_2O \rightarrow Cu + 2H^{+} + CH_2O_2$$

In reality, the exact mechanism is complicated and is not completely elucidated. The best description of the reaction is given as

$$ML_m{}^{Z+} + Red \rightarrow M + mL + Ox^{Z+}$$

where, M is deposited metal, L is complexing agent, m is number molecular of complexing agent, $ML_m{}^{Z+}$ is the ions of deposited ions complexed by m molecular of L, Ox^{Z+}/ Red is redox couple serving as the source of electrons.

The complexing agent keeps the role of reducing the concentration of free metallic ions in the liquid solution in order to satisfy the condition of meta-stability. In case of ELD of copper, the complexing agent is generally EthyleneDiamineTetraAcetic acid (EDTA). Fig. 1.9 introduces how the copper is complexed by EDTA. During this reaction, the cage is in the contact of catalyst on the surface of the object for the reducing of Cu^{2+} by CH_2O and for the depositing of copper on the surface of the object.

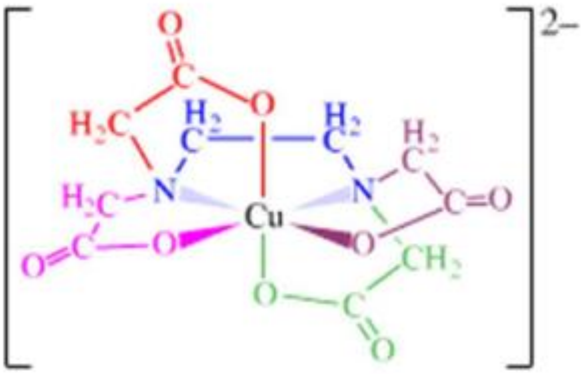

Figure 1.9: Copper in EDTA

In summary, the electroless metallization of copper is systematically composed of the following elements

- A metallic salt, source of metallic ions necessary for the metallization.
- A reducing agent to provide the electrons for the reduction of the metal ions.
- A complexing agent of metallic ion, which is used to reduce the concentration of free ions in the solution in order to satisfy the meta-stability conditions and to prevent the formation/precipitation of metal oxides or hydroxides in a basic medium (which constitute the contamination of the deposition)
- The additives to modify the properties of the tank for the optimization of the deposition such as the size of the grains, the speed of deposition, its stability, the pH of the solution, etc.

It is thus possible to make a metal layer by varying the duration of the deposition. Therefore, this growth stops only if the species present in the solution have been consumed, or if the parameters of the liquid tank (temperature, pH, concentrations, etc.) change, this leads to non-compliance with the meta-stability [29], [30].

In reality, there are other reactions which occur at the same time, which lead, for instance, to the generation of hydrogen within the formed layer, to the induction of impurities. Due to the co-

Cette thèse est accessible à l'adresse : https://theses.insa-lyon.fr/publication/2023ISAL0007/these.pdf
© [X.V.L. NGUYEN], [2023], INSA Lyon, tous droits réservés

deposition of chemical elements from the liquid tank, the purity of electroless copper deposition has a lower purity comparing to the electrolytic counterparts (99.2 % minimum against 99.9%). This will lead the impact on the resistivity: 0.02 to 0.025 µΩ.m for the electroless copper and 0.017 µΩ.m for the bulk copper.

A comparison with respect to printing inks used in antennas and RF circuits manufacturing is listed in Table 1.2.

Table 1.2: Comparison of conductivity of conductors used in antennas and RF circuits manufacturing

Ref.	Type of conductor	Conductivity (MS/m)	Resistivity (µΩ.m)
	Bulk copper	58	0.017
[31]	Silver conductive ink (Capot CS-32)	5	0.2
[32]	Capot Nanoparticle silver ink	3.8-4	0.25-0.26
[33]	Nanoparticle conductive silver ink	9.1	0.11
[34]	Nanoparticle conductive silver ink	8.8	0.11
[35]	Graphene ink for screen-printing technology	7.13	0.14
[36]	Graphite Nanoplate (GNP) printing ink	4.66	0.215
This work	Electroless deposited copper	45±4.5	0.02-0.025

1.3.2.3. Placing and connecting the SMD to the conductive traces.

An important point is the method used for electrically connecting the SMDs on the conductive traces. The method depends on the thermal properties of the polymer (Fig. 1.3). When the polymer can stand the temperatures, conventional brazing is preferred (sometimes brazing with low temperature solder). When this is not possible, the connection is made with conductive paste, which conductivity and reliability are lower that solders. This point is important for RF applications.

1.3.2.4. Concluding remarks

Many metals (but not all) can be deposited by the electroless process. Copper ELD was discussed above, but it is possible to deposit multiple layers with different metals. One important example is the ELD of a tri-layer of copper/nickel-phosphore/gold for PCBs (ENIG finishing) and also for plastronic devices (Fig. 1.10), to prevent copper oxidation [9]

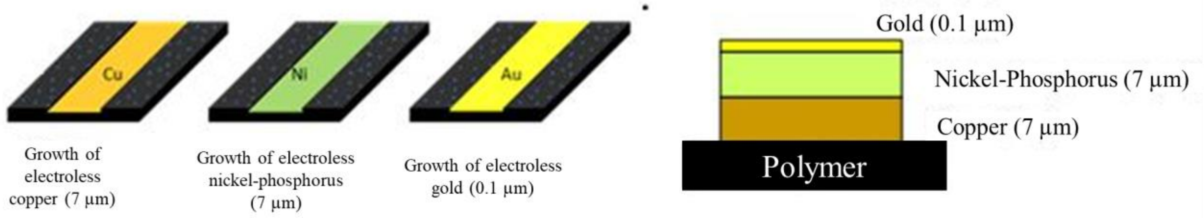

Figure 1.10: Principle of ENIG [9]

Another advantage of ELD is that it is performed in liquids: therefore, it is possible to metallize a hole as long as the liquids can go through the hole. In PCBs and 3D Plastronics, cylindrical holes (called vias) are used to connect different conductive layers separated by non-conductive layers. The internal surface of the vias is metallized with ELD. Therefore, independently of Plastronics, ELD is a process of major importance.

Cette thèse est accessible à l'adresse : https://theses.insa-lyon.fr/publication/2023ISAL0007/these.pdf
© [X.V.L. NGUYEN], [2023], INSA Lyon, tous droits réservés

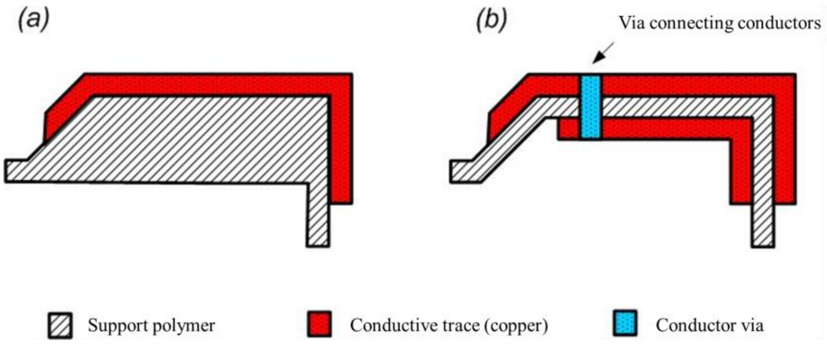

Figure 1.11: Realization of plastronics circuits with one layer (a) and two layer with via (b)

1.3.3. The main technologies used for 3D Plastronics

1.3.3.1. Two shot injection molding

Two shot injection molding (also called 2K injection molding) is one of the oldest and more efficient process for 3D Plastronics. The principle is to inject two polymers of different nature in a mold with a rotating cavity. The injection is performed in two steps (hence the name):

- Firstly, the first polymer is injected into the mold cavity and fill it
- Then the mold is rotated so that the cavity has a new internal empty volume and the second polymer is injected in order to fill the second volume.

The result is a partial over-molding of one polymer of the other. Polymers are chosen for their good adhesion at the interface.

To create the electrical traces, the part is entirely immersed in a liquid chemical etching solution. The outside surface of one polymer is etched whilst the outside surface of the second is not chemically attacked. So, when the catalyzation is performed prior to the ELD of copper, the outside surface of the first polymer is catalyzed, whilst the outside surface of the second polymer is not catalyzed. ELD copper is therefore only created on the first surface.

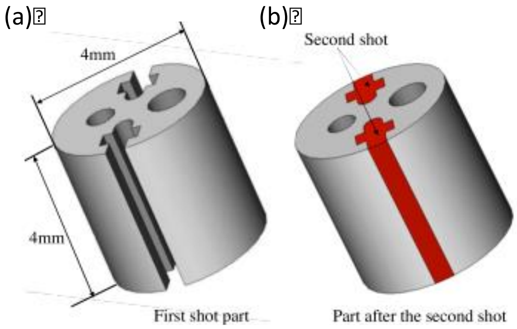

Figure 1.12: Principe for the fabrication of 3D plastronic parts with two shot injection molding [37], [38].

Thin traces can be made on complex 3D surfaces, useful for example for complex electrical connectors [8], [39]. However, the tool for injection molding is very complex and expensive. Therefore, this technology is only used for mass production.

1.3.3.2. Laser Direct Structuring

Laser Direct Structuring (LDS) is a process extensively used in 3D Plastronics [8], [9]. We describe below the “classical” LDS process suitable for mass production and the ProtoPaint LDS process which is interesting for prototyping [9].

Cette thèse est accessible à l'adresse : https://theses.insa-lyon.fr/publication/2023ISAL0007/these.pdf
© [X.V.L. NGUYEN], [2023], INSA Lyon, tous droits réservés

The classical LDS process consists of using thermoplastic pellets with a catalyst filler suitable for ELD. The filler is not an expensive catalyst like palladium, but is a mixture of copper and chromium oxide.

A laser beam draws the pattern on the substrate of the molded devices. This operation aims to reveal the particles dispersed in the matrix by etching the latter, and also to reduce the particles. Once reduced, the substrate is immersed in an electroless metallization tank to grow the metal layer along the pattern. The different steps are illustrated in Fig. 1.13.

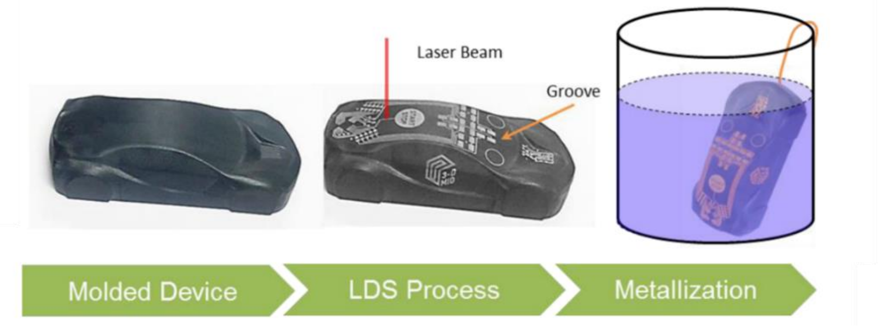

Figure 1.13: Steps of fabricating the object using LDS [8]

This method adapts many polymers as substrates as well as complex geometries. The resolution of the process is directly related to the resolution of the laser as well as the electroless process. The etching the polymer matrix increases its roughness.

The different steps of manufacturing a plastronic device made by laser structuring are as follow

- Injection of the plastic part in a plastic matrix doped with particles of a metallization catalyst
- Definition of the pattern and reduction of particles due to the passage of the laser
- Metallization by soaking the substrate in electroless tanks. The first layer is a layer of electroless copper (the thickness depends on the application). The other layers are protective layers (gold or silver) to limit the oxidation of copper and the soldering of the components
- The finalization step is the deferral of the components.

Figure 1.14: Different steps of realizing a plastronic device using LDS: molding, activation, metallizing and components mounting [40]

Cette thèse est accessible à l'adresse : https://theses.insa-lyon.fr/publication/2023ISAL0007/these.pdf
© [X.V.L. NGUYEN], [2023], INSA Lyon, tous droits réservés

Figure 1.15: Machine LPKF MicroLine3D 160i

However, to validate the functions of a plastronic device, it is possible to print the support directly by additive manufacturing (3D printing), which avoids having to machine an injection mold. The part is then coated with a lacquer containing the additive necessary for laser structuring (ProtoPaint lacquer from LPKF), then it is activated by the laser and metallized as previously indicated.

The use of ProtoPaint lacquer significantly reduces the manufacturing costs of prototypes and can be interesting for very small series of devices.

Nevertheless, this method has disadvantages. Indeed, the materials used in 3D printing are much less efficient, in terms of mechanical properties, than those used in injection. The surface finish of the parts is difficult to control. It depends on the method chosen for 3D printing (including the thickness of the lacquer) but it also depends on the manual sanding phases necessary for the ProtoPaint process.

The further information about this process is detailed in [9]

To conclude, the LDS process was not chosen for this project because of its high cost, which depends on two factors: the cost of the laser machine for performing the laser structuring and the cost of the laser machine for performing the laser structuring.

However, LDS gives access to a series of polymers (which is not the case of Rapid Plastronics) and notably polymers with interesting RF properties as it will be discussed in Section 1.4. Therefore, the LDS may be considered in the future for RFEH. It is worth noting that the LDS ELD copper is quite similar to the Rapid Plastronics copper ELD (thickness, resistivity). However, the difference is still the surface roughness of the copper: 6.4 µm for LDS [41] due to the laser activation and 1 µm for Rapid Prototyping. The point will be discussed in Chapter 3.

It reminds that the “classical LDS” process is not suitable for prototyping. The Protopaint LDS is suitable for this and this process has been extensively reported in [9] a joint project between the company S2P and AMPERE. The process is poorly repeatable. A lot of manual work is necessary to get good results. The polymer used in [9] is the High Temp Resin v1 from Formlabs and also studied in this thesis. However, the effect of the lacquer on the RF properties of the antennas of RFEH should be evaluated.

Cette thèse est accessible à l'adresse : https://theses.insa-lyon.fr/publication/2023ISAL0007/these.pdf
© [X.V.L. NGUYEN], [2023], INSA Lyon, tous droits réservés

1.3.3.3. In Mold Electronics

In Mold Electronics (IME) [42], [43] is a totally different process of growing interest in making “smart surfaces”, that is to say thin polymer shells with embedded sensors or antennas.

The main substrate is a thermoplastic film, typically PolyCarbonate. The principle (Fig. 1.16) is to

- Print the conductive network on the film by means of screen printing or ink jet printing of conductive inks
- Cure the ink with heat, for example
- Place the SMDs with the pick and place machine and connect them to the traces with conductive glue
- Thermoform the assembly in order shape of the substrate (bearing the traces and the SMDs) in 3D
- Place the assembly in the cavity of an injection mold and overmold it with a thermoplastic (of the same nature of the initial sheet for example).

The result is a polymer shell with a thickness of 2-3 mm with embedded conductive trace and SMDs.

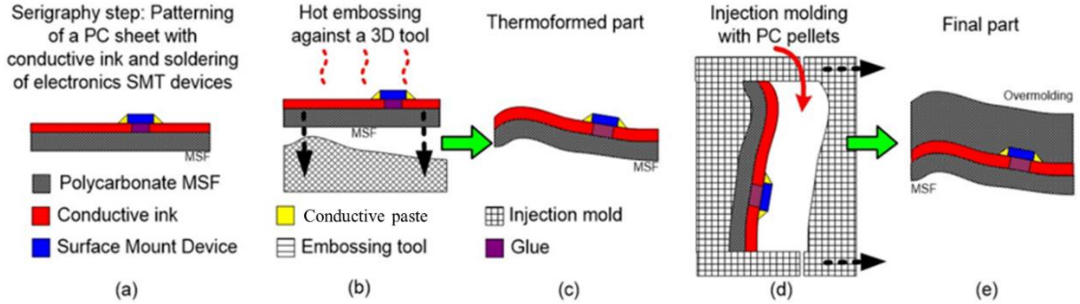

Figure 1.16: Principle of IME

IME was not chosen for this work because it makes use of conductive inks with poor resistivity compared to electroless copper. Also, the main polymer used in IME is so far PolyCarbonate (PC). The RF properties of the PC will be discussed in Chapter 3.

1.3.4. Rapid Plastronics

Rapid Plastronics, developed at AMERE, is still an emerging technology. This technology was extensively used to fabricate the prototypes for this work. Therefore, we summarize here the advantages and drawbacks of this technology.

The principle is to print the polymer with SLA, so that non-porous parts can be obtained. Contrary to most ELD processes, the part is not etched with chemicals like Chromic Acid or SulfoChromic. Instead a non-hazardous not chemical process is applied. Then the part is catalyzed with palladium and copper can be deposited trough ELD as described previously. The surface of the part is thus entirely metallized. Vinyl mask cut with a plotter is placed on the part, so that non-protected copper is chemically etched with iron perchloride. Then the vinyl mask is removed.

This process is described in more details in Chapter 3. It allows quick and lost fabrication of 3D plastronic parts. Neither as a LPK machine, nor the development of an injection mold is necessary. The surface roughness of the copper is significantly better than with the LDS Protopaint process. The adhesion of copper is tested successfully with Scotch Test.

Cette thèse est accessible à l'adresse : https://theses.insa-lyon.fr/publication/2023ISAL0007/these.pdf
© [X.V.L. NGUYEN], [2023], INSA Lyon, tous droits réservés

For the moment, it is used in combination with 3D printing by Stereolithography. To fabricate the support, 3D printing was used and the SLA was chosen because the parts are non-porous and a good surface roughness.

1.3.5. Conclusion

It shows that Rapid Plastronics is a low cost, flexible and performing technology, which allows quick fabrication of prototypes. Manuel soldering is possible as well as the fabrication of vias. However, the devices are brittle. We shall also see in Chapter 3 that the chosen SLA resins have a permittivity comparable with many polymers but present higher RF loss. Table 1.3 is a comparison of electromagnetic properties between the used SLA resins in this thesis with the common antennas' substrate integrated in telephones for communications applications.

Table 1.3: Comparison between used SLA resins with common antennas' substrates in telephones

Material	Relative permittivity	Loss tangent
LCP Vectra E820i	4.3 @ 2.45 GHz	0.004 @ 2.45 GHz
PEEK	3.2 @ 1 MHz	0.002 @ 1 MHz
Pocan DP T 7140 LDS	4.1 @ 1 MHz	0.0138 @ 1 MHz
Pocan TP 710-003 LDS	3.26	0.01
PPS with 40 % of fiber glass for reinforcement	4	0.025
High Temp Resin v1 (for Rapid Plastronics)	(3±0.1) @ 0.5-2.5 GHz	(0.025 ± 0.0025) @ 0.5-2.5 GHz
High Temp Resin v2 (for Rapid Plastronics)	(2.9±0.1) @ 0.5-2.5 GHz	(0.04 ± 0.0025) @ 0.5-2.5 GHz

1.4. 3D plastronic antennas

The following state-of-art of the antennas is classified against the different techniques of fabrication. At the end of the section, Table 1.4 will detail the information of the antennas of our state-of-art.

As mentioned above, the antenna for RF communication is one of a major application of 3D Plastronics. Antennas are integrated in mobile phones housing either by two shot injection molding or by LDS. Fig. 1.17 and Fig. 1.18 give examples of such antennas.

1.4.1. Two shot molding (2K) / ELD

An example of antenna fabricated using two shot molding technique [44] is illustrated in Fig. 1.17.a. The antenna might be a PIFA (Planar Inverted-F Antenna) integrated into the mobile phones for communication applications. The antenna in Fig.1.17.b. is done with two shot molding by Nokia and Hitachi Cable Ltd. [45]. However, the information about the substrates, the conductors as well as the radiating performance of the antennas are not given in the article.

Figure 1.17: a. PIFA antenna; b. Antenna fabricated using two shot molding

Cette thèse est accessible à l'adresse : https://theses.insa-lyon.fr/publication/2023ISAL0007/these.pdf
© [X.V.L. NGUYEN], [2023], INSA Lyon, tous droits réservés

1.4.2. Laser Direct Structuring (LDS) / ELD

The antenna module of the smartphone Samsung Galaxy Note 10 illustrated in Fig. 1.18 is an example of LDS antenna for communication applications. The module consists of the PIFA, monopole antennas. The information about the substrate, the radiating performance of the antennas are not provided.

Figure 1.18: Antenna module of Samsung Galaxy Note 10 fabricated using LDS

A concept of a 3D PIFA antenna, whose resonant frequency is 2.185 GHz, realized by the LDS is introduced in [46] (shown in Fig. 1.19), the antenna is placed on the external surface, meanwhile the ground plane is placed on the internal surface of a thermoplastic shell LCP Vectra E820i (relative permittivity of 4.3 and loss tangent of 0.004). The maximum gain of the antenna is 1.2 dB with an omni-directional radiation pattern.

Figure 1.19: 3D PIFA antenna on LCP Vectra E820i fabricated by LDS

Another example of the LDS antenna is the Inverted-F Antenna (IFA) presented in [47] integrated into the mobile phones for the communications. The first antenna (in green in Fig. 1.20.a) operates in the frequency of 780 MHz and the second antenna (in blue in Fig. 1.20.a) operates in the frequency of 915 MHz. The substrate of the antennas is Pocan DP T 7140 LDS, which is the plastic with the type of PET/PBT (PolyEthylene Terephthalate/PolyButylene Terephthalate). The electrical properties of this substrate at 1 MHz is 4.1 for the relative permittivity and 0.0138 for the loss tangent.

Cette thèse est accessible à l'adresse : https://theses.insa-lyon.fr/publication/2023ISAL0007/these.pdf
© [X.V.L. NGUYEN], [2023], INSA Lyon, tous droits réservés

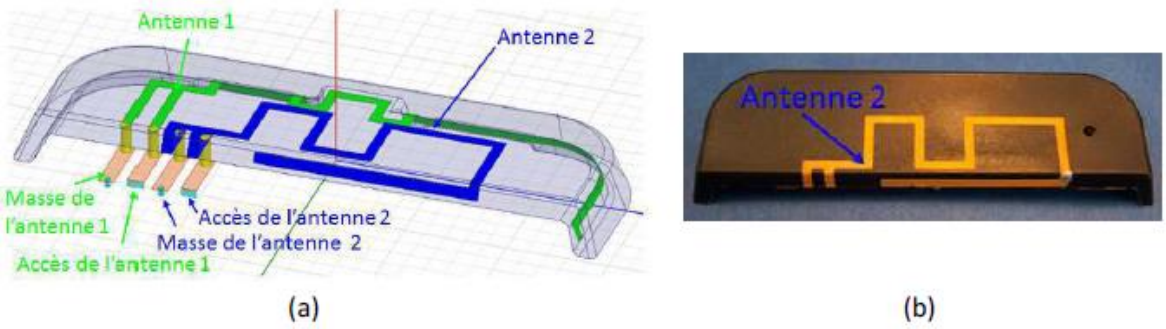

Figure 1.20: IFA antenna fabricated using LDS [47]

The LDS technique can be also used for the manufacturing the 5G antennas integrated into the base-station. Chen et al. introduce a base station antenna for 5G applications (band 41 – 2.5 GHz) [48]. The structure is realized on the substrate of PPS (PolyPhenylene Sulfide) reinforced with 40% of glass fiber to strengthen the solidarity of the substrate (relative permittivity of 4 and loss tangent of 0.0025). The alimented lines, the radiating elements, the phase shifting lines and the ground of the antennas are realized by LDS (in grey in Fig. 1.21). The maximum gain of the antenna at 2.4 GHz and 2.5 GHz are 7.2 dBi and 7.9 dBi, respectively. The dimension of an antenna unit (AU) is 180 mm x 116 mm x 10 mm.

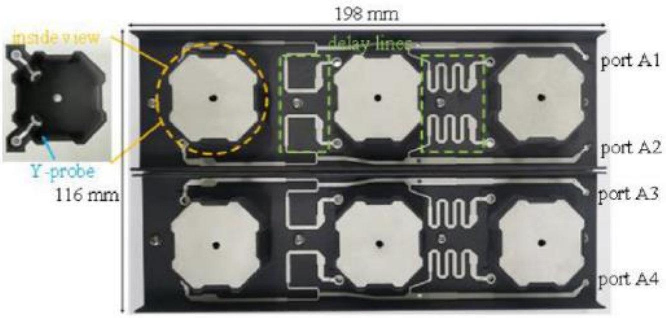

Figure 1.21: Antenna for 5G application in base station antenna fabricated with LDS

LDS can be used for more exotic applications. A dual polarized log periodic antenna printed on conical Molded Interconnect Device (MID) substrate is described in [49]. The antenna provides an input matching better than -8 dB over a range of frequency from 3 GHz to 9 GHz. The antenna encompasses two orthogonal linear polarization patterns. A maximum gain of 5.6 dBi is obtained at 5.5 GHz. The substrate of the antenna is Pocan TP 710-003 LDS (relative permittivity of 3.26 and loss tangent 0.01) and is fabricated using Laser Direct Structuring technique. LPKF-LDS process is applied to deposit the antenna on the surface of the substrate. The principle of this method of depositing is described in [9].

Figure 1.22: Log-periodic four arm antenna realized on MID substrate [49].

Cette thèse est accessible à l'adresse : https://theses.insa-lyon.fr/publication/2023ISAL0007/these.pdf
© [X.V.L. NGUYEN], [2023], INSA Lyon, tous droits réservés

1.4.3. 3D Printing and ELD (non LDS or 2K processes)

In [50], a conformal array antenna is investigated using a combination of FDM 3D printing technique and probably a combination of ELD and copper electroplating plating technique [51]. The circular patch antenna elements are fabricated on a ABS-M30 substrate whose relative permittivity of 2.56 and loss tangent of 0.008 in the range of 1.2 to 1.4 GHz. The nonplanar substrate has a radius of curvature 1.128 m, arc length 1.219 m, and the width 18.034 cm. The front-surface copper plated antenna and the rear-surface plated-copper ground plane are fabricated by RePliForm. For the connection between the SMA feeding probe and the antenna, the silver epoxy is used. The antenna is well-matched at 1.23 GHz and the peak measured gain of the antenna element is 4.7 dBi.

Figure 1.23: The nonplanar patch array with copper plated elements on a 3D-printed substrate [50]

1.4.4. 3D Printing and patterning with conductive ink

In [52], a planar circularly polarized patch antenna fabricated using SLA printing technique and inkjet printing of silver inks for the substrate of the antenna and the conductor respectively. The Formlabs Form 1+ printer is used to fabricate the substrate and the inkjet printer is the Argentum from Cartesian Co. However, the reference of the SLA resin and the silver inks are not indicated in the article. The dielectric of the printed substrate is extracted through transmission line system method, which will be studied in Chapter 3, and is given as 2.83 of relative permittivity and 0.038 of loss tangent. The antenna has a good matching at 1.6 GHz and 2.4 GHz with the corresponding directivity of 7 dB and 5 dB at 1.6 GHz and 5 dB at 2.4 GHz respectively.

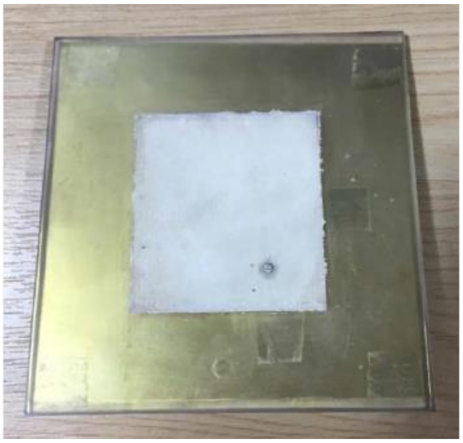

Figure 1.24: Fabricated patch antenna in [52]

In [53], a very wideband double-ridge horn antenna fabricated using SLA method is presented. The selected material for the substrate fabrication is Accura SI 10 due to its high accuracy and stability and the printer is Viper SLA system from 3D Systems. The operating band of frequency of this

Cette thèse est accessible à l'adresse : https://theses.insa-lyon.fr/publication/2023ISAL0007/these.pdf
© [X.V.L. NGUYEN], [2023], INSA Lyon, tous droits réservés

antenna is from 2-12 GHz. The aperture of the antenna is 121×69 mm^2 and the length of the antenna section is 88 mm. The metallization is performed by coating the antenna with a layer of conductive ink with a conductivity of 4×10^5 S/m. Since the antenna is ultra-wideband and waveguide type, the gain and the efficiency are not significantly affected. The simulated (measured) gains at 3, 6.5 and 10 GHz are 9.0 (8.5) dBi, 11.9 (11.3) dBi, and 12.3 (12.2) dBi respectively. The antenna efficiency is larger than 87% over the operating frequency range. This parameter of the antenna can increase to above 95% by using the copper electroplating method. Further information about this antenna is plotted in Fig 1.25.

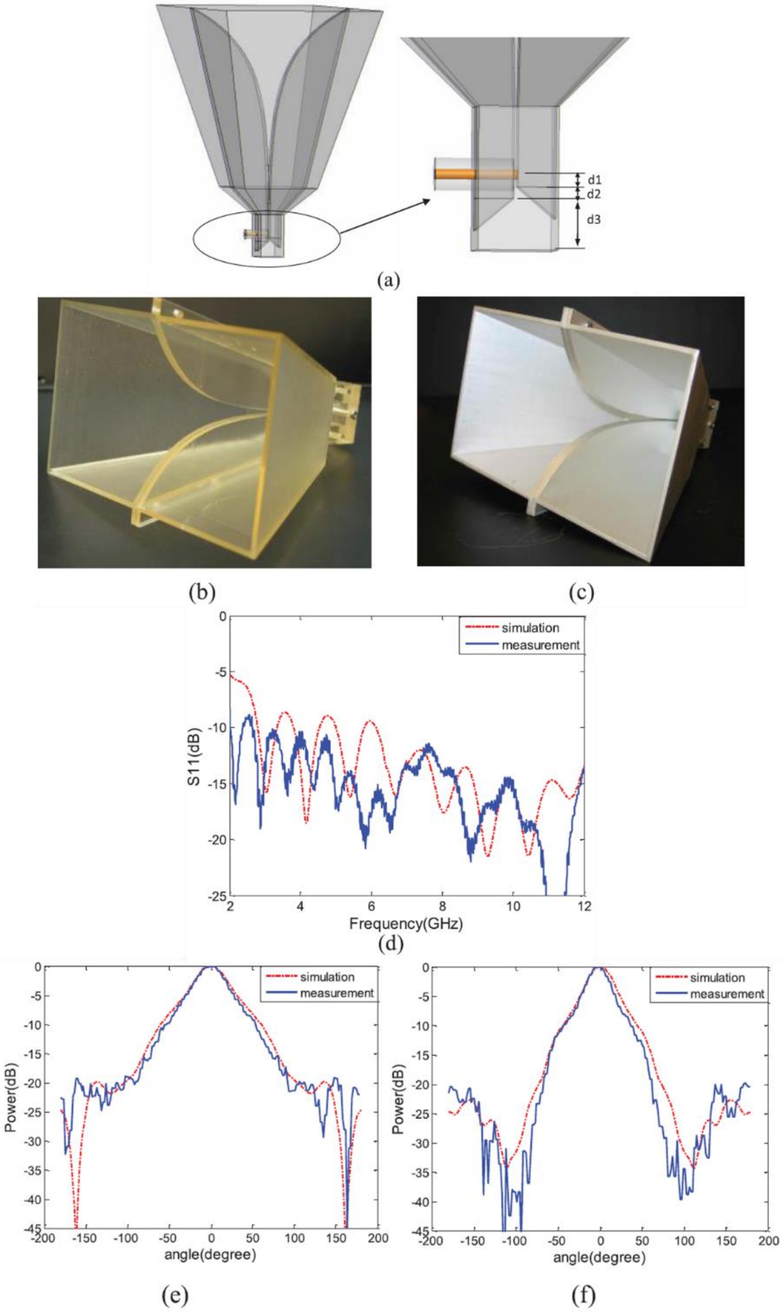

Figure 1.25: Model (a) and realized antenna (b, c); simulated and measured reflection coefficient (d) and simulated and measured radiation pattern in E-plane (e) and H-plane (f).

In [54], a 3D printed circularly polarized 2x2 X-band (8-12 GHz) horn array antenna is presented. The antennas are manufactured by fused deposition modelling of PLA material using Scoovo C170

Cette thèse est accessible à l'adresse : https://theses.insa-lyon.fr/publication/2023ISAL0007/these.pdf
© [X.V.L. NGUYEN], [2023], INSA Lyon, tous droits réservés

3D printer for the shape and then are coated with carbon conductive material on their surface. The antenna has a good measured reflection coefficient over a wide band of 7.5-10 GHz. Additionally, the antenna achieves around 400 MHz axial ratio bandwidth for a circular polarization and a directivity of 10 dB with the center frequency of 8.5 GHz.

Figure 1.26: Printed of array horn antennas by PLA material [54].

1.4.5. 3D Printing and patterning with metal foil

A dual-band and dual-circular polarization stacked patch antenna is developed in [55] operating at 2.75 GHz and 3.2 GHz. The substrate of the antenna is fabricated applying the SLA technique. The material for the SLA printer is WaterShed XC 11122 whose relative permittivity is 3.11 and loss tangent is 0.0253. Concerning the antenna part, a thin aluminum plate is employed as the ground plane and two thin copper slices comprise two patches with the conductivity of 5.7×10^7 S/m. The antenna has dual bandwidth, which are 2.64-2.9 GHz and 3.08-3.36 GHz. The measured gains of the antenna at 2.75 GHz and 3.2 GHz are 6.7 dBic and 7.3 dBic respectively.

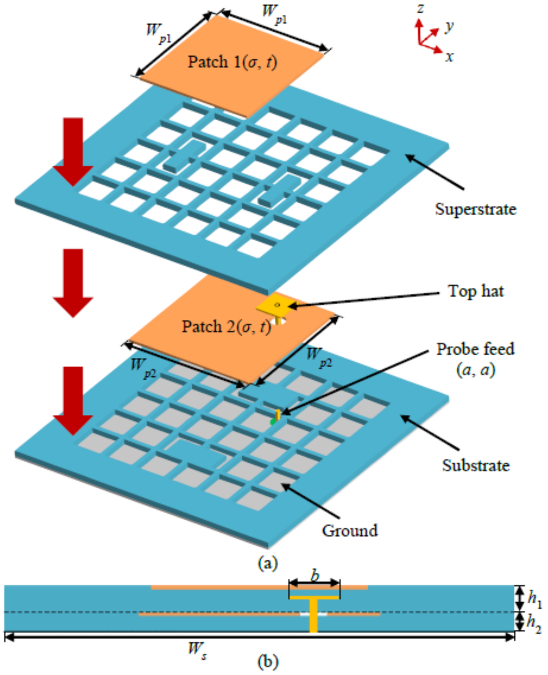

Figure 1.27: Configuration of the proposed dual band and dual circular polarization stacked patch antenna. (a) tear-down view; (b) side view [55].

Farooqui et al. [56] present a 3D printed tunable microstrip patch antenna with an L-slot on the surface for the circular polarization. The substrates of the antenna are made of Acrylonitrile Butadiene Styrene (ABS) whose permittivity is 2.7 and loss tangent is 0.005. The substrate is printed using the MakerBot Replicator2 printer. For the metallized part of the antenna, an aluminum tape is milled to include the L-slot for the patch using the LPKF ProtoMat D104. The

Cette thèse est accessible à l'adresse : https://theses.insa-lyon.fr/publication/2023ISAL0007/these.pdf
© [X.V.L. NGUYEN], [2023], INSA Lyon, tous droits réservés

via holes are metallized using the Circuitworks CW2400 conductive silver epoxy (1×10^4 S/m). The resonant frequency of the antenna can be tuned from 2.36 to 1.64 GHz when DC bias-voltage of the varactors Skyworks SMV2019 varies from 16 to 6 V, respectively. Under the influence of DC bias, the capacitance of the varactor changes, which changes the effective length of the patch, then, frequency tuning of the antenna is achieved. The measured gain of the antenna array is 4.5 dBi at 2.13 GHz and 2.6 dBi at 1.84 GHz.

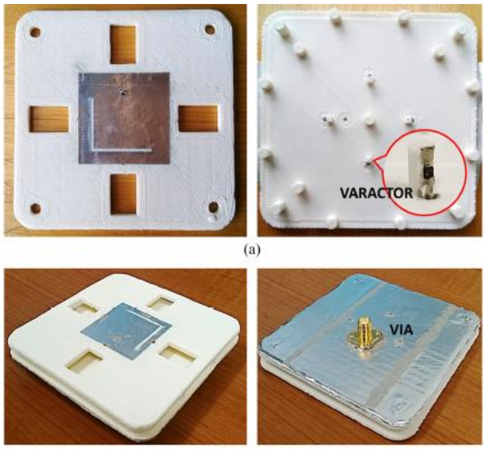

(a)

(b)

Figure 1.28: Tunable microstrip patch antenna introduced in [56] (a. Top (left) and bottom (right) ABS layer; b. Antenna after mounting the connector and realization of the vias) [56].

1.4.6. Conclusion

Table 1.4 summaries the different antennas in category of methods of realizing the conductor, substrate fabrication method, band of frequency, performance of antennas and dimensions. According to the state-of-art, there are three ways of realizing the conductor: applying ELD method, depositing the conductive ink and using metal foil (copper, aluminum).

Cette thèse est accessible à l'adresse : https://theses.insa-lyon.fr/publication/2023ISAL0007/these.pdf
© [X.V.L. NGUYEN], [2023], INSA Lyon, tous droits réservés

Table 1.4: References of 3D plastronic antennas

Ref	Conductor realization method	Substrate (relative permittivity – loss tangent) / Realization method	Band of frequency	Type of antenna	Performance of antenna
[46]	LDS / ELD	LCP Vectra E820i (4.3 – 0.004) / NI	2.185 GHz	PIFA	1.2 dB at 2.185 GHz
[47]		Pocan DP T 7140 LDS (4.1 – 0.0138) / NI	780 MHz 910 MHz	PIFA	NI
[48]		PPS reinforced with 40 % of glass fiber (4 – 0.025) / NI	2.5 GHz	NI	Gain : 7.9 dBi at 2.5 GHz
[49]		Pocan TP 710-003 LDS (3.26 – 0.01) / NI	3-9 GHz	Dual linear polarized log-periodic antenna	Gain: 5.6 dBi at 5.5 GHz
[50]	ELD and Copper Plating	ABS-M30 (2.56 – 0.008) / FDM	1.23 GHz	Patch antenna	Gain 4.7 dBi at 1.23 GHz
[52]	Conductive ink (Silver ink)	SLA Resin of Formlabs (2.83 – 0.038) / SLA	1.6 GHz 2.4 GHz	Planar circularly polarized patch antenna	Directivity: 7 dB at 1.6 GHz Directivity: 5 dB at 2.4 GHz
[53]	Conductive ink (4 x 10^5 S/m)	Accura SI 10 / SLA	2-12 GHz	Horn antenna	Gain: 8.5 dBi at 3 GHz Gain: 11.3 dBi at 6.5 GHz Gain: 12.2 dBi at 10 GHz
[54]	Carbon conductive material	PLA / FDM	8-12 GHz	Circular polarization horn antenna	Directivity: 10 dB at 8.5 GHz
[55]	Metal foil (Copper – 5.7 x 10^7 S/m)	WaterShed XC 11122 (3.11; 0.0253) / SLA	2.75 GHz 3.2 GHz	Dual-circular polarization stacked patch antenna	Gain: 6.7 dBic at 2.75 GHz Gain: 7.3 dBic at 3.2 GHz
[56]	Metal foil (Aluminium)	ABS (2.7; 0.005) / FDM	1.6-2.4 GHz	Planar tunable microstrip patch antenna	Gain: 2.6 dBi at 1.84 GHz Gain: 4.5 dBi at 2.16 GHz

NI: Not Indicated in the article

For the low-power energy harvesting applications, the loss of conductor should be well minimized. With the conductive ink, the conductivity of used ink are lower than the ELD copper and massive copper's value. This can increase the conductive loss in the circuit. Using the metal foil as a conductor can be considered as a solution. However, the method of depositing the foil on the polymer surface in 3D form should be studied. The glue can be used in this situation, but it might have the impact on the performance of the RF circuits. Among them, ELD method has an easier access to achieve a good conductor to manufacture the energy harvesting circuits, especially RF energy harvester.

The substrates should be also studied to design the RFEH circuits. Low loss substrates enable to reduce the dielectric loss at high frequencies and therefore to improve the electrical performance

Cette thèse est accessible à l'adresse : https://theses.insa-lyon.fr/publication/2023ISAL0007/these.pdf
© [X.V.L. NGUYEN], [2023], INSA Lyon, tous droits réservés

of the circuits. The substrates used for antennas of telephones, i.e. LCP, PEEK, etc. might be considered in this case due to their low loss at high frequency.

LDS and two shot molding are the popular methods to fabricate the antennas in telephones for communications [44], [45]. However, these antennas are not preferred for energy harvesting applications. This might come from their low radiating performance (gain, radiation patter, impedance matching, etc.).

The dual-linear polarized antenna proposed in [49] has a very wide band of frequency with a high gain. For the energy harvesting applications, this antenna is a good candidate. However, the form factor of the antenna is a main limit for the choosing. Moreover, our focused band of frequency is Wi-Fi 2.4G band, the wide band in this situation is not truly necessary. Regarding the fabrication technique, the selected method in [49] is quite expensive as indicated below.

SLA and FDM have a lower cost than LDS. Both techniques are able to fabricate not only 2D planar [52] [55] [56], 2D antenna printed on curved surfaces [50] but also 3D form antenna [53] [54]. Compared to FDM technique, SLA can manufacture the objects with a better surface roughness. It should be noticed that the surface roughness of the objects has the impacts on the performance of the RF circuits. These statements will be further mentioned in the next Chapter. In conclusion, the preferred technique for the fabrication of substrate is Stereolithography.

1.5. Wrap-Up

In this chapter, we report the different methods of manufacturing the 2D and 3D form electric circuits, which are PCB and FLEX-PCB, Printed Electronics and 3D Plastronics.

PCB and FLEX-PCB are conventional methods, and are developed and optimized largely. However, these methods use a few substrates for the manufacturing while 3D Plastronics has a wide variety of substrates which are generally not (yet) optimized. This can give the new possibilities of choosing the low loss substrates for RF energy harvesting applications.

Printed Electronics is a method close to 3D Plastronics. The main drawback of this method is the high electrical resistivity of conductive ink used in manufacturing. This can increase the loss in the RFEHs, then, reduce the performance of the circuits.

Comparing to Printed Electronics, for 3D Plastronics, the conductor, called electroless copper, is obtained using ELD method, whose resistivity is close to bulk copper’s one. Another advantage of this metallization method is that the surface of the objects can be metallized as long as the liquid can go through.

In order to manufacture the polymer substrates, in 3D Plastronics, the common methods are injection molding and/or thermoforming. These methods are very suitable for the mass-production. Nevertheless, with a complex form of substrates, the used molds are very expensive and the deployment is complicated. Therefore, 3D printing methods, i.e. Fused Deposition Modeling, Laser Sintering, Stereolithography, are preferred in case of prototyping a few 3D substrates for the research. Among three methods, Stereolithography is a convenient solution due to its good surface finishing before curing and no porosity. In addition, using acceptable thermal performance polymers (High Temp Resin v1 and High Temp Resin v2 in this thesis) may allow us to solder the SMDs on the surface of the polymers.

During our first attempt, SLA resins are selected. However, these resins have poor RF properties (which will be studied in Chapter 3). LCP and PEEK, which are used commonly as substrates of telephone antennas, may be considered to replace these SLA resins due to its good RF and thermal properties.

Cette thèse est accessible à l'adresse : https://theses.insa-lyon.fr/publication/2023ISAL0007/these.pdf
© [X.V.L. NGUYEN], [2023], INSA Lyon, tous droits réservés

CHAPTER 2: STATE-OF-ART ON AMBIENT ENERGY HARVESTING

Cette thèse est accessible à l'adresse : https://theses.insa-lyon.fr/publication/2023ISAL0007/these.pdf
© [X.V.L. NGUYEN], [2023], INSA Lyon, tous droits réservés

Cette thèse est accessible à l'adresse : https://theses.insa-lyon.fr/publication/2023ISAL0007/these.pdf
© [X.V.L. NGUYEN], [2023], INSA Lyon, tous droits réservés

2. STATE-OF-ART ON AMBIENT ENERGY HARVESTING

In this chapter, different energy harvesters and specially Radio Frequency Energy Harvester (RFEH) will be reported. First of all, mechanisms of demonstrated energy harvesters, power density as well as their advantages and disadvantages are discussed. In the second section, the description of a RFEH using antennas (also called rectennas) is studied. Some examples about 3D rectenna in the recent literature are presented afterwards. A conclusion will be given at the end of this chapter.

2.1. Mechanisms of ambient energy harvester circuits

Ambient energies are available under many different forms such as light, temperature, pressure, Radio Frequency, etc. [57]–[59]. In order to harvest these kinds of energy, many mechanisms of harvester are studied and developed for years.

2.1.1. Thermal energy harvester

Thermal energy is usually known as the unavoidable factor when machines or devices are under operation or even in human beings. Thus, this type of loss is considered as a good source of energy due to its availability. The thermal energy harvester is a thermoelectric generator used to convert heat into electrical energy to feed the low power devices. The principle of this harvester is based on the Seebeck effect, the Peltier effect and the Thomson effect [58]. The harvester is a thermocouple producing an electrical current in a closed circuit proportional to the difference in temperature between cold and hot junctions of the semiconductor comprised in the thermocouple. An example of schematic of a thermal energy harvester is illustrated in Fig. 2.1.

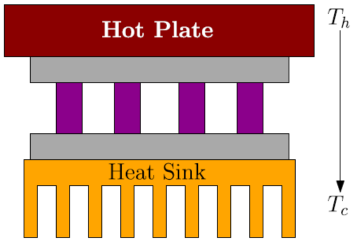

Figure 2.1: Model of a thermal energy generator [57]

2.1.2. Mechanical energy harvester

Electrical energy can be harvested from the mechanical interactions such as vibrations, pressure and stress-strain. Magnetic induction, electrostatic coupling and piezoelectric effect are three main mechanisms utilized to transform mechanical energy into electrical one.

A magnetic induction transducer is based on Faraday’s law of induction. The electric field is created with the variation of magnetic flux through an electrical circuit. This flux variation can be realized with a magnet moving across a fixed inductor or a moving inductor links to a fixed magnet. The first configuration is preferred because the electrical inductor is fixed [59].

Another concept of the mechanical energy harvester is the electrostatic transducer, also known as capacitive transducer. The principle of this mechanism is to place charges on capacitor plates and then to move the plates apart under mechanical energy, i.e. vibration or pressure, that can thus be converted into electrical energy [59], [60].

The last mechanism is based on the piezoelectric effect (see in Fig. 2.2) discovered by Pierre and Marie Currie. The mechanism is linked with the phenomenon changing state of a crystalline material when submitted to a stress-strain force on the objects thus generating electrical energy.

Cette thèse est accessible à l'adresse : https://theses.insa-lyon.fr/publication/2023ISAL0007/these.pdf
© [X.V.L. NGUYEN], [2023], INSA Lyon, tous droits réservés

The amplitude of the generated electrical energy depends on the strength of force applied to the object.

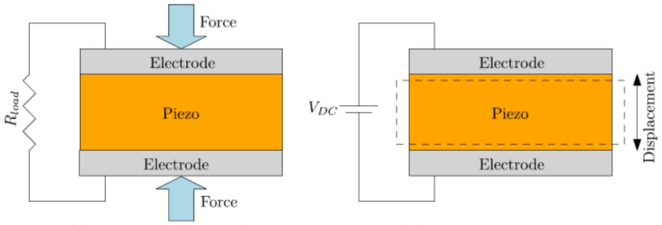

(a) Direct piezoelectric effect (b) reverse piezoelectric effect

Figure 2.2: Direct and reverse piezoelectric effect [57]

2.1.3. Solar energy harvester

Solar energy harvester or Photovoltaic energy harvester is used to harvest the energy from natural or artificial light and convert it into electrical energy using a semiconductor material. The process of conversion is carried out through three processes: absorbing the energy from the light, using the absorbed energy to generate free charge carriers from the semiconductor material and transporting negative charges (electrons) and positive charges (holes) at electrodes when the circuit is closed. An example of using this mechanism of energy harvester is illustrated in Fig. 2.3. The light energy is harvested due to a Photovoltaic (PV) panel, then amplified with the aid of a Power Management Unit LTC4071 to achieve the desired output voltage.

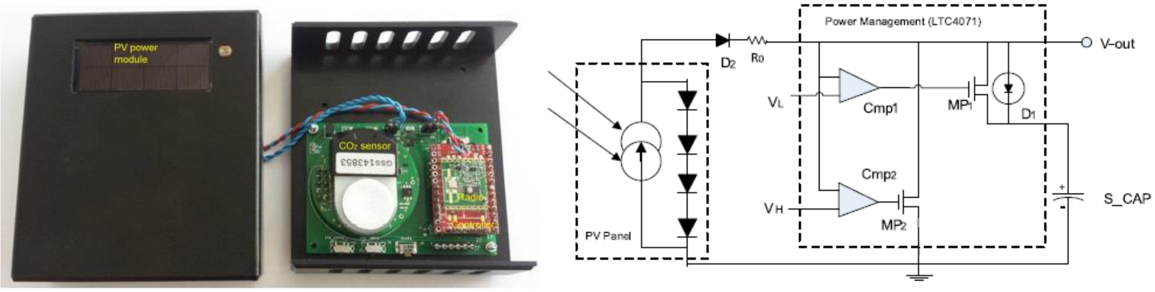

Figure 2.3: Developed 70 x 50 x 20 mm^3 autonomous IoT node for building ventilation [61]

2.1.4. Radio Frequency energy harvester

With the purpose of harvesting the electrical energy from Electromagnetic (EM) waves, Radio Frequency Energy Harvesters (RFEHs) have been studied for decades. To capture the EM waves in the air, RFEH requires a wave capturer or a system of wave capturers. These waves capturers can be antennas or metasurfaces [62], [63]. It should repeat that the metasurfaces are thin metamaterials engineered to manipulate the dispersion properties of surface-waves or the reflection/refraction properties of space waves [64].

In Fig. 2.4, the authors present an EM energy harvester realized on a PCB substrate (Teflon F4B) [65]. The implemented wave capturer is a monopole antenna realized using the copper tape. In Fig. 2.5, the metasurface is applied to harvest the EM wave.

Cette thèse est accessible à l'adresse : https://theses.insa-lyon.fr/publication/2023ISAL0007/these.pdf
© [X.V.L. NGUYEN], [2023], INSA Lyon, tous droits réservés

Figure 2.4: Designed EM energy harvester in [65]

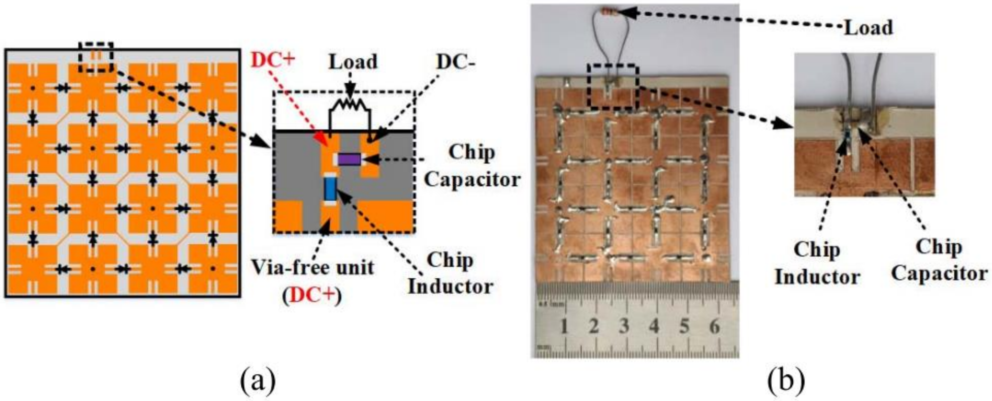

(a) (b)

Figure 2.5: Layout design and fabricated model of the proposed rectifying metasurface (a. Layout design; b. Fabricated model) [62]

2.2. Classification of energy harvesters

The power density, advantages and disadvantages of each energy harvester are listed in Table 2.1. The power density from the sun is the highest value (up to 15 mW/cm^2 in the outdoors) among the detailed sources. The main drawback is the requirement of availability of the light for the energy harvesting operation. Thus, the indoor applications of this mechanism are not preferred because of the shadow.

Thermal energy harvester offers also a fair power density. However, the low conversion efficiency is a barrier to cross. Besides, the miniaturization of this kind of harvester is quite complicated. The separation between low and high temperature parts in small devices is difficult. In addition, fabricating these harvesters requires the polluting materials.

Regarding mechanical energy harvester, even though its power density is high as well as the variety of its sources, the miniaturization of the object is a difficulty for the real-life applications.

Ambient RF energy is free from those limitations. Due to the development of telecommunication devices, the RF waves are becoming omnipresent in our life. In addition, the miniaturization is

Cette thèse est accessible à l'adresse : https://theses.insa-lyon.fr/publication/2023ISAL0007/these.pdf
© [X.V.L. NGUYEN], [2023], INSA Lyon, tous droits réservés

linked to the operating frequency of the objects. However, compared to other sources, Radio Frequency energy provides a very limited power density. This limit can be solved by using a system of antennas to harvest more RF power or by combining many rectennas with different operating frequencies in order to improve the total harvested power [4], [66]

Table 2.1: Classification of different energy harvesters

Energy Harvester	Power Density	Advantage(s)	Disadvantage(s)
Thermal	60 µW/cm^2 [58] 135 µW/cm^2 at 10°C [57] 0.4-100 µW/mm^2 [67] 1-10 mW/cm^2 [68]	Solid state. Acoustically silent. High reliability. Small in size and weight. Able to be oriented in any directions. Electrically safe.	Low conversion efficiency: between 5% to 10%.
Mechanical	4 µW/cm^2 [57] 0.4-30 µW/mm^2 [67] 250-330 µW/cm^2 [68]	Vast number of sources from minor scale (human body, etc.) to major scale (vehicle, building, etc.). Robust.	Difficult for miniaturization
Solar	10 µW/cm^2 (indoor) – 15 mW/cm^2 (outdoor) [57] 10-200 µW/mm^2 [67]	Higher efficiency and power output than other energy harvesting mechanisms.	Limited in number of applications because of the availability of light source. Preferred for large scale energy generation.
Radio Frequency	0.1 µW/cm^2 (GSM) – 0.01 µW/cm^2 (WiFi) [57] 0.1-200 µW/mm^2 [67]	Wireless. Suitable for maintenance-free circuits. Low cost. Easy implementation.	Insufficient power level for the present electronic devices.

2.3. Ambient RF waves

Recently, the interest in the ambient electromagnetic field in the urban environments becomes important with the rise in the number of wireless communications devices. Literally, base stations for mobile phones and RF transmitters appear everywhere to maintain the communication. The common bands of frequency present around us are DTV (470-790 MHz), GSM-900 (921-960 MHz), GSM-1800 (1805-1880 MHz), UMTS (2110-2170 MHz) and Wi-Fi (2400-2480 MHz). Besides, there are also 4G, 5G and soon 6G bands. However, they are out of the scope of this study.

A measurement of electric field strength, from a selection of 20 points close to base stations, was carried out in Paris in 2016 [70]. The results plotted in Fig. 2.6 show that the strength of the electric field of Wi-Fi and GSM-900 varies between 0.1 to 1 V/m as function of measurement points.

Cette thèse est accessible à l'adresse : https://theses.insa-lyon.fr/publication/2023ISAL0007/these.pdf
© [X.V.L. NGUYEN], [2023], INSA Lyon, tous droits réservés

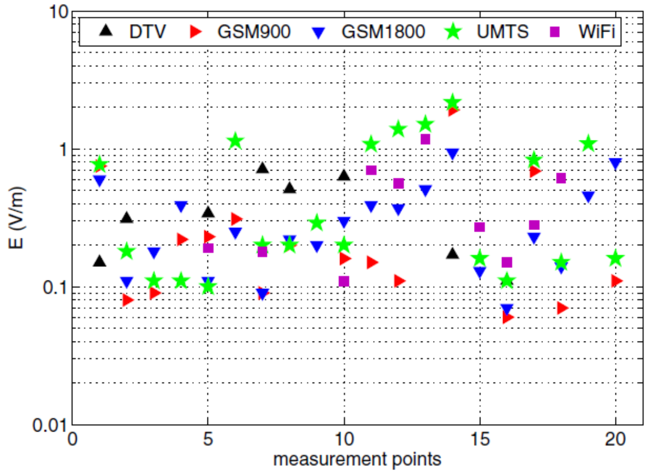

Figure 2.6: Examples of measurements conducted by the ANFR in Paris and surroundings [70]

The ambient RF power levels at seven locations in Paris are measured in [71]. The measured ranges of frequency in this study are GSM900/LTE Band 8, GSM1800/LTE Band 3, UMTS Band 1, ISM Wi-Fi 2.4 GHz and LTE Band 7. The results are plotted in Fig. 2.7. The RF power level varies between 0.1 µW and 100 µW depending on locations. The peak power is around 200 µW (equivalent to -7 dBm) at “Place de la République”. At this location, the main power is originated from GSM 1800, UMTS 2100 and LTE 2600 bands.

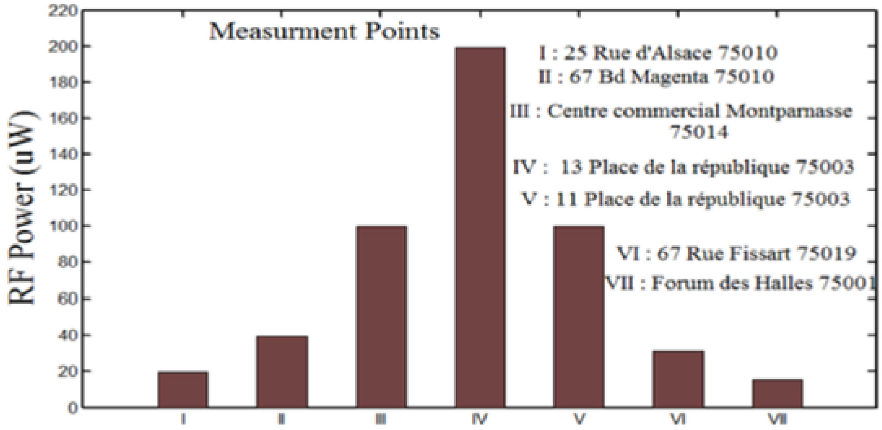

Figure 2.7: Measured ambient RF power level at different locations in Paris [71]

A survey of the RF spectrum in Montreal was performed at different locations: DT Montreal and UT Montreal at different hours of the day [72]. It can be observed in Fig. 2.8 that the power level of the Wi-Fi band stays stable between -70 dBm to -60 dBm meanwhile the value of GSM-900 band is around -40 dBm to -20 dBm at both locations for the outdoor conditions.

Cette thèse est accessible à l'adresse : https://theses.insa-lyon.fr/publication/2023ISAL0007/these.pdf
© [X.V.L. NGUYEN], [2023], INSA Lyon, tous droits réservés

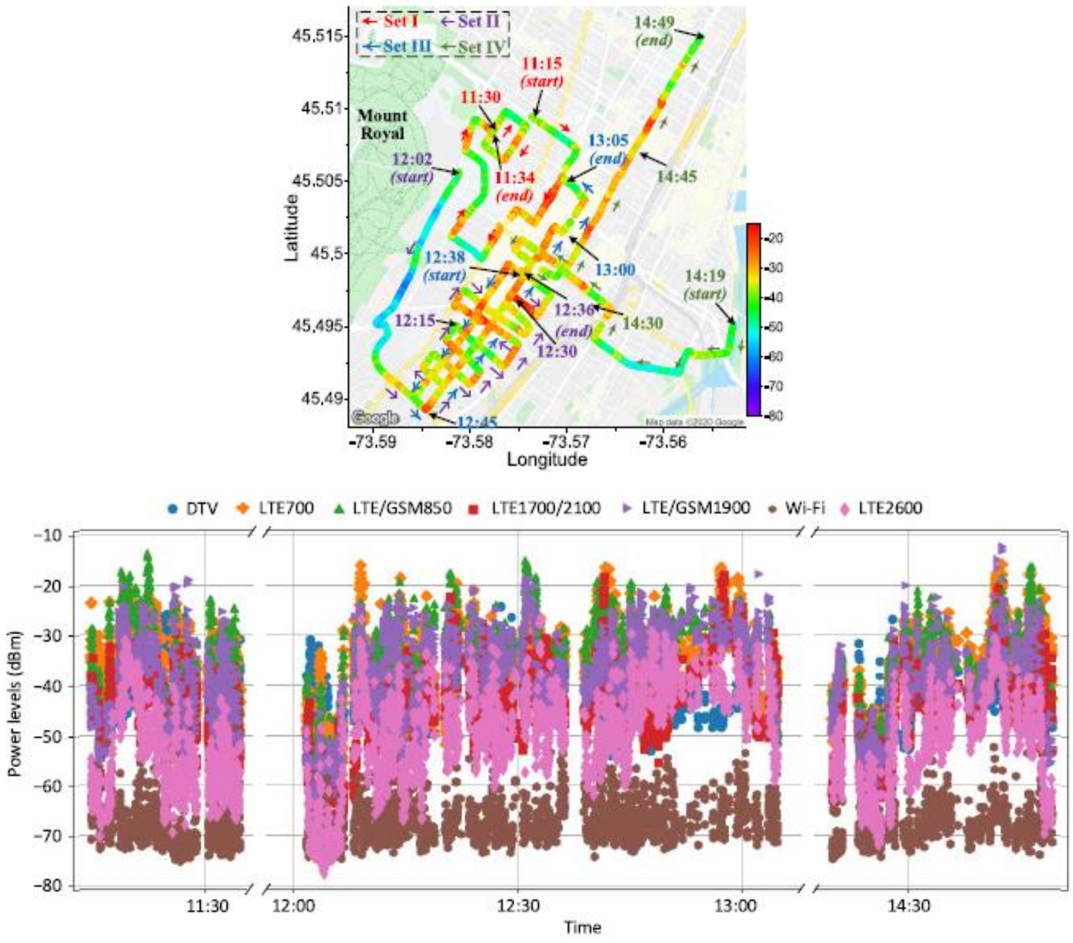

DT Montreal

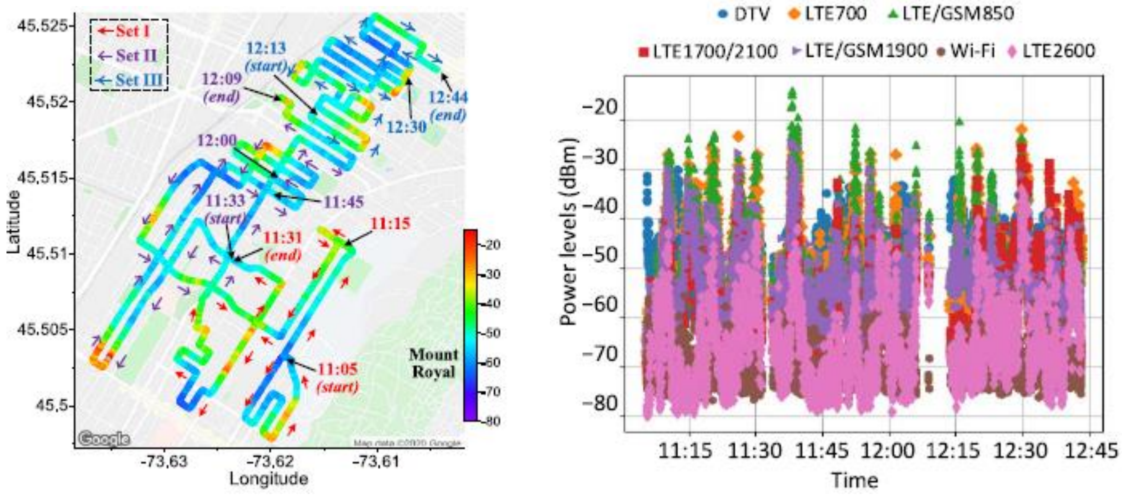

UT Montreal

Figure 2.8: Ambient RF energy mapping of the GSM/LTE850 band with direction and timestamps and RF power levels of all seven frequency bands of interest at the same geographic locations and time slots: DT Montreal and UT Montreal [72].

Additionally, according to the synthesis in [4], for the indoor environments, the power density of Wi-Fi bands varies between 0.18 to 1 nW/cm^2. The level of power density can be achieved up to

Cette thèse est accessible à l'adresse : https://theses.insa-lyon.fr/publication/2023ISAL0007/these.pdf
© [X.V.L. NGUYEN], [2023], INSA Lyon, tous droits réservés

52 nW/cm^2. These values are obtained by estimating and measuring the power density of WLAN signal.

Khalid et al. performed a measurement of ambient power available indoor and outdoor in semi-urban environments [73]. The results are illustrated in Fig. 2.9. According to these results, a slight gap between two conditions exists for the Wi-Fi bands. The peak value of the power of this band is around -50 dBm and -47 dBm for indoor and outdoor environments, respectively.

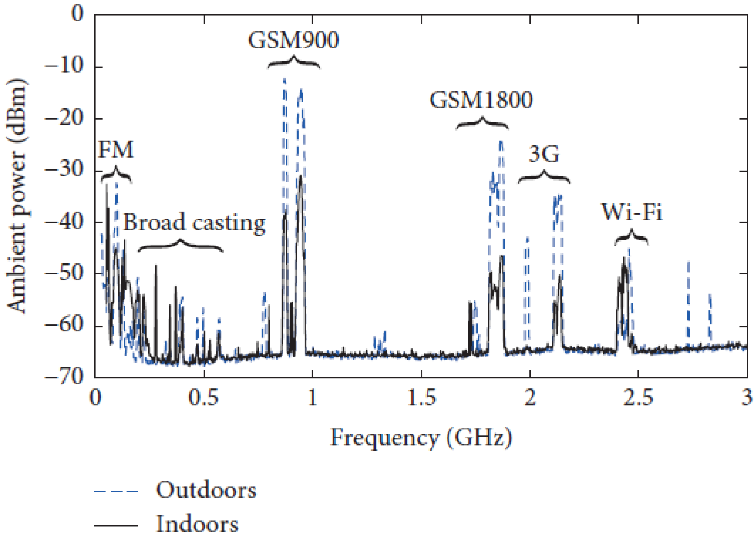

Figure 2.9: Peak ambient versus frequency in a semi-urban environment [73]

In this thesis, the Wi-Fi band is selected due to its high value, which allows us to reduce the form factor of the RFEH circuits for the test, and this band of frequency is accessible with the equipment of Plastronics team. The power levels of the Wi-Fi bands is around -70 to -50 dBm according to the measurement in the literature. These power levels are much smaller than the required minimum cold-start input power of the common Integrated Circuit (IC) Power Management Units (i.e. BQ25504 -18 dBm/15 µW [74], AEM30330 -24 dBm/3 µW [75], etc.) even excluding the rectification loss of the rectifier. Therefore, for our thesis, the minimum studied RF power will be -20 dBm/10 µW for our selected band of frequency. In fact, with our knowledge, -20 dBm is the limit value in RF energy harvesting application. Even though, for our first assessment, we desire to obtain an exploitable demonstrator. Optimizing the demonstrator will be interested later.

2.4. Radio Frequency Energy Harvester with Antennas

RF electromagnetic energy at a sufficiently high frequency may be captured using a RFEH circuit. In case of using the antennas as the wave capturer, the first block of the RFEH is called RECTENNA (RECTifier and antENNA). A basic rectenna consists of an antenna, a RF-DC rectifier and an impedance matching between them and a storage capacitor.

The antennas play a role of capturing the EM waves existing in the environment and transfer them towards the RF-DC rectifiers. The RF-DC rectifiers convert the received EM waves into the DC energy and store them in the storage capacitors.

These storage capacitors can also benefit of a low-pass filter. The low-pass filter in the rectenna can be developed to increase the performance of the whole circuit by implanting a harmonic rejection circuit [76] or RF chokes used to cut off the RF signals [77].

Cette thèse est accessible à l'adresse : https://theses.insa-lyon.fr/publication/2023ISAL0007/these.pdf
© [X.V.L. NGUYEN], [2023], INSA Lyon, tous droits réservés

The rectified energy can be used directly by the consumption load or be processed by the PMU. The PMU is an optional part. This part is preferred in the case when the input power level of the rectenna or the power density of the EM waves are not high enough or not stable to achieve the desired output voltage of the consumption load.

In this section, an overview of the RF-DC conversion efficiency of the rectenna will be reported firstly. The different topologies of the rectifier as well as the impedance matching technique between the antenna and the rectifier are presented then. Afterwards, some PMUs introduced in the literature are mentioned. Finally, the Maximum Power Point condition between the rectifier and the PMU is analyzed.

2.4.1. Overview of RF-to-DC conversion efficiency

Recently, researchers concentrate on improving the RF-DC conversion efficiency of ambient power harvesting techniques. Fig. 2.10 lists the measured conversion efficiency results of studied rectifiers with different rectifying diodes and different operating bands of frequency. Before 2010, high efficiency rectifiers for Wireless Power Transfer (WPT) applications are obtained at input power higher than 1 mW as shown in the right part of Fig. 2.10. After the year 2010, the studies about improving the efficiency of the rectifier at lower input power for energy harvesting applications attract many researchers with the goal of obtaining self-autonomous communication and sensor platforms for IoT industry.

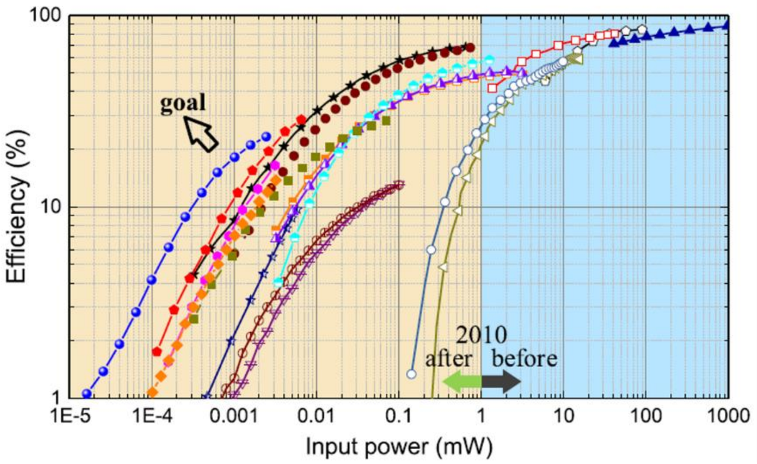

Symbol	Year	Diode	Operating frequency (GHz)	Reference
▲	1982	GaAs	2.45	[5]
□	1998	MA40150-119	5.8	[13]
○	2002	MA4E1317	2.45	[14]
☆	2010	SMS7630	2.45	[15]
△	2010	SMS7630	1.85	[16]
■	2010	SMS7630	2.44	[16]
◁	2010	HSMS2820	2.45	[17]
○	2010	HSMS2860	2.45	[17]
⊕	2014	HSMS2850	1.8	[18]
▽	2014	HSMS2850	2.1	[18]
★	2015	SMS7630	2.15	[19]
●	2016	SMS7630	1.9	[20]
●	2016	VDI ZBD	1.9	[20]
●	2016	Backward tunnel diode	2.4	[12]
◆	2017	SMS7630	1.85	[21]
●	2017	SMS7630	0.85	[22]
■	2018	SMS7630	0.9	[23]
◆	2019	SMS7630	2.4	[24]

Figure 2.10: Measured efficiency results of different rectifiers for wireless power transfer and energy harvesting applications. The references are stated in [78].

In [79], the author categorizes the performance of the RF energy harvesting circuits with different rectifying diode in GSM-900 bands and Wi-Fi 2.45 GHz at different input power.

Cette thèse est accessible à l'adresse : https://theses.insa-lyon.fr/publication/2023ISAL0007/these.pdf
© [X.V.L. NGUYEN], [2023], INSA Lyon, tous droits réservés

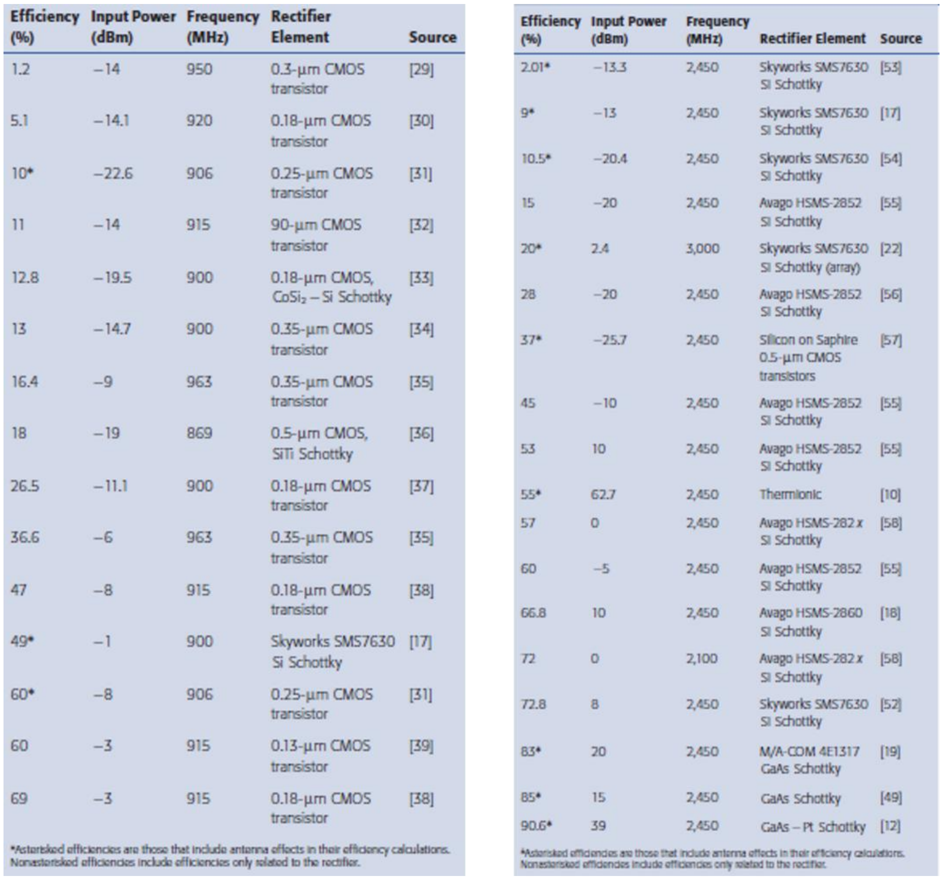

Efficiency (%)	Input Power (dBm)	Frequency (MHz)	Rectifier Element	Source
1.2	−14	950	0.3-µm CMOS transistor	[29]
5.1	−14.1	920	0.18-µm CMOS transistor	[30]
10*	−22.6	906	0.25-µm CMOS transistor	[31]
11	−14	915	90-µm CMOS transistor	[32]
12.8	−19.5	900	0.18-µm CMOS, $CoSi_2 - Si$ Schottky	[33]
13	−14.7	900	0.35-µm CMOS transistor	[34]
16.4	−9	963	0.35-µm CMOS transistor	[35]
18	−19	869	0.5-µm CMOS, SiTi Schottky	[36]
26.5	−11.1	900	0.18-µm CMOS transistor	[37]
36.6	−6	963	0.35-µm CMOS transistor	[35]
47	−8	915	0.18-µm CMOS transistor	[38]
49*	−1	900	Skyworks SMS7630 Si Schottky	[17]
60*	−8	906	0.25-µm CMOS transistor	[31]
60	−3	915	0.13-µm CMOS transistor	[39]
69	−3	915	0.18-µm CMOS transistor	[38]

*Asterisked efficiencies are those that include antenna effects in their efficiency calculations. Nonasterisked efficiencies include efficiencies only related to the rectifier.

Efficiency (%)	Input Power (dBm)	Frequency (MHz)	Rectifier Element	Source
2.01*	−13.3	2,450	Skyworks SMS7630 Si Schottky	[53]
9*	−13	2,450	Skyworks SMS7630 Si Schottky	[17]
10.5*	−20.4	2,450	Skyworks SMS7630 Si Schottky	[54]
15	−20	2,450	Avago HSMS-2852 Si Schottky	[55]
20*	2.4	3,000	Skyworks SMS7630 Si Schottky (array)	[22]
28	−20	2,450	Avago HSMS-2852 Si Schottky	[56]
37*	−25.7	2,450	Silicon on Saphire 0.5-µm CMOS transistors	[57]
45	−10	2,450	Avago HSMS-2852 Si Schottky	[55]
53	10	2,450	Avago HSMS-2852 Si Schottky	[55]
55*	62.7	2,450	Thermionic	[10]
57	0	2,450	Avago HSMS-282*x* Si Schottky	[58]
60	−5	2,450	Avago HSMS-2852 Si Schottky	[55]
66.8	10	2,450	Avago HSMS-2860 Si Schottky	[18]
72	0	2,100	Avago HSMS-282*x* Si Schottky	[58]
72.8	8	2,450	Skyworks SMS7630 Si Schottky	[52]
83*	20	2,450	M/A-COM 4E1317 GaAs Schottky	[19]
85*	15	2,450	GaAs Schottky	[49]
90.6*	39	2,450	GaAs – Pt Schottky	[12]

*Asterisked efficiencies are those that include antenna effects in their efficiency calculations. Nonasterisked efficiencies include efficiencies only related to the rectifier.

Figure 2.11: Measured efficiency of rectifiers in different bands of frequency GSM-900 (left) and WiFi 2.45 GHz (right), input power levels and different rectifying diodes. The references are stated in [79].

In the EH applications, for the band of GSM-900, the RF-DC conversion efficiency of the rectifiers can reach up to 50% with an input power level of 0.1 mW (-10 dBm) and 25% with an input power level of 0.01 mW (-20 dBm). For the band of Wi-Fi 2.45 GHz, this parameter varies between 1% and 35%. Specially, a backward tunnel diode, plotted in Fig. 2.10 helps overcome the limit of RF-DC conversion efficiency of the conventional Schottky diodes. With this diode, the conversion efficiency reaches 20% and 4% at -30 dBm and -40 dBm respectively. These values are the record performance of the rectifier at extremely low-input power levels [78].

2.4.2. Topologies of the rectifier

The topology of the rectifier is decided depending mostly on the incident power level, the frequency of the circuit and the number of the mounted devices in the circuit. The most common topologies are the following.

2.4.2.1. Series diode topology

This is the simplest topology where one diode is used for the configuration. The matching circuit is serially connected to the anode of the rectifying diode. The cathode connects then to a filter and storage capacitor. The rectification of the signal occurs only in the positive half cycle of the waves meanwhile the negative half cycle is rejected. The drawback of this topology is the low output rectified voltage. Moreover, the DC current closed loop in the rectifier has to be carefully taken care of.

Cette thèse est accessible à l'adresse : https://theses.insa-lyon.fr/publication/2023ISAL0007/these.pdf
© [X.V.L. NGUYEN], [2023], INSA Lyon, tous droits réservés

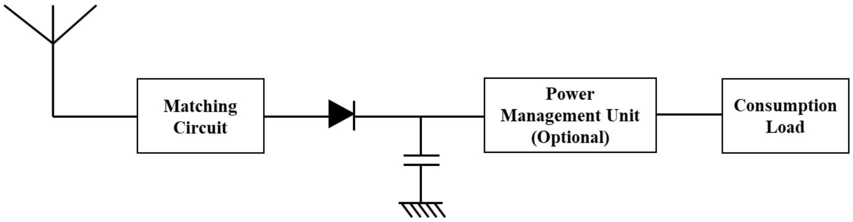

Figure 2.12: Series diode topology

2.4.2.2. Shunt diode topology

Another one-diode topology is shunt configuration. The rectifying diode is set up in parallel to the storage capacitor. The anode of the diode is linked to the ground of the circuit. Unlike the series diode topology, the rectification in this topology happens during the negative half cycle of the waves and the positive half cycle is rejected. The drawback of this topology is also its low output rectified voltage as the series diode topology.

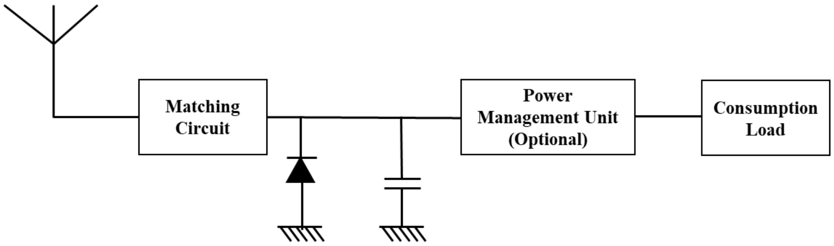

Figure 2.13: Shunt diode topology

2.4.2.3. Voltage doubler – Greinacher topology

In order to push up the output rectified voltage, a voltage doubler topology is proposed. This topology is a combination of the series and the shunt diode topologies. The mechanism of this topology is shown in Fig. 2.14. This topology consists in two rectifying diodes D1, D2 and two storage capacitors C1, C2.

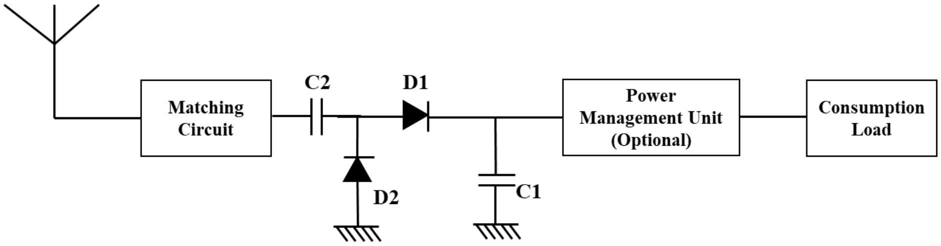

Figure 2.14: Voltage doubler topology

During the positive half cycle of the wave, the series diode D1 takes part in the rectification. The rectified energy is then stored in C1. After that, during the negative half cycle of the wave, the shunt diode D2 rectifies the wave. Since, during this phase, D1 is not forward biased. The rectified energy will be stored in C2 temporally until the next positive half cycle, the stored energy in C2 will be transferred to C1 so that the voltage across C1 is approximately two times higher than the peak voltage in the series or the shunt topology.

2.4.2.4. Multiple diodes topologies

Besides the voltage doubler, with the aim of boosting the output voltage, others topologies are reported such as

Cette thèse est accessible à l'adresse : https://theses.insa-lyon.fr/publication/2023ISAL0007/these.pdf
© [X.V.L. NGUYEN], [2023], INSA Lyon, tous droits réservés

- Dickson topology [80]
- Cockcroft-Walton topology [81]
- Diode bridge topology [82]
- Villard charge pump topology [83]

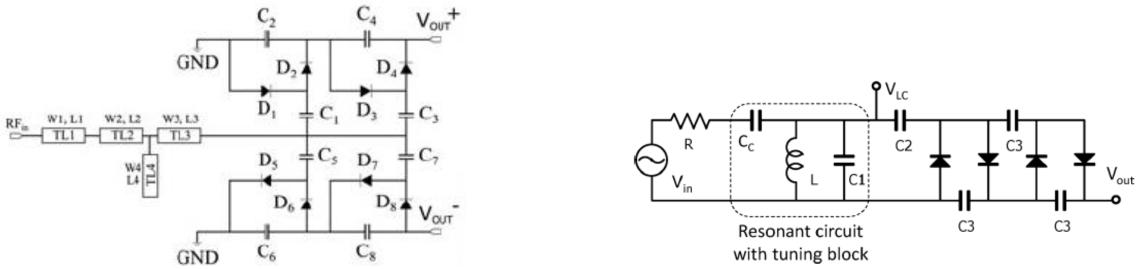

Dickson topology [80] *Cockcroft-Walton topology* [81]

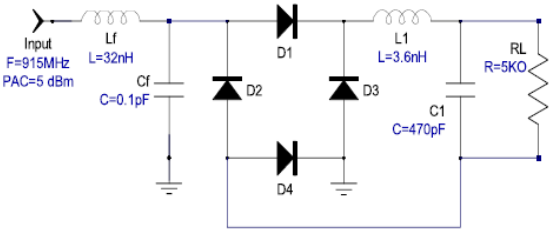

Diode bridge topology [82]

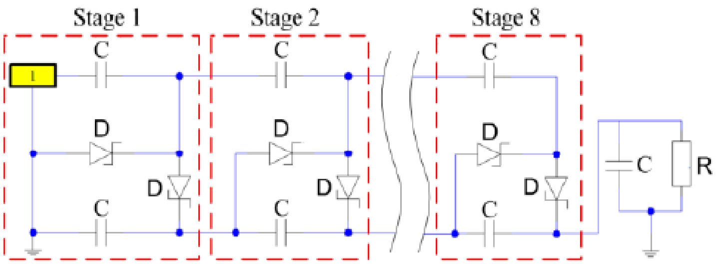

Villard charge pump topology [83]

Figure 2.15: Multiple diodes topologies.

Voltage doubler and multiple diodes topologies help enhance the output voltage of the rectifier. Additionally, in the high-power circuit, they can obtain fair efficiency values. Nevertheless, with the very low input level, the input voltage is much lower than the voltage across the diode and the inefficiency of the diode bridge-based rectification should be concerned. The losses from the diodes increases as their number mounted on the circuit [4]. Thus, in the low input power level of the rectifier, the preferences are the series and the shunt diode topologies.

The authors in [84] introduces a Rectenna Figure of Merit (RFoM) of the rectifier in four different topologies: series, shunt, one stage voltage doubler and two stage voltage doubler with the goal of understanding the performance of each topology at different level of input power. To repeat, RFoM is the product expressed in Eq. (2.1) between the open-circuit DC output voltage and the RF-to-DC efficiency when the rectifier achieves its maximum power. This parameter demonstrates the trade-off between the rectified voltage and the conversion efficiency of the rectifier.

$$RFoM = V_{DC\ open\ circuit} \times \eta_{optimal\ load} \qquad (2.1)$$

Cette thèse est accessible à l'adresse : https://theses.insa-lyon.fr/publication/2023ISAL0007/these.pdf
© [X.V.L. NGUYEN], [2023], INSA Lyon, tous droits réservés

As presented in Fig. 2.16, below -5 dBm, the series topology gives better RFoM than others. The series topology will then be considered here.

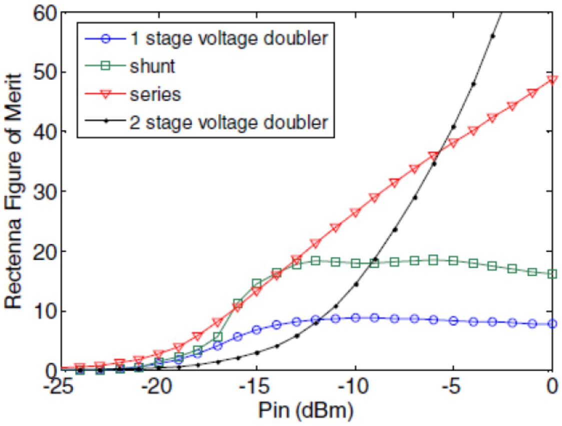

Figure 2.16: Simulated Rectenna Figure of Merit of different topologies of rectenna as function of incident power [84]

2.4.3. Impedance matching techniques

When the impedance of the antenna and the rectifier are not coherent with each other, an impedance mismatch will appear in the wave transmission in the circuit [85]. This will degrade the performance of the rectenna. Hence, matching the impedance between the antenna and the rectifier is necessary. In this section, different impedance matching techniques will be studied.

2.4.3.1. Conjugated impedance matching

This technique of matching the impedance is based on conjugating the complex impedance of the antenna to the input impedance of the rectifier.

In [86], the authors present an array of six elements of 2D rectenna. The rectenna contains a rectangular strip-loop antenna and a coplanar stripline RF-DC rectifier. The dimensions of the circuits (L_1, W_1 and L_3) are studied and configured in order to have a complex conjugate impedance matching with the diode impedance at 2.45 GHz.

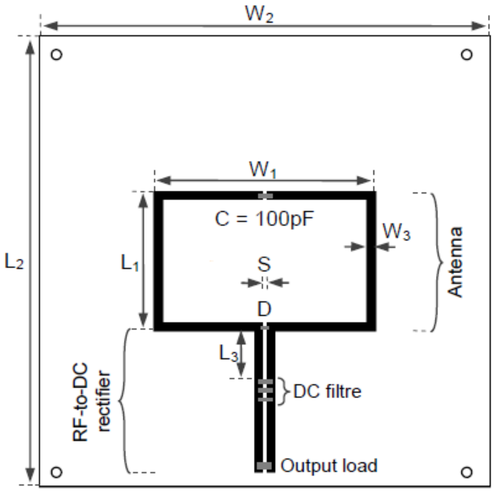

Figure 2.17: Layout of the proposed single rectenna with conjugated impedance matching [86]

Congedo et al. proposed a rectenna consisting of a Vivaldi antenna with a 5-stage multiplier with a load of 10 MΩ [87]. To achieve the conjugated complex impedance matching, a taper line with

Cette thèse est accessible à l'adresse : https://theses.insa-lyon.fr/publication/2023ISAL0007/these.pdf
© [X.V.L. NGUYEN], [2023], INSA Lyon, tous droits réservés

the optimized dimensions is added between the antenna and the rectifier. The schematic of the proposed rectenna is illustrated in Fig. 2.18.

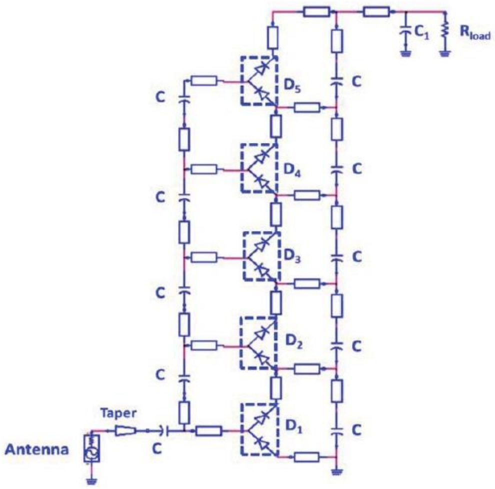

Figure 2.18: Schematic representation of the proposed rectenna in [87].

The advantage of this technique is that the transmitted power to the rectifier from the antenna is maximized [4]. In addition, the implementation of the matching circuit part is not always required in this technique, thus, the losses, i.e. conductor loss, dielectric loss, can be also reduced in the wave transmission. However, the conjugation of the impedances is not easily achieved. Characterizing the circuits respecting this matching technique is quite complicated since the impedance of many instruments is referred to 50 Ω. Moreover, according to the analysis in [4], the interference impedance of 50 Ω can give the quite similar results on RF-DC conversion efficiency of the conjugated matching technique. Consequently, this technique is not studied in this thesis.

2.4.3.2. 50 Ω impedance matching

The most common impedance matching technique is setting up the impedance of the antenna and the input impedance of the rectifier equal to 50 Ω, the reference value of many RF devices and instruments. To realize that impedance matching condition, a matching circuit should be inserted between the antenna and the rectifier. This matching circuit can be built up from lumped elements, i.e. inductors, capacitors, or the microstrip lines, stubs or the mixture of both previous elements.

Lumped elements matching circuit

In this technique, the matching circuit is composed of the inductors, capacitors. These lumped elements are added in the circuit to modify the input impedance of the rectifier to the desired value. The matching circuit can be realized in many topologies, i.e. Pi, T, L or the combination of them, as shown in Fig. 2.19.

Cette thèse est accessible à l'adresse : https://theses.insa-lyon.fr/publication/2023ISAL0007/these.pdf
© [X.V.L. NGUYEN], [2023], INSA Lyon, tous droits réservés

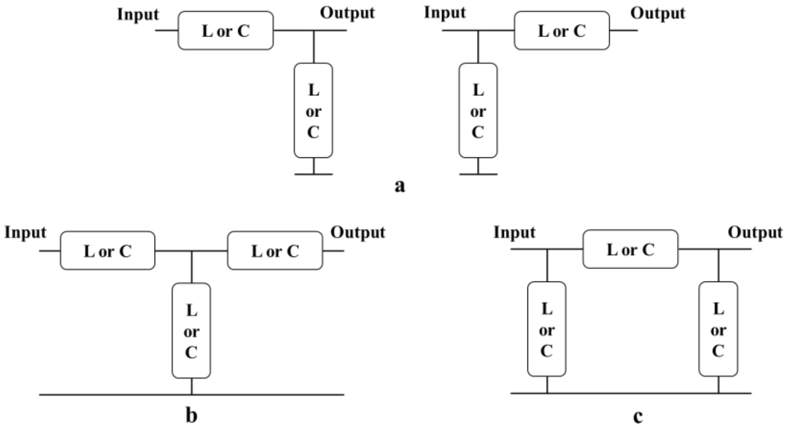

Figure 2.19: Three topologies of lumped elements matching circuit (a. L; b. T; c. Pi)

The advantage of this technique is the capability of minimizing the dimensions of the matching circuit at low frequencies. Nevertheless, the unstable value of the L, C components can influence the performance of the matching circuit. Moreover, the limited operating frequencies of the lumped elements are also a drawback of this technique.

In [88], the authors use this technique to obtain 50 Ω impedance matching between the antenna and the rectifying circuit working at 2.45 GHz. The matching circuit involves a shunt capacitor and a series inductor in L-topology as shown in Fig. 2.20.

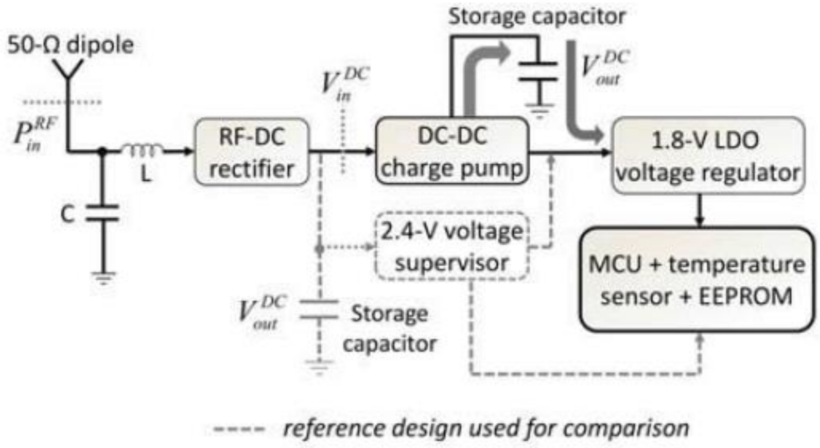

Figure 2.20: Block diagram of the proposed RFEH in [88].

The authors in [82] use a series inductor and a shunt capacitor in L-topology for the matching circuit. The rectenna operates at 915 MHz with the incident power of +5 dBm.

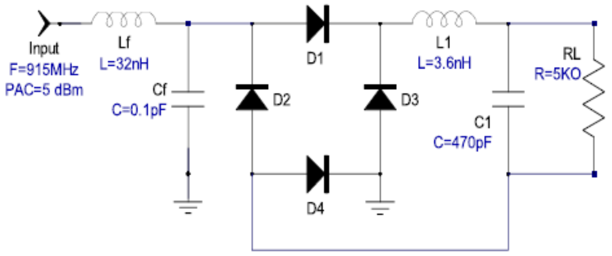

Figure 2.21: Schematic diagram of the bridge rectifier with a L-matching circuit with lumped elements [82].

Cette thèse est accessible à l'adresse : https://theses.insa-lyon.fr/publication/2023ISAL0007/these.pdf
© [X.V.L. NGUYEN], [2023], INSA Lyon, tous droits réservés

Microstrip lines matching circuit

Another technique is to use printed microstrip lines or stubs with different configurations, i.e. radial stub, shorted circuit stub, open circuit stub, quarter-wavelength impedance transformer, etc. to match the impedance of the antenna and the rectifying circuit. This technique is preferred for the circuit operating at high frequency. Additionally, the accuracy of dimensions of printed lines can ensure the desired operation of the matching circuit. The drawback of this technique is the dimensions of the lines at low frequency.

A matching circuit composed of an open circuit stub in parallel of a shorted circuit stub is shown in Fig. 2.22. for the band of GSM 1800 and UMTS 2100 in [89]. The dimensions of lines are optimized for a bi-band circuit.

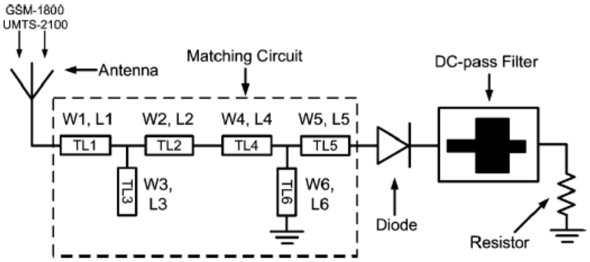

Figure 2.22: Topology of the proposed rectifier with a microstrip matching circuit [89]

In [90], a Grounded CoPlanar Waveguide (GCPW) rectenna working at 2.45 GHz is introduced. In order to get the 50 Ω impedance matching, a GCPW transformer with the width of W_t, the length of L_t and the gap of g_2 is presented between the antenna and the voltage doubler voltage.

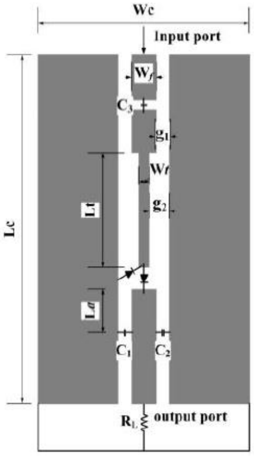

Figure 2.23: Configuration of the proposed grounded coplanar waveguide rectifying circuit in [90]

Mixed matching circuit

Mixed matching circuit is assembled of the two previous presented techniques. This technique allows us to reduce the total dimensions of the circuit compared to microstrip lines matching circuit technique. However, the impact of the value variation of the lumped components on the impedance matching behavior of the circuit stays still. Some works use this technique to match to 50 Ω of impedance.

As a proof, in [91], the matching circuit consisting of a shorted circuit stub in parallel to an open circuit stub and in series to an inductance is produced for a matching at 2.45 GHz.

Cette thèse est accessible à l'adresse : https://theses.insa-lyon.fr/publication/2023ISAL0007/these.pdf
© [X.V.L. NGUYEN], [2023], INSA Lyon, tous droits réservés

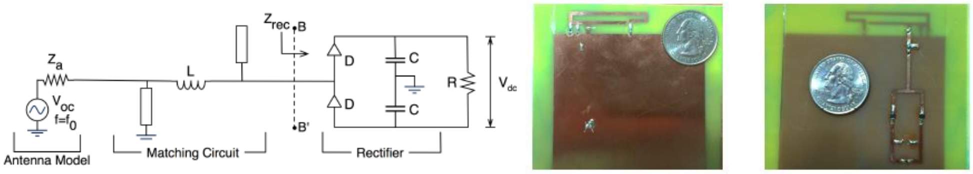

Figure 2.24: Layout design (left) and fabricated model (right) introduced in [91]

For a triple band of GSM 900, GSM 1800 and UMTS 2100 rectenna, in the matching circuit, Shen et al. introduces in [92] a SMD inductance connected in series to two radial stubs in parallel to a shorted circuit stub. The dimensions of lines are optimized for the operation at the input power of -30 dBm.

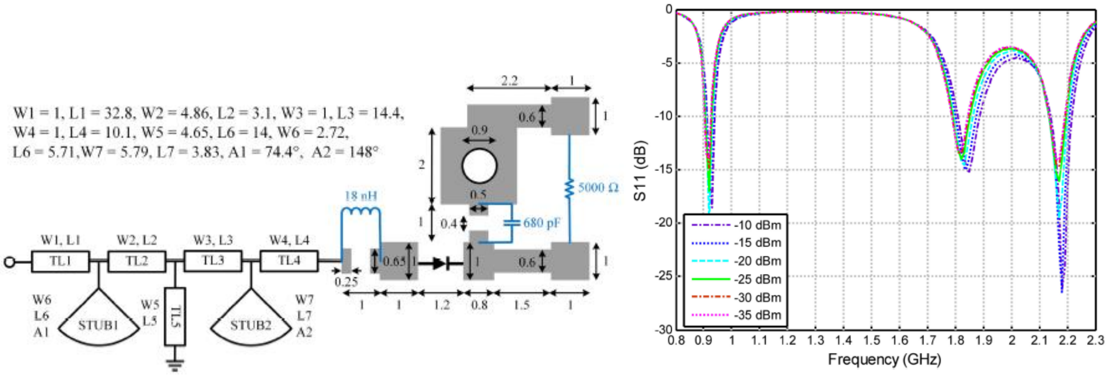

Figure 2.25: Topology of the triple-band rectifier (left) and the corresponding reflection coefficient (right) in [92]

2.4.3.3. Other values of impedance matching

As stated in the previous section, 50 Ω is chosen as the reference impedance of many current RF devices and instruments which allows characterization of a complex system by testing separately each sub-system. In fact, for the RF energy harvesting, this value is not optimal for the connection between the antenna and the rectifier.

As a proof, [84] discusses the improvement of the RF-DC conversion efficiency as functions of the impedance of the antenna, the topologies of the rectifiers and different types of matching circuits. This study is simulated using ADS for the input power level of -15 dBm and the frequency of 2.45 GHz with the Schottky diode HSMS 2850 and the matching circuit involving lumped elements. The results of this study are listed in Fig. 2.26. According to these results, we observe that the performance of the rectenna can be improved by applying another impedance of the antenna. This improvement can be enhanced up to 100 % maximum. Additionally, the optimal impedance of the antenna depends on the topology and the matching circuit of the rectifier. However, this study is still limited only in the case of the lumped elements matching circuit and not in the case of microstrip and mixed matching circuit.

Cette thèse est accessible à l'adresse : https://theses.insa-lyon.fr/publication/2023ISAL0007/these.pdf
© [X.V.L. NGUYEN], [2023], INSA Lyon, tous droits réservés

Topology	Filter	Optimal Zantenna (Ω)	Improvement (%)
Series	Inductor	15	25
	L	11	25
	Pi	56	0
	T	152	68
Shunt	Inductor + series capacitor	10	27
	L + series capacitor	225	50
	Pi + series capacitor	44	0
	T + series capacitor	11	80
Voltage doubler	L + series capacitor	10	100
	Pi + series capacitor	44	3
	T + series capacitor	240	35

Figure 2.26: Optimized results in different topologies of rectennas in [84]

Besides, in [93], the authors demonstrated the minimum required power to generate a rectified voltage of 0.4 V at different values of the real part of the impedance of the antenna (from 10 Ω to 50 Ω). The antenna is then connected serially directly to the CMOS rectifier fabricated in standard 90 nm CMOS technology. To match the impedance between the antenna and the rectifier, the authors use an antenna with an inductive reaction (imaginary part of the impedance is positive) to compensate the rectifier capacitive reaction (imaginary part of the impedance is negative) without using other external components.

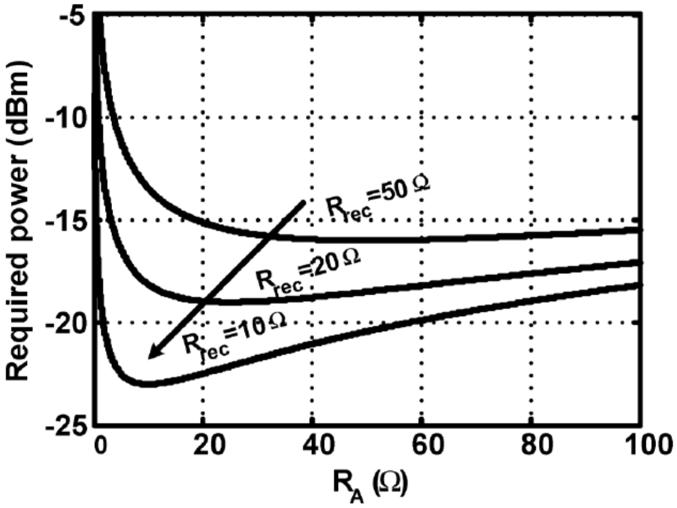

Figure 2.27: Calculated minimum required power to generate 0.4 V of rectified voltage versus antenna resistance for various real part of impedance of the rectifier [93]

According to Fig. 2.27, when the real part of the impedance of the rectifier and the antenna are both equal to 10 Ω, the minimum required power is the lowest. Additionally, while the real part of the impedance of the antenna is far from the rectifier's value, the impedance mismatch loss increases, so a higher level of input power is required to reach the desired output voltage.

2.4.3.4. Conclusion

In this section, the current techniques of impedance matching between the antennas and the rectifiers are introduced. The first technique is about conjugating the impedance of the antenna and the rectifier in order to maximize the transmitted power from the antenna to the rectifier. With this method, the matching circuit is in general not necessary, therefore, the losses from this circuit can be reduced. Nevertheless, the configuration of this method is not easy to obtain.

Cette thèse est accessible à l'adresse : https://theses.insa-lyon.fr/publication/2023ISAL0007/these.pdf
© [X.V.L. NGUYEN], [2023], INSA Lyon, tous droits réservés

The most common technique is to match the impedance of the antennas and the rectifiers to the reference value of 50 Ω. Three concepts of the matching circuit are described, which are lumped elements, microstrip lines and the mixture of both concepts. Each concept has its advantages and disadvantages.

Literally, the value of 50 Ω is not the optimal value of impedance for the matching in EH applications. It was demonstrated in the literature that selecting a low reference impedance is beneficial in the context of RF energy harvesting [84], [93] as shown in Fig. 2.26 and Fig. 2.27. Due to time constraint, this possibility was not investigated.

To conclude, for this thesis, the selected technique is 50 Ω impedance matching even though it is not optimal. The technique is preferred because it allows characterizing separately the different parts of the device, which simplifies the deployment of measurements, comparing to the conjugated matching technique.

2.4.4. Maximum Power Point condition

The rectenna may be seen as a low-voltage source, but with a large internal impedance (which is in scale of kΩ). As a proof, in [94], the author studies experimentally I-V (Current-Voltage) characteristic of the mono-diode series topology rectifier with the diode HSMS286B in different input powers (-20 dBm, -15 dBm, -10 dBm and -5 dBm). The voltage at the load is measured, then the output current of the rectifier is deducted. The results are illustrated in Fig. 2.28. We observe that I-V curves are in parallel, therefore, the rectenna can be modeled as a voltage source with an internal impedance. Moreover, the internal impedance of the rectenna in [94] in mono-diode series topology is 2.4 kΩ.

The study of the internal impedance of our designed rectenna will be detailed in Chapter 5.

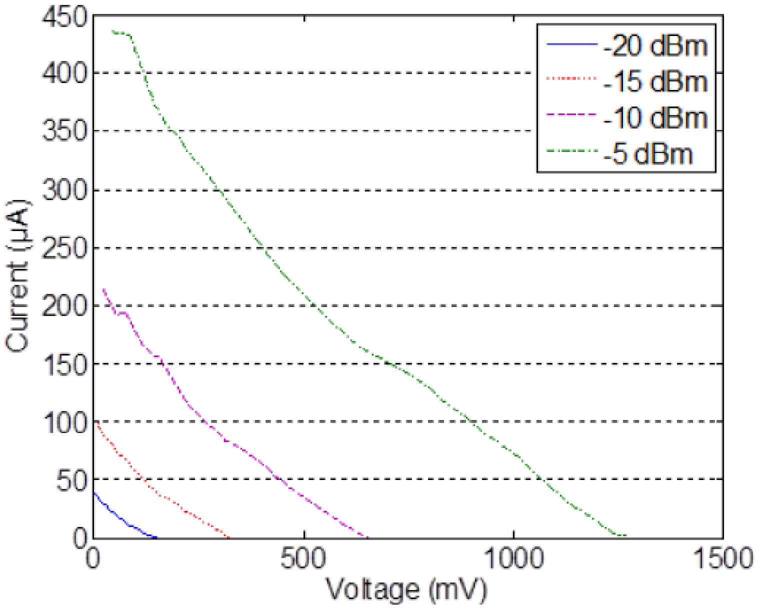

Figure 2.28: I-V curve of the rectifier at different values of input power

The matching between the rectifier internal impedance and the PMU input impedance should be concerned in order to reduce the loss of power transmission between these parts, and thus to enhance the total performance of the whole circuit. In order to get this specific impedance matching condition, the input impedance of the PMU should be tuned so that it equates the output impedance

Cette thèse est accessible à l'adresse : https://theses.insa-lyon.fr/publication/2023ISAL0007/these.pdf
© [X.V.L. NGUYEN], [2023], INSA Lyon, tous droits réservés

of the rectifier in DC. This represents the condition of Maximum Power Point (MPP) in DC [66], [70], [95].

In [95], the authors present a flexible 2.45 GHz rectenna working at -24.3 dBm. The rectenna consists of a patch antenna and a series topology rectifier using SMS7630-079LF as the rectifying diode. The output load is measured and selected as 4 kΩ to obtain the optimal performance of the rectenna at -20 dBm. The rectenna is linked to an inductive Boost converter operating in discontinuous conduction mode. The efficiency of the converter is consistent down to -24.3 dBm with a maximum of 57% at -14.2 dBm. The end-to-end efficiency reaches a maximum of 28.7% at -7 dBm. It should be noticed that the efficiency of rectenna is calculated as the ratio between the rectified power and the transmitted power towards the rectifying diode, not the received power of the rectenna.

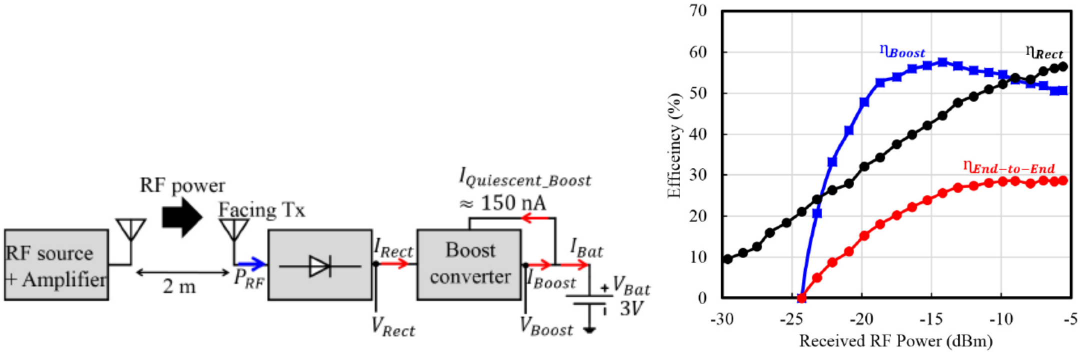

Figure 2.29: Experimental measurement setup of the complete circuit and the corresponding efficiency of each block in [95]

With the same idea of enhancing the output voltage of the circuit, the authors in [66] use a DC-DC converter BQ25504 from Texas Instrument connected in series with their series topology rectifier (SMS7630 diode) and a load of 5.1 kΩ. This value of load is chosen to be close to the junction resistance of the diode for an optimal DC-DC transfer. For a power density of 0.1 µW.cm^{-2}, the open circuit output voltage is boosted from -22 dBV to -17 dBV.

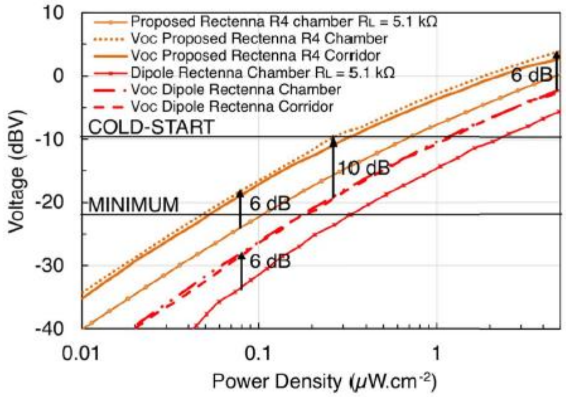

Figure 2.30: Measured output voltage of the rectenna proposed in [66]

2.4.5. Power Management Unit

Power Management Unit (PMU) is an optional electrical part not only for RFEH but also for other energy harvester circuits. This circuit is recommended when the harvested voltage cannot rise up to the required voltage of the consumption load.

Cette thèse est accessible à l'adresse : https://theses.insa-lyon.fr/publication/2023ISAL0007/these.pdf
© [X.V.L. NGUYEN], [2023], INSA Lyon, tous droits réservés

Nowadays, there are many Integrated Circuit (IC) PMU used for energy harvesting applications such as BQ25504 or BQ25570 from Texas Instrument [66], [96], AEM30330 from E-peas Semiconductors [75], LTC3108, LTC3109 from Analog Devices [97], [98], etc. or self-developed PMU [95], [99], [100].

The circuits BQ25504, BQ25570 are the Boost and/or Buck converters used commonly in the applications of energy harvesting. The ultra-low quiescent current (less than 330 nA at 2.2 V) is an advantage of this circuit. To repeat, the quiescent current can be defined simply as the measure describing the current required to operate the circuit's basic functionality when the circuit has no load at the output. This parameter should be low to reduce the self-consumption of the circuit for its operation. The dynamic Maximum Power Point Tracking (MPPT) scheme for optimal energy extraction from a variety of energy generation sources are programmable and integrated in these circuits. However, the limit of these converters is that their cold-start voltage is typically high (at least 600 mV according to the datasheet).

The circuit AEM30330 is an integrated power management unit using Buck-Boost converter as DC/DC converter in the configuration. The MPPT scheme is also integrated in the circuit. The limitation of this circuit is its quiescent current of 875 nA at 3.7 V.

The Step-Up converter circuits LTC3108, LTC3109 are also considered for the energy harvesting applications. Compared to three previous circuits, these converters have a much lower cold-start voltage, 20 mV and 30 mV respectively. The quiescent current of these circuit is lower than the circuits BQ25504, BQ25570 and AEM30330. Nevertheless, the MPPT scheme is not ensured in the configuration of these circuits. Moreover, their input impedance (in the scale of a few **Ω**) is much smaller than the internal impedance of the rectifier (which is a few k**Ω**). This cannot ensure the power reception of the PMUs from the rectifier.

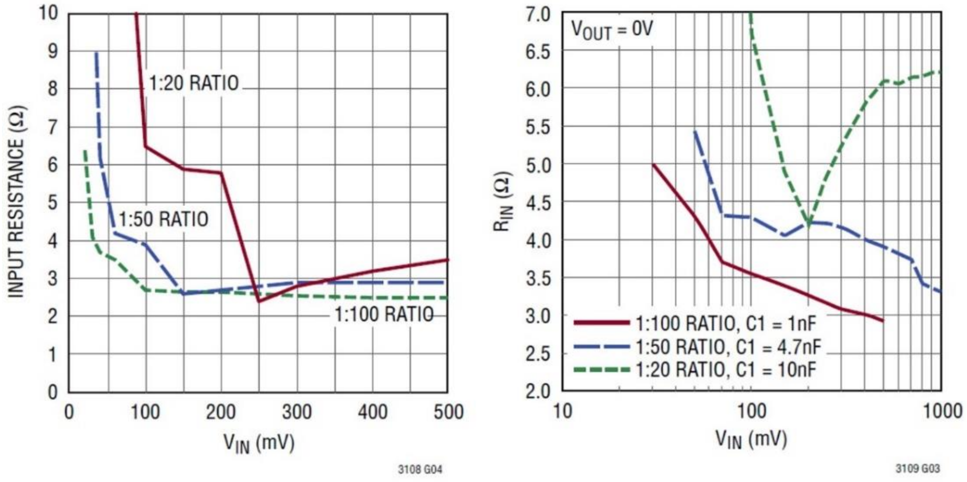

a **b**

Figure 2.31: Input impedance of LTC3108 (a) and LTC3109 (b)

In [95], the authors propose a self-developed PMU for their RFEH circuit. The PMU contains an inductive Boost converter that operates in discontinuous conduction mode. The MPPT scheme is not involved in the circuit. The MPP condition of the PMU is established statically, which means that the input impedance of the PMU is fixed and equates to the optimal load of their rectifier. A limit of their circuit is the high cold start voltage (2 V). Therefore, to make the circuit be in

Cette thèse est accessible à l'adresse : https://theses.insa-lyon.fr/publication/2023ISAL0007/these.pdf
© [X.V.L. NGUYEN], [2023], INSA Lyon, tous droits réservés

operation, a precharged supercapacitor at the output of the circuit is required to kick-start the Boost converter.

Paing et al. introduce an IC for ultralow power RF energy harvesting in [99]. The circuit operates a Boost converter in pulsed fixed-frequency discontinuous conduction mode, which is controlled by two simple oscillators in the form of integrated circuits. Thus, their controller quiescent current is very low. The limitation of this circuit is that a battery of 1.95 V is required at the beginning for the *Cold start* phase of the whole circuit. The autonomous capability of the circuit is not assured.

Heish et al. propose a RFEH with the cold start voltage of 0.3 V [100], which is lower than other works in our state-of-art. Furthermore, the MPPT scheme is also deployed in the circuit. The drawback of this circuit is the high controller quiescent current even though the circuit is fabricated in the form of IC.

The cold-start voltage, the minimum continuous energy harvesting from low-input source voltage, the controller quiescent current and the MPPT scheme are listed in Table 2.2.

For the RF energy harvesting application, a PMU with low cold-start voltage, low minimum continuous energy harvesting who consumes less power in a quiescent state is required. Additionally, the MPPT scheme should be satisfied in order to maximize the performance of the whole circuit. The presented circuits cannot validate at the same time the previous requirements. Therefore, we study our self-developed PMU, which will be presented in Chapter 5 for the principle explanation and Chapter 6 for the characterization, with the purpose of trying to validate simultaneously these requirements.

Cette thèse est accessible à l'adresse : https://theses.insa-lyon.fr/publication/2023ISAL0007/these.pdf
© [X.V.L. NGUYEN], [2023], INSA Lyon, tous droits réservés

Table 2.2: References of PMU circuit of our state-of-art

Reference	Cold start voltage (mV)	Minimum continuous energy harvesting from low-input source voltage (mV)	Controller quiescent consumption	Maximum Power Point Tracking Scheme
BQ25504 [66]	at least 600	130	Less than 0.33 µA at 2.2 V (0.726 µW)	Dynamic
BQ25570 [96]	at least 600	130	Less than 0.33 µA at 2.2 V (0.726 µW)	Dynamic
AEM30330 [75]	275	100	0.875 µA at 3.7 V (3.23 µW)	Dynamic
LTC3109 [98]	30	NI	0.2 µA at 3.3 V (0.66 µW)	NI
LTC3108 [97]	20	NI	0.2 µA at 3.3 V (0.66 µW)	NI
Self-developed (Salah et al.) [95]	2000*	NI	0.15 µA at 3 V (0.45 µW)	Pre-defined the input impedance of the Boost converter
Self-developed (Paing et al.) [99]	1950*	NI	0.2 µA at 1.95 V (0.39 µW)	NI
Self-developed (Hsieh et al.) [100]	300	NI	1.56 µA at 2 V (3.12 µW)	Dynamic

** Precharged supercapacitor/Battery at the output of the circuit*
Dynamic: Using other circuits integrated in the PMU to seek the MPP
NI: Not Indicated in the article/the datasheet

2.5. 3D Rectenna

In this section, the prototypes of Radio Frequency Energy Harvester in 2D and 3D forms realized with different methods will be presented. Three techniques of fabricating the substrates of the circuits are interested, which are Conventional method – Printed Circuit Board, Flexible substrates and 3D printing. In term of the electronics, the operating frequency, the antenna, the topology of the rectifier, the rectified voltage and the efficiency of the rectifier will be mentioned in Table 2.3 at the end of the section. The total dimensions of the rectenna will be also concerned also at that table.

2.5.1. Printed Circuit Board (PCB) – Conventional 2D method rectenna

In [101], a 2.45 GHz rectenna for low-input power energy harvesting is presented. The rectenna is fabricated on a 25-mil-thick (0.6 mm) RT/Duroid 6002 with a dielectric constant of 2.94 and loss tangent of 0.0012 as shown in Fig. 2.32. The antenna is a dipole antenna with a reflecting plane behind in order to improve the gain of the antenna and to obtain the directional radiation in order to receive more power for rectification when the incident power is low. The rectifier is mono-diode in shunt topology using Schottky HSMS-2852 diode. The output load is a resistor of 2.8 kΩ to extract the rectified power. The impedance matching between the antenna and the rectifier is achieved by adjusting the position of the diode and the storage capacitor.

Cette thèse est accessible à l'adresse : https://theses.insa-lyon.fr/publication/2023ISAL0007/these.pdf
© [X.V.L. NGUYEN], [2023], INSA Lyon, tous droits réservés

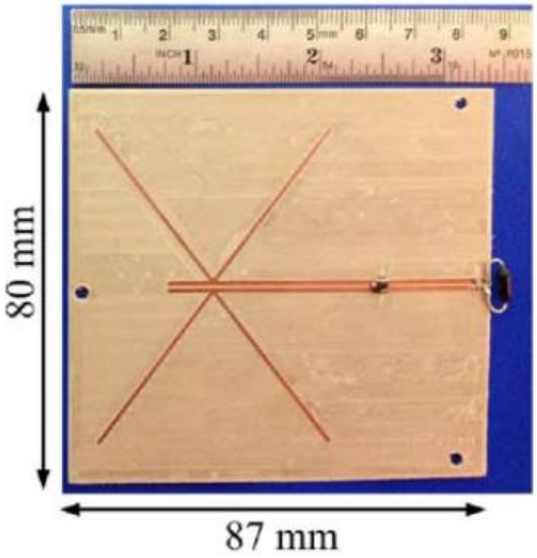

Figure 2.32: 2.45 GHz rectenna proposed in [101]

The advantage of the dipole antenna is its omni-directional radiation pattern, which will be further explained in Chapter 4. This advantage can allow the RFEH to capture more EM waves around the circuit. However, the performance of the antenna can be affected by the objects around the circuits, especially the metallic objects. Another limitation of this kind of antenna is linear polarization of the antenna, which will be further explained in Chapter 4. To overcome this limitation, cross dipole form is proposed in [76]. With this configuration, the rectifier circuit cannot be placed on the same surface with the antenna, therefore, the multi-layer assembly is preferred. The article [76] will be analyzed in the next section.

The idea of improving the antenna's gain of the dipole antenna can be realized by adding the reflecting element and director elements to obtain the Yagi-Uda antenna. As a proof, in [89], the authors present a Yagi-Uda antenna on a 62-mil-thick (1.57 mm) RT/Duroid 5870 substrate with a dielectric of 2.33. It should be noticed that by increasing the number of director elements, the gain of the antenna can be improved. However, the dimensions of the whole antenna will be increased. Moreover, by adding the reflecting element and the director elements, the radiation pattern of the dipole will be turned to directional pattern, which will be explained in Chapter 4. To solve these limitations, in [4], the authors propose a Yagi-Uda antenna printed on flexible substrate. This article will be reported later. The rectifier is placed on 31-mil-thick (0.78 mm) RT/Duroid 5880 with dielectric constant of 2.2. The rectifier consists of a Schottky diode Avago HSMS-2852 placing in series with a load of 5 kΩ. The reason of choosing this value of load is not noted in the article. The rectenna operates at two bands of frequency, which are 1.8 GHz and 2.1 GHz. Here, we focus on the performance of the circuit at 2.1 GHz.

Cette thèse est accessible à l'adresse : https://theses.insa-lyon.fr/publication/2023ISAL0007/these.pdf
© [X.V.L. NGUYEN], [2023], INSA Lyon, tous droits réservés

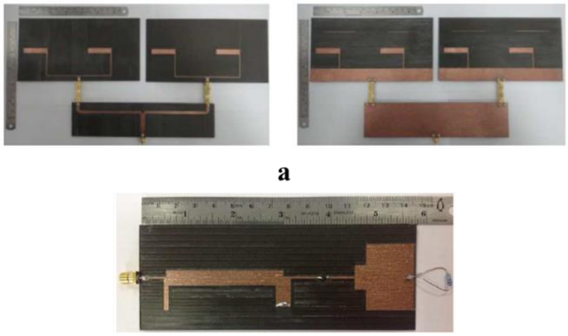

Figure 2.33: Proposed rectenna in [89] (a. Front and Back view of antenna; b. Rectifier)

Patch antennas are also used in the rectenna due to its better gain than the dipole's one theoretically [102]. In [103], a patch antenna with transmission line feeding method connecting a modified bridge rectifier is introduced. The whole circuit is etched on Rogers Duroid 5880 substrate, whose relative permittivity is 2.2 and loss tangent is 0.0009. Even the rectenna is used for the Wireless Power Transfer applications, the idea of using the patch antenna can be considered.

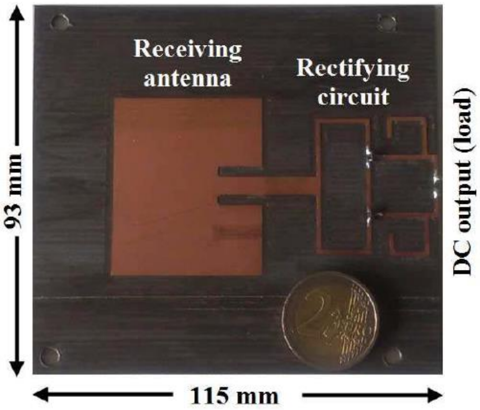

Figure 2.34: Rectenna for Wireless Power Transfer applications in [103]

The limitation of the patch antenna is its directional radiation pattern. An idea is to implement the patch antennas in the face of a 3D object, i.e. a cube, a cylinder [4], [104]. Additionally, to avoid the mismatch polarization loss between the antenna and the received EM waves, the patch antenna is configured to achieve the circular polarization [102]. This idea of antenna concept will be further described in Chapter 4 of this manuscript.

2.5.2. Printed Circuit Board (PCB) – Assembly of PCBs to form a multilayer rectenna

As mentioned previously, crossing two dipoles will allow us to overcome the limitation of linear polarization of the dipole antenna. Nevertheless, it is quite hard to place on the same surface the antenna and the rectifier.

In [76], Song et al. propose a rectenna as multi PCB layers to create 3D form as shown in Fig. 2.35. The antenna and the rectifying circuit are built on FR-4 and Duroid 5880, respectively. The reason of choosing the substrates is not indicated in the article. The rectenna is a dual band circuit composed of two bands of frequency which are 1.8 GHz and 2.5 GHz. The antenna is a cross dipole configuration selected due to its dual polarization and broad beam-width being suitable

Cette thèse est accessible à l'adresse : https://theses.insa-lyon.fr/publication/2023ISAL0007/these.pdf
© [X.V.L. NGUYEN], [2023], INSA Lyon, tous droits réservés

for incoming waves with arbitrary polarization and different incident angles. The rectifier has two branches for two corresponding bands of frequency. Each branch is a full wave rectifier using an SMS 7630 Schottky diode with the output load of 14.7 kΩ where the conversion efficiency is maximized. This value of load is obtained by sweeping the load resistance form 1 kΩ to 100 kΩ during the circuit optimization. The 50 Ω matching circuit between the antenna and the rectifying circuit is based on shorted circuit and radial stubs connected serially with the lumped components.

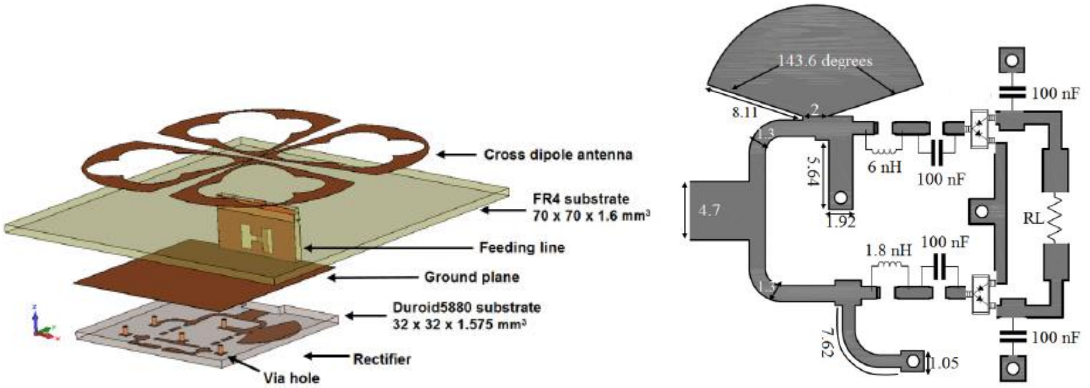

Figure 2.35: Layout design of the rectenna (left) and the schematic of the rectifier (right) [76].

Besides the dipole antennas, the patch antennas are also studied for the application of energy harvesting. Multilayer PCB is preferred in case of using the patch antennas with the slot feeding method [105] or the probe feeding method [80].

In [105], the authors present a 2.4 GHz ISM band rectenna containing an aperture coupled dual linearly polarized patch antenna with two voltage doubler circuits for both polarizations. The patch antenna and antenna feed lines are placed on two Arlon A25N substrates separated by a Rohacell 51 foam layer. The rectifiers are also manufactured on the Arlon A25N substrates. The selected rectifying diode is SMS7630 Schottky diode and the output load is a resistor of 8.2 kΩ. In order to glue together the various layers, the spray adhesive 3M Super 77 is used.

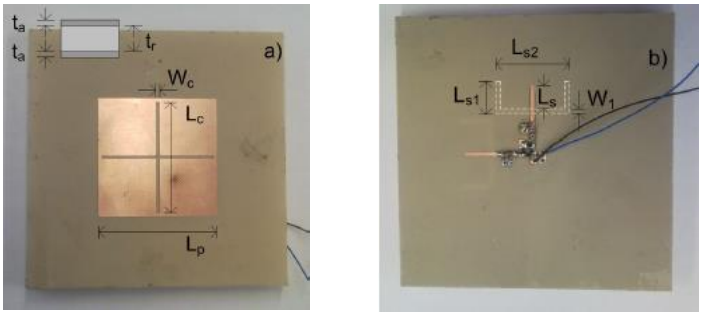

Figure 2.36: Proposed rectenna in [105] (a. Front view; b. Back view)

In [80], a system of multi-layer 2.45 GHz rectenna is introduced for the application of wireless sensor node remote supply. The antenna is a patch antenna with a probe feeding method realized on FR-4. Koch curve fractal method is applied to reduce the size of the antenna and a size reduction of 17% is achieved. The rectifier is a T-junction filter with a dual cascaded Dickson voltage multiplier using SMS7630-079LF Schottky diode shown in Fig. 2.37. The rectifier is also realized on FR-4. The layers of the rectenna are connected to each other through vias.

Cette thèse est accessible à l'adresse : https://theses.insa-lyon.fr/publication/2023ISAL0007/these.pdf
© [X.V.L. NGUYEN], [2023], INSA Lyon, tous droits réservés

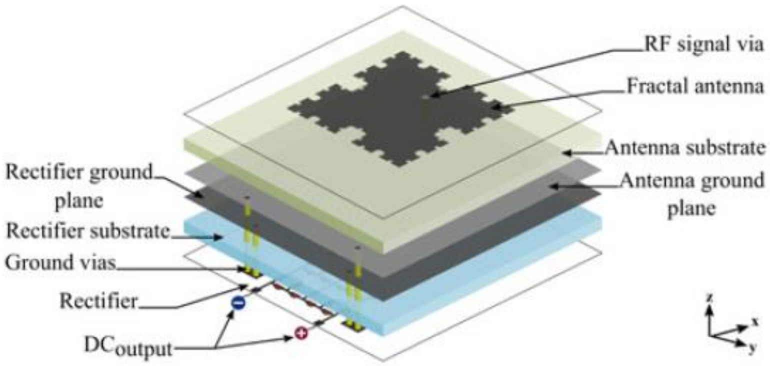

Figure 2.37: 3D view of the basic cell rectenna [80]

2.5.3. Printed Circuit Board (PCB) – Assembly of PCBs to form a 3D shape rectenna

Such systems of rectenna as the form of a box used to harvest the ambient RF energy is introduced in [73]. The system of rectennas is a quad-band energy harvester, which are 98 MHz, GSM 900, GSM 1800 and WiFi 2.45GHz. For the three high bands of frequency, an antenna consisting of a modified cross dipole antenna is designed. In this design of the antennas, the coupling between them becomes a potential problem to study. The performance of the rectenna can be degraded with the high coupling effect between the antennas. In this article, this effect is not clearly mentioned and studied. The antenna is made on FR-4 substrate with the thickness of 1.6 mm. For the frequency of FM 98 MHz, the antenna is an inductively loaded monopole antenna. Between the antenna and the rectifier, a 1x4 Wilkinson power combiner covering a frequency range of 0.5 to 3 GHz is introduced. This circuit is realized on FR-4 with a thickness of 1.6 mm. A voltage doubler is chosen as the topology of the rectifier. This circuit uses SMS7630 Schottky diode with the matching circuit of 4 stubs in parallel for the high frequencies and lumped elements for 98 MHz. The load is chosen as 10 kΩ since this value represents the typical resistance value of IoT sensors.

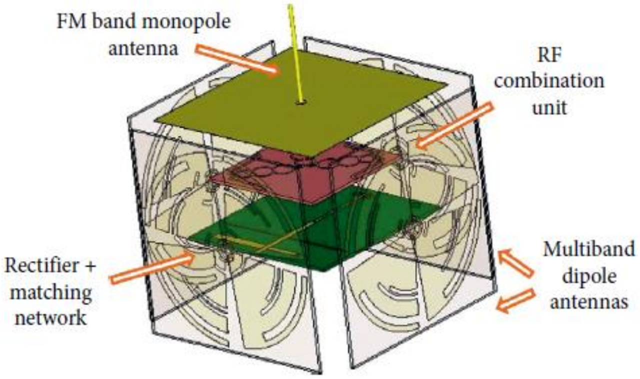

Figure 2.38: 3D cube rectenna structure [73]

2.5.4. Printed Electronics (PE) on flexible films rectenna

In [4], Do et al. use screen printing technology with a silver conductive ink Electrodag PF-410 to fabricate a 2.45 GHz rectenna on a flexible substrate. The selected substrate is Polyethylene Terephthalate (PET) with the thickness of 0.175 mm. The antennas are quasi-Yagi structure with end-fire radiation configuration with the realized gain around 6.1 dB. Moreover, a four-port series topology with SMS7630 diode with shorted circuit stubs with a load of 1.8 kΩ is developed. The value of the load is selected in order to maximize output power in case the rectifier only had one main source and other branches were not excited.

Cette thèse est accessible à l'adresse : https://theses.insa-lyon.fr/publication/2023ISAL0007/these.pdf
© [X.V.L. NGUYEN], [2023], INSA Lyon, tous droits réservés

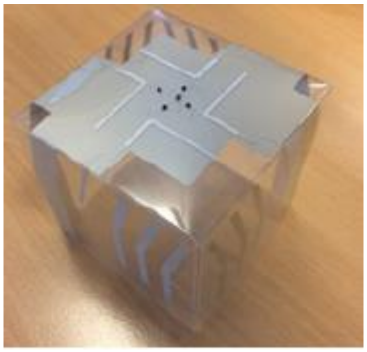

Figure 2.39: Proposed flexible rectenna in [4]

In [106], a combination of screen and inkjet printing, which is direct-write dispenser printing, with the silver conductive ink is used to print a folded dipole antenna on a flexible Kapton substrate of 75 µm thickness. The advantage of the dispencer printing, compared to screen printing and subtractive photolithography of copper sheets, is that this technology is a zero-waste process, only the required ink is deposited on the substrate and no conductive material is wasted. The peak directivity of the antenna is 1.85 dBi with the maximum radiation efficiency of 72%. The antenna is combined to a voltage doubler rectifier optimized for -20 dBm input RF power level. The load is chosen as 7 kΩ to acquire the optimal point of operation with the diode SMS 7630 from Skyworks.

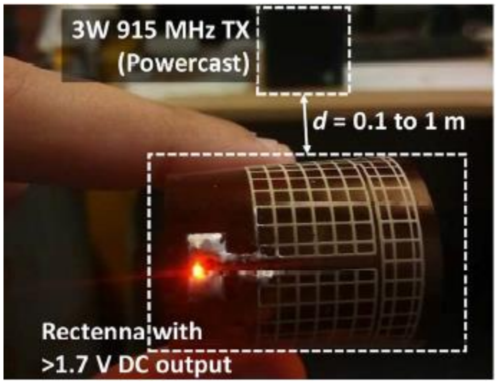

Figure 2.40: Assembled rectenna printed on flexible Kapton substrate using direct-write dispenser printing method [106]

In [107], the authors suggest a rectenna manufactured via embroidery of conductive textiles onto fabric-based substrates. The energy harvester is a 2.45 GHz circuit of a patch antenna and a shunt topology circuit with an SMS 7630 diode with lumped components and microstrip lines for the matching circuit. The output load of the circuit is set to 5.3 kΩ.

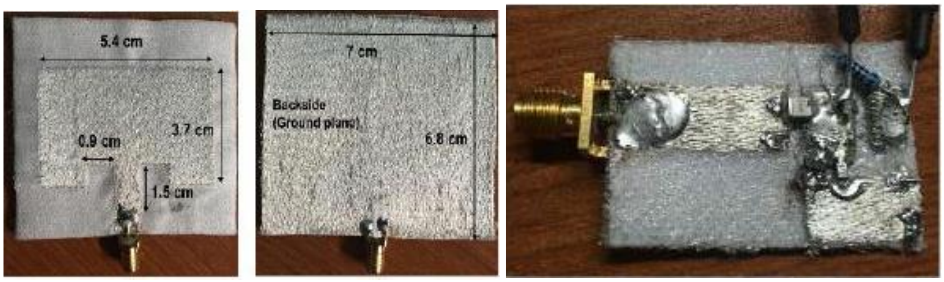

Figure 2.41: Rectenna fabricated onto fabric-based substrates [107].

Cette thèse est accessible à l'adresse : https://theses.insa-lyon.fr/publication/2023ISAL0007/these.pdf
© [X.V.L. NGUYEN], [2023], INSA Lyon, tous droits réservés

2.5.5. 3D printed substrates with ink printing technology

A rectenna from GSM 800, GSM 1800 and 2100 MHz signals in the form of 3D cube-shaped is described in [108]. The rectenna is fabricated through additive manufacturing techniques such as 3D printing and screen printing. The substrate is 3D-printed Vero polymer. The Cantor fractal dipole antenna with the conductive traces are then printed on the surface of the substrate with a screen printing technique. Afterwards, the Surface Mounted Devices (SMD) such as the rectifying diode SMS7630-079, capacitors and a load of 11 kΩ, where the maximum conversion efficiency is obtained, are mounted using conductive epoxy.

Figure 2.42: 3D printed cube-form rectenna (left) and realized rectifier with matching circuit (right) [108].

Another rectenna in the form of a foldable cube is manufactured using 3D printing method in [104]. The antennas are patch antennas printed using ink printing method on each face of the cube connected with wires to the rectifier circuits installed inside the cube. The substrate of the antenna is VeroWhite and the used substrate for the rectifier is Rogers 4003C. The rectifiers have the voltage-doubler topology with the Avago HSMS-285 as rectifying diodes. A load of 2 kΩ is driven at the common output of both circuits. As noticed in [104], this value may be considered as the equivalent load resistance of a low-power microcontrollers used for Wireless Sensor Nodes applications.

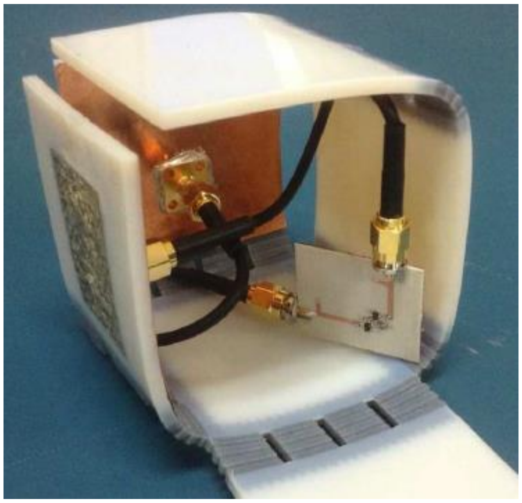

Figure 2.43: 3D foldable printed cube-form antenna with interior rectifiers [104].

Cette thèse est accessible à l'adresse : https://theses.insa-lyon.fr/publication/2023ISAL0007/these.pdf
© [X.V.L. NGUYEN], [2023], INSA Lyon, tous droits réservés

The Additive Manufacturing fabrication process can be applied to realize the RFEH circuits for the 5G bands of frequency. As a proof, a 5G System-on-Package (SoP) module is fabricated using the fully Additive Manufacturing fabrication process summarized in [109]. The module is an energy harvester for 5G embedded inside a 3D-printed cavity to support the endless functionality. The flexible base substrate with ramps, via, and the cavity is 3D printed using the Formlabs Form2 3D printer. The array of patch antennas and the conductive traces of the module are printed on the surface of substrates using inkjet-printing technology. The energy harvester with a 750 kΩ load resistor was tested at 26 GHz.

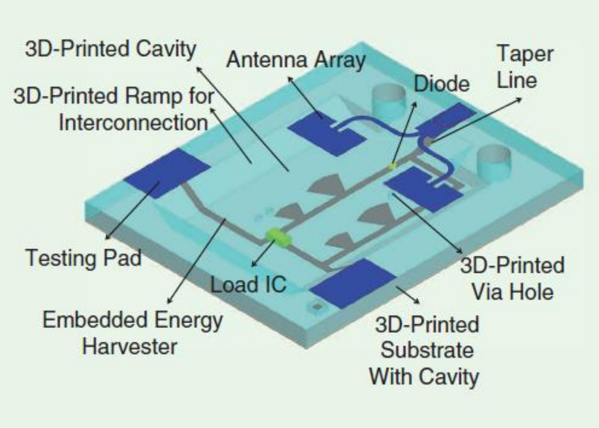

Figure 2.44: The embedded-on-package energy harvester within a 3D-printed, multilayer packaging structure [109].

2.5.6. Conclusion

The antennas used in the rectenna are commonly patch antennas, dipole antennas and its improvements of gain, i.e. adding the director and/or reflector planes, Yagi-Uda antennas, etc.

Concerning the dipole, the advantage of this antenna is its omni-directional radiation pattern while the limitation is its linear polarization [102]. It should be remarked that in RF energy harvesting applications, the possibility of capturing all the waves in any polarizations is strongly recommended. Thus, the idea of using cross-dipole antenna is preferred due to its simplicity. This configuration of dipole antenna allows us to mimic the circular polarization and to have a full cover radiation pattern. However, the radiating performance of the antenna can be affected easily with the presence of other objects, especially metallic objects, magnetic objects, etc. In addition, the coupling effect between the antennas in an array or a system of antennas should be well studied to prevent the degradation of performance of the rectenna. Moreover, it is hard to have the rectifier and the antenna on the same plane with this configuration. For the PCB, using the multilayers is a solution, but for 3D Plastronics, this question is still in research not only for 2D form but also 3D form circuits.

The patch antennas allow us to have a good gain design and circular polarization, which will be discussed in Chapter 4. Furthermore, the full ground surface of the patch can reduce the impacts of elements placed behind the plane on the radiating performance of the antenna. Nevertheless, its directional radiation pattern is a drawback in designing the RFEH. The solution is to place multi patch antennas around to ensure the possibility of the capturing all the waves in the air. The antennas can be fed with the probe feeding method or the coupled line method. These techniques can reduce the total size of the antennas. However, for the probes feed method, the vias are required while for the coupled line method, the multilayer substrates are necessary. For 3D Plastronics, realizing the multilayers for 2D form and 3D form circuits are always in research. In fact, a

Cette thèse est accessible à l'adresse : https://theses.insa-lyon.fr/publication/2023ISAL0007/these.pdf
© [X.V.L. NGUYEN], [2023], INSA Lyon, tous droits réservés

possibility is that the circuit is manufactured on a separated polymer and then is stuck on the surface of other objects.

For this thesis, the selected kind is patch antennas with transmission line feeding configured for circular polarization, which will be further described in Chapter 4. This configuration is selected due to its simplicity of design among other propositions.

The electrical performance of the rectenna at -20 dBm over the band of 2.1-2.5 GHz are listed in Table 2.3. The rectennas are categorized in different methods of manufacturing, operating frequency, the type of antenna, the rectifier, the diode, the loads and the dimensions. Comparing to the circuits fabricated with conventional method and the printed circuits on flexible substrates, the rectennas manufactured with the aid of 3D printing methods have the comparable RF-DC conversion efficiency at the studied power and frequency. This can conclude that the possibility of using 3D printing methods for manufacturing the rectennas with a comparable performance to the conventional circuits' one.

The work of [101], which has a much higher result than other works. This can be explained as the reference impedance for the matching between the antenna and the rectifier are not 50 Ω. The authors mention that 40 + j200 Ω gives the optimal conversion efficiency for their circuit and the matching circuit is studied to optimize the matching performance. The rectenna described in [89] has a higher efficiency than other circuits. This result is discussible since the efficiency of the rectenna is slightly higher than the rectifier when connecting to a RF generator. The antenna and the rectifier are both matched to 50 Ω.

The dimensions of the 3D form circuits are quite identical since their operating bands of frequency are similar. The selected forms of 3D circuits are in the form of a cube, which can be easily obtained by conventional methods. The complexity of form, i.e. bending the substrate, can be further studied to understand its impacts to the performance of the antennas and the RFEH circuits.

Cette thèse est accessible à l'adresse : https://theses.insa-lyon.fr/publication/2023ISAL0007/these.pdf
© [X.V.L. NGUYEN], [2023], INSA Lyon, tous droits réservés

Table 2.3: References of rectennas

Ref.	**Method of realization**	**Operating freq. (GHz)**	**Antenna/Realized gain**	**Rectifier/Diode/Load**	**RF-to-DC conversion efficiency of rectenna**	**Size**
[89]	Conventional 2D method	1.8 2.15	Quasi Yagi array/ 9.9 dBi @ 1.8 GHz; 13.3 dBi @ 2.15 GHz	Series diode/ HSMS-2852/5 kΩ	27% @ -21 dBm @ 2.15 GHz	NI
[101]		2.45	Dipole/ 8.6 dBi (with reflector plane)	Shunt diode/ HSMS-2852/2.8 kΩ	40% @ -20 dBm	87 x 80 mm^2
[76]	Multilayer PCB	1.8 2.5	Cross dipole with slot/ 2.5 dB @ 1.8 GHz 4 dB @ 2.5 GHz	Two Greinacher circuits topology/SMS7630/ 14.7 kΩ	7% @ -20 dBm @ 2.4 GHz	70 x 70 x 13.2 mm^3
[105]		2.45	Dual linearly polarized patch/ 7.5 dB	Two voltage doublers/ SMS7630/8.2 kΩ	15.7% @ -20 dBm	32 x 34 x 7 mm^3
[73]	3D Shape PCB	0.9 1.73 2.4	Slotted dipole antenna/ 3 dBi @ 0.9 GHz; 4.72 dBi @ 1.73 GHz; 4.9 dBi @ 2.4 GHz	Voltage doubler/ SMS7630/ 10 kΩ	3% @ -20 dBm @ 2.4 GHz	100 x 100 mm^2
[107]	PE on flexible films	2.45	Patch antenna/ 5.1 dBi	Shunt diode/SMS7630/ 5.3 kΩ	18.7% @ -20.8 dBm	70 x 68 mm^2
[108]	3D printed substrate	0.9 1.8 2.1	Cantor fractal dipole/ NI	Series topology/SMS7630-079/11 kΩ	17% @ -20 dBm @ 2.1 GHz	50 x 50 x 50 mm^3
[104]		2.3	Patch antenna/ 4-4.2 dBi	Two voltage doublers/ HSMS-285/2 kΩ	4.5% @ -20 dBm (1 port) 7.6% @ -20 dBm (2 ports)	57 x 57 x 57 mm^3

NI: Not Indicated in the article

Cette thèse est accessible à l'adresse : https://theses.insa-lyon.fr/publication/2023ISAL0007/these.pdf
© [X.V.L. NGUYEN], [2023], INSA Lyon, tous droits réservés

2.6. Wrap-Up

In this chapter, we report principle of different mechanisms of ambient energy harvesters, which are thermal, mechanical, solar and Radio Frequency energy harvesters. Their measured energy density available in the environment, their advantages and disadvantages are mentioned later. According to Table 2.1, RFEH is a suitable candidate as a power supply source for the particular cases where no other energy is available of higher potential and if the payload requires a very low level of energy (or accepts to operate sporadically). The low cost and the availability of the RF waves in daily life (indoor and outdoor environments) are the advantages. Nevertheless, the low level of power density of RF waves is a drawback. The concept of RFEH can only address a very low output consumption unless strategies of long-term storage are considered to serve sporadic operating loads.

Thereafter, the electrical structure of a rectenna is presented. Different kinds of existing topologies of the rectifier as well as the impedance interference between this part and the antenna are introduced. 50 Ω impedance matching is selected mostly for pragmatic reason even though it is not the best option. Then, the Power Management Unit is also concerned. This optional electrical part is proposed essentially with the purpose of increasing and controlling the output voltage of the rectenna to a desired value of the consumption load. The impedance matching between the PMU and the rectifier is analyzed as well. The Maximum Power Point condition is suggested for the impedance matching to maximize the output power of the whole system.

The developed 2D and 3D rectennas in the literature are listed as a part of the state-of-art. The common techniques for creating 3D rectennas are

- Assembling the 2D PCB pieces in a simple 3D shape.
- Using flexible materials for the substrates and ink printing technique or conductive textile to obtain the 3D circuits.
- Printing directly the 3D forms for the substrate and using ink printing technique.

The former technique gives us the circuits with a good mechanical resistance with a good electrical performance. Nevertheless, the limitation of this technique is its low diversity and the complexity of the assembly. It seems difficult for example to integrate such fabricated RFEH into most existing devices.

Meanwhile those parameters can be improved with the second technique. However, the rigidity of the fabricated circuits is a main drawback of this technique. In addition, another drawback is the low conductivity of the conductive inks.

With the aid of additive manufacturing, the third technique seems a good choice to enhance the complexity and the rigidity of the fabricated 3D circuits. Additionally, this technique can be applied to manufacture emerging 5G devices [109]. Nevertheless, the low conductivity of the used inks is still a limitation.

In fact, the question about the conductivity of the conductor can be solved by passing the ELD method, which gives us a much better conductor as stated in Section 1.3.2.2 of Chapter 1.

Cette thèse est accessible à l'adresse : https://theses.insa-lyon.fr/publication/2023ISAL0007/these.pdf
© [X.V.L. NGUYEN], [2023], INSA Lyon, tous droits réservés

CHAPTER 3: MANUFACTURING AND CHARACTERIZATION OF MATERIALS

Cette thèse est accessible à l'adresse : https://theses.insa-lyon.fr/publication/2023ISAL0007/these.pdf
© [X.V.L. NGUYEN], [2023], INSA Lyon, tous droits réservés

Cette thèse est accessible à l'adresse : https://theses.insa-lyon.fr/publication/2023ISAL0007/these.pdf
© [X.V.L. NGUYEN], [2023], INSA Lyon, tous droits réservés

3. MANUFACTURING AND CHARACTERIZATION OF MATERIALS

This chapter discusses the manufacturing method of the plastronic circuits. Firstly, the selected method of creating the polymer substrates for the circuits, Stereolithography, will be introduced. Afterwards, the method of depositing the conductor on the surface of the printed objects will be presented. Then, the etching method and the component mounting method will be also concerned. Finally, a summary of the manufacturing process will be illustrated to provide a global view about one of a method of manufacturing the plastronic circuits.

3.1. Manufacturing

3.1.1. Stereolithography (SLA)

In this thesis, the SLA objects are printed with a Form2 SLA and Form3 SLA printers using the High Temp (HT) Resin v1 and HT Resin v2 photopolymer from Formlabs. These resins are selected due to its good resistance to high temperature (around 289°C at 0.45 MPa for HT Resin v1 and 238 °C at 0.45 MPa for HT Resin v2) [110] which allows the electrical components to be easily soldered on the surface of the substrates later.

Figure 3.1: Form2 (left) and Form3 (right) SLA printers from Formlabs

Stereolithography (SLA) is developed based on the polymerization of photosensitive resins [23]. As this method is additive, the manufactured object is built up layer by layer in a tank of photopolymer under the action of a laser of a defined wavelength. A SLA machine contains hardware parts, which are a built platform submerging the tank of liquid resin and the laser source, and a software part used to control the printing process. The 3D objects with supporting structures, which are necessary to prop up and to maintain the form of printed parts during the process, are converted into the assembling of 2D slices. These 2D slices correspond to the track of the laser solidifying the resin and thus creating the layers of the objects. This process will be repeated until the objects are completed. The duration depends on the amount of printing 2D slices, the dimensions, the area of these slices, the type of resin, etc. Afterwards, the printed objects are removed from the machine and the remains of liquid resin on the objects are cleaned by application of a solvent, i.e. isopropanol. The objects produced by SLA generally are not fully polymerized. Therefore, UV ovens are required for a final curing. The supporting structures can be removed manually either before or after curing in the UV ovens. Finally, the objects are then sanded to remove completely remains of supporting structures on their surfaces.

3.1.2. Electroless Deposition (ELD)

Metallizing the object is the next step in the fabrication process. The object is immerged in a tank of palladium catalyst solution (Macuplex Activator-D34C, MacDermid), rinsed in water, and deposited in an electroless copper tank (MidCopper 100XB, MacDermid) for about 120-180 min.

Cette thèse est accessible à l'adresse : https://theses.insa-lyon.fr/publication/2023ISAL0007/these.pdf
© [X.V.L. NGUYEN], [2023], INSA Lyon, tous droits réservés

As a result, the surface of the objects is entirely metallized with copper of 6-7 µm typical of thickness. The further detail of this step is given in Section 1.3.2.2 of Chapter 1.

3.1.3. Etching method

After depositing a conductive layer by applying ELD method, in order to craft the desired conductive traces on the surface of the objects, a step of etching is necessary. A subtractive method is applied for this step. The masks of a specific polyvinyl are cut with the aid of cutter machine CAMM-1 GS-24 of Roland following the design of the circuits with the minimum cutting dimension of 12.5 µm per cut. Literally, the accuracy of the etched conductive traces depends on this parameter of the cutter machine. These masks will cover the desired conductive traces deposited on the objects. After that, the masked objects will be dipped in an iron perchloride bath to clear totally the unwanted deposited conductive parts away. The process duration depends on the thickness of the deposited conductor. In our case, the average time for the etching is around 1 minute. Once the etching process is done, the objects are cleaned with water and the masks are pulled out mechanically. The objects are then dried by the compressed air to remove the remaining water on the surface of the objects.

3.1.4. Component mounting methods

Mounting the electrical components on the surface of electrolessly metallized objects is the last step in the manufacturing process. The components can be soldered manually using standard brazing material on the surface of the object. However, this method spends time to finish, the quality of the solders is not ensured and not precise.

Another method is to use a reflow oven in order to realize the soldering. The oven has a form of a long tunnel consisting of a conveyor belt to travel the circuits. In the oven, there are several sources of heat. The speed of the conveyor belt and the temperature of the oven are controlled by a computer to respect the recommended reflow profile of the applied soldering paste. The reflow profile is a temperature profile in the oven according to the recommended variation of temperature for the soldering of parts to take place. In general, there are four steps with different thermal zones: *preheat, soak, reflow* and *cooling.*

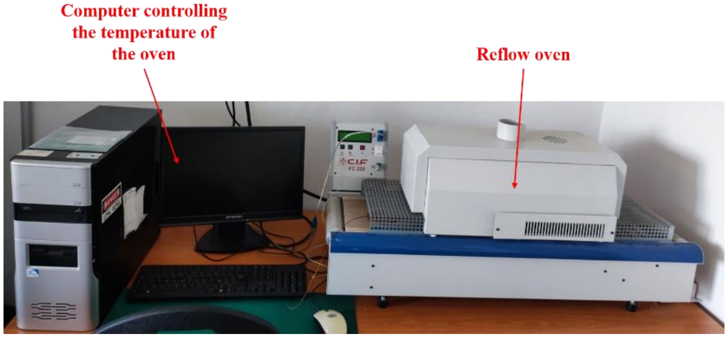

Figure 3.2: Reflow oven with controlling computer

Firstly, in the preheat zone, the circuits will be heated towards to a desired soak temperature. The goal of this step is to get the entire assembly safely to a soak temperature. After that, in the second zone, the volatiles in the solder paste are removed and the fluxes are activated. The fluxes start the redox on the components' pads. The maximum temperature of the mounting process is reached in the third zone where the paste will be completely in liquidus. The liquidus of paste will afterwards stick the components on the conductors. Finally, the circuits will be cooled down and the solder joints will be solidified simultaneously. This zone should be held gradually to avoid the damage to the soldered circuits because of thermal shock.

Cette thèse est accessible à l'adresse : https://theses.insa-lyon.fr/publication/2023ISAL0007/these.pdf
© [X.V.L. NGUYEN], [2023], INSA Lyon, tous droits réservés

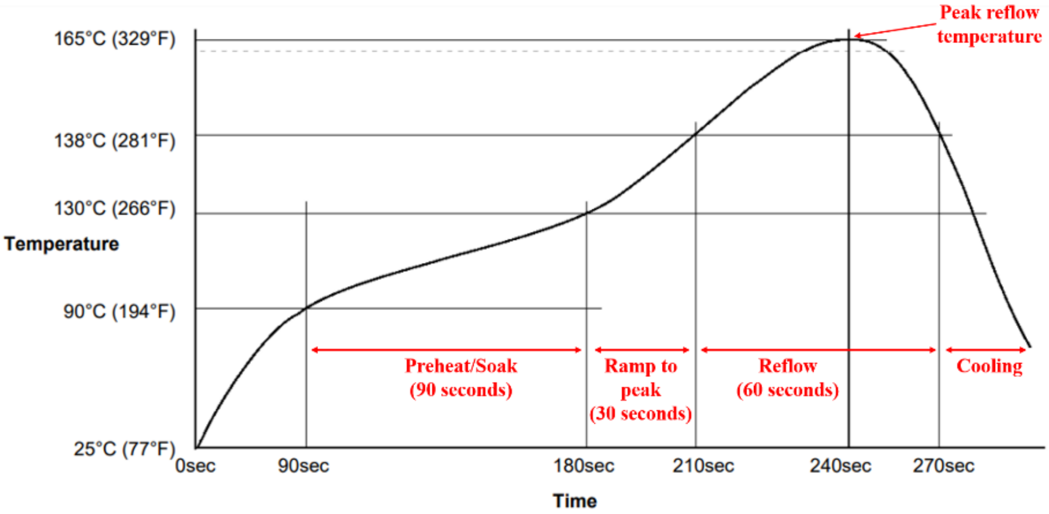

Figure 3.3: Reflow profile of TS391LT from Chipquik

The selected solder paste for this thesis is TS391LT from Chipquik due to its low peak reflow temperature (~165°C). The soldering paste is deposited where the electrical components are mounted.

The high temperature of the oven has the impacts on the manufactured electrical circuits, i.e. the oxidation, the burn of conductor, the degradation of material as shown in Fig. 3.4. Because of the high temperature, the reaction between the ELD copper with the oxygen in the air is speeded up, and the oxidation of the conductor happens. Additionally, the copper will be burned and its properties will change as Fig. 3.4.b. As mentioned previously in Section 1.3.2.1 in Chapter 1, the printed SLA objects always absorb the energy. When the objects are put in the oven, the energy is provided for the objects and this can degrade the form of the objects.

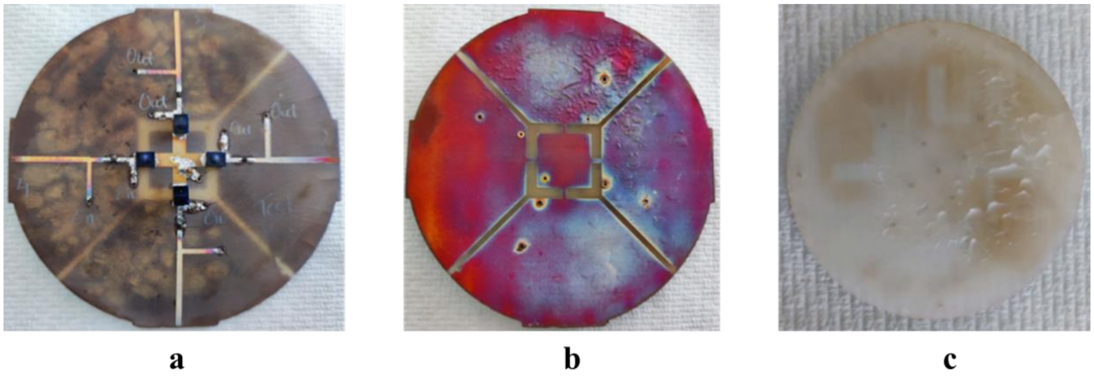
a b c

Figure 3.4: Surface degradation and oxidation of conductor (a), burned conductor (b) and substrate degradation (c)

Hence, to reduce these impacts from the high temperature to the conductors and the objects, Kapton tape is applied on the non-soldering parts. Here, Kapton tape is preferred since this material is a good thermal insulator.

Cette thèse est accessible à l'adresse : https://theses.insa-lyon.fr/publication/2023ISAL0007/these.pdf
© [X.V.L. NGUYEN], [2023], INSA Lyon, tous droits réservés

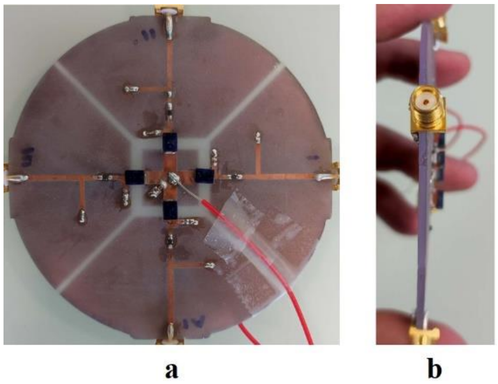

Figure 3.5: Fabricated circuit with mounted components (a. Front view; b. Side view)

As shown in Fig. 3.5, the surface of the conductor is not damaged because of the oxidation. The Kapton tape covers the conductor and prevent the reaction between the oxide in the air and the conductor. Moreover, the surface of the object is not burned or degraded by the heat of the oven. Kapton reduces the absorbed thermal energy of the printed SLA object. Nevertheless, the object is still slightly deformed as the thermal energy from the oven is not fully reduced by the Kapton tape. This phenomenon is explained in Section 1.3.2.1 of Chapter 1.

3.1.5. Summary of manufacturing steps

The manufacturing steps can be summarized as follow:

- Printing the plastic objects using SLA method and removing the supporting structures. The supporting structures are sanded for the removing.

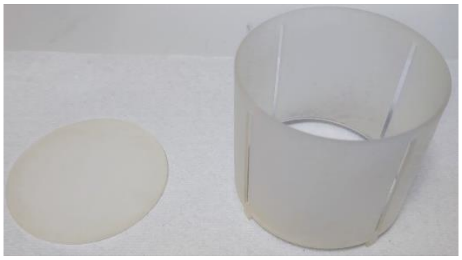

Figure 3.6: Printed SLA objects

- Treating the surface of the objects in order to improve the adhesion between the conductor and the deposited surfaces, whose description is outside the scope of this work.

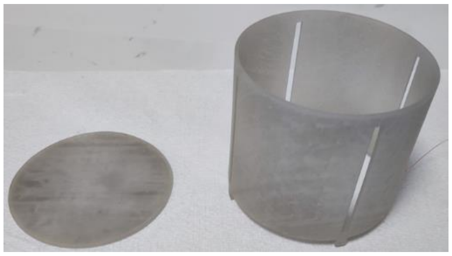

Figure 3.7: The objects with the treated surfaces (the surfaces turned to black because of the treatment process).

- Depositing Pd layer on the surfaces of the objects. The Pd layer is served as the catalyzer to start the oxydo-reduction reaction for the deposition purpose. The objects are immerged deeply in the tank of Pd.

Cette thèse est accessible à l'adresse : https://theses.insa-lyon.fr/publication/2023ISAL0007/these.pdf
© [X.V.L. NGUYEN], [2023], INSA Lyon, tous droits réservés

Figure 3.8: The objects are immerged in the tank of Pd.

- Immerging the treated objects in the tank of Cu^{2+} deeply for the ELD after depositing Pd layer. The reaction between the Cu^{2+} and Pd occurs in the tank. The blue color of the liquid indicates the presence of the ion of Cu^{2+}. To assure the safety during the manufacturing, this step is done in the fume hoods.

Figure 3.9: The objects are immerged in the tank of Cu2+.

- Finishing the electroless deposition process. The objects are then washed with the water and dried before passing the etching process.

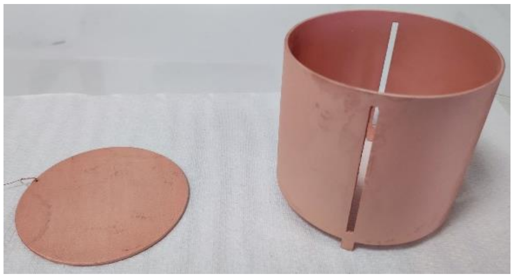

Figure 3.10: The objects with electrolessly deposited copper.

- Masking the objects with polyvinyl masks from the cutting machine for the etching process.

Cette thèse est accessible à l'adresse : https://theses.insa-lyon.fr/publication/2023ISAL0007/these.pdf
© [X.V.L. NGUYEN], [2023], INSA Lyon, tous droits réservés

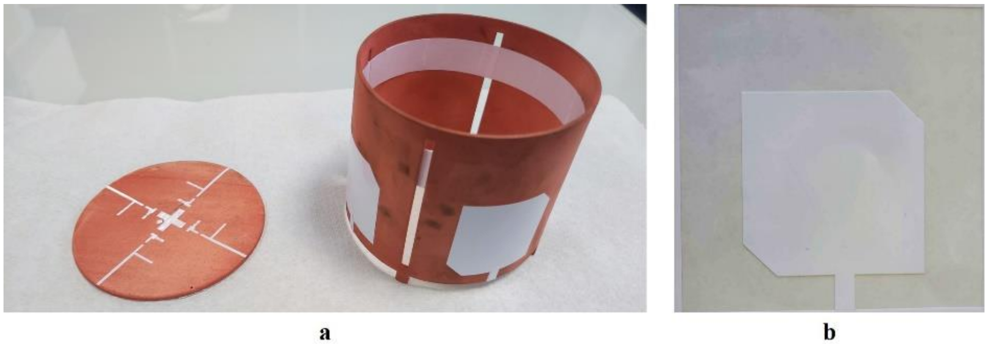

Figure 3.11: The masked objects for the gravure process (a. The objects with the masks; b. The masks cut from the cutting machine)

- Finishing the etching process to obtain the desired conductive traces. The objects are then washed with the water and the masks are removed. The desired conductive traces are deposited on the surface of the objects as shown in Fig. 3.12.

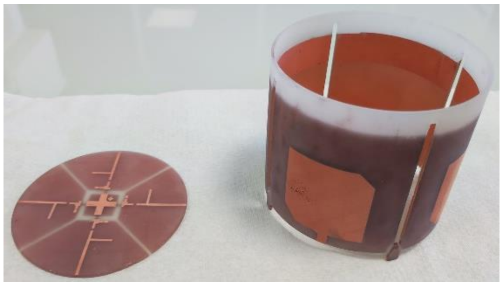

Figure 3.12: The objects after the gravure process.

- Soldering the electrical components on the surface of the objects (Fig. 3.13). The objects are ready for electrical testing.

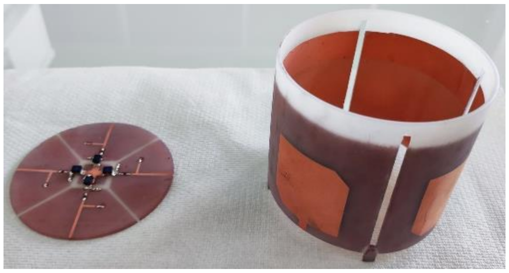

Figure 3.13: The objects with soldered electrical components on their surfaces.

3.2. Characterization of materials

Characterizing the electromagnetic properties of components such as conductors and substrates, plays a crucial role in designing Radio Frequency (RF) circuits. The designers require parameters related to materials.

In this chapter, the properties such as conductivity, thickness, surface roughness, of the electroless deposited copper will be studied. Afterwards, the method of determining the relative permittivity (ε_r) and the loss tangent ($\tan(\delta)$) of selected Stereolithography (SLA) substrates as well as the results will be presented.

Cette thèse est accessible à l'adresse : https://theses.insa-lyon.fr/publication/2023ISAL0007/these.pdf
© [X.V.L. NGUYEN], [2023], INSA Lyon, tous droits réservés

3.2.1. Conductors

The conductors always have lossy effects on the performance of antennas as well as RF circuits [111]. These effects come from the effective conductivity, the thickness and the surface roughness of the conductors. By measuring these parameters, it is possible to encompass the impact of conductors on the performances of designs.

3.2.1.1. Thickness of the deposited conductor

The thickness of the deposited conductor is measured using X-ray fluorescence machine from Bowman [112]. The measurements are deployed over 10 samples. The average measured value is (7 ± 1) µm. This value of the thickness of the conductor can be obtained after 120 min to 180 min of the conductor electroless deposition process.

At high frequency, particularly in the RF domain, the phenomenon of skin depth effect on the performance of the conductor is always concerned. Because of the skin depth effect, the electrical charges will concentrate at the edge of the conductor, the effective surface of the current flow crossing the conductor core is reduced. Consequently, the resistance of the conductor at high frequency will increase. The further explanation and calculation of the skin effect are expressed in [9]. At the scale of 2.45 GHz, the thickness of the skin depth effect (δ) related to the ELD copper, which will be presented in the next section, is around 1.4 to 1.6 µm.

To take into account this effect, the dimensions as the thickness and the width of the conductive line cross-section should be 2 times the skin effect thickness δ, i.e. 2.9 to 3.2 µm [113], [114]. However, such small dimensions are introducing issues with respect to components soldering points, as the necessary heat budget of the process can damage the adhesion of the conductor to the surface of the objects. Furthermore, reducing these dimensions can increase the DC current resistance of the conductor.

When the ratio between the dimensions of the cross-section surface and δ is higher than 2, at high frequency, the total attenuation in the line is nearly identical as the increment of the conductor's thickness [113], [115]. Therefore, increasing the thickness of the ELD copper is not required in this case. Furthermore, for the components mounting process, the ELD copper thickness of 7 µm can ensure the adhesion of the conductor to the surface of the objects.

Figure 3.14: X-ray fluorescence of Bowman used to measure the conductor's thickness

3.2.1.2. Surface roughness of the deposited conductor

In general, most of the calculations in RF design are simplified by the assumption of perfectly smooth surface of the conductor. Nevertheless, the surface of the conductor is always rough and this assumption may not be reasonable.

Cette thèse est accessible à l'adresse : https://theses.insa-lyon.fr/publication/2023ISAL0007/these.pdf
© [X.V.L. NGUYEN], [2023], INSA Lyon, tous droits réservés

In order to evaluate the surface roughness of the conductor, the microscope RH-2000 by Hirox [116] is used.

The surface of the copper on a Rogers 4003C substrate fabricated by Rogers Corp. is shown in Fig. 3.15 as a reference. The copper layer is laminated from a foil. The measured root-mean-square surface roughness of the conductor is $(0.5\ \pm 0.2)$ µm. This parameter will be used later for the RF properties characterizing step.

In fact, the surface roughness of the conductor influences the performances of RF circuits, i.e. the conductive loss of transmission lines [117]–[120], which will be described in the next part. The measured root-mean-square surface roughness of the ELD copper is (1 ± 0.2) µm, which is close to the value of copper layer of Rogers 4003C.

The surface of ELD copper is rougher than the surface of copper laminated on Rogers' substrate. The surface roughness of ELD copper might be improved with a sanding step of the polymer substrate before the deposition process. Nevertheless, if the surface is smoother, it will be detrimental on the adhesion of the deposited conductor. So far we estimate that a trade-off is obtained between the adhesion and the roughness (i.e. impact of RF properties).

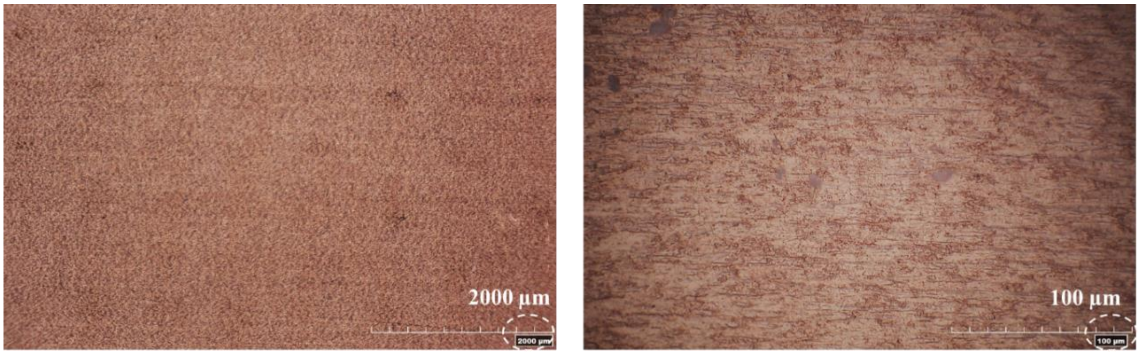

a b

Figure 3.15: The surface state of Rogers 4003C with different zooming scales (a – 2000 µm; b – 100 µm)

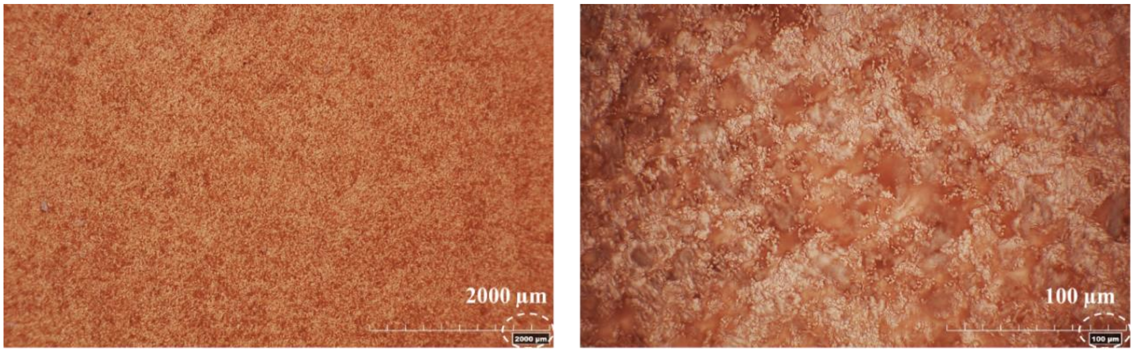

Figure 3.16: The surface state of SLA substrate after ELD copper step with different zooming scales (a – 2000 µm; b – 100 µm)

3.2.1.3. Resistivity of the ELD copper

The resistivity (ρ) of a conductor line sample is measured using the station S302 by Signatone with a Keithley 2450 Sourcemeter and the four-probe method. The conductivity (σ) of the deposited copper is then deduced.

Cette thèse est accessible à l'adresse : https://theses.insa-lyon.fr/publication/2023ISAL0007/these.pdf
© [X.V.L. NGUYEN], [2023], INSA Lyon, tous droits réservés

Figure 3.17: Four probe station by Signatone used to measure the resistivity of conductor

The evaluation of the conductivity of ELD copper on an SLA substrate is carried out over 10 samples. These measurements use the same samples produced to carry out the conductor thickness measurements (previous subsection). The measured conductivity is $(45 \pm 4.5) \times 10^6$ (S/m) corresponding to a resistivity of 0.02-0.025 μΩ.m.

The resistivity of the electroless deposited copper is very close to the bulk copper value and from 5 to 10 times lower than the value offered by printing inks used in antennas and RF circuits manufacturing. This is an advantage to reduce the lossy impacts of conductor on the performance of RF circuits [111].

3.2.1.4. Conclusion

The thickness of (7 ± 1) µm of the ELD copper should be considered as good enough from the electromechanical point of view in the process of mounting the electrical components on the surface of the SLA objects.

The surface roughness of the ELD copper is approaching the value of the copper laminated on the Rogers 4003C substrate (Rogers Corp).

The resistivity of the ELD copper (0.02-0.025 μΩ.m) is much lower than the printing inks' values and very close to the bulk copper one. In fact, with lower resistivity, we can reduce the conductive losses in the RFEH circuits, especially in the low power density environment. Therefore, this is one of the major advantages of this technology and this is the reason why, for this research, we put apart all technologies based on screen printing or ink jet printing.

3.2.2. SLA substrate

In this section, the so-called Two Transmission Lines (TTL) method [121] is used for measuring the electromagnetic properties of substrates and the experimental results will be presented. Firstly, a synthesis of characterization methods will be introduced. Then, the TTL method as well as the measurement setup are described. The results and a comparison to the state-of-art are given.

3.2.2.1. Measuring methods

Many methods for characterizing RF properties of substrates are studied and developed, such as the I-V method or capacitor method [122]–[124], Nicholson-Ross-Weir (NRW) method [122], [125], [126], the resonator method [128], the resonant cavity method [123], [129]–[131], THz-time domain spectroscopy method [132], [133] or the transmission-line method [95]. The main principle, the advantages and the disadvantages of each method are summarized in Table 3.1.

Cette thèse est accessible à l'adresse : https://theses.insa-lyon.fr/publication/2023ISAL0007/these.pdf
© [X.V.L. NGUYEN], [2023], INSA Lyon, tous droits réservés

Table 3.1: Summary of some different material characterizing methods

Method	Deployable band	Principle	Advantage(s)	Disadvantage(s)
Resonator methods	Discrete point	Measuring the quality factor (Q) of resonator circuits to determine ε_r and $\tan(\delta)$.	Give a good precision at a defined point of frequency	Being able to be deployed only at resonant frequencies of circuits
Resonant cavity methods	Discrete point	Measuring the difference of quality factors (Q) of the cavity with and without characterized sample being inside to determine ε_r and $\tan(\delta)$	Give a good precision at a defined point of frequency	Can be deployed only at the resonant frequency of cavities
THz-time domain spectroscopy method	Discrete point	Measuring the difference of phase and magnitude of signals propagating in the environment with and without the sample material.	Can be deployed at THz	Complicated algorithms and complicated deployment of measurement
I-V method	Wide band	Measuring ε_r of a dielectric sandwich by 2 electrodes forming a capacitor	Easy to deploy over a wide band of frequency	Being not the best appropriate to measure $tan\delta$ of the dielectrics, the substrates
NRW method	Wide band	Studying the phenomenon of reflection and transmission. The phenomena come from the electromagnetic difference between two environments (inside and outside the substrate).	Good precision over a wide band of frequency	Complicated algorithms and complicated deployment of measurement
Transmission lines methods	Wide band	Measuring the phases of the signals transmitted along the transmission lines and the losses in transmission lines to determine ε_r and $\tan(\delta)$ of characterized substrates.	Easy to deploy with a good precision over a wide band of frequency	The losses in the lines have to be identified clearly to improve the precision. Band of measurement depends on the length of lines.

According to Table 3.1, the selected method for this work is the Two Transmission Lines, an improved method of Transmission lines, due to its simple deployment over a wide band of frequency. Moreover, the effects of the connectors, i.e. SubMiniature version A (SMA), and the

Cette thèse est accessible à l'adresse : https://theses.insa-lyon.fr/publication/2023ISAL0007/these.pdf
© [X.V.L. NGUYEN], [2023], INSA Lyon, tous droits réservés

solder parts on the measurements could be neglected thanks to a de-embedding technique described in [121], [129], [134]. Hence, a good accuracy should be obtained.

The method as well as the measurement setup will be described in the next part.

3.2.2.2. Two Transmission Lines (TTL) method

Theory

Two Transmission Line method is a matrix-based method, which allows to extract the transmission parameters, which are the attenuation coefficient α, the phase constant β, from the measurements of S-parameters of the transmission lines [121]. To repeat, the attenuation constant describes the total losses, i.e. conductive loss, radiating loss, dielectric loss, existing in a unity of the length of the transmission lines. It causes the degradation of amplitude of the waves propagated along the transmission line. The phase constant is a measurement giving the variation of the phase of the waves propagated along the transmission line at a given time instant.

The method is carried out with sets of two microstrip lines of different lengths, but same width, deposited on the substrate-under-test to study the relative permittivity and loss tangent. Fig. 3.18 illustrates the structures of two microstrip lines with the lengths l_1 and l_2 ($l_2 > l_1$) and SMA connectors.

It should be noticed that the ABCD matrix of SMA#L is the transpose of the ABCD matrix of SMA#R. Since the ABCD matrix of the SMA connectors can be considered to be symmetrical [135], we have the following property

$$[M]_{SMA\#R} = [M]^T_{SMA\#L} = [M]_{SMA\#L} \tag{3.1}$$

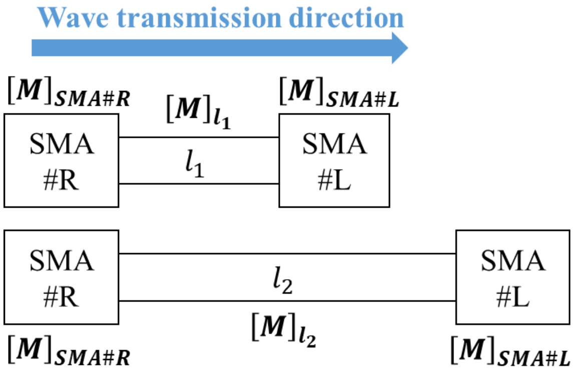

Figure 3.18: Two-Transmission-Line structures. SMA#R represents the SMA connectors for wave input. SMA#L represents the SMA connectors after wave propagation.

Fig. 3.18 can be reconfigured as Fig. 3.19 under the symmetry assumption.

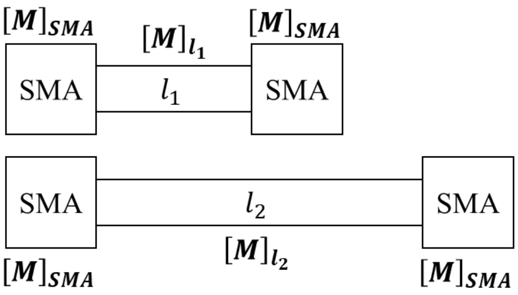

Figure 3.19: Two-Transmission-Line model

Cette thèse est accessible à l'adresse : https://theses.insa-lyon.fr/publication/2023ISAL0007/these.pdf
© [X.V.L. NGUYEN], [2023], INSA Lyon, tous droits réservés

When the S-parameters of both lines are measured, an ABCD matrix ($[M]_{l_i}$) of each line can be deduced. As stated previously, the SMA connectors always have effects on the S-parameter measurement, the ABCD matrix of these lines should then be written as.

$$[M]_{l_i} = [M]_{SMA} \times [M]_{line_i} \times [M]_{SMA} \tag{3.2}$$

where, $[M]_{l_i}$ is the ABCD matrix of the i^{th} line, $[M]_{SMA}$ is the ABCD matrix of the SMA connectors and $[M]_{line_i}$ is the ABCD matrix of non-conductor part of the i^{th} line.

Thereafter, since this kind of matrix is cascadable, ABCD matrix of different length of lines ($[M]_{l_2-l_1}$) is determined by the following equation.

$$[M]_{l_2-l_1} = [M]_{l_2} \times [M]_{l_1}^{-1} = [M]_{SMA} \times [M]_{line_2} \times [M]_{line_1}^{-1} \times [M]_{SMA}^{-1} \tag{3.3}$$

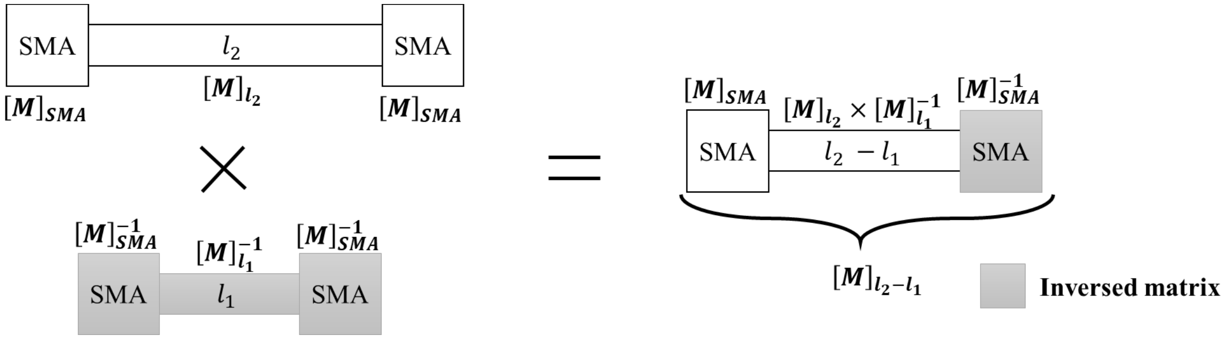

Figure 3.20: Combination of matrices in TTL method

In addition, the propagation constant (γ) and the characteristic impedance of lines (Z_c) can be obtained from $[M]_{l_2-l_1}$ [121]

$$[M]_{l_2-l_1} = \begin{bmatrix} \cosh\gamma(\mathrm{l}_2 - l_1) & \mathrm{Z_c}\sinh\gamma(\mathrm{l}_2 - l_1) \\ (\sinh\gamma(\mathrm{l}_2 - l_1))/\mathrm{Z_c} & \cosh\gamma(\mathrm{l}_2 - l_1) \end{bmatrix} \tag{3.4}$$

where, l_2 and l_1 are the respective lengths of the lines (m).

The propagation constant is now obtained by calculating the trace (Tr) of the matrix $[M]_{l_2-l_1}$

$$Tr\left([M]_{l_2-l_1}\right) = 2\cosh\left(\gamma(l_2 - l_1)\right) \tag{3.5}$$

$$\gamma = (\cosh^{-1}\left(0.5\, Tr\left([M]_{l_2} \times [M]_{l_1}^{-1}\right)\right))/(l_2 - l_1) \tag{3.6}$$

In general, the propagation constant is a complex value written as

$$\gamma(\omega) = \alpha(\omega) + j\beta(\omega) \tag{3.7}$$

where, $\alpha(\omega)$ is the attenuation coefficient of the transmission line (Np/m), $\beta(\omega)$ is the phase constant of the transmission line (rad/m), ω is the angular velocity (s^{-1}).

It is worthy to notice that $\alpha(\omega)$ is the sum of three losses, namely the conductive loss (α_c) (Np/m), the radiation loss (α_r) (Np/m) and the dielectric loss (α_d) (Np/m) in Eq. (3.8). The loss tangent of substrate can be determined whenever the dielectric loss of lines is obtained.

$$\alpha(\omega) = \alpha_c(\omega) + \alpha_r(\omega) + \alpha_d(\omega) \tag{3.8}$$

Cette thèse est accessible à l'adresse : https://theses.insa-lyon.fr/publication/2023ISAL0007/these.pdf
© [X.V.L. NGUYEN], [2023], INSA Lyon, tous droits réservés

In fact, the radiation loss α_r of microstrip lines is difficult to determine. Additionally, this loss is generally overlooked compared to the conductive loss and the dielectric loss [120]. Eq. (3.8) is then simplified as

$$\alpha(\omega) \approx \alpha_c(\omega) + \alpha_d(\omega) \tag{3.9}$$

In addition, the conductive loss of lines can be expressed as

$$\alpha_c(\omega) = R_s/(Z_0 W) \tag{3.10}$$

with

$$R_s = \sqrt{\frac{\mu_0 \omega}{2\sigma}} \tag{3.11}$$

where R_s is a linear resistance (Ω/m), σ is the conductivity of the conductor (S/m), μ_0 is the magnetic permeability constant ($4\pi \times 10^{-7}$) (H/m), Z_0 is the reference impedance of the line (Ω) (in this work, Z_0 is mostly set to 50Ω) and W is the width of the line (m).

Eq. (3.10) is applied when the surface of the conductor is perfectly smooth. However, in reality, this condition will never occur. The studies about the surface roughness are mentioned in section 3.2.1.2.

In 1980, Hammerstad and Jensen [136] proposed a simple equation to calculate the conductor loss of a rough conductor ($\alpha_{c,rough}$). The equation introduces a correction factor (K_{SR}) and an attenuation constant calculated for a smooth conductor ($\alpha_{c,smooth}$). The equation is expressed as

$$\alpha_{c,rough} = K_{SR} \cdot \alpha_{c,smooth} \tag{3.12}$$

where K_{SR} can be written as

$$K_{SR} = 1 + \frac{2}{\pi}\arctan\left(1.4\left(\frac{S_{rms}}{\delta}\right)^2\right) \tag{3.13}$$

where S_{rms} is root-mean-square surface roughness (m) and δ is skin depth at studied frequency (m)

According to Eq. (3.13), at low frequency where the skin depth thickness is very large or when the surface is extremely smooth, K_{SR} will be close to one. The value of this parameter saturates to two as the ratio becomes large with higher frequency and higher surface roughness. This result implies the maximum effect of surface roughness can double the conductive loss.

However, Eq. (3.12) is only correct at frequency below 5 GHz. This argument is commented in [118]. The authors measured the insertion loss of a 7-inch-long transmission line printed on FR-4 over a wide band of frequency from 0-50 GHz and studied the accuracy of Eq. (3.12). The authors presented also a new approximation, expressed as Eq. (3.14), describing the conductor resistive loss associated to a number of deposited copper "snowballs" as illustrated in Fig. 3.21 and their radius. The approach stays correct over a band of 0-50 GHz. The results of these studies are illustrated in Fig. 3.22.

$$\frac{P_{rough}}{P_{smooth}} = \frac{A_{matte}}{A_{hex}} + \frac{3}{2}\sum_{i=1}^{j}\left(\frac{N_i 4\pi a_i^2}{A_{hex}}\right)/\left(1 + \frac{\delta}{a_i} + \frac{\delta^2}{2a_i^2}\right) \tag{3.14}$$

where a_i is the radius of the i^{th} snowball, N_i/A_{hex} is the number of snowballs with radius a_i per unit flat hexagonal area and A_{matte}/A_{hex} is the relative surface area without snowball per unit flat hexagonal area.

Cette thèse est accessible à l'adresse : https://theses.insa-lyon.fr/publication/2023ISAL0007/these.pdf
© [X.V.L. NGUYEN], [2023], INSA Lyon, tous droits réservés

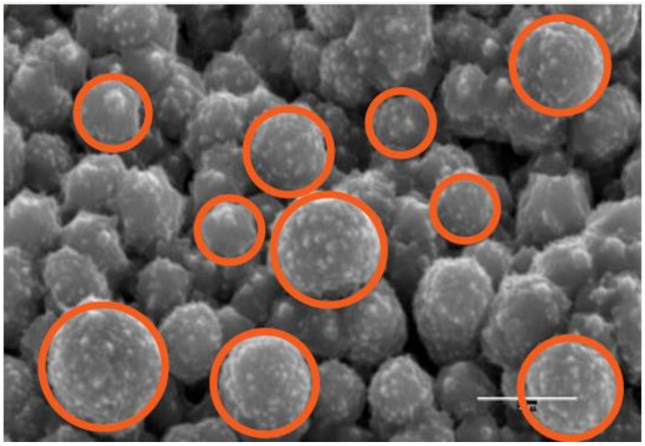

Figure 3.21: Image of spherical "snowball" particular copper of deposited copper [118]

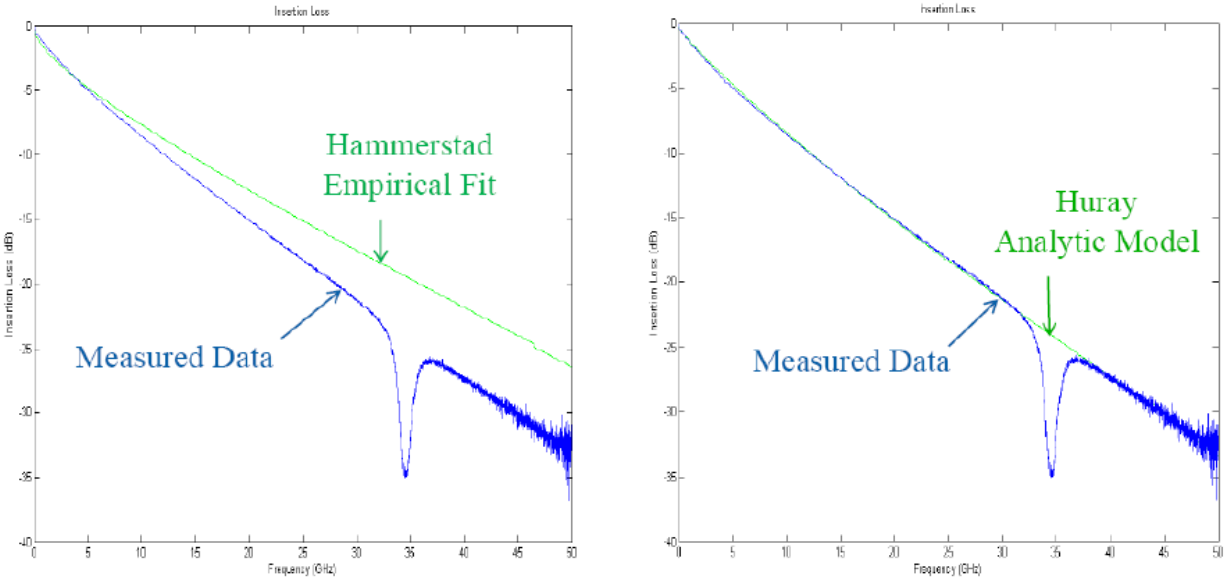

Figure 3.22: Comparison between different relations and measured data of insertion loss as function of frequency [118]

Since the highest studied band of frequency in this work is Wi-Fi 2.4 GHz band, Eq. (3.12) is selected due to its simple directness and its good accuracy at frequency below 5 GHz. Consequently, the conductor loss of the transmission line will be determined as

$$\alpha_c(\omega) = \left(\sqrt{\frac{\mu_0\omega}{2\sigma}}/(Z_0W)\right)\left(1 + \frac{2}{\pi}\arctan(1.4(S_{rms}/\delta)^2)\right) \qquad (3.15)$$

Whenever the conductor loss is obtained, from Eq. (3.9), the dielectric loss can be extracted as Eq. (3.16).

$$\alpha_d(\omega) = \alpha(\omega) - \alpha_c(\omega) \qquad (3.16)$$

With the obtained dielectric loss ($\alpha_d(\omega)$) and the phase constant ($\beta(\omega)$), a new propagation constant without the loss of conductor ($\gamma_{wo}(\omega)$) can be written as

$$\gamma_{wo}(\omega) = \alpha_d(\omega) + j\beta(\omega) \qquad (3.17)$$

Cette thèse est accessible à l'adresse : https://theses.insa-lyon.fr/publication/2023ISAL0007/these.pdf
© [X.V.L. NGUYEN], [2023], INSA Lyon, tous droits réservés

The relation between the propagation constant and the complex effective permittivity can be expressed as [134]

$$\gamma_{wo}(\omega) = j\frac{\omega}{c}\sqrt{\varepsilon_{eff}(\omega).\mu_{eff}(\omega)} \tag{3.18}$$

with, $\mu_{eff}(\omega)$ is effective permeability of the substrate (unitless). This parameter is equal to 1 since the substrate is a non-magnetic material.

Thereafter, the complex effective permittivity ($\varepsilon_{eff}(\omega)$) can be determined using the following equation [134]

$$\varepsilon_{eff}(\omega) = -(\gamma_{wo}(\omega)c/\omega)^2 \tag{3.19}$$

where c is the velocity of light ($3 \times 10^8\ m/s$).

The complex permittivity $\varepsilon_{complex}(\omega)$ of the substrate is obtained as [111]

$$\varepsilon_{\text{complex}}(\omega) = \left(2\varepsilon_{\text{eff}}(\omega) + \frac{1}{\sqrt{\left(1+\frac{12\text{h}}{\text{W}}\right)}} - 1\right) \times \left(\frac{\sqrt{\left(1+\frac{12\text{h}}{\text{W}}\right)}}{1+\sqrt{\left(1+\frac{12\text{h}}{\text{W}}\right)}}\right) \tag{3.20}$$

where h is the thickness of the substrate (m) and W is the width of the microstrip line (m).

The relative permittivity of the substrate (ε_r) is the real part of ($\varepsilon_{complex}(\omega)$).

$$\varepsilon_r(\omega) = Re(\varepsilon_{complex}(\omega)) \tag{3.21}$$

Since, the imaginary part of $\varepsilon_{complex}(\omega)$ is smaller and negligible with respect to the real part, in general, the relative permittivity of the substrate can be understood as

$$\varepsilon_r(\omega) \approx \varepsilon_{complex}(\omega) \tag{3.22}$$

In addition, the loss tangent of the substrate ($tan\delta$) is the ratio between the real and the imaginary part of $\varepsilon_{r\ complex}(\omega)$.

$$\tan(\delta) = Re\left(\varepsilon_{complex}(\omega)\right)/Im\left(\varepsilon_{complex}(\omega)\right) \tag{3.23}$$

<u>Characterization setup</u>

We proposed the following steps for the deployment of the TTL method for the characterization of selected SLA substrates shown in Fig. 3.23.

Cette thèse est accessible à l'adresse : https://theses.insa-lyon.fr/publication/2023ISAL0007/these.pdf
© [X.V.L. NGUYEN], [2023], INSA Lyon, tous droits réservés

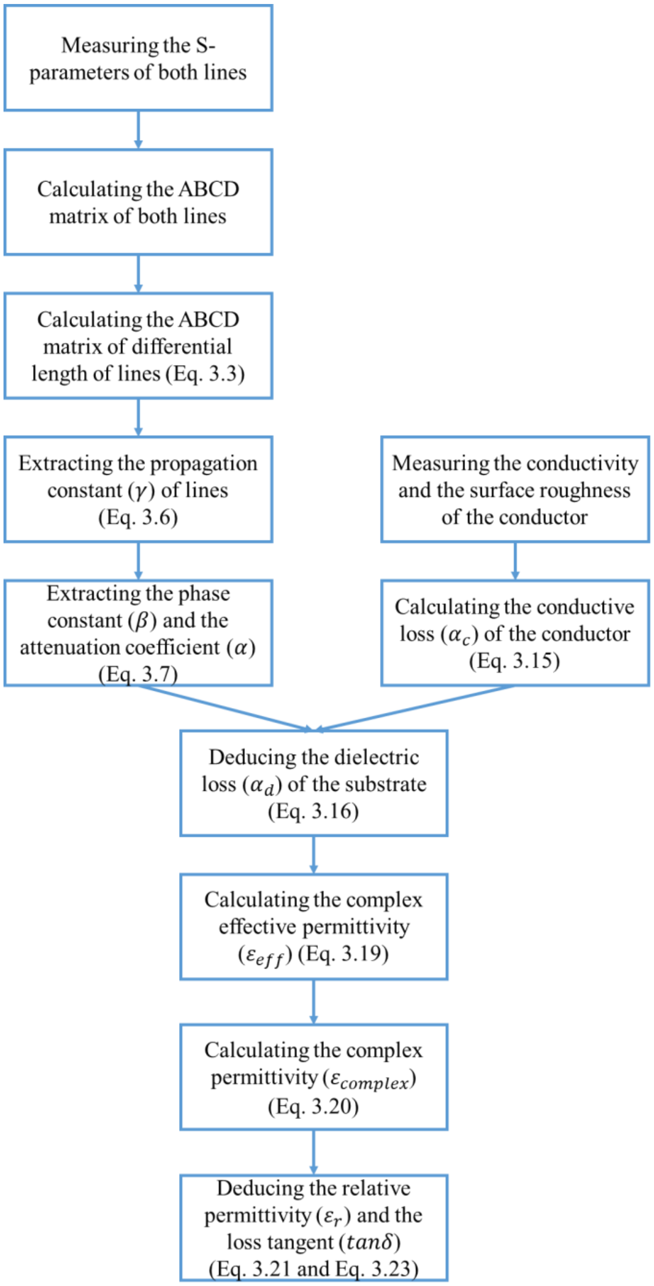

Figure 3.23: The proposed TTL method

As mentioned in the previous section, in order to extract the relative permittivity and the loss tangent of the substrate, the S-parameters of the microstrip lines should be measured. A Vector Network Analyzer (VNA) by Rhode & Schwarz (ZNL3) is used for the measurements. The VNA is calibrated with the Short-Open-Load-Through (SOLT) calibration method to define the reference plane of measurements, thus, to cancel the effects of connecting coaxial cables on the accuracy of measurements.

Cette thèse est accessible à l'adresse : https://theses.insa-lyon.fr/publication/2023ISAL0007/these.pdf
© [X.V.L. NGUYEN], [2023], INSA Lyon, tous droits réservés

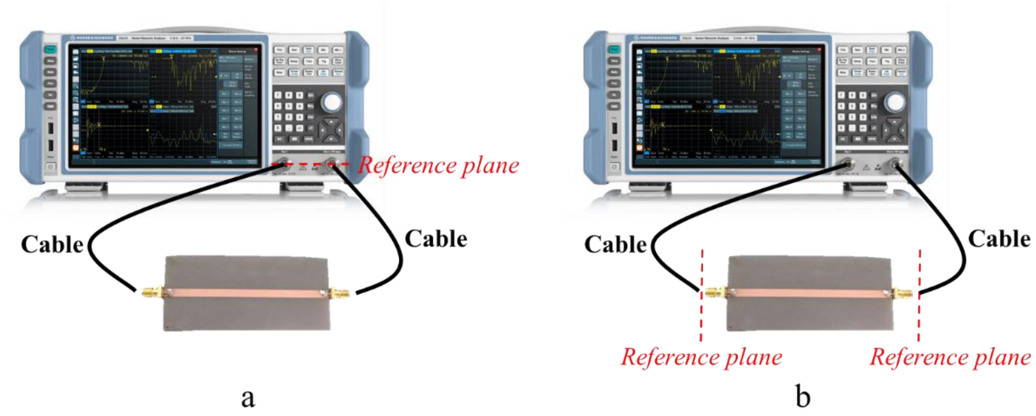

Figure 3.24: Reference plane of VNA before the calibration (a) and after the calibration (b)

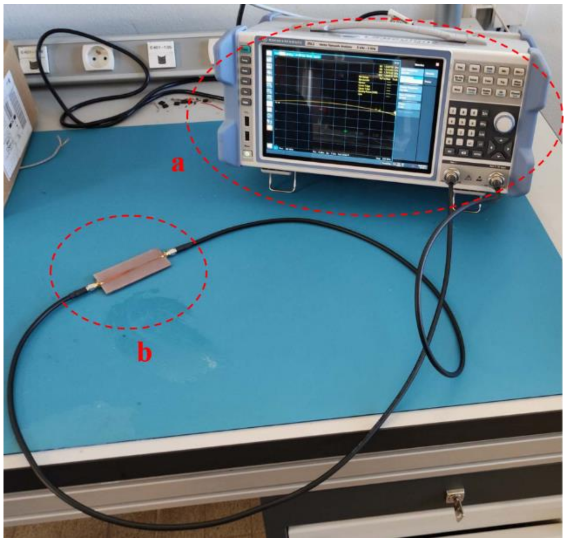

Figure 3.25: Measurement setup for TTL method (a. VNA; b. Microstrip transmission line printed on SLA substrate)

Since the impedance of the VNA as well as the cable is set to 50 Ω, the width of the microstrip line should be well-calculated such that the characteristic impedance of the lines is around 50 Ω. In addition, to assure the propagation of waves in the lines, their length should be at least $\lambda_{g\,min}/10$, where $\lambda_{g\,min}$ is the effective wavelength of wave at the lowest studied frequency. The default phase of measured S-parameters by the VNA is generally between $-180°$ to $180°$ that leads the inaccurate results of phase constant. The difference in length of two lines should be less than $\lambda_{g\,max}/2$, where $\lambda_{g\,max}$ is the effective wavelength of the wave at the highest studied frequency. Moreover, the longer line should be two times longer than the shorter one to improve the accuracy of the results.

Characterization results

A validation step is necessary. The Rogers 4003C substrate, a very well-known substrate in RF applications, is selected as a reference. Its relative permittivity and loss tangent are stated as 3.55-3.56 and 0.0021 in the datasheet. The conductor laminated on 1.55 mm Rogers substrate is copper, whose measured conductivity is $58\ \times 10^6\ S/m$ and measured thickness is $17.5\ \mu m$. The measured root-mean-square surface roughness (S_{rms}) is 0.4 μm. The width of lines is calculated as $3.4\ mm$ to have a characteristic impedance of 50 Ω and their lengths are $46.5\ mm$ and $62\ mm$ respectively.

Cette thèse est accessible à l'adresse : https://theses.insa-lyon.fr/publication/2023ISAL0007/these.pdf
© [X.V.L. NGUYEN], [2023], INSA Lyon, tous droits réservés

The measurements are deployed over a band of frequency of 0.5-2.5 GHz. The measured results are illustrated in Fig. 3.27 and Fig. 3.28.

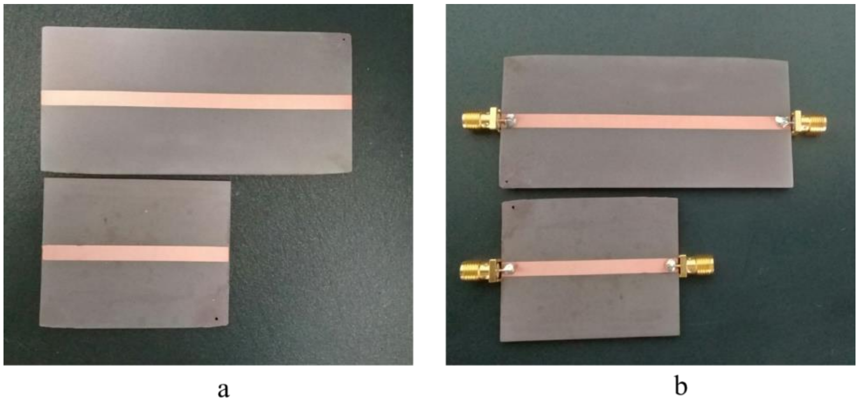

Figure 3.26: Transmission microstrip lines printed on SLA substrate using Plastronics without SMA connectors (a) and with SMA connectors (b)

According to Fig. 3.27 and Fig. 3.28, the measured relative permittivity and loss tangent of the reference substrate are 3.55-3.57 and 0.001-0.0025, respectively. These values are very close to the datasheet values (3.55 and 0.0021). The slight difference may come from the measurement setup.

In conclusion, the selected method is validated and can be applied for the characterization of SLA substrates, which are HT Resin v1 and HT Resin v2. The dimensions of lines printed on Rogers 4003C, HT Resin v1 and HT Resin v2 are summarized in Table 3.2.

Table 3.2: The dimensions of transmission lines

Parameters	**Rogers 4003C**	**HT Resin v1**	**HT Resin v2**
Substrate's thickness (mm)	1.55	1.63	1.60
Conductor thickness (µm)	17.5	7	7
Resistivity (µΩ.m)	0.017	0.022	0.022
S_{rms} (µm)	0.4	1.7	0.7
Width of lines (mm)	3.4	3.95	3.9
Length of lines (mm)	46.5 62	44.5 79.3	50 84.6

The measured relative permittivity and the loss tangent of the substrates are illustrated in Fig. 3.27 and Fig. 3.28.

Cette thèse est accessible à l'adresse : https://theses.insa-lyon.fr/publication/2023ISAL0007/these.pdf
© [X.V.L. NGUYEN], [2023], INSA Lyon, tous droits réservés

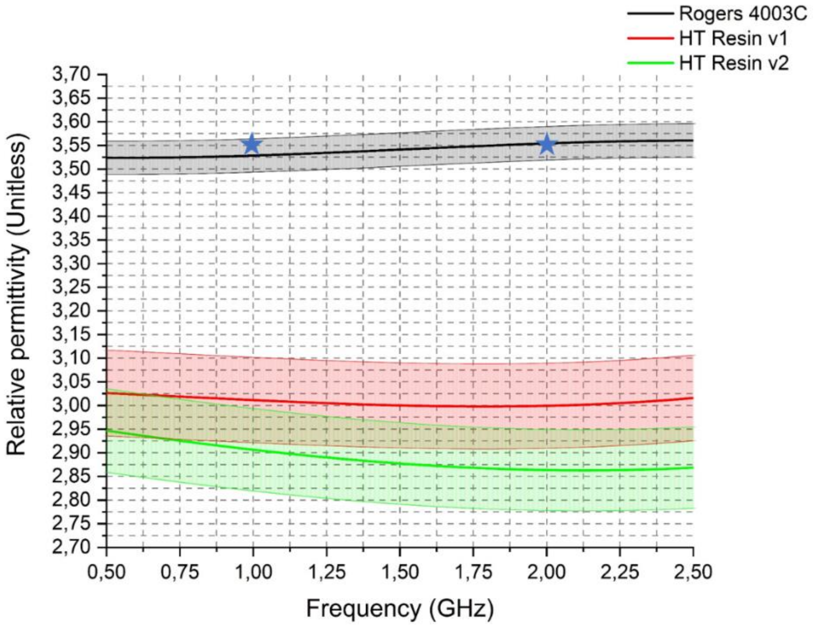

Figure 3.27: Measured relative permittivity of Rogers 4003C, HT Resin v1 and HT Resin v2 substrate (Star: Reference of Rogers 4003C given by manufacturer)

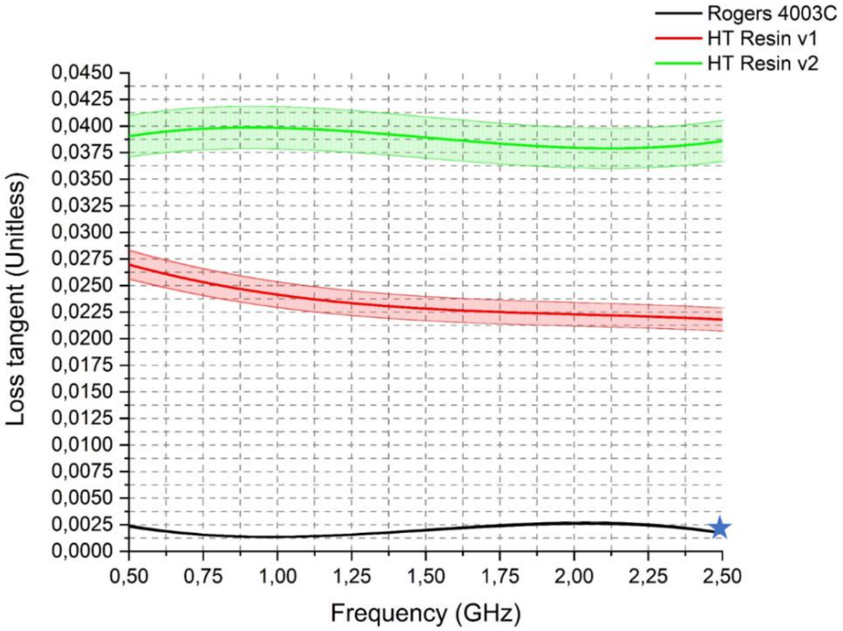

Figure 3.28: Measured loss tangent of Rogers 4003C, HT Resin v1 and HT Resin v2 substrate (Star: Reference of Rogers 4003C given by manufacturer).

Conclusion

The SLA substrates are characterized using TTL method over a wide band of 0.5-2.5 GHz covering the UHF RFID 850-960 MHz and WiFi 2.4 GHz band. The measured relative permittivity of HT Resin v1 and HT Resin v2 substrates are (3 ± 0.1) and (2.9 ± 0.1) respectively. The measured loss tangent values are (0.025 ± 0.0025) and (0.04 ± 0.0025) respectively. A comparison of substrate properties is presented in Table 3.3. Compared to the other specific substrates for RF applications, i.e. Rogers 4003C, Rogers 4350B, Polyethylene Terephthalate (PET), Liquid Crystal Polymers (LCP), Kapton, etc., and other SLA substrates, the relative permittivity of the selected substrates

Cette thèse est accessible à l'adresse : https://theses.insa-lyon.fr/publication/2023ISAL0007/these.pdf
© [X.V.L. NGUYEN], [2023], INSA Lyon, tous droits réservés

are close to them. Concerning the loss tangent, the SLA substrates show a higher value than the specific substrate one. This can lead to lossy impacts on the performance of antennas and RF circuits.

Table 3.3: Comparison between this work to the state-of-art

Ref.	**Type of substrate**	**Band of frequency**	**Relative permittivity**	**Loss tangent**	**Method of characterization**
[4]	PET	2.45 GHz	3.21	0.0049	NI
[95]	FR-4	2.45 GHz Band	4.22	0.017	TTL method
	Flexible thin Kapton polyimide film		2.8	0.014	
	Polyester felt		1.2	0.023	
[130]	PC	2.45 GHz	2.64	0.0018	Cavity method
[131]	ABS-PC Xantar LDS	0.8-1.8 GHz	2.8	0.006	Cavity perturbation method
	LCP Vectra		4.4-4.5	0.004	
Rogers Corp.	Rogers 4003C	1-3 GHz	3.55	0.0021	Differential phase length method and IPC-TM-650 2.5.5.5
	Rogers 4350B		3.66	0.0031	
[52]	Clear Resin From Formlabs	1.575 GHz	2.83	0.038	Transmission lines method
[125]	Clear Resin from Formlabs	2.2-3.3 GHz	2.8	0.03	Nicholson-Ross-Weir
[137]	Flexible Resin from Fomlabs	0.8-0.9 GHz	2.78	0.06	NI
[126]	High Temp Resin from Formlabs	NI	2.6-2.8	NI	Nicholson-Ross-Weir
This work	High Temp Resin v1 from Formlabs	0.5-2.5 GHz	3±0.1	0.025 ± 0.0025	TTL method
	High Temp Resin v2 form Formlabs		2.9±0.1	0.04 ± 0.0025	

NI: Not Indicated in the article

3.3. Wrap-up

In this chapter, Stereolithography (SLA) manufacturing method is presented. This method is based on the polymerization of the photosensitive resins, which is a reaction of transiting from liquid to solid phase of the materials. This low-cost method exhibits the possibility of manufacturing the 2D and 3D form objects with high complexity easily. Additionally, comparing to other methods such as material injecting, fused depositing modeling, etc., this method gives us a benefit of higher resolution and better surface qualities. In our thesis, the selected resin is High Temp Resin v1 and v2 from Formlabs due to their high thermal resistance. This allows us to facilitate the components mounting step of the manufacturing process. The drawback of this SLA resin is its high loss. In fact, Rogers Corporation offers a new material compatible to the SLA manufacturing method with a much lower loss, whose loss tangent is 0.0043 at 10 GHz. Nevertheless, its heat deflection temperature are very low, 76.7 °C at 0.455 MPa and 59.1 °C at 1.82 MPa. Therefore, this material does not seem suitable for our manufacturing process.

Cette thèse est accessible à l'adresse : https://theses.insa-lyon.fr/publication/2023ISAL0007/these.pdf
© [X.V.L. NGUYEN], [2023], INSA Lyon, tous droits réservés

In other hands, the studies of the electromagnetic properties of the electroless deposited copper and the selected SLA substrates are also presented.

For the conductor, the measured thickness is around (7 ± 1) µm with an acceptable surface roughness, which is (1 ± 0.2) µm. This value of surface roughness is comparable to the one of commercial Rogers 4003C, a very-well known substrate for RF application, (0.5 ± 0.2) µm. Low profile surface roughness is an advantage of Plastronics in RF circuits fabrication. Besides, the resistivity of ELD copper is measured using the four-probe method. The measured value is 0.02-0.025 (μΩ.m), which is very close to the bulk copper resistivity, 0.017 (μΩ.m). Comparing the resistivity of the proposed deposited conductor and the one of printing inks used in antennas and RF circuits fabrication, proves a better result, from 5 to 10 times lower. This allows us to count on less conductive loss in designing circuits. This is another advantage of 3D Plastronics in RF circuits fabrication.

A wideband method for determining the dielectric properties of substrates – Two Transmission Line method – is studied and developed to characterize Rogers 4003C for validation and then evaluate the selected Stereolithography substrates, which are HT Resin v1 and HT Resin v2 from Formlabs. With the measured conductivity and the measured surface roughness of electroless deposited copper, the relative permittivity of HT Resin v1 and HT Resin v2 are obtained as (3 ± 0.1) and (2.9 ± 0.1), respectively, and their measured loss tangent is (0.025 ± 0.0025) and (0.04 ± 0.0025), respectively. Their relative permittivity is very close to the one of state-of-art substrate, but their loss tangent is higher by a factor of 1.5 to 10. This is an issue as it will enhance the lossy impacts on the electrical behavior of antennas and RF circuits.

Cette thèse est accessible à l'adresse : https://theses.insa-lyon.fr/publication/2023ISAL0007/these.pdf
© [X.V.L. NGUYEN], [2023], INSA Lyon, tous droits réservés

Cette thèse est accessible à l'adresse : https://theses.insa-lyon.fr/publication/2023ISAL0007/these.pdf
© [X.V.L. NGUYEN], [2023], INSA Lyon, tous droits réservés

CHAPTER 4: ANTENNAS

Cette thèse est accessible à l'adresse : https://theses.insa-lyon.fr/publication/2023ISAL0007/these.pdf
© [X.V.L. NGUYEN], [2023], INSA Lyon, tous droits réservés

Cette thèse est accessible à l'adresse : https://theses.insa-lyon.fr/publication/2023ISAL0007/these.pdf
© [X.V.L. NGUYEN], [2023], INSA Lyon, tous droits réservés

4. ANTENNAS

In a Radio Frequency Energy Harvester (RFEH) concept, the antenna keeps a crucial role of capturing the electromagnetic (EM) waves and delivering the received power into the rectifier. Therefore, the design of the antenna being suitable for the RFEH should be concerned carefully. In this chapter, we will introduce the antennas fabricated using Rapid Plastronics technique. The aim is to verify the possibility of using this emerging manufacturing technique to yield antenna suitable for energy harvesting applications.

4.1. Radiating parameters

Scattering parameters (S-parameters) are one of the most important parameters to study the electrical behavior of an antenna.

Reflection coefficient or return loss, noted as S_{xx} or $\boldsymbol{\Gamma}$, of antenna is a measurement of how much radiated/absorbed power is reflected by that antenna. The phenomenon comes from the mismatch impedance between the antenna and the other electrical components, circuits, etc. at a defined reference impedance. For the impedance matching conditions of RF components, the value is set as purely resistive 50 Ω in this work. The reflection coefficient in linear scale of the antenna can be expressed as

$$S_{xx} = (Z_{ant} - Z_s)/(Z_{ant} + Z_s) \tag{4.1}$$

where Z_{ant} is the input impedance of the antenna (Ω), Z_s is the reference impedance (Ω).

Once the reflection coefficient of the antenna is measured, the bandwidth can be identified, i.e. where the reflection coefficient is lower than a pre-defined value (normally -10 dB).

When two or multi antennas are very close to each other, S_{xy} (with $x \neq y$) is a measurement of how much power is radiated by the antenna "x", absorbed by the antenna "y". In other words, the S-parameter describes the mutual coupling between two near antennas.

Directivity (D) is the parameter describing the capturing performance of the antenna theoretically. The directivity of an antenna is defined as the ratio of the radiation intensity in a given direction from the antenna to the radiation intensity averaged over all directions [102].

Gain is the parameter describing the capturing performance of the antenna in reality. The gain of an antenna is defined as the ratio between the actual radiated power from the antenna in a given direction and the power that would be obtained if the power accepted by the antenna were radiated isotropically [102]. Generally, the studied given direction specifies the main direction of the antenna. The larger the gain of the antenna, the higher the amount of power radiated or absorbed by this antenna. The antenna radiates only if its gain is strictly positive. When the gain is noted in dB, this means that the losses (mismatch impedance loss, conductive loss, and dielectric loss) of the antenna are included into the parameter. The relation between the directivity and the gain of the antenna can be expressed as

$$G = e_r . e_c . e_d . D \tag{4.2}$$

where, G is gain of the antenna (unitless), e_r is mismatch efficiency (unitless), e_c is conduction efficiency (unitless), e_d is dielectric efficiency (unitless). The mismatch efficiency, the conduction efficiency and the dielectric efficiency come from the mismatch loss, conductive loss and dielectric loss in an antenna.

The Eq. (4.2) can be expressed in decibel scale as

Cette thèse est accessible à l'adresse : https://theses.insa-lyon.fr/publication/2023ISAL0007/these.pdf
© [X.V.L. NGUYEN], [2023], INSA Lyon, tous droits réservés

$$G_{dB} = e_{r\,dB} + e_{c\,dB} + e_{d\,dB} + D_{dBi} \tag{4.3}$$

Polarization of the antenna in a given direction is defined as the polarization of the wave radiated by the antenna. The polarization of a radiated wave is the property of an EM wave describing time-varying direction and relative magnitude of the E-field vector. In other words, this parameter describes the rotating tendency of the EM waves radiated by the antenna in a given direction of propagation.

There are three types of polarization of an EM wave

- Linear polarization

- Elliptical polarization

- Circular polarization

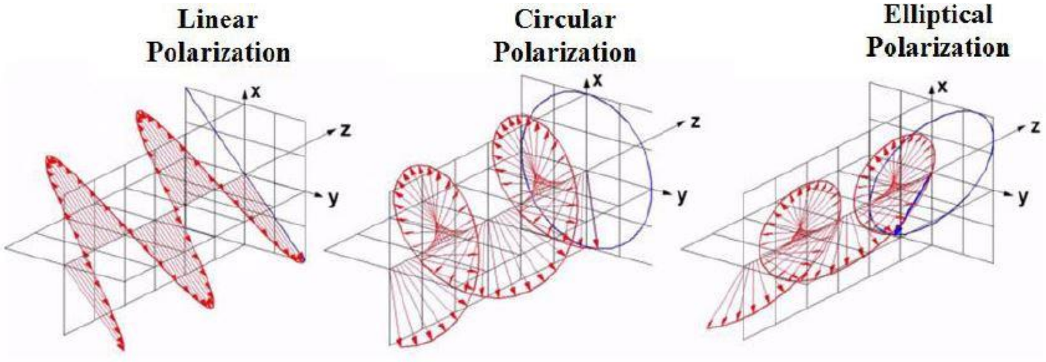

Figure 4.1: Three types of polarization of electromagnetic waves [138]

In order to indicate the polarization of the antenna, an axial ratio (AR) is introduced.

- If $1/2 \leq AR \leq 2$, the polarization of the antenna is circular.
- If $AR = 0$ or $AR = \infty$ the polarization of the antenna is linear.
- Otherwise, the polarization of the antenna is elliptical.

When the polarization of the antenna and of the received EM waves by that antenna is not aligned, it exists a loss coming from the polarization mismatch. Thus, the circular polarization is preferred to reduce this loss [138]. This loss (PLF) can be expressed as

$$PLF = \left|\vec{t}.\vec{r}\right|^2 = |\cos(\theta)|^2 \tag{4.4}$$

where $\vec{t}$ is the unit vector (align with the polarization vector) of the transmitted wave, $\vec{r}$ is the unit vector of the receiving antenna and θ is the angle between $\vec{t}$ and $\vec{r}$.

Radiation pattern of an antenna is a pattern presenting where the power is radiated by the antenna or where the antenna can receive the EM waves. There are two principal types of radiation pattern.

- Directional: a directional antenna features of the property of radiating or receiving EM waves more effectively in some directions than in others.

- Omnidirectional: an omnidirectional antenna is essentially non-directional in a given place and features a directional pattern in any orthogonal plane. An omnidirectional pattern is a special type of a directional pattern. A perfect omnidirectional radiation pattern will be in the form of a “donut”.

Cette thèse est accessible à l'adresse : https://theses.insa-lyon.fr/publication/2023ISAL0007/these.pdf
© [X.V.L. NGUYEN], [2023], INSA Lyon, tous droits réservés

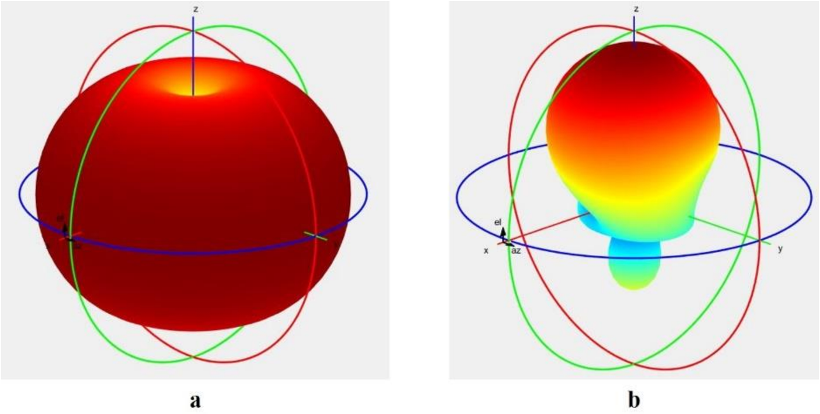

Figure 4.2: 3D forms of radiation pattern of antennas (a. Omnidirectional; b. Directional)

Beamwidth is a parameter associated with the radiation pattern of the antenna. The beamwidth is defined as the angular separation between two identical points on the opposite side of the pattern extremum points [102].

Half-Power BeamWidth (HPBW) is defined as the angle between the two directions in which the radiation intensity of the beam is one-half of the maximum of a beam [102]. In this work, the HPBW of the antenna is chosen to indicate the radiating/absorbing space of the antenna in a defined plane of a given direction.

4.2. Pre-defined requirements

As discussed in Chapter 2, the available frequency bands that we can scavenge are the bands of GSM 900, GSM 1800, UMTS, 2.45 GHz Wi-Fi. Selecting the bands and designing the antennas being coherent with those bands are necessary to optimize the performance of the created RFEH. In this work, the studied band of frequency will be Wi-Fi 2.45 GHz band.

Ambient RF waves exist around the objects. However, they propagate in any arbitrary directions and their polarization, i.e. linear, elliptical, circular, is not fixed. Therefore, the ability of capturing those waves is a case study. Using a system of antennas may be favorable to ensure the covering of the radiation pattern of the antennas on the objects, but the isolation between the antennas should be taken care of as well. A high isolation is necessary to reduce the self-absorption and the re-radiation phenomenon of the antennas. Additionally, the gain of the antennas should be evaluated.

The pre-defined requirements of designed antennas can be summarized from high to low as

- Operating band frequency: 2.45 GHz Wi-Fi band.
- Capture all the polarizations in the air around the object in any directions.
- High isolation between the antennas in case of using an array of antennas.
- Gain of the antennas should be as high as possible.
- Antenna features should be relatively immune to the actual accuracy of manufacturing.

4.3. Designed antennas

The patch antenna is selected first for the sake of simplicity. Patch antenna is a printed circuit with the radiating element on one face and the ground surface on the other face of the substrate.

As discussed in Chapter 3**,** the conductor is ELD copper with 7 µm thickness.

The thickness of the printed SLA substrates is set to (1.5 ± 0.1) mm. This value is chosen to equate the standard thickness of the reference substrate, Rogers 4003C from Rogers Corp. The idea is to

Cette thèse est accessible à l'adresse : https://theses.insa-lyon.fr/publication/2023ISAL0007/these.pdf
© [X.V.L. NGUYEN], [2023], INSA Lyon, tous droits réservés

have a comparison of performance of the plastronics antennas and the antennas printed on Rogers 4003C with the same thickness of the substrate. In fact, the printed SLA substrates can be thicker by modifying their CAD printing model. According to [139]–[141], increasing the thickness of the substrate can improve the performance of the patch antenna, i.e. bandwidth, gain, etc. However, the philosophy of the work is to functionalize a given polymer object. The targeted usage of the object defines at the first order the required thickness of the outer shell (mainly for mechanical reasons). The antenna is dependent on that aspect. Whatever, the polymer thickness could be increased locally if it were too small to give access to an antenna with acceptable performances. As a conclusion, the thickness of the polymer substrate is not considered here as a key factor.

4.3.1. Linear polarization 2D patch antenna

The length (L) of the antenna can be calculated as [102]

$$L = \upsilon_0/(2f_r\sqrt{\varepsilon_r}) \tag{4.5}$$

where, υ_0 is the velocity of light in vacuum (m/s), ε_r is the relative permittivity of the substrate of the antenna (unitless), f_r is the desired resonant frequency (Hz) and L is the length of the antenna (m).

With the desired resonant frequency of 2.45 GHz, the calculated length of the patch antenna is 35.3 mm when it is manufactured on HT Resin v1 substrate whose relative permittivity is (3.00 ± 0.1).

The antenna is simulated using CST Studio Suite 2019 with the measured values of ε_r and $\tan(\delta)$ for the HT Resin v1 substrate and the measured resistivity of ELD copper. The dimensions of the antenna are presented in Fig. 4.3. Here, a nearly square patch is preferred for latter circular polarization antenna design. A discussion about this antenna is detailed in the next section. To feed the antenna, a transmission line is chosen that eases the manufacturing. A transmission microstrip line with a notch is placed in the middle of one side of the antenna, shown in Fig. 4.3, to obtain a 50 Ω input impedance.

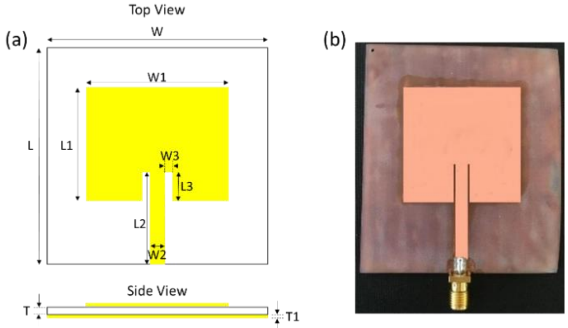

Figure 4.3: Patch antenna printed on HT Resin v1 (a. geometry – b. picture) (W = 60mm, W1 = 36.1mm, W2 = 4mm, W3 = 0.7mm, L = 70mm, L1 = 35.15mm, L2 = 33mm, L3 = 11.05mm, T = 1.5mm, T1 = 0.007mm)

The reflection coefficient of the manufactured antenna is measured using the VNA Rhode&Schwarz ZNL3 calibrated with the SOLT calibration method. The simulated and measured reflection coefficients of this antenna are illustrated in Fig. 4.4. According to the results, the antenna has a good matching at 2.45 GHz. The simulated and measured resonant frequency of the antenna is 2.45 GHz and 2.455 GHz, respectively.

Cette thèse est accessible à l'adresse : https://theses.insa-lyon.fr/publication/2023ISAL0007/these.pdf
© [X.V.L. NGUYEN], [2023], INSA Lyon, tous droits réservés

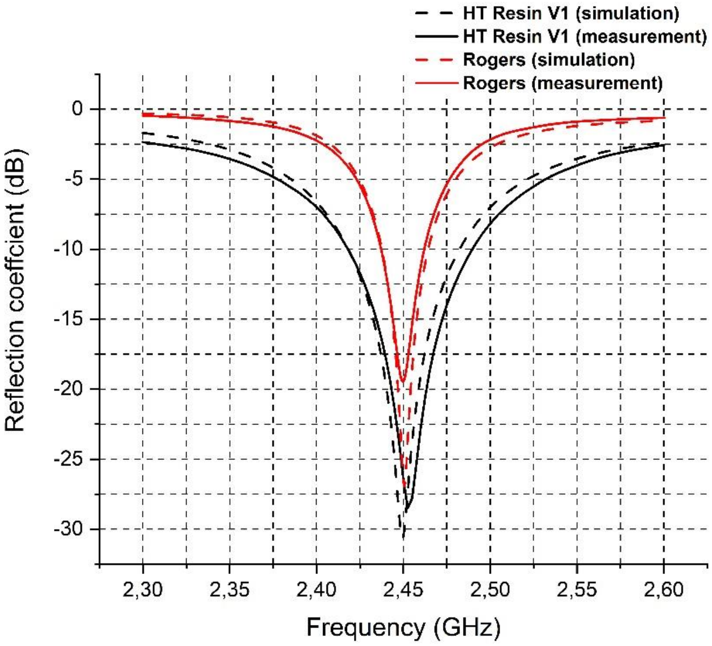

Figure 4.4: Simulated and measured reflection coefficient of linear polarization 2D patch antenna printed on HT Resin v1 and Rogers 4003C

The radiation pattern in vertical and horizontal planes along the feeding line of the patch are characterized in an anechoic chamber with a horn antenna as the reference with the gain of 9.8 dB at 2.45 GHz. The experimental results are shown in Fig. 4.5. A difference of -15 dB of received power between two planes concludes about the linear polarization of the antenna. With the proposed design, the polarization of the antenna is parallel to the feeding line of the antenna. Moreover, the simulated and measured bandwidth of the antenna are closely overlapped. The simulated and measured gains are +2.6 dB and +2.5 dB, respectively.

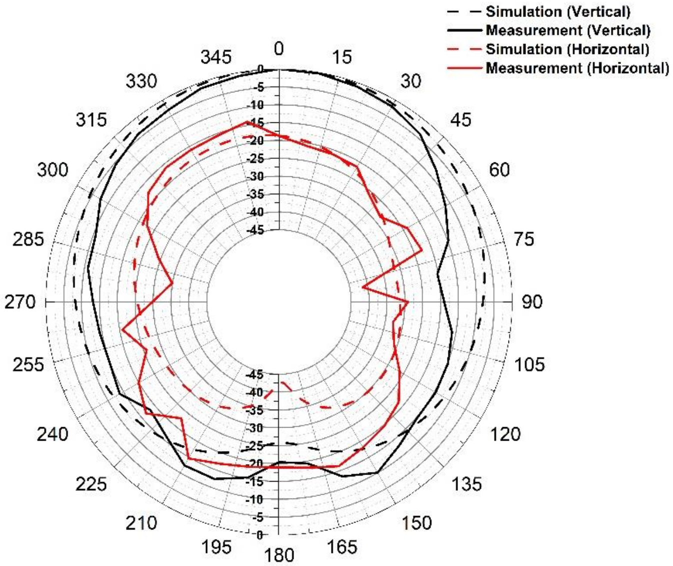

Figure 4.5: Simulated and measured radiation pattern of linear polarization 2D patch antenna printed on HT Resin v1 in vertical and horizontal planes along the feeding line

Cette thèse est accessible à l'adresse : https://theses.insa-lyon.fr/publication/2023ISAL0007/these.pdf
© [X.V.L. NGUYEN], [2023], INSA Lyon, tous droits réservés

Impact of the substrate and the conductors on the radiating parameters

With the purpose of evaluating the impact of the loss tangent of the selected substrate and the conductor resistivity on the bandwidth and the gain of the patch antenna, an antenna with identical shape is fabricated on the Rogers 4003C substrate with laminated copper. It should be repeated that the resistivity of ELD copper is 0.02-0.025 (μΩ.m) meanwhile the value of bulk copper is around 0.017 (μΩ.m). Since the relative permittivity of Rogers 4003C (3.55) is higher than the one of the HT Resin v1 (3.00 ± 0.1), the dimensions of the antenna printed on Rogers 4003C are slightly modified to achieve the resonant frequency of 2.45 GHz.

As illustrated in Fig. 4.4, the antenna fabricated on Rogers 4003C substrate has narrower bandwidth than the one on HT Resin v1, of 23 MHz and 85 MHz respectively, because of the lower loss tangent of Rogers 4003C substrate ($\tan(\delta)$ = 0.0021).

Furthermore, the measured gain of the antenna on the Rogers 4003C substrate is around +5.3 dB. This value is higher than the measured result of the antenna manufactured on HT Resin v1 (+2.5 dB). It should be noticed that the radiation pattern in both planes of the antenna printed on the Rogers 4003C substrate is similar to the one of the antenna on HT Resin v1. Thus, the directivity of both antennas is identical. In addition, both antennas have a good matching at 2.45 GHz, the mismatch loss can be neglected. Then, as indicated in Eq. (4.3), the difference in gain between the antennas can be supposed to come from the dielectric loss and the conductive loss in the antennas.

According to the calculation and the simulation in CST Studio Suite 2019, the dielectric loss accounts for 2.77 dB of the degradation of the gain of the patch antenna meanwhile the conductive loss accounts for 0.03 dB.

The conductive loss can be reduced by decreasing the resistivity of the conductor. According to the simulation, this loss is supposed as negligible, which is less than 0.1 dB, when the resistivity of the conductor is lower than 0.021 μΩ.m.

In addition, the conductive loss is much lower than the dielectric loss in the performance of the patch antenna. To enhance the performance of the antenna, a substrate with a lower loss is considered, i.e. LCP, PEEK. The loss tangent of these substrates are quite similar to the Rogers 4003C's one. The gain of the antenna may increase 3 dB, but the bandwidth of the antenna will be narrowed.

4.3.2. Circular polarization patch antenna

As stated previously, being able to capture all the polarizations available in the air is a remarkable requirement in RF energy harvesting applications. Firstly, the polarization of the antennas should be circular or multi-linear in order to reduce the polarization loss between the antennas and the incident EM waves [102], [142]. Secondly, the radiation pattern of the antennas should also be able to cover all the volume around the objects to insure the possibility of detecting the RF signals.

For that requirement, the proposed design of a circular polarization (CP) patch antenna and a system of this type of antenna will be described. A CP 2D patch, and a system of CP patch antennas will be studied. The analysis of the dimensions to obtain the satisfying design will be introduced. Reflection coefficient, axial ratio, half-power beamwidth of the antennas are interested. It is worthy to repeat that the axial ratio has to be close to 0 dB to achieve the circular polarization meanwhile the HPBW is used to define the capturing volume of the antenna to the EM waves.

Cette thèse est accessible à l'adresse : https://theses.insa-lyon.fr/publication/2023ISAL0007/these.pdf
© [X.V.L. NGUYEN], [2023], INSA Lyon, tous droits réservés

4.3.2.1. Some techniques of designing circular polarization patch antennas

Circular polarization patch antennas can be created using multi-feed or single-feed technique [102], [142]. The principle of multi-feed technique is based on feeding a square or a circular patch antenna by many orthogonal microstrip feeding lines. As discussed in Section 4.3.1, the polarization of a linearly polarized patch antenna is parallel along the feeding line in the middle of the antenna. With the mentioned technique, the patch antenna can radiate in many linearly polarized planes simultaneously, and this allows to mimic the polarization of the antenna as circular. It is worthy to notice that the difference of phase between ports has to be carefully addressed as well. For a dual-feed antenna, the difference of phase should be 90°. An example of dual-feed technique is illustrated in Fig. 4.6 and in Fig. 4.7. Obviously, the feeding lines can be replaced by the feeding probe to reduce the size of the antenna, shown in Fig. 4.8.

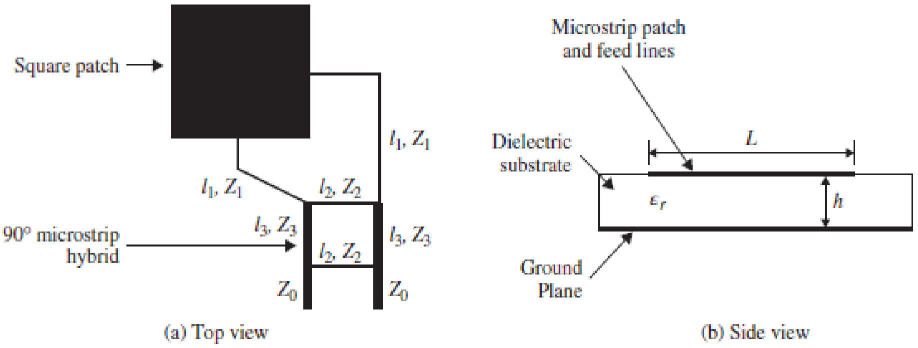

(a) Top view (b) Side view

Figure 4.6: A microstrip-feed patch antenna with a 90° hybrid [142]

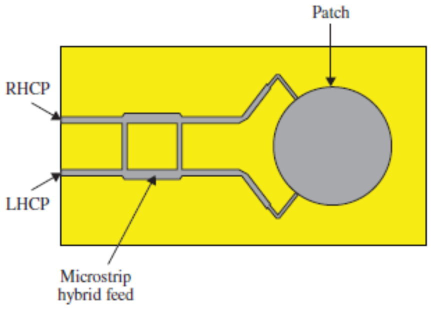

Figure 4.7: Circular patch antenna with a hybrid coupler [142]

(a) Top view (b) Side view

Figure 4.8: A probe feed patch antenna with 90° phase shifter [142]

Multi-feed technique can enhance the purity of circular polarization and the bandwidth of the patch antennas by increasing the number of feeding ports. Nevertheless, this can lead to an increase in size and complexity of the feeding network [142].

Cette thèse est accessible à l'adresse : https://theses.insa-lyon.fr/publication/2023ISAL0007/these.pdf
© [X.V.L. NGUYEN], [2023], INSA Lyon, tous droits réservés

Therefore, a single-feed technique is preferred to simplify the design of the antennas. Fig. 4.9 features different single-feed techniques to achieve a CP patch antenna. The feeding point can be placed on the diagonal of the antenna as shown in Fig. 4.9.a and Fig. 4.9.b. With this technique, regular shapes, i.e., square, circular, etc. of the antenna is not strictly required. The elliptical or rectangular patch can be used in this case. However, to design a CP antenna, a relation on the dimensions should be respected. For the elliptical patch, the ratio between the major axis “a” and the minor axis “b” is expressed as [142]

$$a/b = 1 + 1.0887/Q \tag{4.6}$$

where, Q is the quality factor of the antenna. This parameter can be estimated using results from a full-wave electromagnetic analysis [142]

$$Q = \frac{f_0}{\Delta f}\frac{VSWR-1}{\sqrt{VSWR}} \tag{4.7}$$

where f_0 is the resonant frequency of the antenna (Hz), Δf is the bandwidth of the antenna (Hz) and VSWR is the Voltage Standing Wave Ratio of the antenna (unitless).

For the CP rectangular patch, the condition of dimensions is given by [142]

$$L = W\left(1 + \frac{1}{Q}\right) \tag{4.8}$$

where L and W are the length (m) and the width (m) of the rectangle respectively.

Another idea to have a CP patch with a single feed is to remove conductive parts of the antenna. Fig. 4.9.c and Fig. 4.9.d show the square patch with truncated corners and a circular patch with notches, respectively. Both antennas use a single probe feed positioned as in the figures. Modification of the patch shape can be applied under the form of a narrow slot interior of the antenna, illustrated in Fig. 4.9.e and Fig. 4.9.f. The main drawback of this technique is the narrowband axial ratio performance of the antenna.

Cette thèse est accessible à l'adresse : https://theses.insa-lyon.fr/publication/2023ISAL0007/these.pdf
© [X.V.L. NGUYEN], [2023], INSA Lyon, tous droits réservés

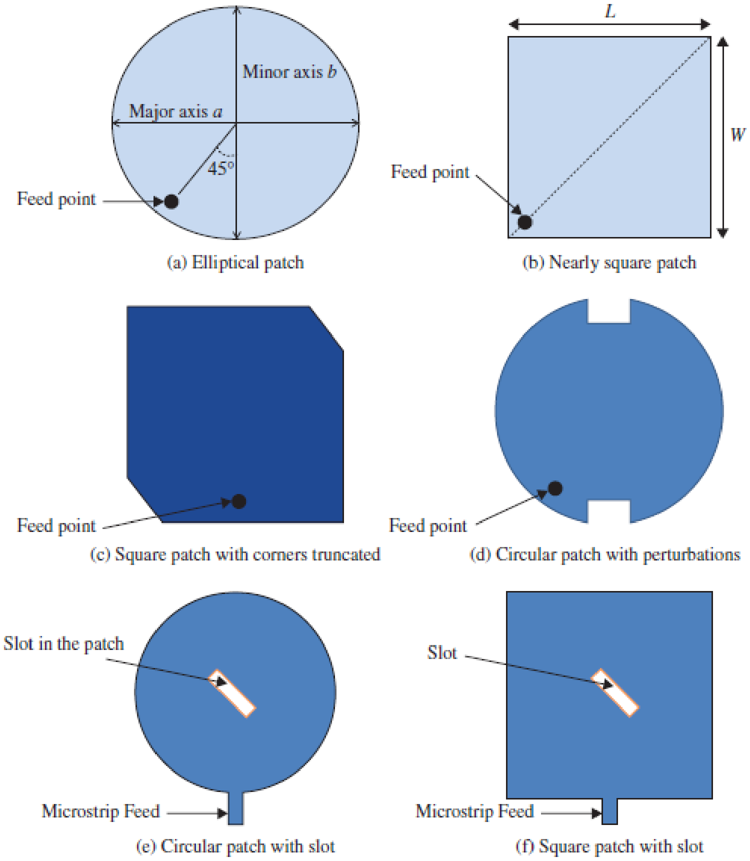

(a) Elliptical patch (b) Nearly square patch

(c) Square patch with corners truncated (d) Circular patch with perturbations

(e) Circular patch with slot (f) Square patch with slot

Figure 4.9: Different single-feed schemes for CP patch antenna [142]

In this work, a square patch antenna with truncated corners shape is chosen for the sake of design simplicity and possible immunity to manufacturing variability. As described in [143], [144], the antenna in this configuration will radiate in two diagonal planes for two different modes of excitation, which are Mode #1 and Mode #2 as shown in Fig. 4.10. These two modes have equal amplitude and in phase quadrature at the desired resonant frequency f_r. Since two linear polarizations of the antenna are orthogonal, the antenna can be considered to polarize circularly. In addition, the probe feed is replaced by the feeding line with the purpose of simplifying the connection between the antenna and the rectifier in the RFEH. Further information will be detailed in the next section.

Cette thèse est accessible à l'adresse : https://theses.insa-lyon.fr/publication/2023ISAL0007/these.pdf
© [X.V.L. NGUYEN], [2023], INSA Lyon, tous droits réservés

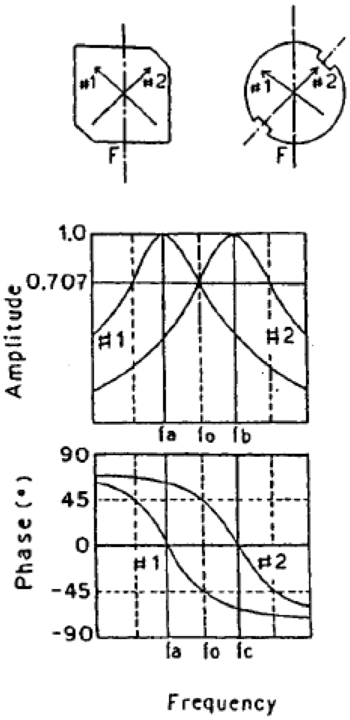

Figure 4.10: Amplitude and phase of orthogonal modes of excitation in a single-feed CP patch antenna [143]

4.3.2.2. Design of CP 2D patch antenna

Since the desired resonant frequency of the patch antenna is 2.45 GHz, the length of the antenna can be determined using Eq. (4.5). Because of the shortage in HT Resin v1 from Formlabs, a replacement is selected as HT Resin v2 ($\varepsilon_r = 2.9 \pm 0.1$). With this value of relative permittivity, the length of the antenna is calculated as 36 mm. Additionally, the width should be equal to the length of the antenna to have a square patch antenna. To feed the antenna, a 50 Ω microstrip transmission line is placed in the middle of one side of the antenna firstly. The length of the feeding line is shortened to weaken its effect on the radiation pattern of the antenna.

The corners are truncated and the dimension "t" of truncated parts as illustrated in Fig. 4.11 are then studied in CST Studio Suite 2019 such that two peaks of frequency appear in S_{11} as shown in Fig. 4.12. Here, two desired peaks of frequency are around 2.4 GHz and 2.5 GHz in order to overlap totally the 2.45 GHz Wi-Fi band.

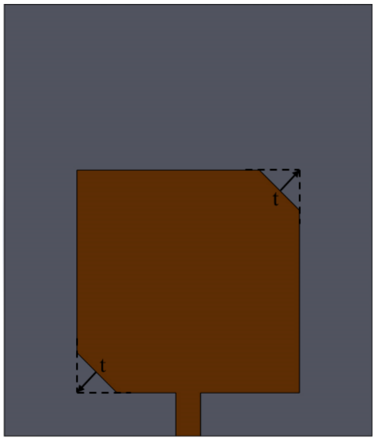

Figure 4.11: Patch antenna with the truncated parts with the dimension "t"

Cette thèse est accessible à l'adresse : https://theses.insa-lyon.fr/publication/2023ISAL0007/these.pdf
© [X.V.L. NGUYEN], [2023], INSA Lyon, tous droits réservés

The axial ratio of the antenna at the center frequency 2.45 GHz should be concerned as well in order to verify the polarization of the antenna. The simulated axial ratios and simulated gains as function of different values of truncated part dimensions are shown in Table 4.1.

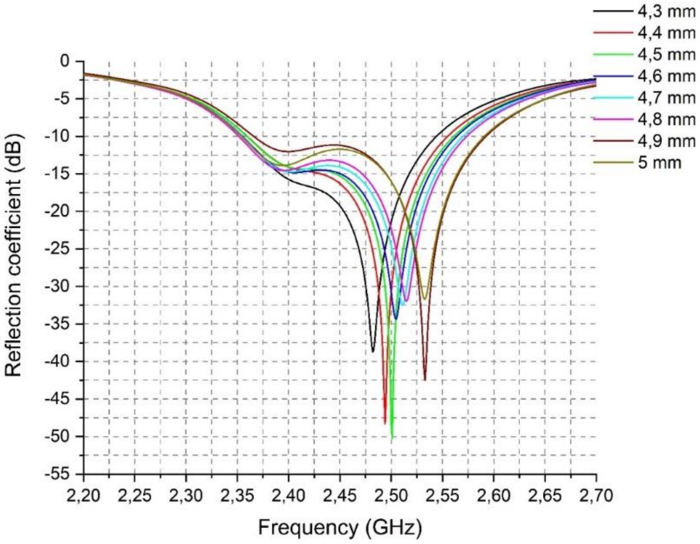

Figure 4.12: Simulated reflection coefficient of the antenna with respect to dimension "t" of truncated parts

Table 4.1: Simulated axial ratio and gain of the antenna with respect to dimension "t" of truncated parts

t (mm)	Simulated axial ratio at 2.45 GHz (dB)	Simulated gain at 2.45 GHz (dB)
4.3	3.55	2.00
4.4	3.55	2.04
4.5	3.19	2.06
4.6	2.78	2.07
4.7	**2.59**	**2.08**
4.8	2.83	2.10
4.9	3.02	2.09
5	2.68	2.11

According to Fig 4.12, the reflection coefficient at the first resonant frequency of 2.4 GHz varies slightly when the dimension of the truncated parts changes. This can be explained as the length of the longer diagonal of the patch antenna is kept constant. The second resonant frequency is modified as function of the dimension of the truncated parts. The simulated gain of the antenna at 2.45 GHz increases with "t". The simulated axial ratio of the antenna at 2.45 GHz does not vary monotonously as the simulated gain. The best value of axial ratio is 2.59 dB with "t" of 4.7 mm. The corresponding simulated gain is 2.08 dB. Moreover, with the latter value of the dimension "t" of the truncated parts, the reflection coefficient of the antenna is -15 dB at 2.45 GHz, which means that the antenna has a good impedance matching at that point. Therefore, the selected value of t is 4.7 mm.

Afterwards, the position of the feeding line is analyzed to improve the impedance matching and the axial ratio at 2.45 GHz [143], [144]. Here, a parameter "*m*" is used to define the distance between the middle axis of the substrate and the feeding line's one, as shown in Fig. 4.13. The variation of the reflection coefficient of the antenna as function of "*m*" is illustrated in Fig. 4.14. The simulated axial ratio and gain of the antenna are listed in Table 4.2.

Cette thèse est accessible à l'adresse : https://theses.insa-lyon.fr/publication/2023ISAL0007/these.pdf
© [X.V.L. NGUYEN], [2023], INSA Lyon, tous droits réservés

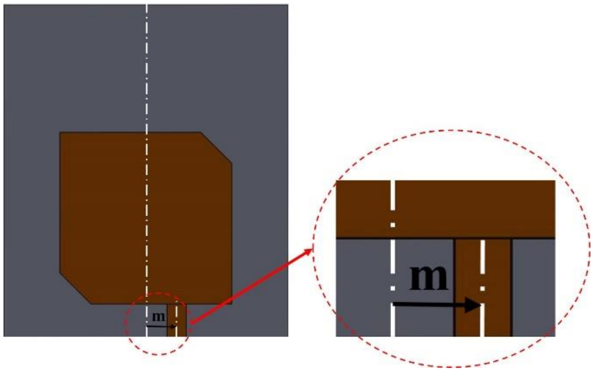

Figure 4.13: Patch antenna with different width of feeding line "m"

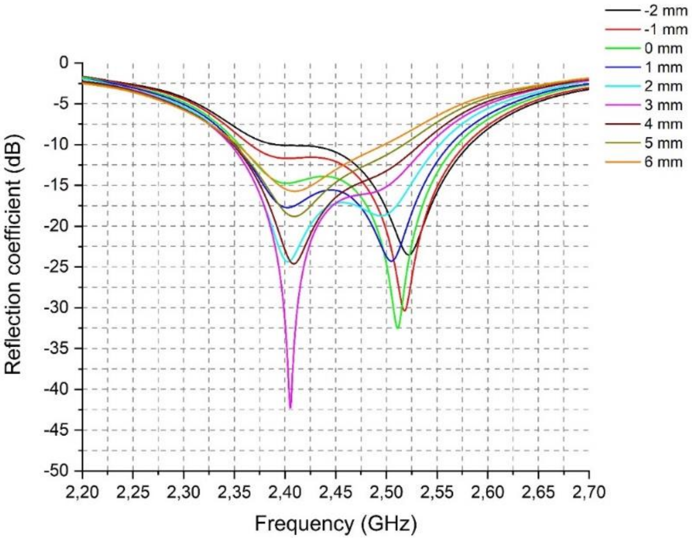

Figure 4.14: Simulated reflection coefficient of antenna with respect to the feeding line width "m"

Table 4.2: Simulated axial ratio and gain of antenna with respect to the feeding line width "m"

m (mm)	**Simulated axial ratio at 2.45 GHz (dB)**	**Simulated gain at 2.45 GHz (dB)**
-2	5.25	2.09
-1	4.06	2.09
0	2.59	2.08
+1	1.69	2.07
+2	**0.70**	**2.03**
+3	1.19	2.00
+4	2.34	1.96
+5	3.53	1.91
+6	4.73	1.86

We have the best reflection coefficient, -18 dB, at 2.45 GHz with the value of +2 mm for "*m*". Additionally, the axial ratio of the antenna at 2.45 GHz is reduced to 0.70 dB when "*m*" is equal to +2 mm. The gain of the antenna decreases when "*m*" increases. However, this variation is very small and can be neglected. Therefore, the chosen value of "*m*" should be +2 mm to acquire the minimum axial ratio for a circular polarization.

Cette thèse est accessible à l'adresse : https://theses.insa-lyon.fr/publication/2023ISAL0007/these.pdf
© [X.V.L. NGUYEN], [2023], INSA Lyon, tous droits réservés

Finally, according to the previous studies, the length and the width of the antenna are set to 36 mm. Additionally, the dimension of the truncated part is 4.7 mm and the distance between the middle axis of the substrate and the feeding line’s one is selected as +2 mm. The dimensions of the antenna are shown in Fig. 4.15.

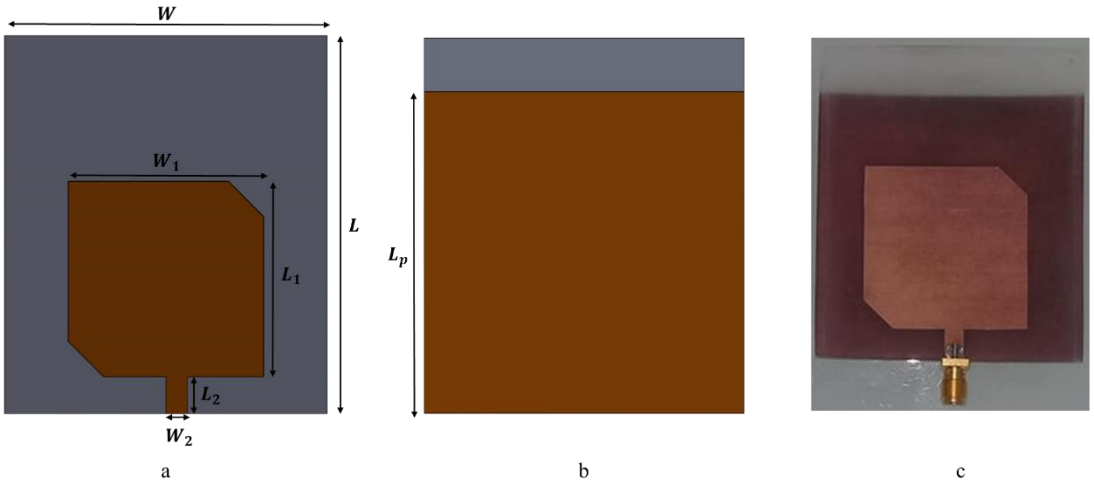

Figure 4.15: Proposed CP patch antenna (a. CAO design, front view; b. CAD design, back view; c. realized antenna) (W = 60 mm; L = 70 mm; W1 = 36 mm; L1 = 36 mm; W2 = 4 mm; L2 = 7 mm; Lp = 60 mm)

The measurements of the reflection coefficient, the radiation pattern as well as the gain are shown in Fig. 4.16 and Fig. 4.17.

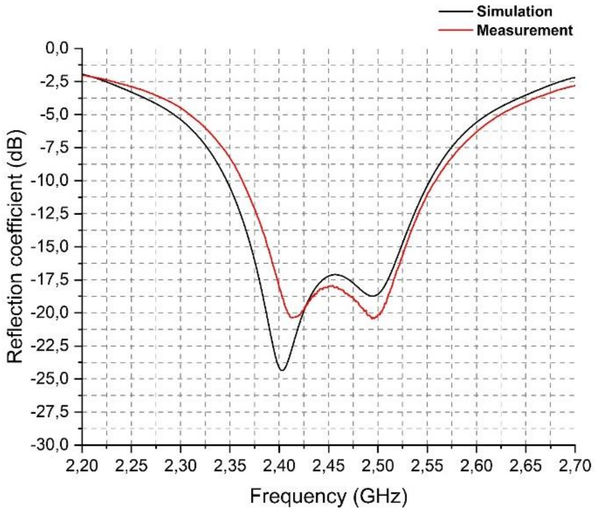

Figure 4.16: Simulated and measured reflection coefficient of CP 2D patch antenna

As illustrated in Fig. 4.16, there are two peaks of frequency in the measured reflection coefficient, which are 2.41 GHz and 2.5 GHz. Compared to the simulation, there is a minor difference. This difference can be originated from the variation of relative permittivity of the SLA substrate and/or the variation of dimensions of the actual antenna, what comes from the resolution of the masks in the etching process.

The radiation pattern of the antenna in vertical and horizontal planes the feedline of the antenna is measured in an anechoic chamber with a horn antenna whose gain is 9.8 dB at 2.45 GHz. Here, we have a good agreement between the simulated and measured results. The HPBW of the antenna in both planes are noted in Table 4.3. In addition, the difference in measured received power from the

Cette thèse est accessible à l'adresse : https://theses.insa-lyon.fr/publication/2023ISAL0007/these.pdf
© [X.V.L. NGUYEN], [2023], INSA Lyon, tous droits réservés

antenna in both planes is around 0.5 dB. That concludes on the circularity of polarization of the antenna. Concerning the gain of the antenna, the simulated and measured values are 2.03 dB and 1.70 dB, respectively. This gain ensures the radiating capability of the antenna. The slightly low gain of the antenna is affected by the high dielectric loss of the HT Resin v2 substrates and affected slightly by the ELD copper and probably the surface roughness of the antenna. A discrepancy may come from the inaccuracies in the setup during the measurements.

Table 4.3: Simulated and measured HPBW of CP 2D patch antenna in vertical and horizontal planes at 2.45 GHz

	Vertical plane	**Horizontal plane**
Simulated HPBW	87.1°	87.9°
Measured HPBW	85°	80°

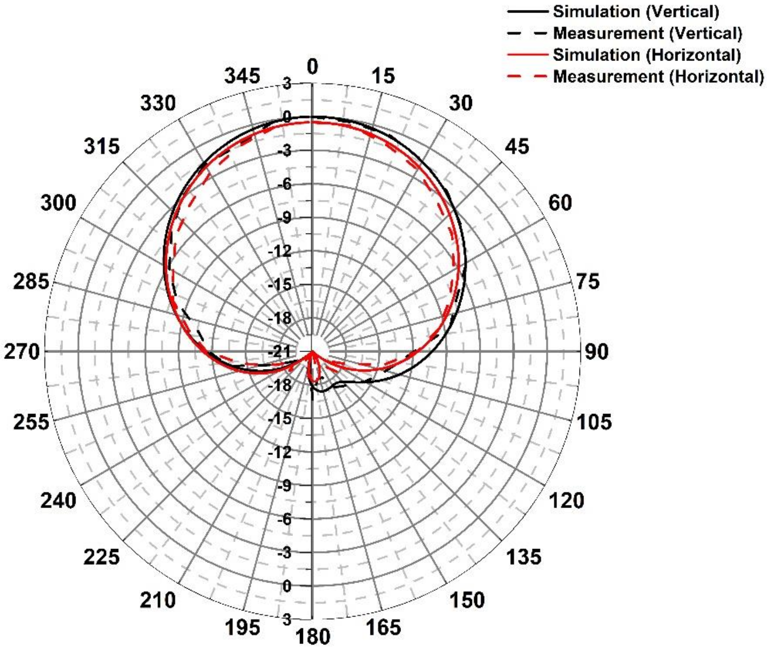

Figure 4.17: Simulated and measured radiation pattern of CP 2D patch antenna manufactured with HT Resin v2 in vertical and horizontal planes along the feeding line at 2.45 GHz

4.3.2.3. Circularly polarized 3D patch antenna

The limit of a patch antenna is its directional radiation pattern shown in Fig. 4.18.a. With this kind of radiation pattern, covering all the space around the object is not ensured. Hence, the idea of assembling four CP patch antennas in quadrature position is proposed [4], [104].

Cette thèse est accessible à l'adresse : https://theses.insa-lyon.fr/publication/2023ISAL0007/these.pdf
© [X.V.L. NGUYEN], [2023], INSA Lyon, tous droits réservés

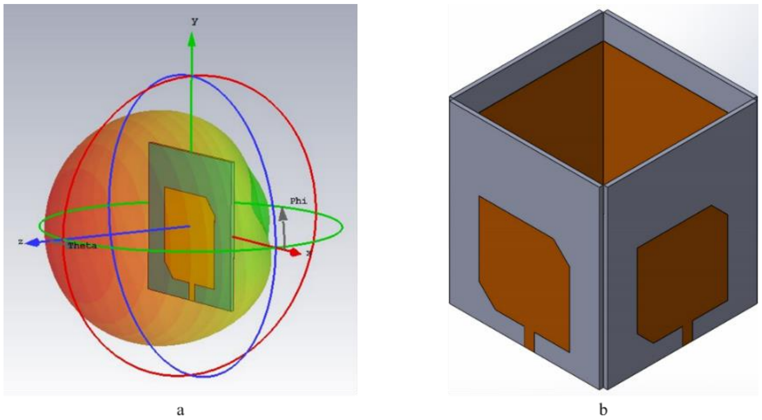

Figure 4.18: CP 2D patch antenna with 3D radiation pattern (a. Directional radiation pattern of the patch antenna; b. Assembly of four patch antennas in quadrature position)

In this case, the question about the HPBW of the antenna should be mentioned. For the previous 2D design of CP patch antennas, as noted in Table 4.3, the measured HPBW is around 85° in the vertical plane and 80° in the other plane along the feedline of the antenna. This value of HPBW cannot ensure the full cover of radiation pattern. Thus, the idea is to curve the form of the antennas as shown in Fig. 4.19 in order to increase the HPBW, so that this parameter can reach 90° [145], [146]. In [147], the authors show that with the curving radius of 0.25λ for the patch antenna, the radiation pattern can be broadened better than the other curving radius, such as 0.5λ and λ. However, the back-lobe of the radiation pattern is bigger with a smaller curving radius that can lead to the degradation of the gain of the antenna. In addition, in [148], the author studies the impacts of the curving radius on the performance of the circular polarization nearly-square patch antenna at 2.3 GHz. According to the study, the author presents that when the radius is approximately higher than 3λ, the curvature does not affect the axial ratio of the patch antenna. Thus, the radius of curved form of the substrate here is calculated as 40 mm using CST Studio Suite 2019. Since the antenna is deformed, its dimensions are slightly modified to obtain the circular polarization at 2.45 GHz. Due to the flexibility of manufacturing (advantage of Plastronics), a prototype of four curved CP patch antennas placed in quadrature position is then manufactured easily. The antennas possess a common ground surface metallized completely inside the object as in Fig. 4.19. A notable advantage of this configuration is that the impact of other components inside the object will be limited due to the full ground surface of the antennas.

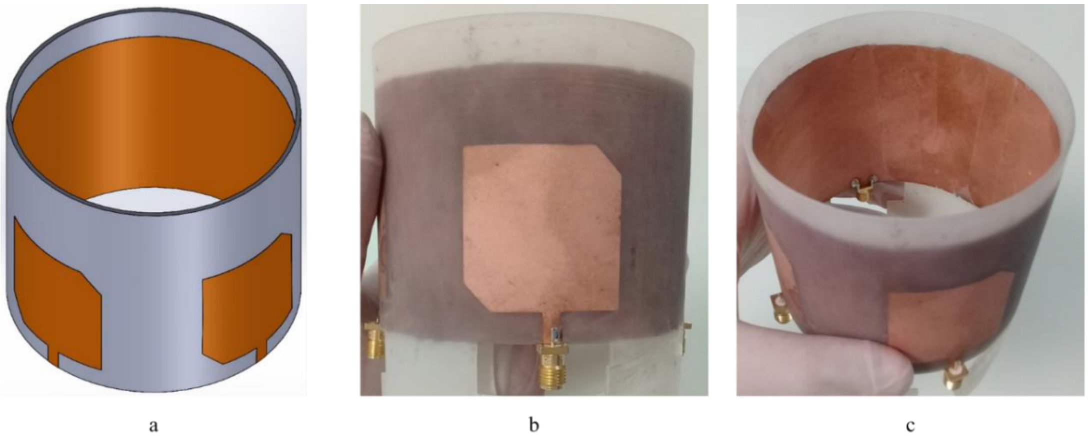

Figure 4.19: Four curved CP patch antenna manufactured with HT Resin v2 cylinder (a. CAD design of the system; b. Realized antennas, front view; c. Realized antennas, top view)

Cette thèse est accessible à l'adresse : https://theses.insa-lyon.fr/publication/2023ISAL0007/these.pdf
© [X.V.L. NGUYEN], [2023], INSA Lyon, tous droits réservés

The simulated and measured reflection coefficients and the radiation pattern in vertical and horizontal planes along the feedline of the antenna are presented in Fig. 4.20 and Fig. 4.21 respectively. The antennas have a good impedance matching over a wide band of frequency, which is from 2.35 GHz to 2.55 GHz covering the 2.4 GHz Wi-Fi band. The discrepancy between the simulation and the measured results may come from the slight variation of dimensions of the realized antenna during the etching process. The polarization of the antennas at 2.45 GHz stays circular since the difference of the main lobe of both measured planes is less than 0.1 dB. The simulated and measured HPBW as well as the gain of the antennas before and after the curving process are introduced in Table 4.4.

When curving the antenna, the HPBWs in both planes are improved. In the vertical plane, this parameter is increased from 85° to 90° experimentally. The same tendency is obtained in the other plane. The HPBW in the horizontal plane enhances from 80° to 83°. With the configuration of four curved CP patch antennas, the requirement of an adequate radiation pattern is assured. However, a drawback of broadening the HPBW is that the gain of the antenna will be degraded. As a proof, the simulated and the measured gain are decreased. The measured gain of the CP 2D planar antenna is 1.7 dB while the one of the curved antenna is 1 dB at 2.45 GHz, which means 0.7 dB of degradation. As mentioned, this degradation is predicted because of the enhancement of the back-lobe and the broadening of the main lobe of the radiation pattern when the patch antenna is curved. Literally, this value of gain can be raised up by separating the ground surface of each antenna. The further details will be mentioned in the next section.

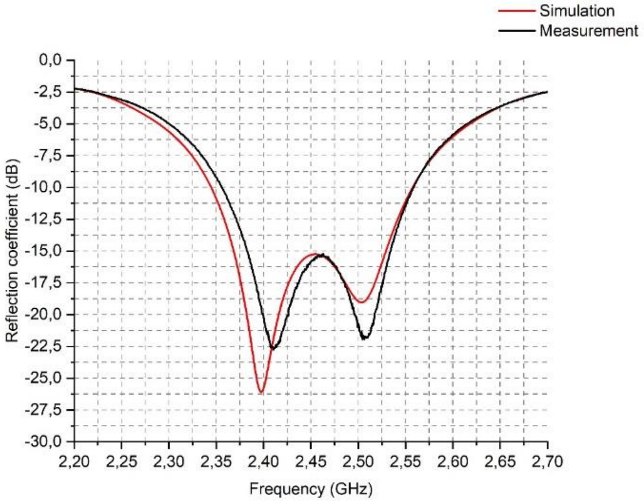

Figure 4.20: Measured and simulated reflection coefficient of the curved CP patch antenna manufactured with HT Resin v2

Cette thèse est accessible à l'adresse : https://theses.insa-lyon.fr/publication/2023ISAL0007/these.pdf
© [X.V.L. NGUYEN], [2023], INSA Lyon, tous droits réservés

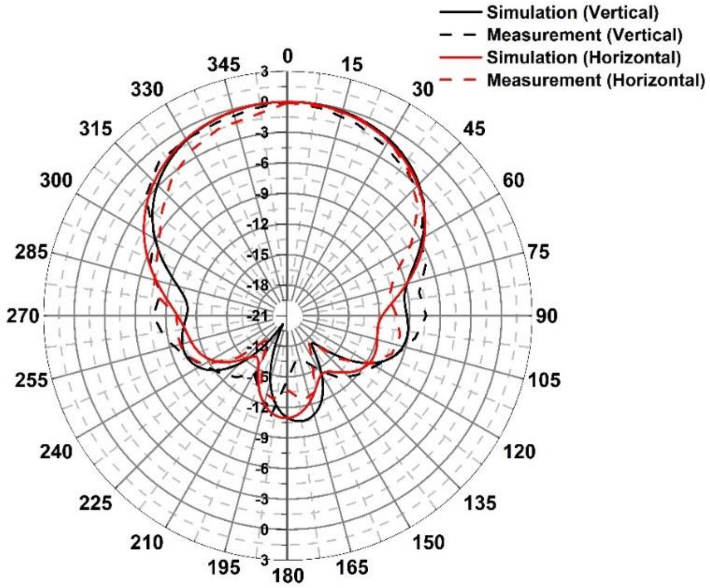

Figure 4.21: Measured and simulated radiation pattern of the curved CP patch antenna manufactured with HT Resin v2 in vertical and horizontal planes along the feeding line at 2.45 GHz

Table 4.4: Simulated and measured HPBW of the curved CP patch antenna manufactured with HT Resin v2 in vertical and horizontal planes at 2.45 GHz

	Planar patch antenna	**Curved patch antenna**
Simulation (Vertical plane)	87.1°	92°
Measurement (Vertical plane)	85°	90°
Simulation (Horizontal plane)	87.9°	94.8°
Measurement (Horizontal plane)	80°	83°
Simulation (Gain)	2.03 dB	1.26 dB
Measurement (Gain)	1.7 dB	1 dB

The measurement of isolation between the antennas of the proposed configuration is also carried out. The simulated and measured results are illustrated in Fig. 4.22. With this proposed concept of four curved CP patch antennas, the RFEH circuit accomplishes the possibility of capturing polarizations available around the object. The configuration of using the common ground plan gives us a good isolation between the antennas, which is lower than -32.5 dB for side-by-side position and lower than -37.5 dB for opposite position over the range of 2.2-2.7 GHz. Literally, the isolation can be better by segmenting the ground surfaces of each antenna. The studied results as well as the measurements will be described in the next section.

Cette thèse est accessible à l'adresse : https://theses.insa-lyon.fr/publication/2023ISAL0007/these.pdf
© [X.V.L. NGUYEN], [2023], INSA Lyon, tous droits réservés

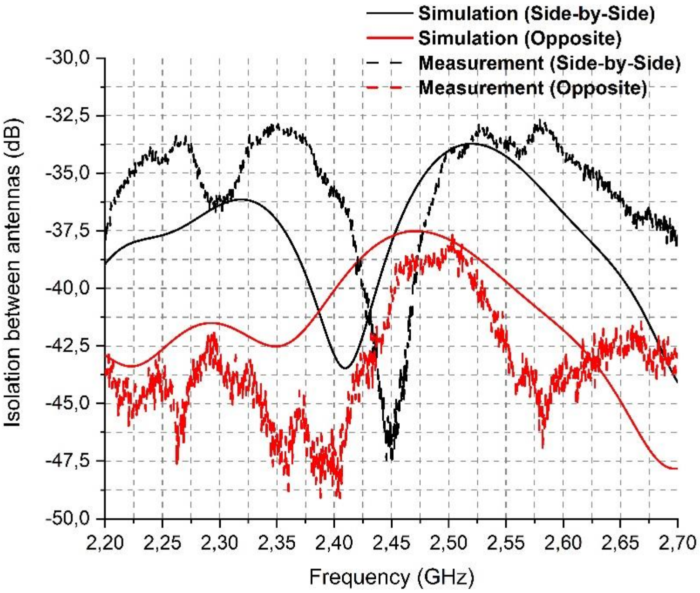

Figure 4.22: Simulated and measured isolation between antennas in different positions in the system of four curved CP patch antennas.

4.3.2.4. Improved design – Flower Pot

Instead of using a common ground surface for all antennas in the system, each antenna is mirrored by its own ground surface in order to isolate them more effectively. The new configuration of the array of antennas is illustrated in Fig. 4.23.

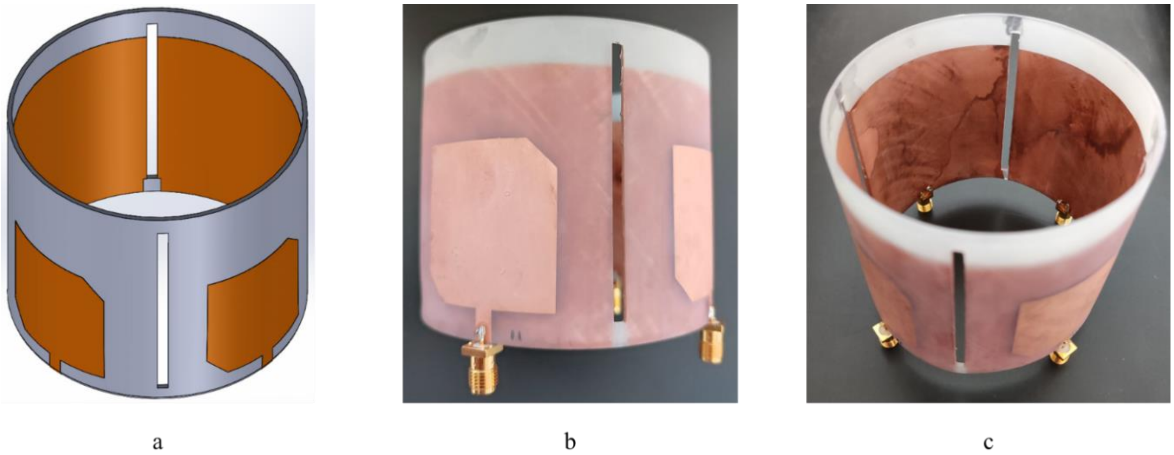

Figure 4.23: Improved design of the system of four curved CP patch antennas – Flower Pot (a. CAD design; b. Manufactured antennas, front view; c. Manufactured antennas, top view)

A comparison of the isolation between the common and the segmented ground surface configuration is presented in Fig. 4.24 and Fig. 4.25 respectively. The tendencies of the curves are nearly similar for both configurations with different positions of the antennas. The discrepancy between the simulation and the measurement may come from the effect of the SMA connectors or the setup inaccuracies. For the side-by-side position, the isolation between antennas of the segmented ground surface configuration is higher than with the previous configuration over a band of 2.2-2.7 GHz. The maximum measured isolation of the common ground configuration is around -34 dB meanwhile the segmented configuration offers around -38 dB. The maximum measured

Cette thèse est accessible à l'adresse : https://theses.insa-lyon.fr/publication/2023ISAL0007/these.pdf
© [X.V.L. NGUYEN], [2023], INSA Lyon, tous droits réservés

value of the common ground configuration is -38 dB and this value in the segmented ground configuration is around -45 dB.

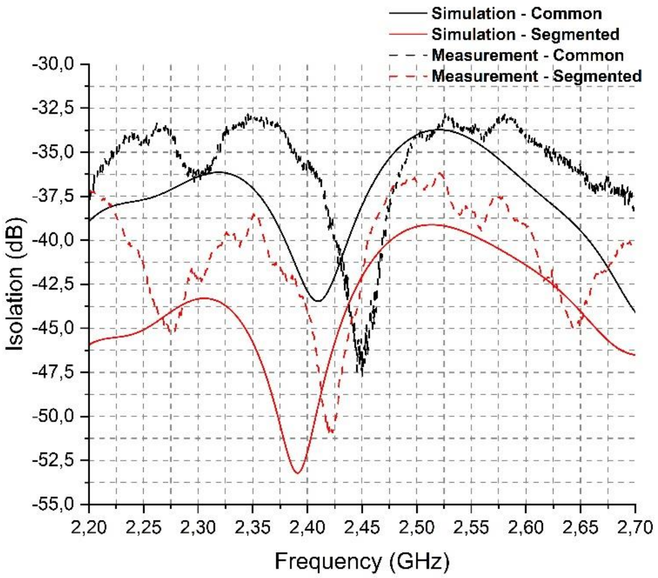

Figure 4.24: Simulated and measured isolation between antennas (side-by-side position) with common and segmented ground surface

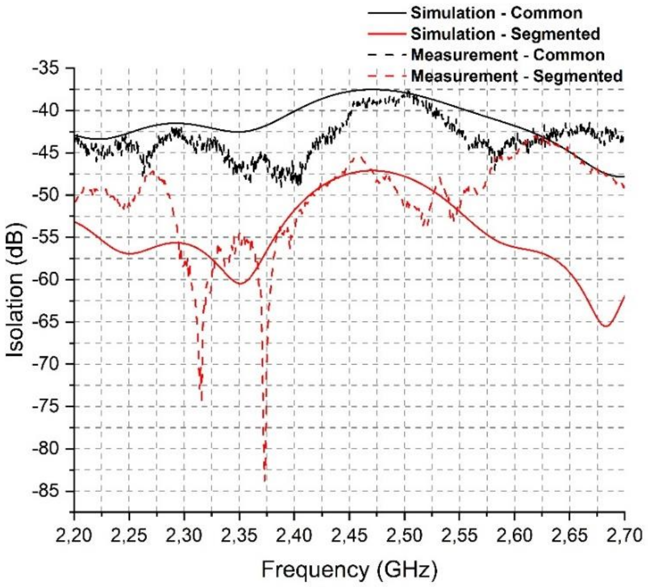

Figure 4.25: Simulated and measured isolation between antennas (opposite position) with common and segmented ground surface

Additionally, the gain of the antennas is also augmented from 1.26 dB to 1.6 dB in simulation and from 1 dB to 1.35 dB experimentally comparing between the common and segmented ground surface. The increment in isolation and gain can be explained by the reduction of mutual effects when the ground surface is segmented. The isolation is thus increased. Moreover, the side lobes and the back lobe are smaller with the segmented ground surface configuration in both radiation planes, consequently, the gain of the antenna is enhanced.

Cette thèse est accessible à l'adresse : https://theses.insa-lyon.fr/publication/2023ISAL0007/these.pdf
© [X.V.L. NGUYEN], [2023], INSA Lyon, tous droits réservés

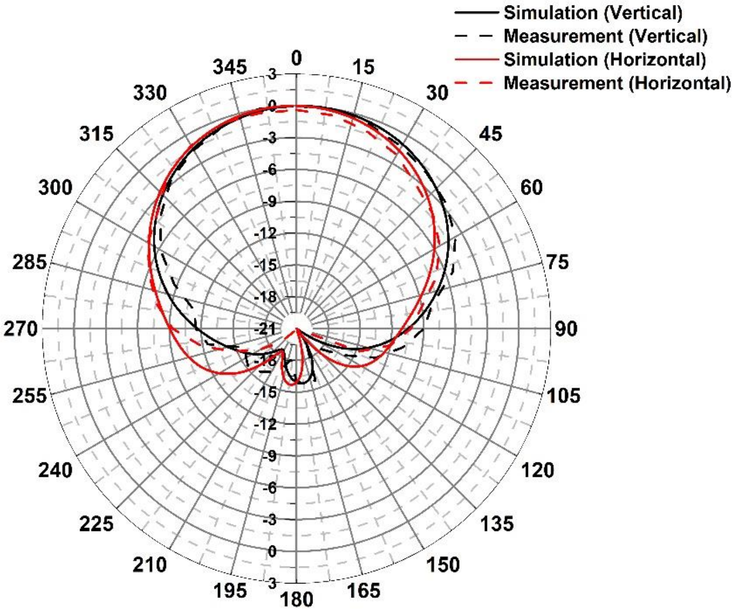

Figure 4.26: Simulated and measured radiation pattern of antennas in the Flower Pot manufactured with HT Resin v2 in vertical and horizontal planes along the feeding line at 2.45 GHz

The simulated and measured radiation pattern of this configuration are plotted in Fig. 4.26. The HPBW and the gain of the antenna in both configurations are compared and listed in Table 4.5.

Table 4.5: Simulated and measured HPBW in vertical and horizontal planes and gain of antennas in the Flower Pot at 2.45 GHz

	Common ground surface	**Segmented ground surface**
Simulation (Vertical plane)	92°	94°
Measurement (Vertical plane)	90°	90°
Simulation (Horizontal plane)	94.8°	88°
Measurement (Horizontal plane)	83°	87°
Simulation (Gain)	1.26 dB	1.6 dB
Measurement (Gain)	1 dB	1.35 dB

Nonetheless, the axial ratio of the antenna changes with segmented ground surfaces. According to the simulation, this parameter is around 0.59 dB compared to 0.46 dB in the common ground configuration. There is an increment of 0.13 dB, slight thus negligible. The simulated axial ratio of the new configuration is also quite small. Furthermore, the difference in received power in vertical and horizontal planes along the feedline of the antenna is less than 0.4 dB. We can conclude that the polarization of the antennas is nearly circular.

This configuration of four antennas will be selected in the system presented in the next chapter.

4.4. Wrap-Up

We have presented patch antennas for energy harvesting applications fabricated using Rapid Plastronics. The thickness of the fabricated substrate is set to 1.5 mm with ELD copper of 7 µm for all antennas.

First, a linear polarization 2D patch antenna manufactured with a HT Resin v1 substrate operating at 2.45 GHz is created. The antenna has a bandwidth of 85 MHz with a measured gain of +2.5 dB at 2.45 GHz.

Cette thèse est accessible à l'adresse : https://theses.insa-lyon.fr/publication/2023ISAL0007/these.pdf
© [X.V.L. NGUYEN], [2023], INSA Lyon, tous droits réservés

Another patch antenna on the Rogers 4003C substrate, using conventional manufacturing method is used to compare the bandwidth and the gain to the patch. The Rogers substrate patch yields a bandwidth of 23 MHz and a gain of +5.3 dB. The lower bandwidth of the Rogers substrate patch comes from the lower loss tangent of this substrate. Meanwhile, the higher gain benefits from the lower loss tangent and the higher conductivity of copper sheet. The breakdown of gain difference is estimated through simulation as the dielectric loss accounts for 2.77 dB of the degradation of the gain of the patch antenna meanwhile the conductive loss accounts for 0.03 dB.

The gain of the plastronic antenna is smaller but satisfying enough to consider the manufacturing process and the chosen polymer for the substrate (which will be also the one of the shells of the final device).

Secondly, circular polarization patch antennas are introduced. To simplify the design, a single feed with truncated corner patch antenna is selected. The principle of excitation and the steps of design of this antenna are detailed. A 2D circular polarization patch antenna manufactured with a HT Resin v2 is concerned in the first study. A good circular polarization patch antenna is obtained. However, the impacts on the radiation pattern (directional pattern, half-power beamwidth) are highlighted. Two objects with different configurations of ground surface (common and segmented ground surfaces) of four curved circular polarization patch antennas arranged as a cylinder are proposed as the solution for mitigating those impacts. The radiating performances of these two configurations are analyzed. The system of patches with segmented ground surfaces is selected due to the satisfying isolation between antennas and the satisfying gain.

A comparison between the experimental results and the ones in the state-of-art is shown in Table 4.6. To have a fair observation about the performance of the antennas, the selected references are related to patch antennas operating in the band of 2.45 GHz. Table 4.6 classifies different methods of substrate manufacturing and deposited conductors, as well as the corresponding type of substrates, conductors and their electrical properties (relative permittivity, loss tangent, resistivity at 2.45 GHz), feeding methods, measured gain, and dimensions of radiating parts of antennas.

Firstly, if we compare the antenna design reported on the Rogers 4003C substrate with the design in [4], the gain of our antenna is better. This can be explained as their substrate are thinner than ours. Therefore, the gain is improved as stated previously.

Secondly, comparing our antenna on HT Resin v1 to the antenna on FR-4 in [80], the gain of both antennas is closely similar. This may be explained as the loss tangent of both substrates is nearly identical. Additionally, the resistivity of both deposited conductors is also close to each other.

The gain of our circular polarization patch antennas on HT Resin v2 is comparable to the value given in [149], whose substrate has the same loss tangent as HT Resin v2. The higher gain of the patch proposed in [149] can be explained by the thicker substrate used in their work even if the conductor is not ideal. Furthermore, our design is a wideband circular polarization patch antenna, the gain of the antenna will be consequently degraded compared to conventional patch’s values.

The antenna introduced in [104] has a better gain than our antennas realized on SLA substrates, even the used conductor is worse. This can be explained because of the thicker substrate and maybe the selected substrate has a lower loss.

According to these results, the Rapid Plastronics technique allows us to obtain antennas with comparable performances. As discussed in Chapter 3, the advantages of this technique are to be able to give rise not only to 2D but also to 3D antennas easily. The unavoidable drawbacks are the dielectric loss of the SLA substrates and the conductive loss from the ELD. The dielectric loss

Cette thèse est accessible à l'adresse : https://theses.insa-lyon.fr/publication/2023ISAL0007/these.pdf
© [X.V.L. NGUYEN], [2023], INSA Lyon, tous droits réservés

depends on the polymer material and results from the manufacturing process. If the process is kept unchanged, there is still room for the choice of polymer. This question was not part of the study. Let’s say that the dielectric loss represents a good order of magnitude for a large choice of polymers, including recycled ones. It is worth recalling that the philosophy is not to select the polymer for the sake of antenna performances, but to accommodate an antenna, whatever the polymer chosen to manufacture the object to functionalize.

Cette thèse est accessible à l'adresse : https://theses.insa-lyon.fr/publication/2023ISAL0007/these.pdf
© [X.V.L. NGUYEN], [2023], INSA Lyon, tous droits réservés

Table 4.6: Comparison between our works and state-of-art

Ref	**Substrate Fabricating/ Type ($\boldsymbol{\varepsilon_r, tan(\delta)}$)**	**Conductor Fabricating/ Type (Resistivity)**	**Freq. (GHz)**	**Antenna**	**Feeding method**	**Meas. gain**	**Size of radiating part (mm^3)**
[80]	Conventional/FR-4 (4.3, 0.02)	NI	2.45	Fractal patch	Probe	2.72 dBi	26.4 x 26.4 x 1.6
[4]	Conventional/ Rogers 4003C (3.55, 0.0021)	NI	2.45	Patch	Probe	5 dBi	32 x 31.5 x 0.83
[149]	Flexible materials/Felt (1.3, 0.044)	170um-thick ShieldIt conductive fabric (8.47 μΩ.m)	2.4	Reconfigurable patch	Probe	2-3.9 dB	46.5 x 39 x 3.3
[104]	3D printing method/VeroWhite (NI)	Inkjet printing/20 µm-thick silver nanoparticles ink then diammine-silver acetate ink (0.2 μΩ.m)	2.3	Patch	Probe	4-4.2 dBi	27.9 x 35.9 x 3
This work	Conventional/ Rogers 4003C (3.55, 0.0021)	Laminated copper	2.45	Patch	Feeding line	5.3 dB	32 x 56.1 x 1.5
	SLA/HT Resin v1 (3, 0.025)	ELD copper (0.02-0.025 μΩ.m)	2.45	Patch	Feeding line	2.5 dB	36.1 x 57.15 x 1.5
	SLA/HT Resin v2 (2.9, 0.04)		2.45	Circular polarization patch	Feeding line	1.7 dB	36 x 43 x 1.5
	SLA/HT Resin v2		2.45	Circular polarization curved patch (Common ground)	Feeding line	1.26 dB	36 x 43 x 1.5
	SLA/HT Resin v2		2.45	Circular polarization curved patch (Segmented ground)	Feeding line	1.6 dB	36 x 43 x 1.5

NI: Not Indicated in the article

Cette thèse est accessible à l'adresse : https://theses.insa-lyon.fr/publication/2023ISAL0007/these.pdf
© [X.V.L. NGUYEN], [2023], INSA Lyon, tous droits réservés

Cette thèse est accessible à l'adresse : https://theses.insa-lyon.fr/publication/2023ISAL0007/these.pdf
© [X.V.L. NGUYEN], [2023], INSA Lyon, tous droits réservés

CHAPTER 5: RF-DC RECTIFIER CIRCUIT AND POWER MANAGEMENT UNIT

Cette thèse est accessible à l'adresse : https://theses.insa-lyon.fr/publication/2023ISAL0007/these.pdf
© [X.V.L. NGUYEN], [2023], INSA Lyon, tous droits réservés

Cette thèse est accessible à l'adresse : https://theses.insa-lyon.fr/publication/2023ISAL0007/these.pdf
© [X.V.L. NGUYEN], [2023], INSA Lyon, tous droits réservés

5. RF-DC RECTIFIER CIRCUIT AND POWER MANAGEMENT UNIT

In a Radio Frequency Energy Harvester (RFEH) circuit, the captured EM waves by the antenna will be converted to DC energy for further applications. The rectifier has a crucial role of converting the EM waves into the DC energy. Nevertheless, in the aspect of energy harvesting, the rectified voltage of the rectifier is generally very low and far from the minimum operating voltage of many electronic devices. In addition, this value of the voltage depends also on the value of the load. Therefore, a Power Management Unit (PMU) is proposed as the output load of the rectifier in order to boost and to regulate the rectified voltage of the RFEH to the required voltage of the consumption loads, i.e. the sensors, the micro-controllers, etc. To maximize the performance of the RFEH, the rectifier and the PMU should be well-studied.

In this chapter, the procedure of simulation and the measurement results of our rectifiers will be introduced firstly. After that, our proposed PMU will be presented. The electrical interface between the rectifier and the PMU to achieve the Maximum Power Point will be mentioned as well. A wrap-up will be deduced at the end of this chapter.

5.1. RF-DC rectifier circuit

The simulation procedure and the measurement results of our rectifier will be shown in this section. Our rectifiers are fabricated on the (1.5 ± 0.1) mm thick SLA substrates and the conductor is ELD copper with a thickness of 7 µm.

5.1.1. The rectifier for the linear polarization patch antenna

5.1.1.1. Rectifying diode selection

Selecting an appropriate diode is important in designing the rectifier because diodes are the main source of loss and their performance determines the circuit performance. According to [150], the conversion efficiency of the rectifier depends on: zero-bias junction capacitance (C_{j0}), the series resistance (R_s) and the breakdown voltage (V_{br}). An appropriate diode should have low junction capacitance, low series resistance, and high breakdown voltage. However, it is very hard to have these three conditions simultaneously because of the physical mechanism of diodes and those inter-correlated parameters [150].

In addition, a diode with low threshold voltage (V_{th}) is desired in the rectifier design. Reverse saturation current (I_s) of the diode is also one of the important characteristic parameters [151]. For the large I_s, the diode resistance reduces, hence, the diode allows to start the conduction at low input power levels, the turn-on voltage of the diode becomes low. Thus, the diode with a large I_s will be easier to be turned on at low input power levels. Moreover, the diode with large I_s will offer better conversion efficiency comparatively [151]

To conclude, a desirable rectifying diode for the rectifier design should have simultaneously the following condition

- Low threshold voltage V_{th}
- Low series resistance R_s
- Low zero-bias junction capacitance C_{j0}
- High reverse saturation current I_s
- High breakdown voltage V_{br}

Table 5.1 summaries the characteristic parameters of some recent Schottky diodes

Cette thèse est accessible à l'adresse : https://theses.insa-lyon.fr/publication/2023ISAL0007/these.pdf
© [X.V.L. NGUYEN], [2023], INSA Lyon, tous droits réservés

Table 5.1: Characteristics parameters of recent Schottky diodes models [151]

Diode	V_{th} (V)	R_s (Ω)	C_{j0} (pF)	V_{br} (V)	I_s (µA)
SMS7630	0.09	20	0.14	2.0	5.0
MA4E1317	0.7	4.0	0.02	7.0	0.1
HSMS 2852	0.15	25	--	3.8	3.0
HSMS 2860	0.25	6.0	--	7.0	0.05
HSMS 2850	0.15	25	0.18	3.8	3.0
HSMS 286B	0.69	6.0	0.18	7.0	0.05
HSMS 2820	0.15	6.0	0.7	15.0	0.022

Among the diodes, SMS7630 Schottky diode has the lowest threshold voltage and highest reverse saturation current. However, its series resistance is higher than other diodes, except HSMS 2850. Furthermore, its junction capacitance is slightly lower than HSMS 2850 and HSMS 286B's value, but much higher than the value of MA4E1317. The breakdown voltage of SMS7630 is the lowest value, which can be estimated since its threshold voltage is very low.

Our studied RF input power level is around -20 dBm or higher (maybe 0 dBm max), the high value of breakdown voltage is not truly necessary but the threshold voltage plays a crucial in this case [151]. Therefore, MA4E1317, HSMS 2860, HSMS 286B and HSMS 2820 will not be our interest. In [152], the authors show that the diode SMS 7630 gives a better performance for power levels below 13 dBm. To conclude, for our thesis, the selected rectifying diode is SMS7630.

5.1.1.2. Simulation procedure

As described in Chapter 4, our first studied antenna is a linearly polarized 2.45 GHz patch antenna in 2D form deposited on HT Resin v1 substrate. To examine the possibility of applying Rapid Plastronics in fabricating the RFEHs as well as their performance, a rectifier operating at 2.45 GHz should be concerned.

The rectifier circuit is presented in Fig. 5.1. The simulation procedure is introduced as below.

Since the targeted input power of the rectifier is -20 dBm at 2.45 GHz, the series diode topology is selected to get a good RFoM of the circuit as stated in Chapter 2 of this manuscript. For the rectifying diode, Schottky diode SMS7630-079LF from Skyworks Solutions Inc. is selected. Here, SPICE model of the rectifying diode is used because other practical models are not available.

The SPICE model is provided in [153] by the manufacturer. Additionally, because the diode is inside a 79LF package, the interior elements of this package can add parasitic impacts on the performance of the circuit at high frequency. These parasitic elements given in [153] are also added in the simulation.

The storage capacitor of the rectifier is a Surface Mounted Device (SMD) capacitor of 12 pF used for low-power applications from Murata. In fact, the capacitor can be higher to store more rectified energy, but it might increase the size of the circuit. A bigger capacitor for energy storage can be afterwards integrated in the PMU. The output load is a 10 kΩ resistor from Yageo Corp.

In order to match the impedance at 50 **Ω**, a mixed circuit of a lumped inductor and a shorted circuit stub is deployed here. The idea of using a mixed circuit is to reduce the size of the matching circuit, thus, the size of the circuit as indicated in Chapter 2. Here, the shorted circuit stub is preferred in order to ensure the closed loop of the DC current, which is rectified by the diode, as stated previously. The inductor is a SMD component of 9.1 nH fabricated by Murata.

Cette thèse est accessible à l'adresse : https://theses.insa-lyon.fr/publication/2023ISAL0007/these.pdf
© [X.V.L. NGUYEN], [2023], INSA Lyon, tous droits réservés

The circuit is simulated and optimized using Advanced Design System (ADS) 2019 and then validated by Co-Simulation of ADS Momentum. Since the packages of SMD components lead also to parasitic impacts, ADS models of the components from Murata, i.e. storage capacitor, inductor, are used in the simulation. In these models, the parasitic elements of the packages are characterized and modeled for ADS simulations.

The substrate parameters, i.e. relative permittivity and loss tangent, and the deposited conductor properties characterized in Chapter 3 are inserted in the simulation.

The circuit has three PCB vias in the substrates. Literally, the vias are the conductors used to connect two or multi conductive faces of the circuits. The resistive effect of the vias comes from the conductors consequently. Not only a resistive but also an inductive effect exists simultaneously in the vias [154].

In [154], the inductance L_{via} presenting the inductive effect of the via can be calculated as

$$L_{via} = \frac{\mu_0}{2\pi}\left[h.\ln\left(\frac{h+\sqrt{r^2+h^2}}{r}\right)+\frac{3}{2}\left(r-\sqrt{r^2+h^2}\right)\right] \tag{5.1}$$

where, h is the substrate thickness (m), r is radius of the via hole, μ_0 is the permeability of free space ($4\pi \times 10^{-7} H/m$).

Additionally, the resistance of a via may be approximated as, taking into account the skin effect

$$R_{via} = R_{DC}\sqrt{1+f/f_\delta} \tag{5.2}$$

where,

$$f_\delta = 1/(\pi\mu_0\sigma t^2) \tag{5.3}$$

with σ is conductivity of via's conductor (S/m), f is frequency (Hz), t is thickness of the conductor (m).

Since R_{DC} is proximity to 0 Ω, R_{via} can be neglected therefore.

The circuit is afterwards fabricated on a 30 mm x 40 mm x 1.5 mm HT Resin v1 board.

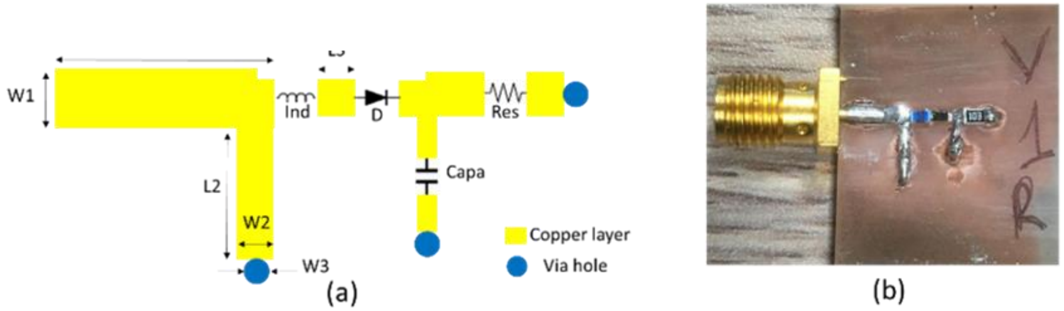

(a) (b)

Figure 5.1: Rectifier circuit for the 2D linear polarization patch antenna (a. Geometry; b. Manufactured circuit) (W1 = 2mm, W2 = 1mm, W3 = 0.7mm, L1 = 4mm, L2 = 3.1mm, L3 = 1mm)

5.1.1.3. S-parameters measurements

In order to verify the matching impedance condition of the circuit, the measurement of S_{11} of the circuit is carried out using a calibrated VNA with variable output power level. Since the circuit is optimized at -20 dBm and 2.45 GHz, the output power of the VNA is set at -20 dBm. The measured results are plotted in Fig. 5.2.

Cette thèse est accessible à l'adresse : https://theses.insa-lyon.fr/publication/2023ISAL0007/these.pdf
© [X.V.L. NGUYEN], [2023], INSA Lyon, tous droits réservés

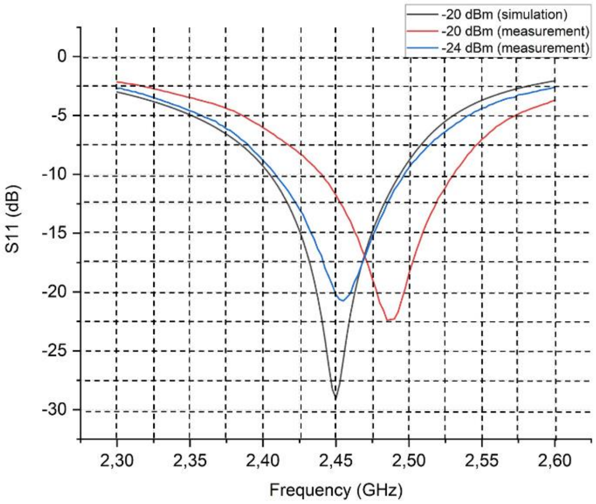

Figure 5.2: Simulated and measured reflection coefficient of the rectifier

As shown in Fig. 5.2, at -20 dBm, we have a shift in resonant frequency between the simulation and the measurement. This discrepancy may come from the variation of the inductor used in the matching circuit and the parasitic elements of the package of the rectifying diode. However, at this power level, the impedance of the circuit is sufficiently matched to 50 Ω as the reflection coefficient is around -11.8 dB. Another measurement is deployed to obtain the power level where the peak of resonant frequency is at 2.45 GHz. At -24 dBm, the measured S_{11} of the circuit is minimum, which is -20 dBm. This concludes on the satisfying matching of the rectifier at -24 dBm and 2.45 GHz. The measurements of the rectified voltage and the conversion efficiency will be deployed at -24 dBm.

5.1.1.4. Rectified voltage and conversion efficiency measurements

The rectifier circuit is connected to the 2D linearly polarized patch antenna described in Chapter 4. The rectenna is characterized in an anechoic chamber. A standard horn antenna is placed opposite to the rectenna at a distance of 2.9 m. The horn antenna is set up such that its polarization is aligned with the patch antenna's one to cancel the polarization loss between the two antennas. In order to have the input power of -24 dBm in the rectenna plane, the transmitting power of the horn antenna is set at a value of 15 dBm. This value of transmitting power is obtained by measuring the distance between the horn antenna and the rectenna, the attenuation of cables, then, by applying the Friis' equation (Eq. 5.4)

$$P_r = P_t + G_t + G_r + A_{total} + 2\,(\log_{10}(\lambda) - \log_{10}(4\pi R)) \tag{5.4}$$

where, P_r is received power of the antenna of the rectenna (dB), P_t is transmitted power of the horn antenna (dB), G_t and G_r is gain of transmitting and receiving antenna (dB), A_{total} is total attenuation (dB), λ is wavelength at the defined frequency (m), R is the distance between two antennas (m).

The rectified voltage at the output of the rectifier is then measured using a Fluke 175 Multimeter.

The measured rectified voltage (V_{DC}) and the conversion efficiency (η_{RF-DC}) of the rectenna are presented in Fig. 5.3 and Fig. 5.4 respectively. The conversion efficiency is calculated as

$$\eta_{RF-DC} = V_{DC}^2/(R_L P_{RF}) \tag{5.5}$$

where, R_L is output load of the rectifier (Ω), P_{RF} is received power of the patch of the rectenna (W).

Cette thèse est accessible à l'adresse : https://theses.insa-lyon.fr/publication/2023ISAL0007/these.pdf
© [X.V.L. NGUYEN], [2023], INSA Lyon, tous droits réservés

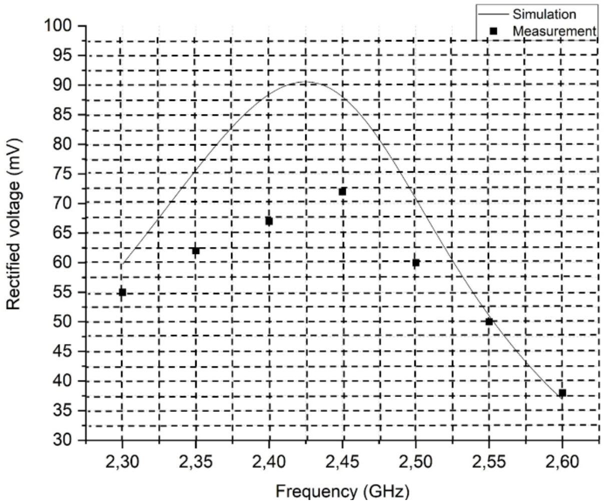

Figure 5.3: Simulated and measured rectified voltage at the load of the rectenna

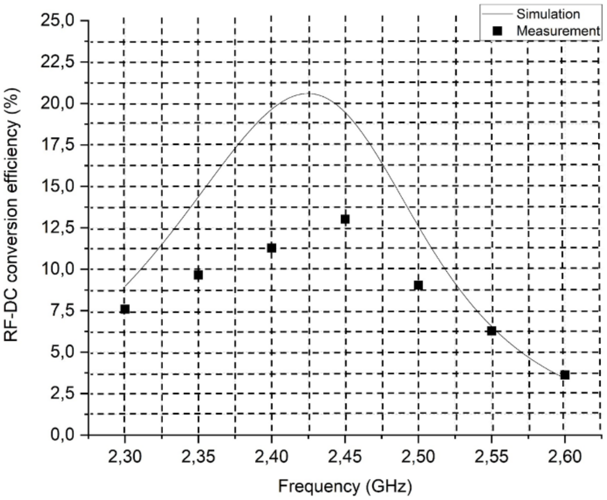

Figure 5.4: Simulated and measured conversion efficiency of the rectenna

The measured rectified voltage at 2.45 GHz is 72 mV on the 10 kΩ load corresponding to a conversion efficiency of 13% while the simulated value is 88 mV. The difference may come from the loss in the SMA connectors used to connect the rectifier and the antenna and the variation of parameters of the model used in the simulation. The tendencies of the measurements' curves and the ones from the simulation are in agreement. Additionally, the rectified voltage keeps practical value over the range of frequency. We can conclude that the rectifier may operate over a quite large band of frequency.

5.1.1.5. Comparison and Conclusion

The measured RF-DC efficiency, a comparison of the experimental results, the substrates and the deposition techniques against the state-of-art are listed in Table 5.2. The performances of the rectenna are comparable to the ones of other circuits deposited on specific dedicated RF substrates. In addition, the proposed fabrication technology (SLA) and the used materials have no significant effects on the performances of the rectenna.

Cette thèse est accessible à l'adresse : https://theses.insa-lyon.fr/publication/2023ISAL0007/these.pdf
© [X.V.L. NGUYEN], [2023], INSA Lyon, tous droits réservés

Table 5.2: Comparison between our work to state-of-art

Ref	**Freq. (GHz)**	**Substrate/ Deposition technique**	**In. pow. (dBm)/ Pow. den. (μW/cm^2) @ Load (kΩ)**	**PCE (%)**	**Size (mm^3)**
[76]	1.85	FR4/Printed Circuit Board	-24/NI @ 14.7	23	70 x 70 x 13.2
	2.15			15	
	2.3			5	
[66]	2.42	Flexible RO5880 (Antenna) and RO6002 (Rectifier) /Conventional deposition	NI/0.2 @ 5.1	26	290 x 130^{2}π
[95]	2.45	Polyester felt and woven polyester/Copper-coated polyester fiber (Antenna) Duroid 5880/Conventional deposition (Rectifier)	-24.3/NI @ 4	21	105 x 87 x 3.7
[155]	0.9	Flexible photo-paper/Copper adhesive tape	NI/0.2 @ 3	25	110 x 110 x 0.37
	1.8			12	
	2.6			8	
[108]	0.9	3D printing substrate/Screen printing (conductive silver paste from DuPont)	-24/NI @ 11	12	50 x 50 x 50
	1.8			12	
	2.1			3	
This work	2.45	SLA 3D printing polymer/ Electroless deposition	-24/0.2 @ 10	13	60 x 83 x 1.5

NI: Not Indicated in the article

The rectenna may be fabricated on the surface of a given 3D polymer package of device as opposed to 2D hard-type RF substrates or flexible RF substrates as stated in Chapter 2. To reduce the impact of the discrete components used in the mixed between lumped components and microstrip lines matching circuit to the resonant frequency of the rectifier and the number of soldering parts, microstrip matching circuit is preferred. In the next section, this kind of matching circuit is used in the rectifier.

5.1.2. The rectifier for the Flower Pot

5.1.2.1. Simulation procedure

A system of four circular polarization patch antennas operating at 2.45 GHz is developed in Chapter 4 as the EM wave receiver of the RFEH circuit. The topology of one rectifier for one corresponding patch antenna and then a DC power collector at the end of the circuit is studied. The schematic of the circuit is illustrated in Fig. 5.5. The advantage of this topology is that each rectenna is able to work individually and separately without the concern of phase between the EM waves received by the antennas of the system, thus, a coupler is not necessary.

Cette thèse est accessible à l'adresse : https://theses.insa-lyon.fr/publication/2023ISAL0007/these.pdf
© [X.V.L. NGUYEN], [2023], INSA Lyon, tous droits réservés

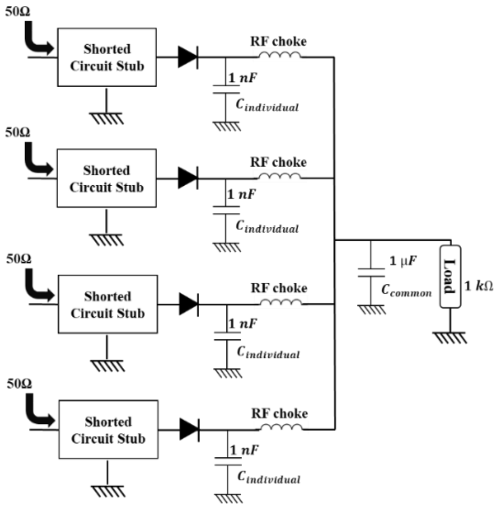

Figure 5.5: Schematic of the proposed rectifier for the Flower Pot

Each branch of the rectifier consists of a shorted circuit stub for the matching circuit and for the closed loop of the DC current in the circuit, a Schottky diode SMS7630-079LF from Skyworks Solutions Inc. as rectifying diode, an individual capacitor of 1 nF ($C_{indivual}$) used to store the rectified power at the diode cathode. In order to block any RF signals entering the Power Management Unit (PMU), a quasi RF attenuator, which is configured from a RF choke, is added in series after each individual capacitor. Furthermore, the ground plane of each branch of the rectifier is separated from each other in order to have the individuality and is connected to the DC ground plane via a thin and short line as shown in Fig. 5.13 to improve the capability of protecting the PMU from RF signals.

A study of the impacts of this configuration of blocking the RF signals is performed. Four testing samples are manufactured on Rogers 4003C with the deposited copper. These samples are shown in Fig 5.6.

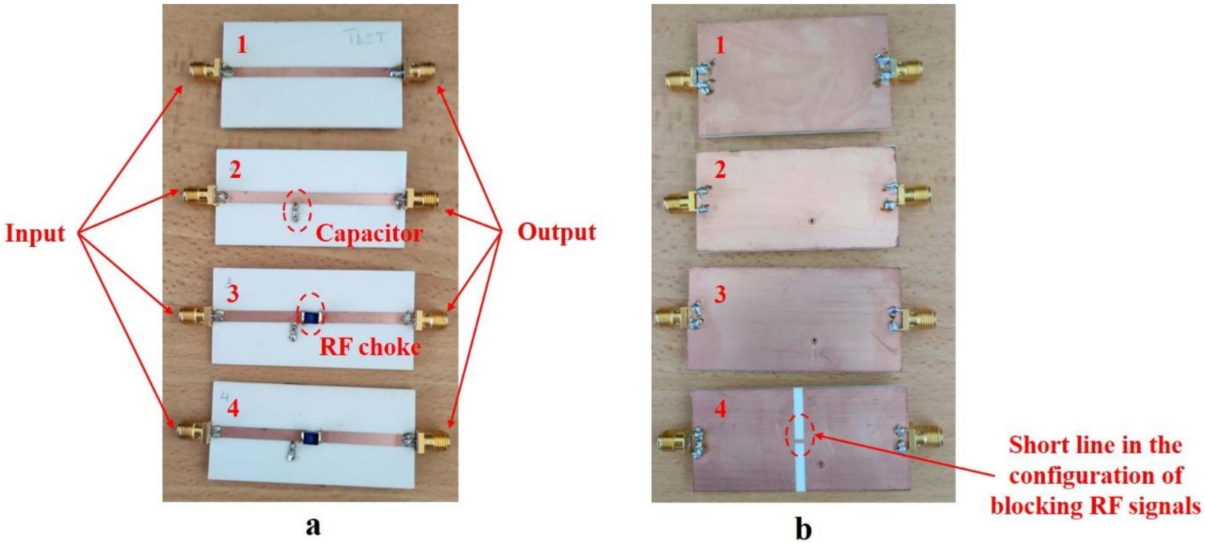

Figure 5.6: Samples for the RF choke tests

Cette thèse est accessible à l'adresse : https://theses.insa-lyon.fr/publication/2023ISAL0007/these.pdf
© [X.V.L. NGUYEN], [2023], INSA Lyon, tous droits réservés

The sample 1 is a 50 Ω transmission line with a length of 58 mm to ensure the wave propagation at the frequency of 2 GHz and higher. Here, the 50 Ω line is considered to avoid the impedance mismatch between the samples and the measurement setup.

The sample 2 is similar to the sample 1 except for the capacitor of 1 nF placed in the middle of the line. The value of this capacitor is identical to the individual capacitor of the four-branch rectifier.

In the sample 3, a RF choke of 1 mH from Coilcraft, which is characterized at 2.5 MHz, is added in the middle of the transmission line to block the RF signals. The difference between the sample 3 and the sample 4 is that the ground plane of the sample 4 is set up as shown in Fig. 5.7. Each large ground plane presents input and output ground planes of the line. A thin and short line is used to connect these two planes. The width and the length of this line are 1 mm and 0.8 mm, respectively. With these dimensions, the line can be assumed as an opened circuit in the RF bands, thus the RF signals will be blocked toward the input ground plane.

In order to verify the capability of blocking the RF signals of the samples, a manipulation using a RF generator CXG N5166B of Keysight and a Spectrum Analyzer CXA N9000B of Keysight is performed. The input of the samples is connected to the RF generator while their output is cabled to the Spectrum Analyzer. The Spectrum Analyzer will allow us to analyze the attenuation of the blocking configurations, which are a shunt 1 nF capacitor as sample 2, the shunt 1 nF capacitor with the RF choke of 1 mH as sample 3, and the shunt 1nF capacitor with the RF choke and a short thin line used for the ground planes connection as sample 4. It should be noticed that the higher attenuation is, the higher blocking RF signals capability is. The measurement setup is illustrated in Fig 5.7.

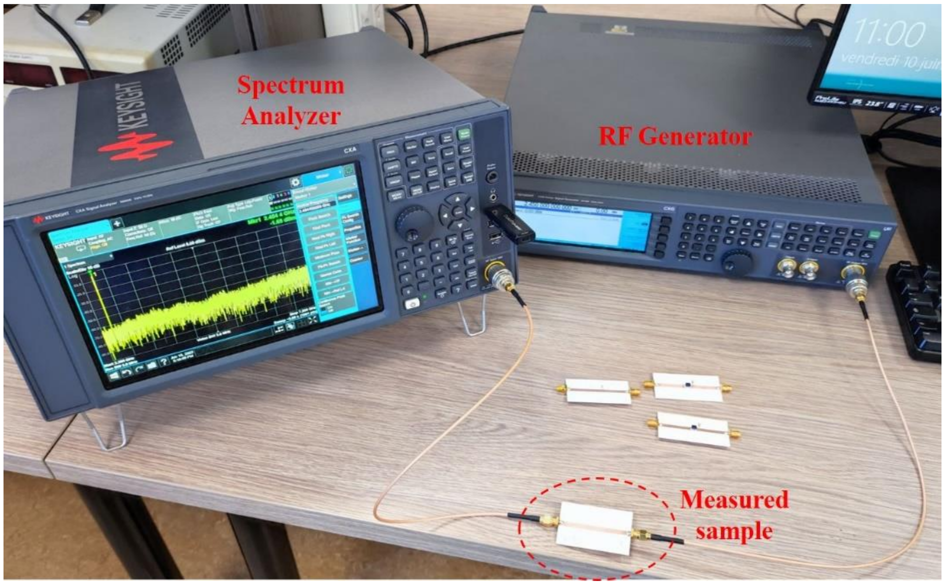

Figure 5.7: Measurement setup for the RF choke test

Since the operating frequency of the rectifier is at 2.45 GHz, the signal generated by the RF generator is also fixed at 2.45 GHz with a power level of 0 dBm. The measured spectrum at the output of each sample is plotted in Fig. 5.8.

Cette thèse est accessible à l'adresse : https://theses.insa-lyon.fr/publication/2023ISAL0007/these.pdf
© [X.V.L. NGUYEN], [2023], INSA Lyon, tous droits réservés

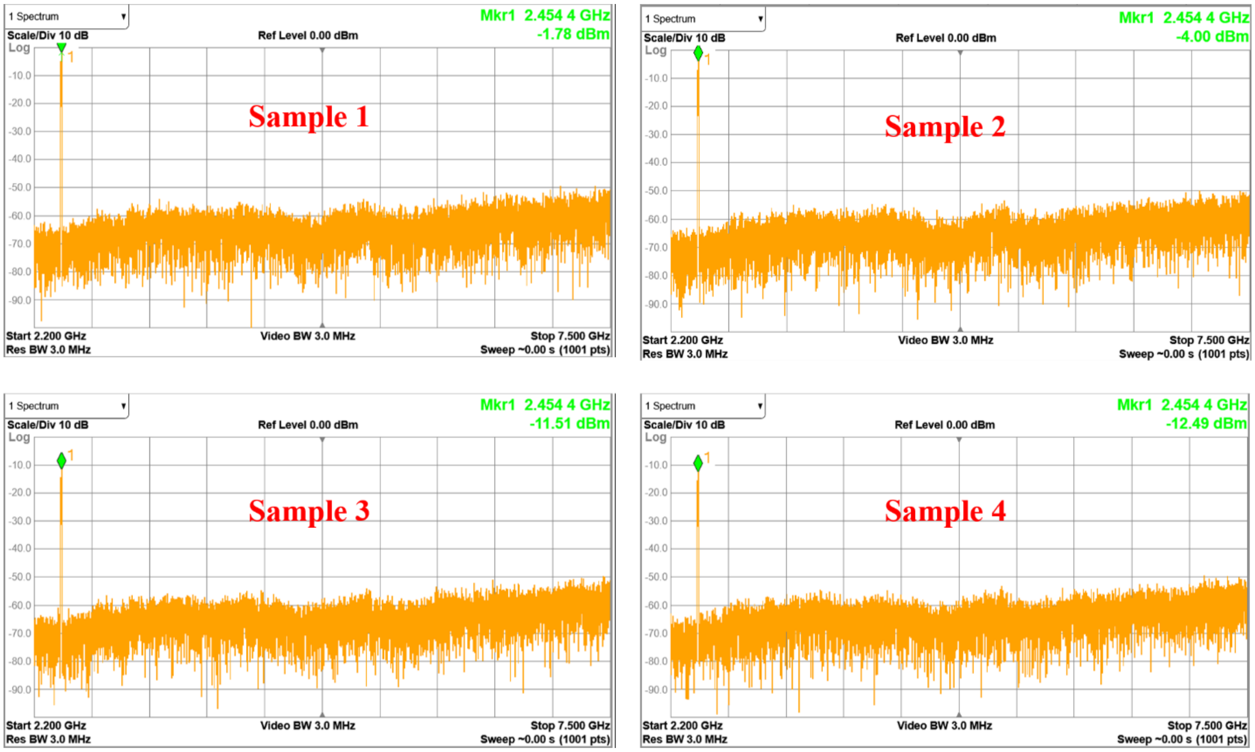

Figure 5.8: The measured spectrum at the output of different samples

The measured spectrum magnitude at the output of sample 1, 2, 3 and 4 are -1.78 dBm, -4 dBm, -11.51 dBm and -12.49 dBm, respectively. The spectra are decreased of 1.78 dBm because of the attenuation of the connecting cables at 2.45 GHz. Comparing the results, we may observe that using a solo capacitor can block only a part of RF signals (around 2.2 dBm). This cannot protect the PMU from the RF signals originated from the rectifier. By adding the RF choke, the attenuation is improved to 9.7 dBm and with the segregated ground plane configuration, this value reaches 10.7 dBm, which means that the magnitude of the RF signals is reduced up to 11.75 times. We can conclude that the RF signals are nearly blocked totally due to the implantation of the RF chokes and the segregated ground planes. Therefore, this configuration is applied in our design of four branches rectifier.

At the common output of the rectifier circuit, the common storage capacitor (C_{common}) is selected as 1 µF and the output load of the circuit is chosen as 1 kΩ as detailed in the next section of this chapter.

The capacitors used in the circuit are from Murata and the RF chokes are from Coilcraft. The ADS models of capacitors as well as the SPICE models with parasitic elements of the diode are used in the simulation. The model of vias calculated as Eq. (5.1) is also inserted in the simulation since the rivets are used to create the vias in the circuit.

The circuit is simulated and optimized at 2.45 GHz and -20 dBm as input with the aid of ADS and Co-Simulation ADS Momentum. The steps of simulating the circuit are listed as follows.

1) The set of diodes, individual capacitors, RF chokes, common capacitor, the load and the connecting microstrip lines between the components are drawn and simulated in Co-Simulation ADS Momentum at the defined frequency 2.45 GHz and input power of -20 dBm as in Fig. 5.9. According to the simulations, the simulated input impedance at the anode of the diode is

Cette thèse est accessible à l'adresse : https://theses.insa-lyon.fr/publication/2023ISAL0007/these.pdf
© [X.V.L. NGUYEN], [2023], INSA Lyon, tous droits réservés

(35.2 – j121.8) Ω. This value is collected using the tool "Zin" of ADS. This tool will calculate the input impedance of the circuit from its reflection coefficient (S_{11}).

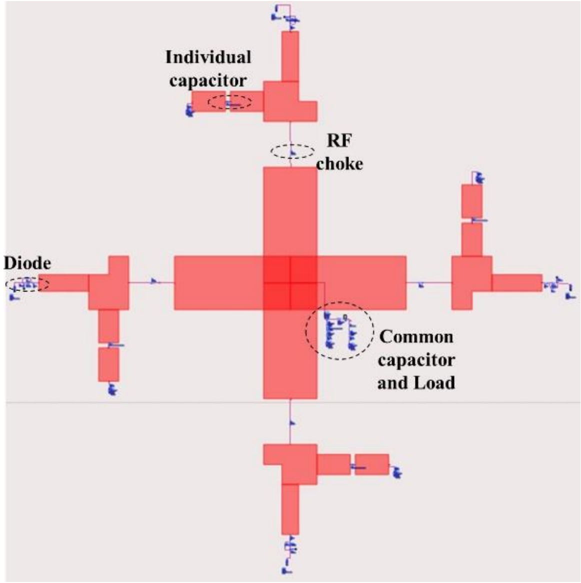

Figure 5.9: Schematic view with the model of Momentum of the common part of the rectifier

2) Afterwards, a short-circuit stub is added at the anode of the diode to perform the 50 Ω impedance matching in the schematic view of ADS as shown in Fig. 5.10. As stated previously, the shorted circuit stub is proposed in order to ensure the closed loop of the DC current in the rectifier. The dimensions of the stub are then optimized using ADS.

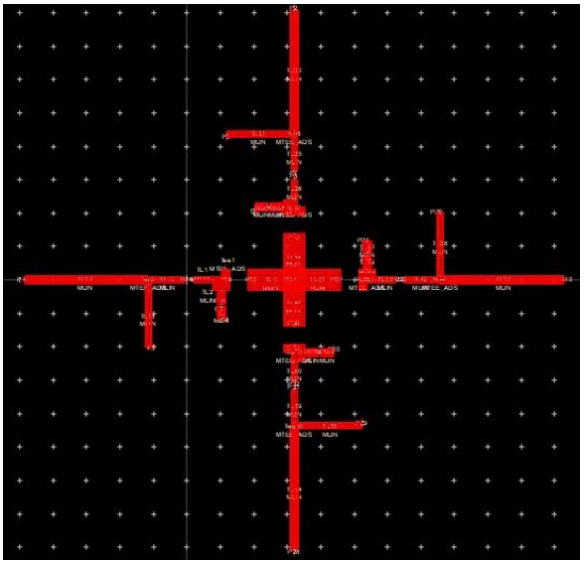

Figure 5.10: The rectifier in Momentum view of ADS

3) The stubs are then considered in Co-Simulation ADS Momentum of the previous set of the rectifier. The dimensions of the stubs are then tuned to obtain a satisfying impedance matching. When the final dimensions are found, another run in Momentum is required to validate if the circuit is matched at the desired point. When the circuit is validated, the final circuit is obtained as Fig. 5.11.

Cette thèse est accessible à l'adresse : https://theses.insa-lyon.fr/publication/2023ISAL0007/these.pdf
© [X.V.L. NGUYEN], [2023], INSA Lyon, tous droits réservés

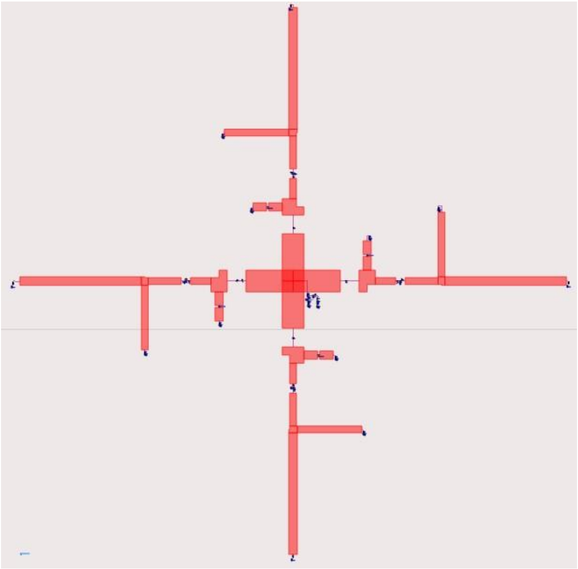

Figure 5.11: Schematic view with the model of Momentum of the rectifier

The rectifier is then manufactured on a SLA substrate of HT Resin v2. The schematic and the realized rectifier circuit are figured in Fig. 5.12. The radius of the substrate is set as 40 mm, which is identical to the radius of the Flower Pot, in order to simplify the connection between the antenna and the rectifier of the final demonstrator.

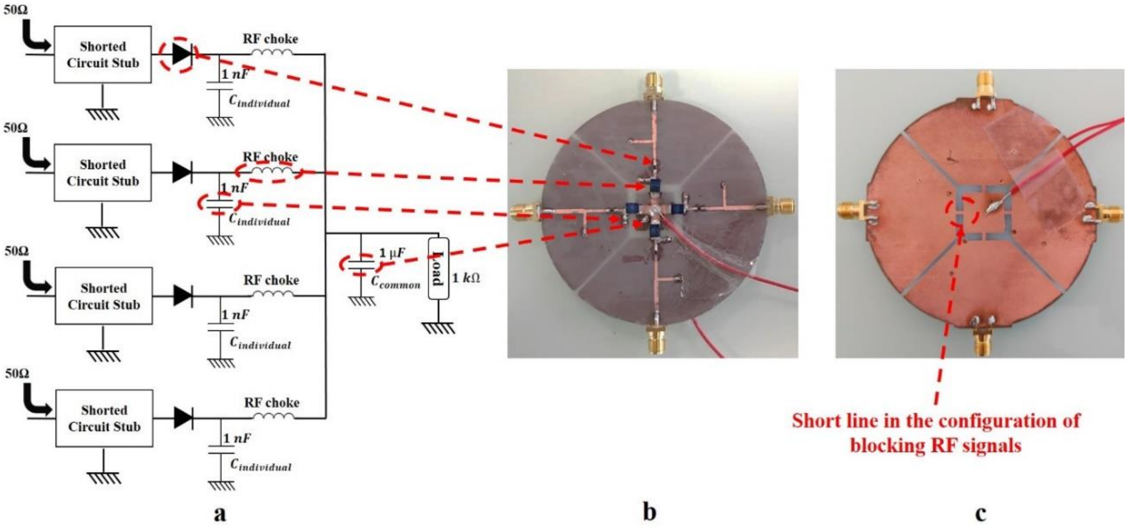

Figure 5.12: The rectifier for Flower Pot (a. Schematic; b. Manufactured circuit – Upper view; c. Manufactured circuit – Bottom view)

5.1.2.2. S-parameters measurements

Firstly, the reflection coefficient of one input of the circuit is measured using a calibrated VNA with different power levels, which are -30 dBm, -20 dBm, -10 dBm and 0 dBm at 2.45 GHz and an output load of 1 kΩ.

Cette thèse est accessible à l'adresse : https://theses.insa-lyon.fr/publication/2023ISAL0007/these.pdf
© [X.V.L. NGUYEN], [2023], INSA Lyon, tous droits réservés

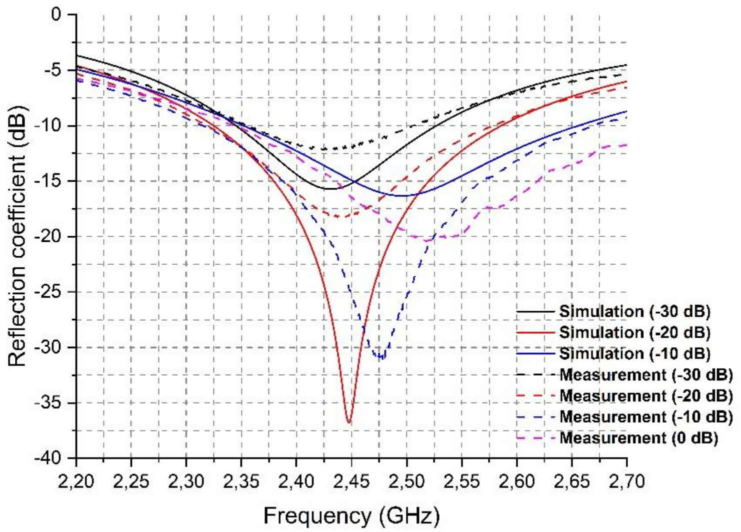

Figure 5.13: Simulated and measured reflection coefficient at different input power of the rectifier

Fig. 5.13 shows the reflection coefficient of the rectifier at different values of input power. According to the measurements, the rectifier has a satisfying impedance matching over a wide band of frequency which covers the band of Wi-Fi 2.45 GHz. The simulated and measured resonant frequencies of the rectifier are nearly similar. The same observation is obtained with the bandwidth of the rectifier at the different values of input power. The discrepancy of the value of the reflection coefficient between simulation and measurement may come from the variation of the parasitic elements in the package of the diode. Otherwise, when the input power of the rectifier increases, the operating point of the diode in the non-linear I-V curve changes what leads to the up-shifting of the resonant frequency of the circuit [95].

The output load of the rectifier is a Power Management Unit (PMU) with discrete components. The impedance of this PMU varies as its different phases of operation. Thus, a study of impedance matching behavior of the rectifier with different values of load is necessary in order to assure the good operation of the RFEH. The study is performed at -30 dBm, -20 dBm, -10 dBm and 0 dBm with the loads of 0.5 kΩ, 1 kΩ, 4 kΩ, 7 kΩ and 10 kΩ. The measured results are plotted in Fig. 5.14, Fig. 5.15, Fig. 5.16 and Fig. 5.17 respectively.

Cette thèse est accessible à l'adresse : https://theses.insa-lyon.fr/publication/2023ISAL0007/these.pdf
© [X.V.L. NGUYEN], [2023], INSA Lyon, tous droits réservés

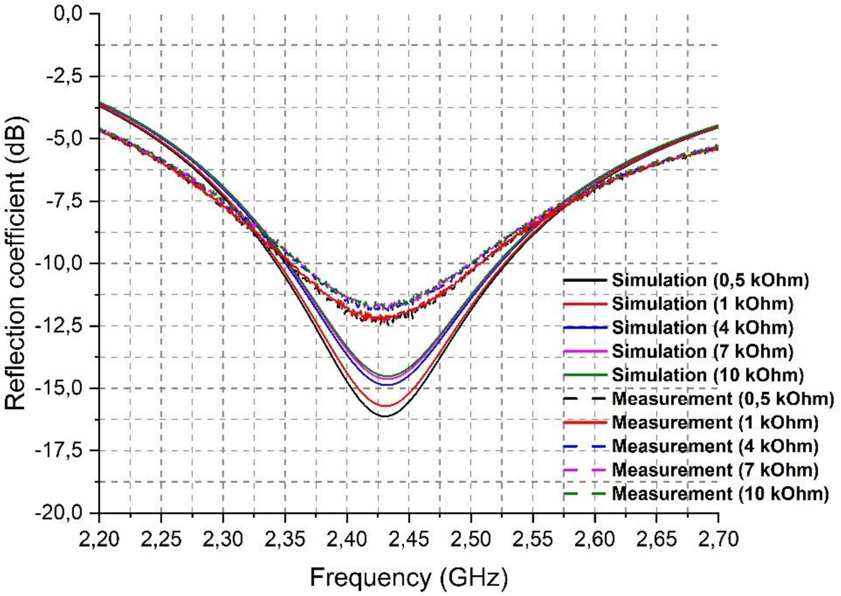

Figure 5.14: Simulated and measured reflection coefficients of the rectifier at -30 dBm under different load values

At -30 dBm, the circuit always has a satisfying impedance matching over a band of 2.35-2.53 GHz and the resonant frequencies of the rectifier stay identical when the load varies. The phenomenon of shifting the resonant frequencies does not occur here since the input power of the circuit is very low, thus, the displacement of the operating point of the diode is small and negligible. When the input power is higher, the phenomenon of frequency shifting can be observed more clearly.

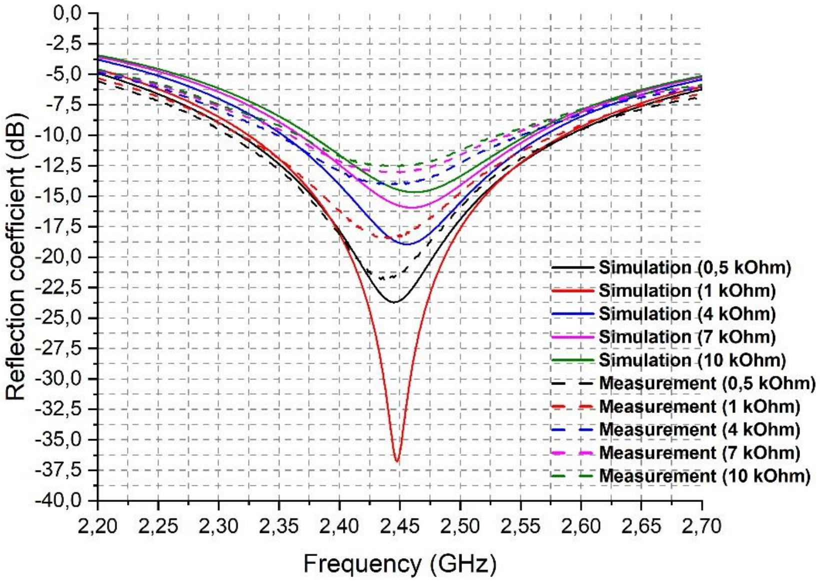

Figure 5.15: Simulated and measured reflection coefficients of the rectifier at -20 dBm under different load values

At -20 dBm, the circuit is always matched to 50 Ω for a band of 2.35-2.55 GHz. At this level of input power, the shifting of the resonant frequencies can be observed in the simulation. However, according to the measurements, it is hard to deduce this phenomenon. The discrepancy may come from the non-ideality of the diode mounted on the circuit.

Cette thèse est accessible à l'adresse : https://theses.insa-lyon.fr/publication/2023ISAL0007/these.pdf
© [X.V.L. NGUYEN], [2023], INSA Lyon, tous droits réservés

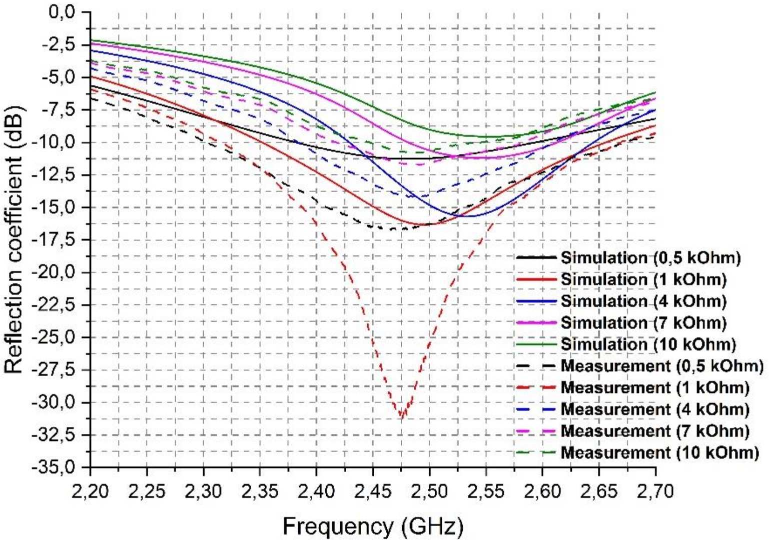

Figure 5.16: Simulated and measured reflection coefficients of the rectifier at -10 dBm under different load values

The input power of the rectifier is increased to -10 dBm. The rectifier is matched at 2.45 GHz at the load of 0.5 kΩ, 1 kΩ and 4 kΩ respectively. Nonetheless, the circuit is not matched to 50 Ω at 7 kΩ and 10 kΩ at 2.45 GHz. At these values of load, the resonant frequencies of the circuit are shifted to the right and quite far from 2.45 GHz, which are 2.55 GHz. This can be explained as with the higher input power, the displacement of operating point of the diode in I-V curve happens more clearly, the frequency shifting is higher. Moreover, the impedance matching bandwidth at 7 kΩ and 10 kΩ are not broad enough to cover the frequency of 2.45 GHz. The discrepancy between simulation and measurement may come from the parasitic elements of the package and the model of the diode used in the simulation. At this high input power level, the shifting of resonant frequencies can be observed since the operating point of the diode displaces more effectively.

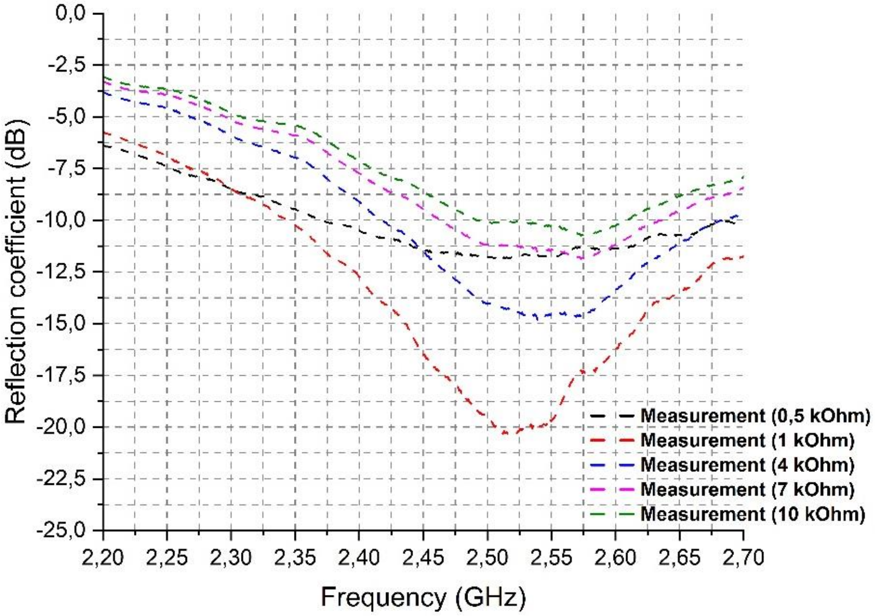

Figure 5.17: Simulated and measured reflection coefficients of the rectifier at 0 dBm under different load values

At this input power level, the SPICE model of the diode cannot give good results as the models are identified for small-signal simulation meanwhile 0 dBm is considered as a large signal. Therefore,

Cette thèse est accessible à l'adresse : https://theses.insa-lyon.fr/publication/2023ISAL0007/these.pdf
© [X.V.L. NGUYEN], [2023], INSA Lyon, tous droits réservés

to achieve good results, a large signal model of diode should be studied. The circuit is matched at 2.45 GHz with the load of 0.5 kΩ, 1 kΩ and 4 kΩ according to the measurements.

5.1.2.3. Rectified voltage and conversion efficiency

The measurement of rectified voltage is performed at 2.45 GHz under -20 dBm, -10 dBm and 0 dBm input power levels respectively. Three different cases are studied: one port, two ports and four ports are fed simultaneously with the same power levels of -20 dBm, -10 dBm and 0 dBm. The conversion efficiency of the circuit is then calculated as

$$\eta_{RF-DC} = \frac{V_{out}^2}{R_L \times \sum P_{RF}} \qquad (5.6)$$

The measurement results are plotted in Fig. 5.18, Fig. 5.19 and Fig. 5.20 respectively. The discrepancy between simulation and the measurement comes from the difference in matching condition of the rectifier. As presented previously, at -20 dBm and above, we notice that the difference increases when the load increases. Therefore, from 2 kΩ and higher, this discrepancy appears. To better understand this discrepancy, modeling the diode process is necessary. Because of the time constraint, this process is not covered in this thesis.

According to the simulated and measured results, we can observe that when the number of supplied ports increases, the rectified voltage also increases. Regarding the conversion efficiency, at -20 dBm, the maximum value is obtained when the load is near 1 kΩ. This can be explained as the rectifier is optimized for this value of the input power and the load. Otherwise, at -10 dBm, we have a shifting of the point of maximum conversion efficiency of the rectifier. With one port fed, this value is around 1 kΩ meanwhile with two or four ports fed, the value of the optimal load decreases, around 0.5 kΩ. At 0 dBm, we have the same phenomenon as the input power of -10 dBm.

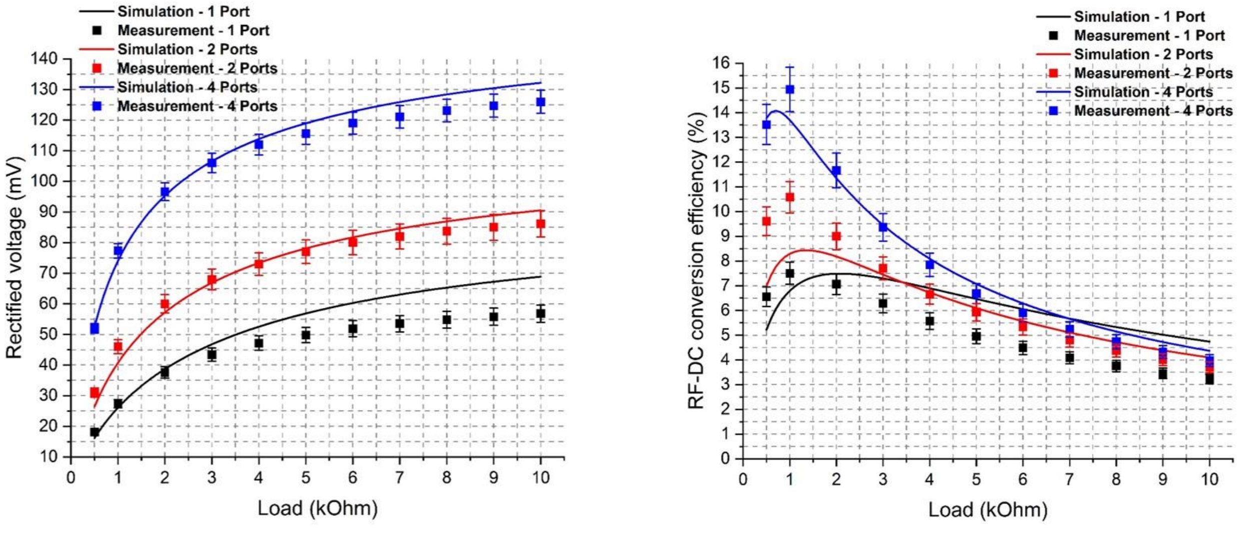

a **b**

Figure 5.18: Simulated and measured (a. Rectified voltage, b. Conversion efficiency) of the rectifier at -20 dBm under different load values and with different number of input ports.

Cette thèse est accessible à l'adresse : https://theses.insa-lyon.fr/publication/2023ISAL0007/these.pdf
© [X.V.L. NGUYEN], [2023], INSA Lyon, tous droits réservés

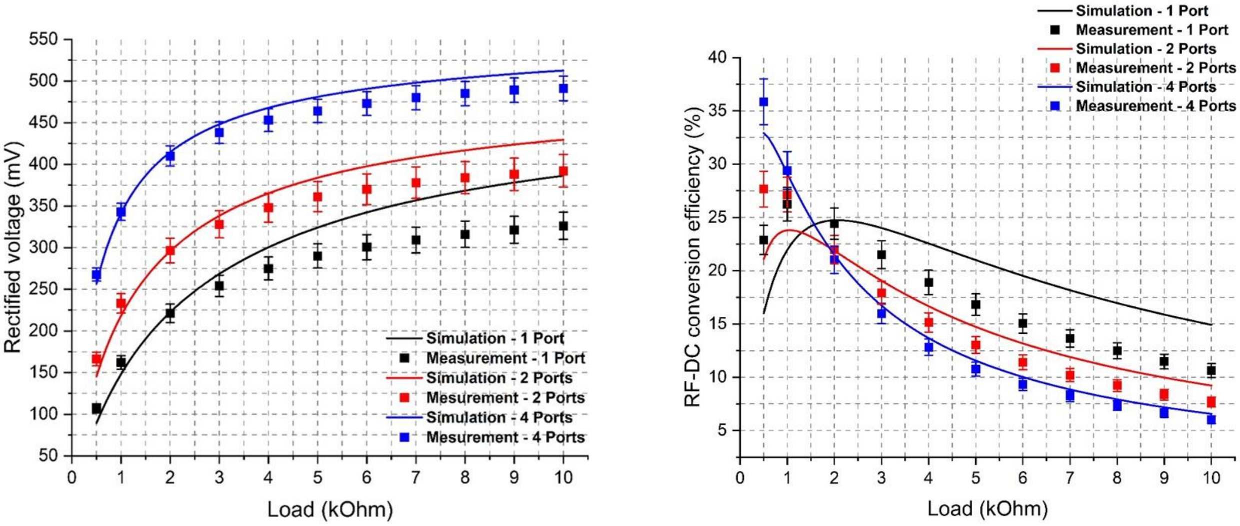

a b

Figure 5.19: Simulated and measured (a. Rectified voltage, b. Conversion efficiency) of the rectifier at -10 dBm under different load values and with different number of input ports.

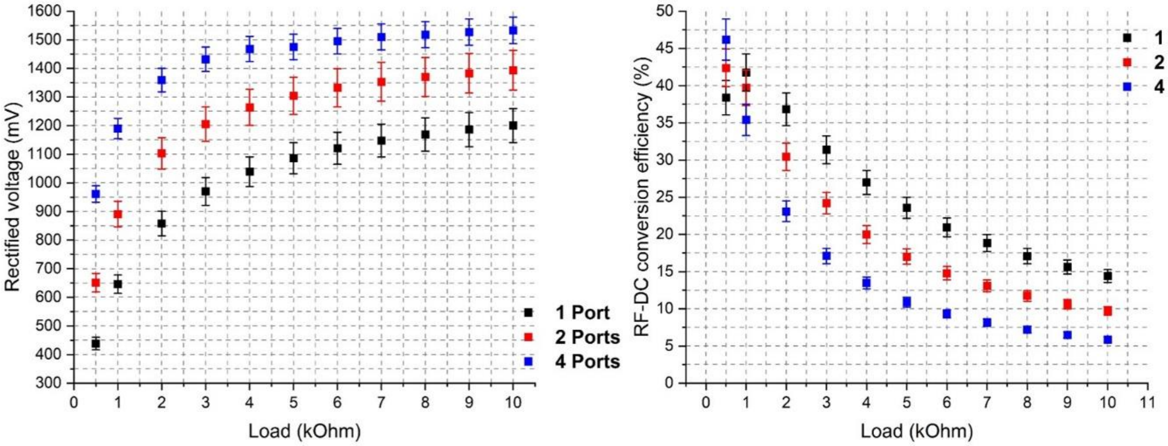

a b

Figure 5.20: Simulated and measured (a. Rectified voltage, b. Conversion efficiency) of the rectifier at 0 dBm under different load values and with different number of input ports.

5.1.2.4. Comparison and Conclusion

A comparison between our work and the state-of-art is presented in Table 5.3 with respect to manufacturing technique, substrate, topology of the rectifier, rectifying diode, output load, rectified voltage, conversion efficiency and footprint of the circuit. To have a fair comparison between the works, the selected band of frequency is nearly identical to 2.45 GHz.

Comparing our results to the work of [156], which has the same series topology of the rectifier and rectifying diode and the output load are closely equal, the output voltages are quite similar in both cases: one and four fed ports of the rectifier. The slight difference between these results may come from the higher value of load in [156] and the lower loss substrate and conductor. In addition, at three different input power levels of our rectified voltages are comparable to the work presented in

Cette thèse est accessible à l'adresse : https://theses.insa-lyon.fr/publication/2023ISAL0007/these.pdf
© [X.V.L. NGUYEN], [2023], INSA Lyon, tous droits réservés

[108]. Since the topology of the voltage doubler and the higher load are used in [108], the output voltage is consequently higher.

Concerning the conversion efficiency, our circuit gives also a comparable value as in other works, especially for input power of -20 dBm and -10 dBm. However, at 0 dBm, our circuit has a lower conversion efficiency than the value given in [76] and [77]. This can be explained as the authors use specific substrates for RF applications. Additionally, the topology of the rectifier plays an important role to enhance the conversion efficiency at this value of power.

Our rectifier is larger than the other circuits. In fact, the dimensions of our circuit can be reduced by using the meander line technique for the microstrip lines. The idea of setting these dimensions up for our circuit to fit the concept of the designed antennas.

Cette thèse est accessible à l'adresse : https://theses.insa-lyon.fr/publication/2023ISAL0007/these.pdf
© [X.V.L. NGUYEN], [2023], INSA Lyon, tous droits réservés

Table 5.3: Comparison to State-of-Art

Ref.	Freq. (GHz)	Fabrication technique/Substrate	Topology/Diode/Load	Rectified voltage	Conversion efficiency	Dimensions
[76]	2.45	Conventional technique/FR-4	Voltage doubler/SMS7630/ 14.7 kΩ	NI	-20 dBm – 13% -10 dBm – 40% 0 dBm – 58%	32 x 32 x 1.575
[80]	2.45	Conventional technique/FR-4	2 stages of Dickson /SMS7630-079LF/ Open circuit	-20 dBm – 0.25 V -10 dBm – 2 V	NI	Ni
[156]	2.45	Conventional technique/Rogers 4003C	Series/SMS7630/ 1.8 kΩ	***1 port of rectifier*** -20 dBm – 0.046 V	NI	NI
				4 ports of rectifier -20 dBm – 0.12 V		
[104]	2.3	Conventional technique/Rogers 4003C	Voltage doubler/ HSMS-285/2 kΩ	***1 port of rectifier*** -20 dBm – 0.032 V -10 dBm – 0.2 V 0 dBm – 0.85 V	NI	NI
				2 ports of rectifier -20 dBm – 0.055 V -10 dBm – 0.3 V 0 dBm – 1.2 V		
[77]	2.4	Flexible substrate using inkjet printing and masking technique followed by etching/Liquid crystal polymer (LCP)	Shunt/SMS7630/ 1 kΩ	NI	-20 dBm - 10% -10 dBm - 25% 0 dBm - 40%	11.5 x 25 x 0.18
		Conventional technique/Rogers 3203		NI	-20 dBm - 17% -10 dBm - 40% 0 dBm - 58%	32.21 x 17.54 x 0.508
[155]	2.6	Paper substrate using the adhesive copper laminate technology/Photopaper Model CK-D715	Series/HSMS2850/ 3 kΩ	NI	-20 dBm - 6% -10 dBm - 21% 0 dBm - 26%	35 x 30 x 0.37

NI: Not Indicated in the article
The dimensions of circuits are in mm

Cette thèse est accessible à l'adresse : https://theses.insa-lyon.fr/publication/2023ISAL0007/these.pdf
© [X.V.L. NGUYEN], [2023], INSA Lyon, tous droits réservés

Table 5.3: continue

Ref.	**Freq. (GHz)**	**Fabrication technique/Substrate**	**Topology/Diode/Load**	**Rectified voltage**	**Conversion efficiency**	**Dimensions**
[108]	2.1	3D printed substrate and screen printing of the layout/Vero (0.02)	Series/SMS7630/ 11 kΩ	NI	-20 dBm - 7% -10 dBm - 18%	50 x 50
This work	2.45	Rapid Plastronics/SLA HT Resin v2	Series/SMS7630-079LF/1 kΩ	***1 port of rectifier*** -20 dBm – 0.027 V -10 dBm – 0.162 V 0 dBm – 0.646 V	***1 port of rectifier*** -20 dBm – 7.3 % -10 dBm – 26.2 % 0 dBm – 41.7 %	80 x 80 x 1.5
				2 ports of rectifier -20 dBm – 0.046 V -10 dBm – 0.233 V 0 dBm – 0.891 V	***2 ports of rectifier*** -20 dBm – 10.7 % -10 dBm – 27.2 % 0 dBm – 39.8 %	
				4 ports of rectifier -20 dBm – 0.077 V -10 dBm – 0.343 V 0 dBm – 1.19 V	***4 ports of rectifier*** -20 dBm – 14.9 % -10 dBm – 29.6 % 0 dBm – 35.6 %	

NI: Not Indicated in the article
The dimensions of circuits are in mm

Cette thèse est accessible à l'adresse : https://theses.insa-lyon.fr/publication/2023ISAL0007/these.pdf
© [X.V.L. NGUYEN], [2023], INSA Lyon, tous droits réservés

5.2. Discrete Power Management Unit

The operation of the DC/DC converter demands generally an oscillating signal for the transition state of MOSFET in the circuit. However, the switching frequencies are usually provided by an external oscillator requiring an external source, i.e. batteries, etc. for supply. The purpose of not using the batteries for the IoT devices is not ensured. Therefore, self-operating or self-autonomous Power Management Unit becomes a favor in the concept of RFEH of energy harvesting applications.

In this section, the proposed PMU will be introduced. The function of each block as well of the whole circuit will be presented. The PMU is assembled using discrete components to verify the operation of the circuit. The list of these components will be also mentioned to clarify our choice.

5.2.1. Functional blocks of the PMU

The PMU consists of an Armstrong converter acting as the starter of the whole circuit, a flyback converter performing the voltage-amplification capability, and two Under-Voltage-Lock-Out circuits managing the different operation phases of the PMU with respect to the load.

5.2.1.1. Under-Voltage-Lock-Out (UVLO)

This circuit is used to turn on and/or turn off the electronic devices in the event of the input voltage reaching above or dropping below the defined operational values. Our proposed UVLO shown in Fig. 5.21 has two different operational states: *closed* and *opened*. These states are controlled by the transistors PMOS, NMOS #1 and NMOS #2 and the value of R_1, R_2, R_3, R_4, and R_p. R_p is used to control the grille-source voltage (V_{gsP}) of the transistor PMOS. The value of R_1 and R_2 are set to configure the high-level threshold voltage of closed state (V_{high}) while R_3 and R_4 identify the low-level threshold voltage of opened state of the UVLO (V_{low}).

$$V_{high} = \left(\frac{R_1}{R_2} + 1\right) V_{gs1\ typ} \tag{5.7}$$

$$V_{low} = \left(\frac{R_3}{R_4} + 1\right) V_{gs2\ typ} \tag{5.8}$$

Where, $V_{gs1\ typ}$ and $V_{gs2\ typ}$ are the typical grille-source voltage of the transistor NMOS #1 and NMOS #2.

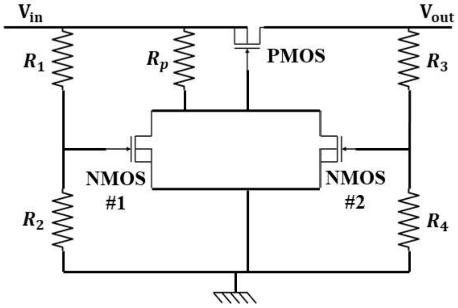

Figure 5.21: Schematic of an Under Voltage Lock Out circuit

When the input voltage V_{in} of the UVLO is lower than V_{high}, the grille-source voltage of the NMOS #1 (V_{gs1}) is consequently lower than $V_{gs1\ typ}$, the transistor NMOS #1 is opened. In this case, V_{gsP} is zero and the PMOS is opened. The UVLO is assumed as opened circuit, the connection between the electrical source at the input and the consumption load at the output is not yet established. When V_{in} is higher than V_{high}, the transistor NMOS #1 is closed and links the grille of PMOS to the ground. The grille-source voltage of PMOS is now equal to -V_{in}. The PMOS is closed,

Cette thèse est accessible à l'adresse : https://theses.insa-lyon.fr/publication/2023ISAL0007/these.pdf
© [X.V.L. NGUYEN], [2023], INSA Lyon, tous droits réservés

the UVLO is then in *closed* stated. In this state, the circuit can be assumed as a shorted circuit, the electrical source at the input is connected to the consumption load at the output. The circuit will stay in *closed* state as long as V_{in} is higher than V_{low}. It should be noticed that in the *closed* state, the transistor NMOS #2 is also closed.

When V_{in} drops lower than V_{high} but still higher than V_{low}, the transistor NMOS #1 is opened, but the transistor NMOS #2 is still closed that maintains the *closed* state of the UVLO. When V_{in} is lower than V_{low}, the transistor NMOS #2 is opened, the grille of PMOS is no longer linked to the ground, PMOS is consequently opened, the connection between the electrical source at the input and the consumption load at the output is interrupted. The UVLO is in the *opened* state.

The simulated example of the circuit is plotted in Fig. 5.22.

Figure 5.22: Simulated waveform results of Under-Voltage-Lock-Out

As shown in Fig. 5.22, our circuit has three distinct zones, which are zone 1, zone 2 and zone 3.

In the zone 1, when the input voltage V_{in} increases, the transistor NMOS #1 start to be closed. A slight voltage is obtained at the output of the UVLO. This phenomenon comes from the non-ideal grille-source behavior of the transistor NMOS #1. When V_{in} reaches to V_{high}, a drop of the output voltage occurs, which comes from the effect the drain-source voltage of the transistor PMOS.

In the zone 2, the UVLO is fully in the *closed* state. The output voltage is identical to the input voltage.

In the zone 3, the input voltage decreases lower than V_{low}, the UVLO is in the *opened* state. The output voltage does not drop immediately because of the behavior of the grille-source voltage of the NMOS #2.

5.2.1.2. Armstrong converter

Armstrong Oscillator (AO), invented by Edwin Armstrong in 1913 [94], is a harmonic oscillator which generates a high oscillation level from a low supply voltage. The generated signal is in range of Ultra High Frequency (UHF), thus, this circuit is applied previously in the RF receptor. However, because of the non-linearity of the transistor, the parasitic effects of the transistor and the transformers, nowadays, this circuit is seldom used in RF applications.

Cette thèse est accessible à l'adresse : https://theses.insa-lyon.fr/publication/2023ISAL0007/these.pdf
© [X.V.L. NGUYEN], [2023], INSA Lyon, tous droits réservés

Literally, the AO circuit can be used in power electronics applications. Due to the high amplification ratio of the transformer, this circuit is able to obtain an oscillation signal with high amplitude from its low input voltage. By adding a rectifier at the output of the AO circuit, we can get a DC output voltage being higher than the input voltage.

This circuit is classified as a resonant converter. Its principle is illustrated in Fig. 5.23 and the simulated result is presented in Fig. 5.24.

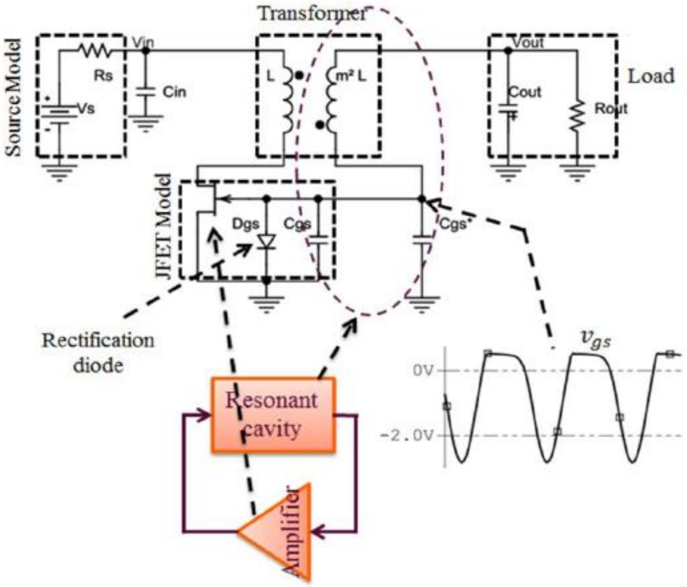

Figure 5.23: Schematic of the Armstrong converter extracted from [94]

The circuit has two fundamental elements: a high ratio transformer and a Normally-On JFET. The oscillator of the converter is generated due to the resonant circuit LC formed from the secondary inductor of the transformer and the gate-source capacitor (C_{gs}) of the Junction Field-Effect Transistor (JFET). The resonant frequency (f_r) of this LC circuit is expressed as

$$f_r = 1/(2\pi m\sqrt{LC}) \tag{5.9}$$

where m is the turn ratio between the secondary and primary inductors of the transformer (unitless), L is the inductor of the primary inductor of the transformer (H), C is the gate-source capacitor of the JFET (F).

Additionally, the JFET plays also a role of an amplifier with a negative gain. The intrinsic diode D_{gs} of the JFET enables to rectify the signal to obtain a DC voltage at the output of the converter as shown in Fig. 5.24. The further details about this circuit is explained in [94].

Cette thèse est accessible à l'adresse : https://theses.insa-lyon.fr/publication/2023ISAL0007/these.pdf
© [X.V.L. NGUYEN], [2023], INSA Lyon, tous droits réservés

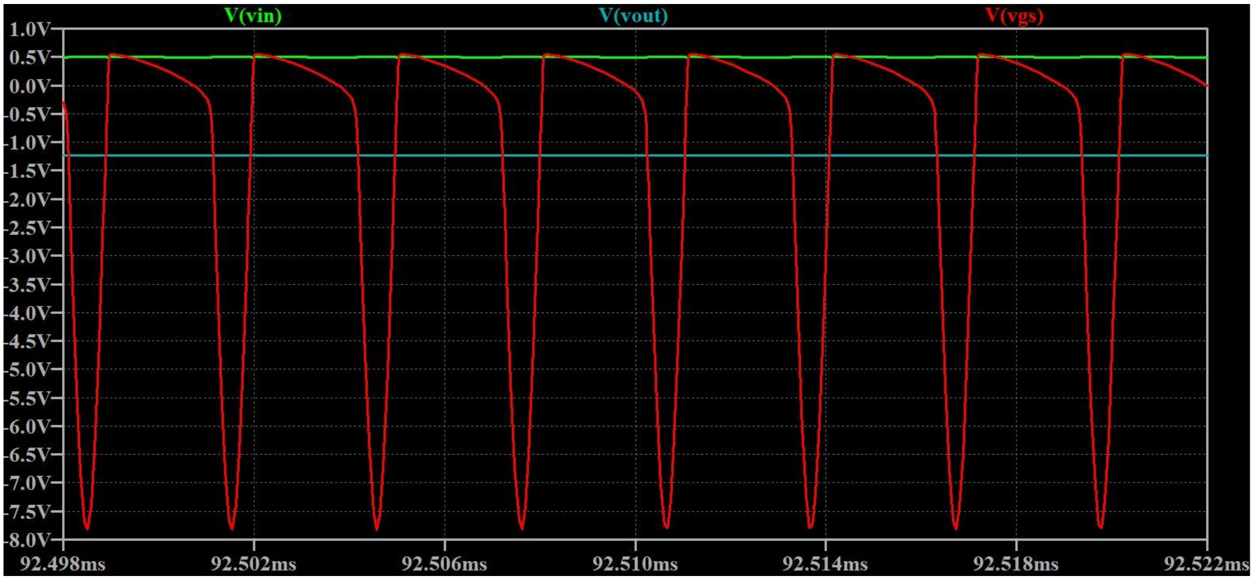

Figure 5.24: Simulated waveform results of two coils configuration Armstrong converter

The advantage of an Armstrong converter is its capability of self-autonomous. The circuit can generate the oscillating signal by itself, thus, an external source of the oscillating signal is not demanded in the circuit.

Nevertheless, with Armstrong converter, the function of impedance matching between the converter and the rectifier is not introduced in order to maximize the power transferred from to the rectifier to the converter [94]. Moreover, another drawback of this circuit is that the efficiency of the circuit tends to degrade when the sensitivity to the input voltage is increased [94].

As shown in Fig. 5.23, a two-coil transformer is used in the converter. However, the drawback of this configuration is that the output voltage has the opposite sign of the input voltage as shown in Fig. 5.24. Therefore, the configuration of three-coil transformer is proposed to solve this drawback. With this configuration, the output voltage presents the same sign as the input voltage of the converter. Fig. 5.25 illustrates the concept of the three coils transformer configuration of the Armstrong converter. The principle of this configuration is similar to the two-coil transformer configuration. The coil L_g is used for auto-oscillating function meanwhile that the third coil of transformer L_r is used to inverse the sign of the amplified voltage as shown in Fig. 5.26. A rectifying diode is added at the output of the third coil to smooth the output voltage.

Cette thèse est accessible à l'adresse : https://theses.insa-lyon.fr/publication/2023ISAL0007/these.pdf
© [X.V.L. NGUYEN], [2023], INSA Lyon, tous droits réservés

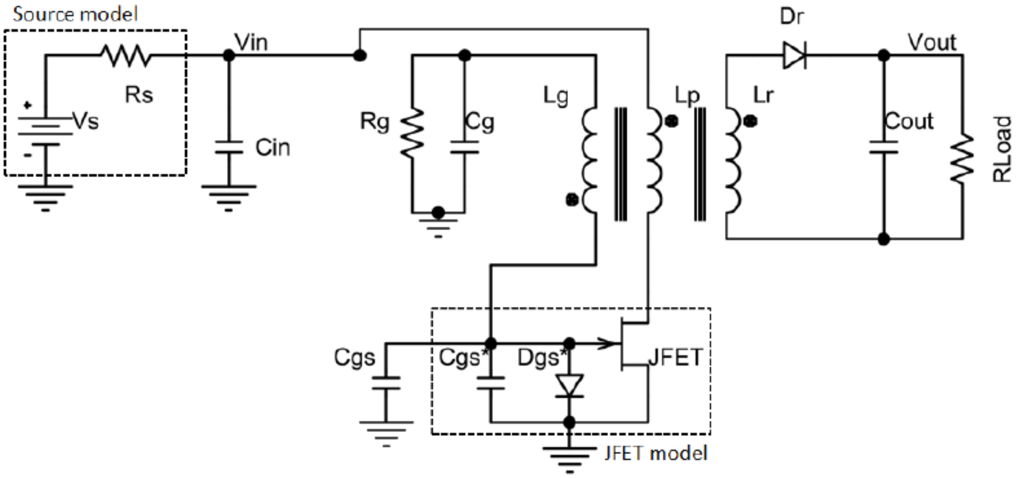

Figure 5.25: Three-coil transformer configuration of the Armstrong converter [94]

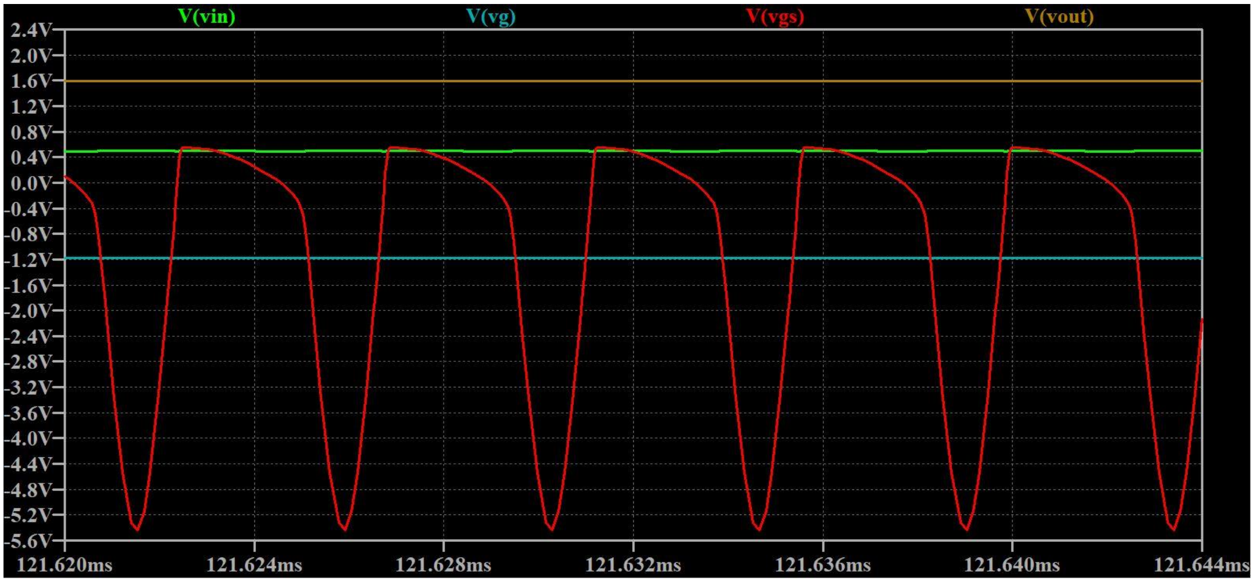

Figure 5.26: Simulated waveform results of three-coil configuration Armstrong converter

For our thesis, the configuration of three-coil transformer is selected since a positive output voltage is required in the circuit.

5.2.1.3. Flyback converter

The structure of the flyback converter is quite similar to Buck-Boost's structure. The difference between two circuits is the amplification part in the circuit, only one inductor for Buck-Boost and coupled inductor for the flyback. In this thesis, the flyback converter is preferred since the gate-source voltage of the Metal-Oxide-Semiconductor Field-Effect (MOSFET) transistor used in the circuit is referenced to ground, the control voltage originated from the control circuit will be independent of the input voltage of the converter.

Cette thèse est accessible à l'adresse : https://theses.insa-lyon.fr/publication/2023ISAL0007/these.pdf
© [X.V.L. NGUYEN], [2023], INSA Lyon, tous droits réservés

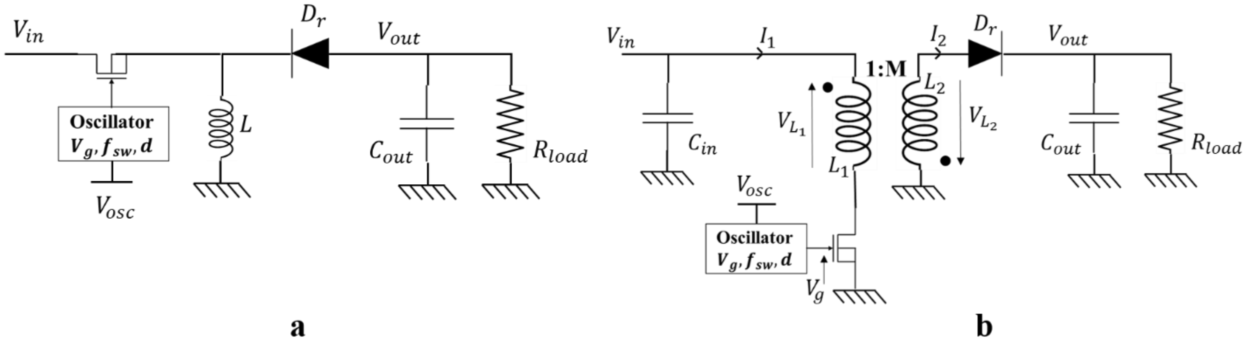

Figure 5.27: Schematic of the Buck-Boost converter (a) and the flyback converter (b)

The flyback circuit has two different modes of operation: the Continuous-Conduction Mode (CCM) and the Discontinuous-Conduction Mode (DCM).

In the CCM mode, the input impedance (R_{in}) of the circuit is given as [94]

$$R_{in} = \frac{2Lf}{d}\left(\frac{M+1}{M}\right) \tag{5.10}$$

where L is the inductor of the converter (H), f is switching frequency of the converter (Hz), d is duty cycle of the oscillating signal (unitless) and M is the effective amplification ratio of the converter (unitless).

In CCM, the parameter “M” of the converter is largely varying. Accordingly, this requires a variation of the switching frequency in order to maintain the value of R_{in}, thus, a circuit controlling the frequency in closed loop is needed. However, this configuration may increase the consumption in the circuit [94].

Meanwhile, in the DCM mode, the converter effective input impedance becomes [94], [157]

$$R_{in} = 2Lf/d^2 \tag{5.11}$$

The input impedance of the converter in this mode is no longer depending on the parameter “M” as previously. The frequency can be fixed initially to achieve the desired value of the input impedance without using a closed loop as in CCM mode. This can help us simplify the configuration and reduce the consumption of the oscillator circuit of the flyback converter, which generates the switching frequency of the converter, comparing to the CCM mode [94].

For our circuit, the DCM mode of the flyback converter is selected consequently. The principle of this converter is described in [157]. Fig. 5.28 presents the typical waveforms of the flyback converter in DCM mode. V_{in} and V_{out} are considered to be stable. The voltage applied to the grille of the MOSFET transistor is in rectangular form with a switching period of T_{sw} and duty cycle of D, and varies from zero to V_{G_ON}.

$$T_{sw} = 1/f_{sw} \tag{5.12}$$

<u>Phase 1</u> $\forall t \in [0; DT_{sw}]$

When the positive voltage V_{G_ON} is applied to the grille of the NMOS transistor, the transistor is closed and the current will pass into the primary inductor. If we neglect the static drain-source on-resistance R_{DS_ON} of the transistor, V_{L1} equates to V_{IN} and the current I_1 increases linearly (Eq. 5.13) up to the maximum value (Eq. 5.14)

Cette thèse est accessible à l'adresse : https://theses.insa-lyon.fr/publication/2023ISAL0007/these.pdf
© [X.V.L. NGUYEN], [2023], INSA Lyon, tous droits réservés

$$I_1(t) = \frac{V_{IN}}{L_1} t \tag{5.13}$$

$$I_{1\_MAX} = \frac{V_{IN} D}{L_1 f_{sw}} \tag{5.14}$$

The voltage at the diode D_r is then expressed as

$$V_{diode} = -(MV_{IN} + V_{OUT}) \tag{5.15}$$

This value is negative and the diode will be in reversed bias. Therefore, the current I_2 will stay zero.

During this phase, the provided energy from the rectifier will be stored in the primary inductor of the coupled inductor of the flyback converter.

Phase 2 $\forall t \in [DT_{sw}; D_2 T_{sw}]$

When V_G becomes zero, the NMOS transistor opens and the current I_1 drops to zero. The stored energy in the primary inductor provokes the apparition of the current I_2. In addition, an inversion of polarity of V_{L1} and V_{L2} is obtained. The diode D_r is in forward bias. If we neglect the threshold voltage of the diode, V_{L2} equates to V_{OUT} and the current I_2 firstly achieves its maximum value (Eq. 5.16) and decrease linearly until zero (Eq. 5.17).

$$I_{2\_MAX} = \frac{I_{1\_MAX}}{M} \tag{5.16}$$

$$I_2(t) = I_{2\_MAX} - \frac{V_{OUT}}{L_2} t \tag{5.17}$$

During this second phase, the stored energy in the primary inductor L_1 is transmitted towards the secondary inductor L_2 and stored in the storage capacitor C_{out}.

Phase 3 $\forall t \in [D_2 T_{sw}; T_{sw}]$

The last phase starts when the current I_2 becomes zero and finishes when the NMOS transistor is closed. During this phase, the diode D_r is in reversed bias. The current I_1 and I_2 are zero and V_{L1} equates to V_{IN}.

Cette thèse est accessible à l'adresse : https://theses.insa-lyon.fr/publication/2023ISAL0007/these.pdf
© [X.V.L. NGUYEN], [2023], INSA Lyon, tous droits réservés

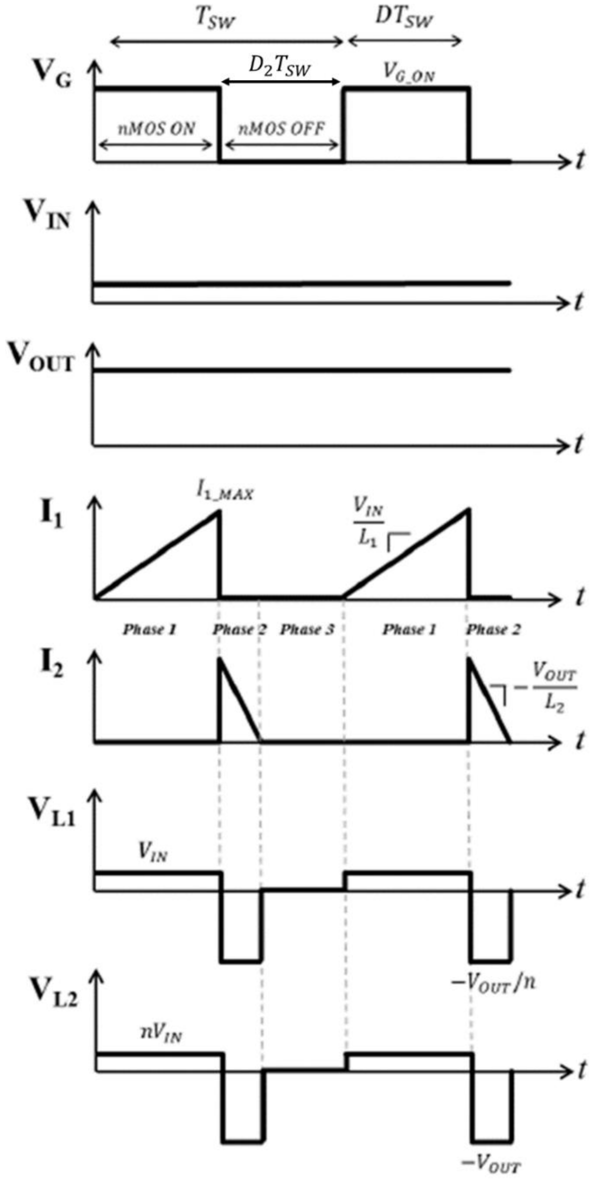

Figure 5.28: Typical waveforms of the flyback converter in DCM mode adapted from [157]

The drawback of flyback converter is that an external oscillator circuit is necessary to provide the oscillating frequency to the converter. Hence, the self-oscillating capability is not ensured for this circuit.

5.2.2. Practical implementation

The designed Power Management Unit (PMU) is related to [94] and schematized as Fig. 5.29. The circuit features the four following operation phases: *cold start, transition, normal operation* and *deactivation*.

Cette thèse est accessible à l'adresse : https://theses.insa-lyon.fr/publication/2023ISAL0007/these.pdf
© [X.V.L. NGUYEN], [2023], INSA Lyon, tous droits réservés

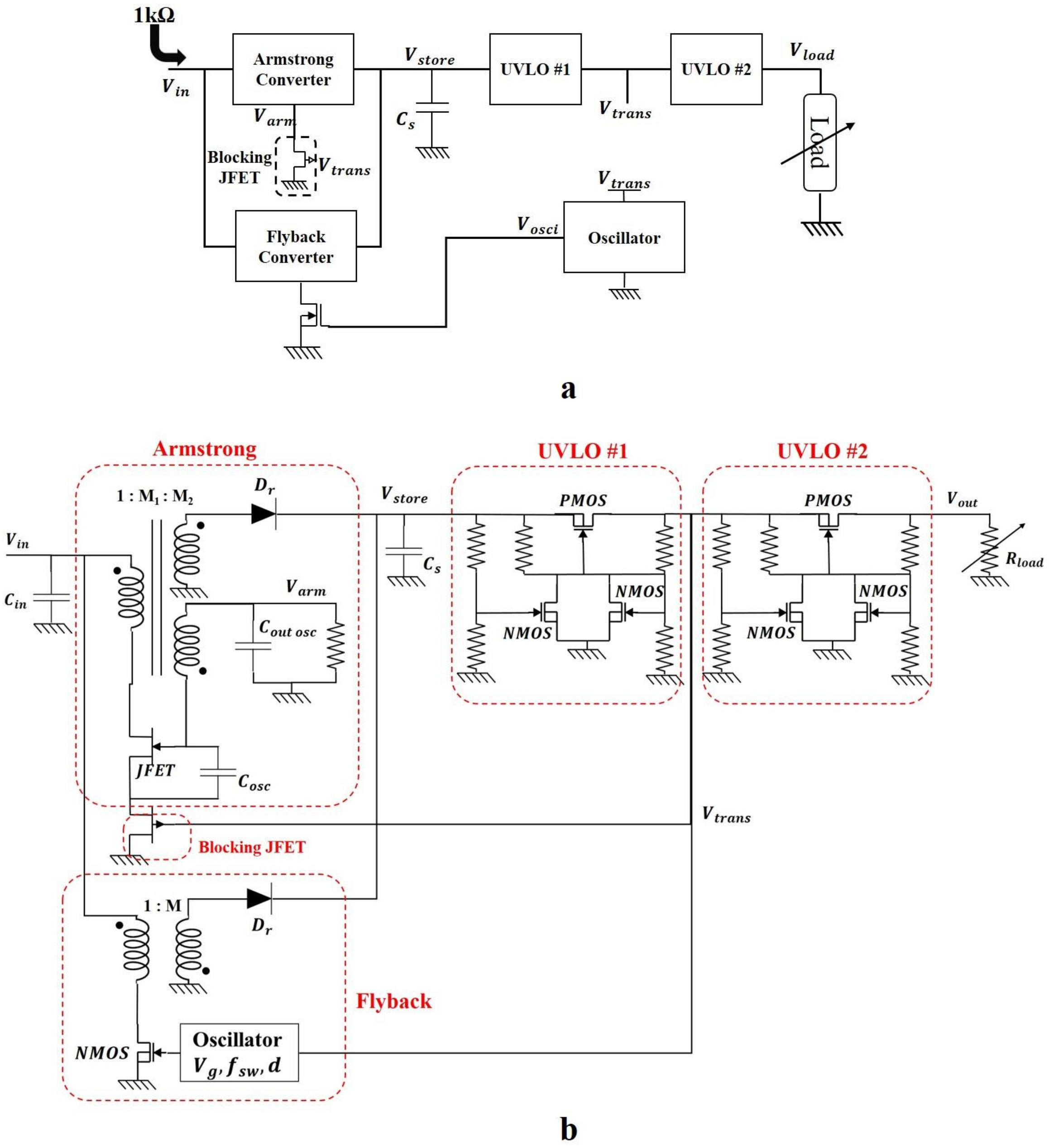

Figure 5.29: Schematic of our proposed Discrete Power Management Unit (a. Bloc schematic; b. Electrical schematic)

As stated above, the Armstrong converter is able to operate without requiring an external oscillator, but the lack of the impedance matching configuration in order to attract at most the power from the rectifier is a drawback of this circuit [94]. Therefore, this converter is proposed only as a starting trigger of the PMU in the *Cold start* phase. The theoretical minimum cold-start voltage ($V_{start\ min}$) of the circuit can be estimated as [94]

$$V_{start\ min} \approx (2I_{DSS}R_S + |V_p|)/m \tag{5.18}$$

where R_S is internal impedance of the source (Ω), I_{DSS} is zero-gate voltage drain current (A), V_p is threshold voltage of the JFET (V) and m is turn ratio of the transformer (unitless).

Cette thèse est accessible à l'adresse : https://theses.insa-lyon.fr/publication/2023ISAL0007/these.pdf
© [X.V.L. NGUYEN], [2023], INSA Lyon, tous droits réservés

For our Armstrong converter, the selected JFET is the Normally-On J201 (I_{DSS} = 0.6 mA and V_p = -0.6 V) and the three-coil transformer is WE750311681 from Würth Elektronik (m = 10 for both turn ratios). This JFET is chosen due to its low threshold voltage meanwhile the transformer is used because of its three-coil configuration. Another reason of choosing this component is that among the transformers being available on the market, the transformer WE750311681 owns the highest turn ratios, which allows us to decrease the cold-start voltage of the circuit. Because of the time constraint of this thesis, we are unable to fabricate the three-coil transformers with higher turn ratio and characterize them by ourselves.

Using Eq. (5.18), the estimated minimum cold-start voltage is 0.18 V. A comparison of the minimum cold-start voltage of the PMU to the other works will be introduced in the next chapter.

The voltage (V_{store}) across the storage capacitor (C_s) is pulled up by the Armstrong converter. When this voltage reaches the high-level threshold voltage of the UVLO #1 ($V_{high\ 1}$), the UVLO#1 will operate as a shorted circuit, and the circuit goes to the *transition* phase then. In this phase of operation, the Armstrong converter should be deactivated. Another JFET, noted as Blocking JFET, is connected as shown in Fig. 5.29 in order to turn off the Armstrong converter. Due to the discharge of the storage capacitor C_s, this JFET is opened and this will cut the connection of the Armstrong converter to the ground. It should be noticed that this JFET is a Normally-On PFET and has to be bidirectional. The source of the Blocking JFET should be linked to the ground of the circuit. The idea of this implantation is that the grille-source voltage of the Blocking JFET will not be affected by the input voltage of the circuit, thus, the operation of this transistor is always ensured during the variation of the input voltage. The PFET J177 is used thanks to its low threshold voltage (0.8 V).

In the *transition* phase, meanwhile the Armstrong converter is being shut down, the flyback converter enters operation simultaneously since the oscillator is fed by the discharging of the storage capacitor C_s when the UVLO #1 is closed.

When the Armstrong converter is completely deactivated and the flyback converter is totally in operation, the *normal operation* phase is achieved. In this phase, the input impedance of the PMU (R_{input}) can be calculated as Eq. (5.11). This parameter is fixed to 1 kΩ in open-loop. The oscillator of the flyback converter is a low-consumption circuit TS3002 from Silicon Labs (supply current of 1 µA at 25 kHz and typical supply voltage of 1 V). To optimize the operation of the flyback converter, the duty cycle of oscillating frequency is set to 50 % [157]. The coupled inductor used in the converter is LPD6235-205 from Coilcraft, which is selected due to its high primary inductance (2 mH at 100 kHz) and its small dimensions. Since the input impedance of the flyback converter should be 1 kΩ, the oscillating frequency f should be then 62.5 kHz. V_{store} is boosted with the aid of the flyback converter and the power is stored in C_s. When V_{store} is higher than the high-level threshold voltage of the UVLO #2 ($V_{high\ 2}$), the UVLO #2 will be closed, the load is actually supplied by the PMU.

When V_{store} becomes low because of the drop in the input voltage V_{in} or a high demand of power from the load occurs, the PMU will turn to *deactivation* phase. Firstly, V_{trans} is degraded and becomes lower than the low-level threshold voltage of UVLO #2. UVLO #2 is opened and disconnects the load. If V_{trans} and the power stored in C_s are high enough to keep the operation of the oscillator of the flyback converter, and to maintain the blocking state of the Amstrong oscillator blocking JFET, the flyback converter will continue to operate. Actually, the system returns to the *normal operation* phase and the time to do so depends on the RF input power. We call this mode the *Standby mode* of the flyback converter. If not, UVLO #1 will be opened, the flyback converter

Cette thèse est accessible à l'adresse : https://theses.insa-lyon.fr/publication/2023ISAL0007/these.pdf
© [X.V.L. NGUYEN], [2023], INSA Lyon, tous droits réservés

then the PMU will be totally turned off. In this situation, the PMU will be reactivated whenever V_{in} is higher than $V_{start\ min}$.

The input capacitor (C_{in}) of the PMU is chosen as 1 µF. This value of the capacitor is calculated in order to optimize the performance of the flyback converter [157] since in *normal operation* phase, this converter takes the full role of amplifying the voltage of the PMU. This value can be expressed as [157]

$$C_{in} = 100 \times \frac{(2-D)^2}{4R_{in}f_{sw}} \tag{5.19}$$

where, D is the duty cycle of the oscillator of the flyback converter (50 %), R_{in} is the input impedance of (1 kΩ) and f_{sw} is the switching frequency of the flyback converter (Hz).

The duty cycle of the oscillator is set as 50 % here to reach the optimal point of the flyback converter [157].

The operation of this PMU will be verified by connecting the four-port rectifier for the Flower Pot in Chapter 6.

Table 5.4: Discrete components used in the proposed PMU

Electrical part	Components	Reference
Armstrong	Transformer	WE750311681
	JFET	J201
	Blocking PFET	J177
	Rectifying diode	BAT54
Flyback	Transformer	LPD6235-205
	Oscillator	TS3002
	NMOS	FDV301N
	Rectifying diode	BAT54
UVLO #1 and UVLO #2	NMOS #1	FDV301N
	NMOS #2	FDV301N
	PMOS	FDV304P

5.3. Maximum Power Point

In order to attract more power from the rectifier to the PMU, the Maximum Power Point (MPP) condition should be created. The input impedance of the PMU should be the optimal load of the rectifier. The optimal load is at which the RF-DC conversion efficiency of the rectifier achieves its maximum.

As introduced in the previous sections of this chapter, for the impedance matching between the rectifier and the PMU, the selected impedance is 1 kΩ. In this section, the reason of choosing this value will be justified.

5.3.1. Estimating the optimal load of the rectifier

Identifying the optimal load of the rectifier is an essential step to match the impedance between the rectifier and the PMU. In fact, this value of load is related to the junction resistance (R_j) or Zero-Bias Resistance (ZBR) of the rectifying diode [66], [85].

In [85], Simon et al. show the differential R_j of the diode as function of DC current through two types of diode: high Schottky barrier (MACOM MA4E1317) and low Schottky barrier (Skyworks SMS7630). According to the results illustrated in Fig. 5.30, SMS7630 has a theoretical ZBR of

Cette thèse est accessible à l'adresse : https://theses.insa-lyon.fr/publication/2023ISAL0007/these.pdf
© [X.V.L. NGUYEN], [2023], INSA Lyon, tous droits réservés

5 kΩ. Additionally, the authors measure also the parasitic elements of this diode. The measured ZBR is 7 kΩ.

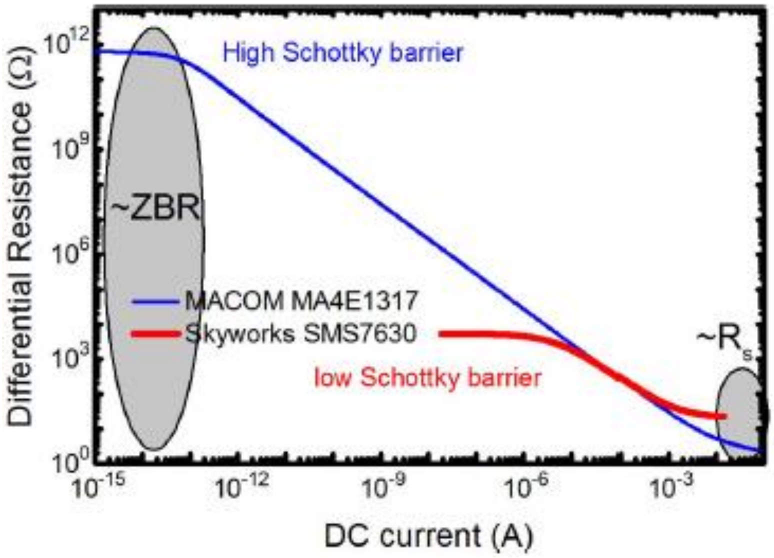

Figure 5.30: Differential resistance of two different diodes in [85].

In [78], the authors studied the electrical performance of the series rectifier as variations of temperature with different zero-bias diodes: SMS7630 and HSMS-2850. The studies are carried out at 900 MHz and different level of input power: -20 dBm, -30 dBm and -40 dBm over a temperature range of -10°C to 30°C. In order to determine the optimal load of the rectifier, the authors measure the reflection coefficient of the circuit using a VNA in continuous wave mode at a defined frequency. Afterwards, the required external available source power P_{avs} to compensate for the mismatch loss is calculated as

$$P_{avs} = \frac{P_{in}}{1-|S_{11}|^2} \tag{5.20}$$

Where P_{in} is the level of power injected actually into the rectifier. P_{avs} is adjusted to maintain P_{in} at the desired level. The RF-DC conversion efficiency is then calculated. The optimal load is concluded when the efficiency is maximized. The results of these measurements are illustrated in Fig. 5.31. According to these results, at 20°C, the optimal load of the circuit based on SMS7630 is around 7 kΩ for three different values of input power.

Cette thèse est accessible à l'adresse : https://theses.insa-lyon.fr/publication/2023ISAL0007/these.pdf
© [X.V.L. NGUYEN], [2023], INSA Lyon, tous droits réservés

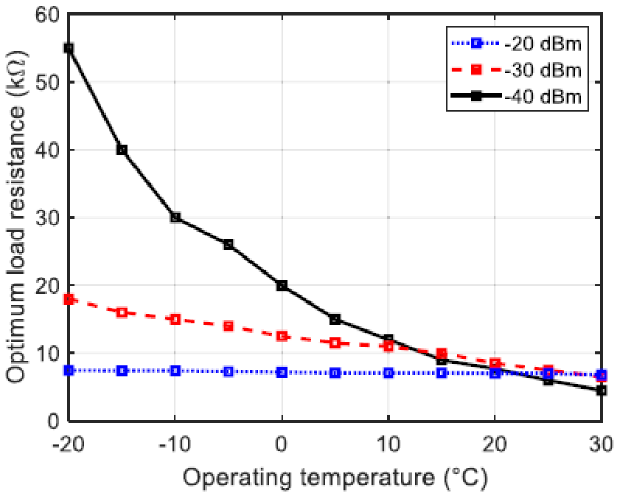

Figure 5.31: Optimal load resistance of SMS7630 at different input power level and temperature [78].

As presented in [85], the matching circuit always has lossy impacts on the performance of the rectifier. It should be noticed that these losses come from the mismatch of impedance at the desired operating frequency and the desired input power of the rectifier. These losses reduce the received power by the rectifying diode. The relation between the input power (P_{ir}), the reflected losses because of the matching circuit (P_{rr}) and the transmitted power towards the diode (P_{tr}) in a rectifier can be expressed as

$$P_{ir} = P_{rr} + P_{tr} \tag{5.21}$$

When the RF matching circuit is well-designed, P_{rr} can be neglected and then, Eq. (5.21) can be rewritten as

$$P_{ir} \approx P_{tr} \tag{5.22}$$

In fact, the impedance matching of the rectifier does not stay constant under variation of the load of the rectifier. Since the operating point of the rectifying diode changes when the load varies, the impedance matching at the input of the rectifier will be modified. In other words, the matching circuit can be designed for only one value of load corresponding to only one frequency and one input power level. Thus, the way of estimating the optimal load of the rectifier with the impacts of the matching circuit becomes an issue. In the next sub-sections, two different methods of estimating the optimal load of the rectifier will be presented. They will be simulated in ADS to check their accuracy and their feasibility. Afterwards, a comparison between them will be studied to select the method for the measurements.

5.3.1.1 The first method – Method of optimizing the matching circuit at the input of the rectifier

As presented previously, the matching circuit is set to a defined value of load, frequency and input power level. The RF matching circuit at the rectifier input is optimized using ADS for each value of load (from 0.5 kΩ to 10 kΩ) such that S_{11} is lower than -50 dB, which is equivalent to an input impedance purely resistive of 50 Ω. With such a value of S_{11}, the losses of the matching circuit are minimized. Consequently, the received power by the rectifying diode will be mostly identical to the input power of the rectifier. From that, the conversion efficiency (η_{RF-DC}) of the rectifier can be determined as Eq. (5.5).

Cette thèse est accessible à l'adresse : https://theses.insa-lyon.fr/publication/2023ISAL0007/these.pdf
© [X.V.L. NGUYEN], [2023], INSA Lyon, tous droits réservés

The input power levels injected in the rectifier circuit are set to -30 dBm, -20 dBm and -10 dBm with the frequency of 2.45 GHz.

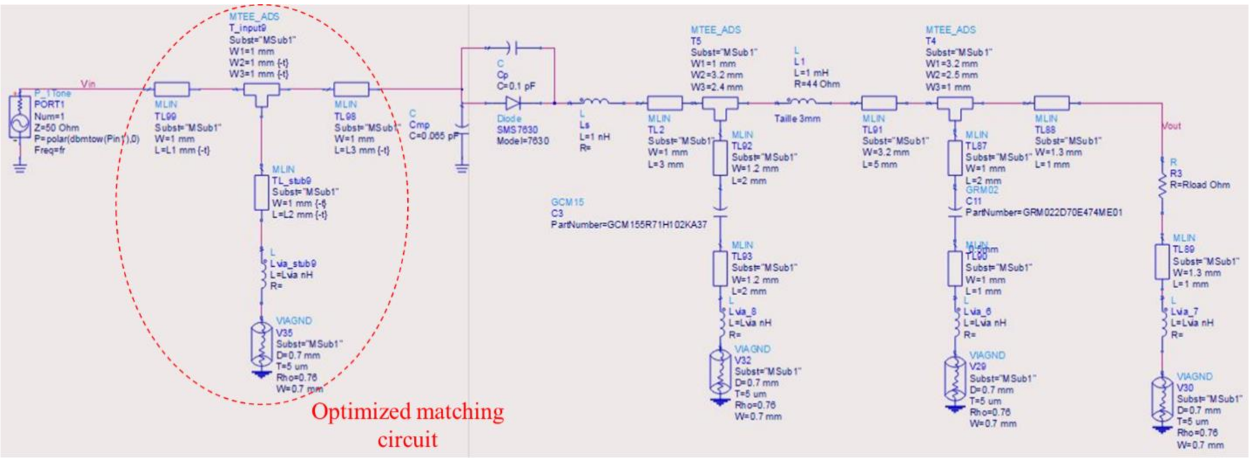

Figure 5.32: Schematic view of the circuit of the first method

5.3.1.2 The second method – Method of estimating the optimal load from the reflected power of the rectifier

In this method, the matching circuit is not required to be optimized for a certain value of the load, the input power or the frequency. The principle of this method is to measure the reflected power (P_r), which comes from the imperfect RF matching circuit of the rectifier, then, adjusting the input power of the rectifier (P_i) such that the received power (P_t) by the rectifying diode is set at the desired value (-30 dBm, -20 dBm and -10 dBm). The RF-DC conversion efficiency is calculated for different values of load to obtain the value of the optimal load afterwards. The configuration of the simulation is pictured in Fig. 5.33 and Fig. 5.34. For this method, two directional couplers are necessary. One coupler is used to measure P_i and the other is used to measure P_r. It should be noted that the attenuation of the coupler, connectors, cables, etc. (P_{loss}) have to be identified precisely to achieve satisfying results. The received power by the rectifying diode can be calculated using the following equation

$$P_t = P_i - P_{loss} - P_r \tag{5.23}$$

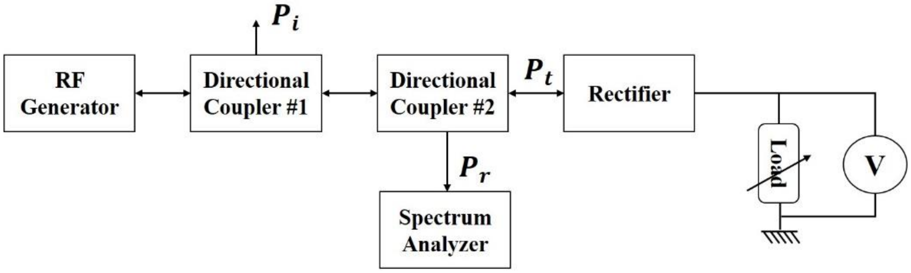

Figure 5.33: Schematic of the second method

Cette thèse est accessible à l'adresse : https://theses.insa-lyon.fr/publication/2023ISAL0007/these.pdf
© [X.V.L. NGUYEN], [2023], INSA Lyon, tous droits réservés

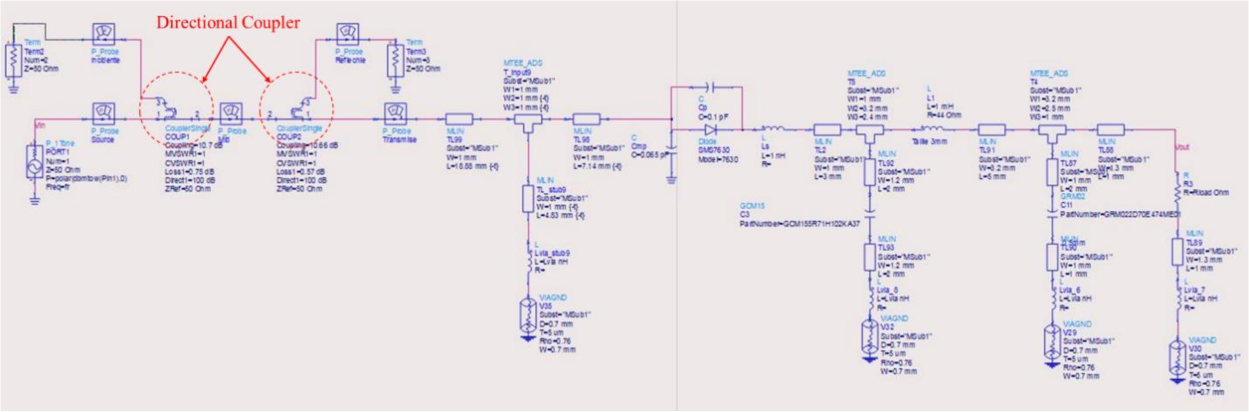

Figure 5.34: Schematic view of the circuit for the second method

5.3.1.3 Simulation results

The rectifier consists in the series topology with a Schottky diode SMS7630-079LF with two possible values of the storage capacitor (1 nF and 1 µF), an inductor of 1 mH at 2.5 MHz used as a RF choke at the output and a variable load. The chosen substrate is Rogers 4003C. The schematic of the rectifier is illustrated in Fig. 5.35. The simulations are carried out at 2.45 GHz at different input power levels, -30 dBm, -20 dBm and -10 dBm. The load is varied from 0.5 kΩ to 10 kΩ. The simulated results are shown in Fig. 5.36.

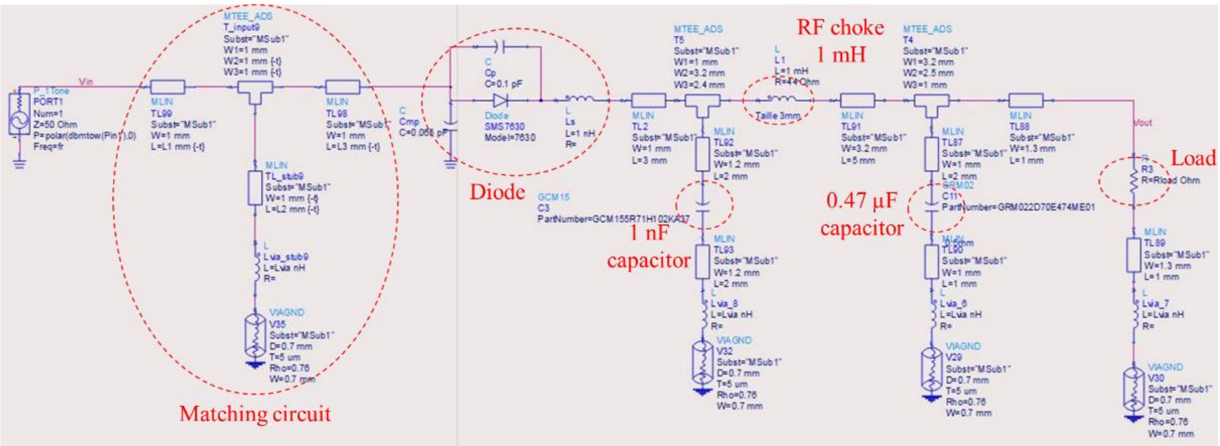

Figure 5.35: Schematic view of the circuit for both methods in ADS

Cette thèse est accessible à l'adresse : https://theses.insa-lyon.fr/publication/2023ISAL0007/these.pdf
© [X.V.L. NGUYEN], [2023], INSA Lyon, tous droits réservés

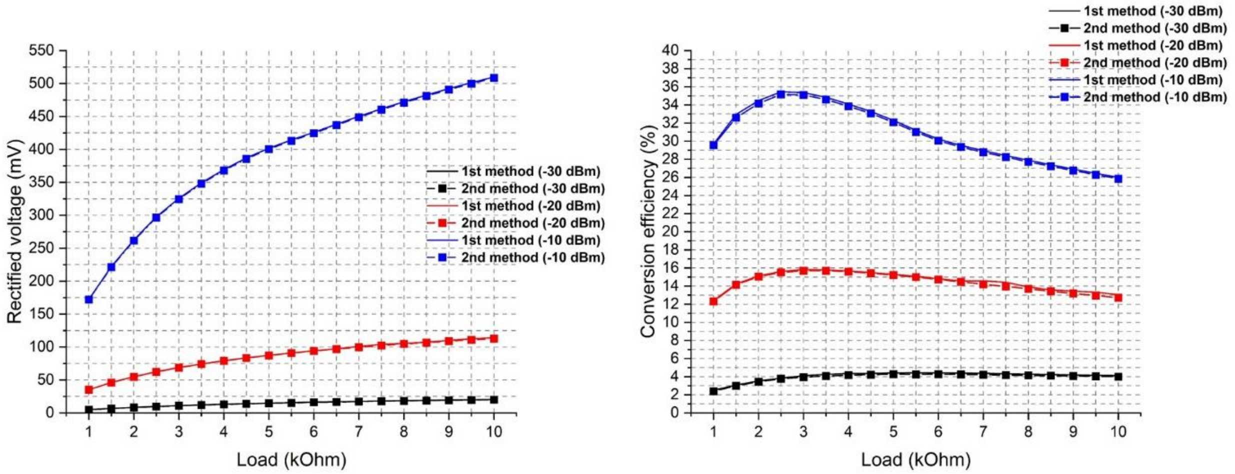

a

b

Figure 5.36: Simulated results at -30 dBm, -20 dBm and -10 dBm

There is slight but negligible difference between the methods based on the simulation. Theoretically, the first method can give us accurate results since the losses of the RF matching circuit are minimized. However, method #1 is not able to be deployed easily in reality because of the defaults of manufacturing of the circuits and the requirements for a high amount of circuits for the measurement. The method #2 is easier to carry out and produce results in line with the ones from method #1. A perfect RF matching circuit is not demanded in this method. The limit of this method #2 can come from the attenuation of the instruments used during the measurement (0.1 dB of difference of received power of the diode can lead to 2% of error in the calculation of the conversion efficiency). Therefore, the second method is considered for the measurement.

By checking the tendencies of the conversion efficiency curves, we find that the simulated optimal load of a series rectifier with a SMS7630-079LF diode is around 5 kΩ at -30 dBm, 3 kΩ at -20 dBm and 2.5 kΩ at -10 dBm.

5.3.1.4 Measurement results

The method #2 is selected for the sake of easier experimental details. The measurement setup is illustrated in Fig. 5.37. The directional coupler #1 is used to evaluate the input power P_i of the rectifier meanwhile the directional coupler #2 gives access to the reflected power P_r from the RF matching circuit. The rectifier is connected to a variable load.

The attenuation of the cables, the connectors and the couplers are studied prior to measurement using the VNA Rhode & Schwarz (ZNL3) calibrated with SOLT calibration method and the Spectrum Analyzer CXA N9000B of Keysight. The rectified voltage is measured using the Multimeter FLUKE 21 Series 2 (the accuracy is 0.4% + 1 digit and the internal impedance is higher than 10 MΩ). Since the output load of the rectifier varies from 1 kΩ to 10 kΩ, the internal impedance of the used multimeter will not have any impacts on the measurements.

Cette thèse est accessible à l'adresse : https://theses.insa-lyon.fr/publication/2023ISAL0007/these.pdf
© [X.V.L. NGUYEN], [2023], INSA Lyon, tous droits réservés

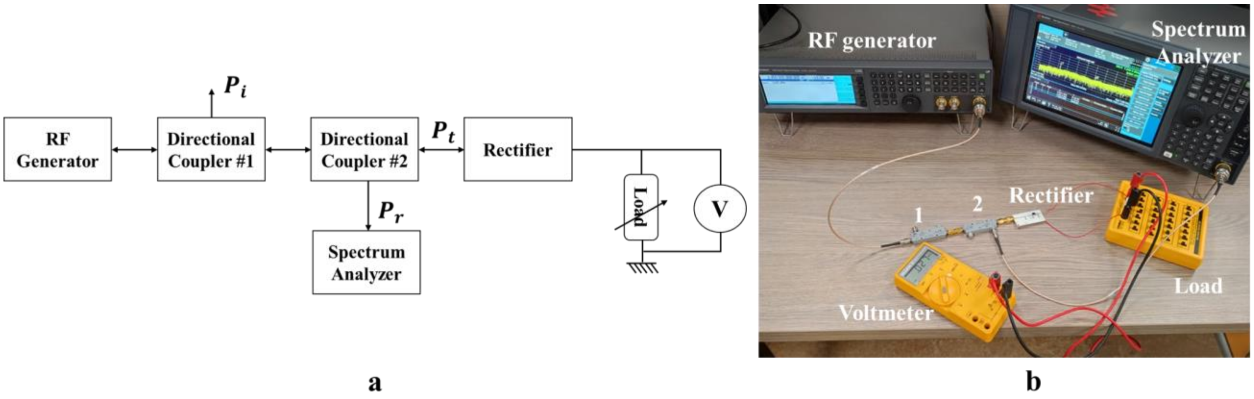

Figure 5.37: Schematic (a) and realized (b) measurement setup

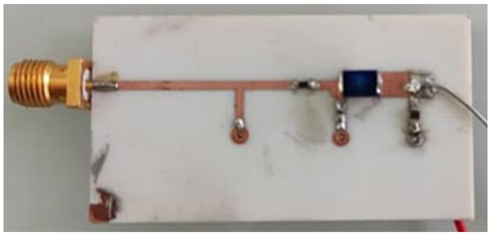

Figure 5.38: Rectifier circuit used for the measurement

The measurements are deployed at 2.45 GHz for different values of load. The output power of RF generator is adjusted according to Eq. (5.17) to achieve the desired value of the injected power in the rectifying diode, P_t (-30 dBm, -20 dBm, -10 dBm and 0 dBm). The results of measured rectified voltages and the corresponding RF-DC conversion efficiency are plotted in Fig. 5.39.

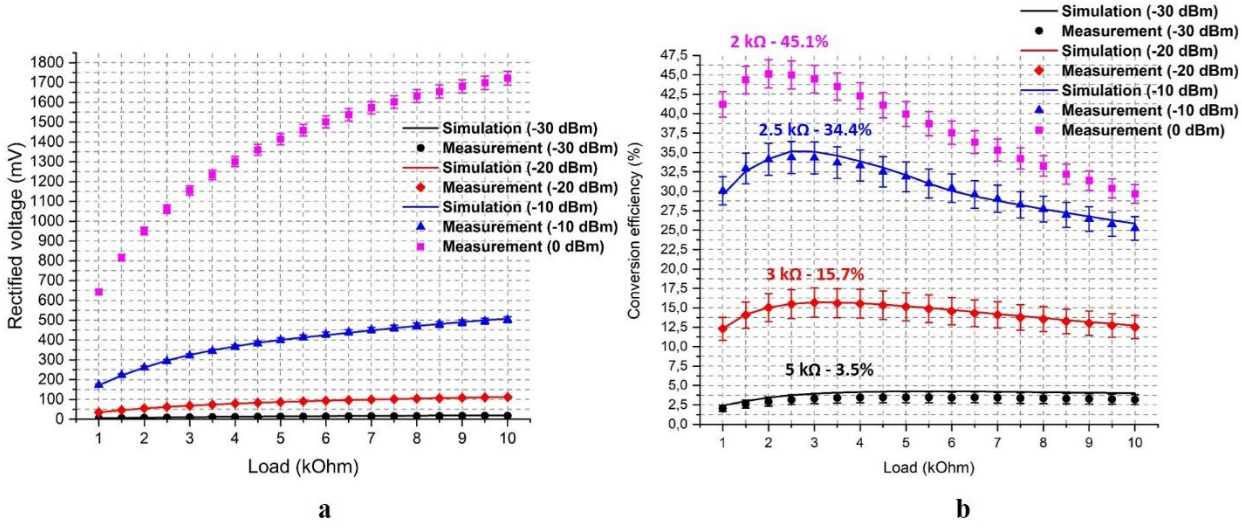

Figure 5.39: Simulated and measured results of optimal load of the rectifier (a. Rectified voltage; b. Conversion efficiency)

Additionally, the Current-Voltage (I-V) characteristics of the mono-diode series topology in different input power of -30 dBm, -20 dBm, -10 dBm and 0 dBm are illustrated in Fig. 5.40 and Fig. 5.41. We realize that the I-V curve characteristics are nearly the parallel lines. The simple model of a mono-diode series topology rectifier can be suggested as a voltage source in series with an internal resistance, which is the characterized ZBR as below.

Cette thèse est accessible à l'adresse : https://theses.insa-lyon.fr/publication/2023ISAL0007/these.pdf
© [X.V.L. NGUYEN], [2023], INSA Lyon, tous droits réservés

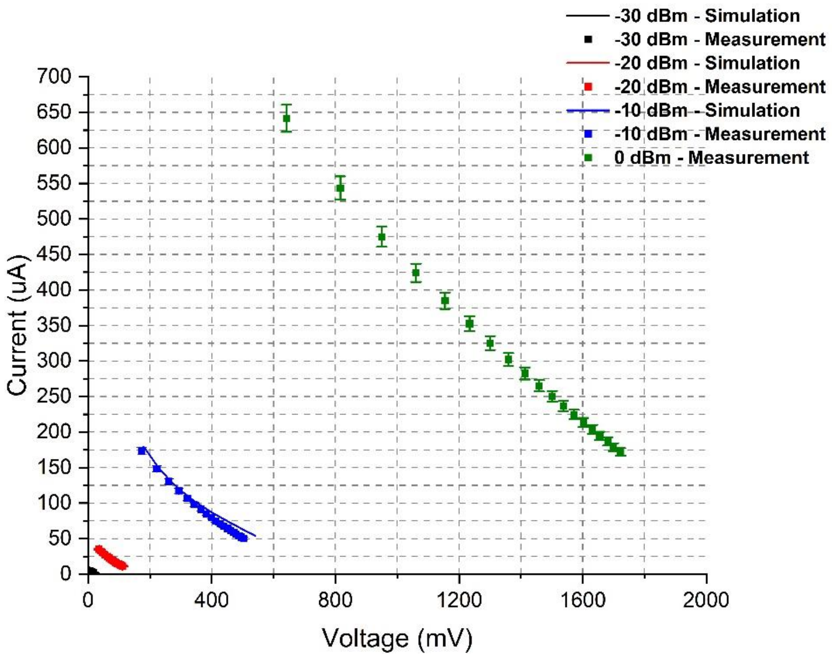

Figure 5.40: The simulated and measured I-V curve of the mono-diode series topology rectifier for different values of input power

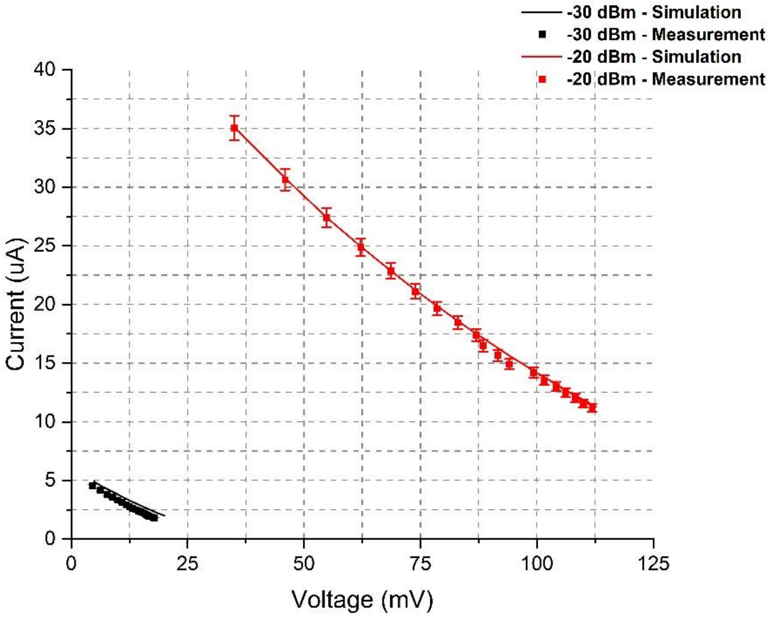

Figure 5.41: The results of I-V curve of Figure 5.40 at -30 dBm and -20 dBm

5.3.1.5 Conclusion

As shown in Fig. 5.39, we have a good agreement between simulation and measurement. The optimal load of the rectifier or the ZBR of the diode decreases when the input power level increases. At -30 dBm, -20 dBm, -10 dBm and 0 dBm, the optimal load is 5 kΩ, 3 kΩ, 2.5 kΩ and 2 kΩ, respectively.

In [85], the authors mention that the measured ZBR of the diode is around 7 kΩ meanwhile the theoretical value is indicated as 5 kΩ. Additionally, in Fig. 5.30, the tendency of ZBR of the diode is illustrated. This parameter stays constant when the DC current through the diode in the order of

Cette thèse est accessible à l'adresse : https://theses.insa-lyon.fr/publication/2023ISAL0007/these.pdf
© [X.V.L. NGUYEN], [2023], INSA Lyon, tous droits réservés

1 µA. The ZBR decreases linearly when this current increases in the order of 1 mA. Afterwards, the value of this parameter saturates at around 100 Ω.

In [78], the measurements of the ZBR are performed at -20 dBm, -30 dBm and -40 dBm and different temperature values at 900 MHz. The measured results show that the ZBR of the diode can be obtained as 7 kΩ.

In [95], the optimal load of the rectifier is characterized at different input power levels, i.e. -35 dBm, -20 dBm and 0 dBm. The corresponding measured optimal loads are 7.2 kΩ, 4 kΩ and 2.6 kΩ.

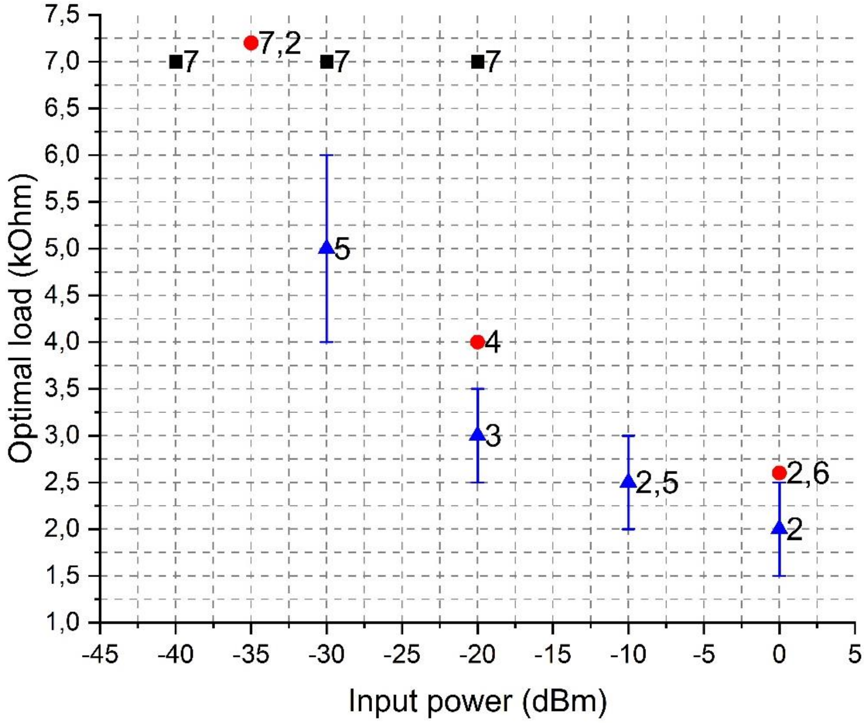

Figure 5.42: Optimal load of the mono-series diode topology of rectifier with SMS7630-079LF diode (Black dot: [78] ; Red dot: [95] ; Blue dot : This work)

Comparing to [95] and [85], we have the same tendency of decrease in the optimal load when the input power increases. The difference between our results to their given values may come from the error of the experimental setup. Moreover, in [78], the authors indicate that the load resistance adjustments are done manually and a mathematical calculation of the conversion efficiency is required. The measurement offers a limited resolution obtaining the optimum load resistance. This may lead to a discrepancy with respect to [78] and other works.

Moreover, the I-V characteristics of the rectifier is also studied. The quasi-parallel characteristic lines are obtained. The mono-diode series topology rectifier is suggested to model as a voltage source with an internal resistance, which is the ZBR of the rectifying diode.

5.3.2 Optimal load of four-input rectifier

The concept of the rectifier designed for the Flower Pot is a four-series-topology rectifier in parallel with a common output at the end, where the rectifier will connect to the PMU. Therefore, in order to maximize the power at the output load of the rectifier, the value of the load (Z_{load}) can be calculated as

Cette thèse est accessible à l'adresse : https://theses.insa-lyon.fr/publication/2023ISAL0007/these.pdf
© [X.V.L. NGUYEN], [2023], INSA Lyon, tous droits réservés

$$\frac{1}{Z_{load}} = \sum_{i=1}^{4} \frac{1}{Z_i} \tag{5.24}$$

where, Z_i is the optimal load of each branch of the rectifier at different input power level (Ω).

Since, when the input power level is lower than -30 dBm, the rectified voltage as well as the output power of the rectifier is very small thus negligible, to simplify the calculations, an assumption is introduced: "*The input power of each branch is considered as zero if its level is lower than -30 dBm. The corresponding branch will be assumed as opened circuit.*". Additionally, another assumption in which all the branches are supposed to be identical is also applied.

Because the input power levels to the four branches are not identical nor constant (from -30 dBm to 0 dBm), the optimal load of each branch will not be identical, and the optimal load of the rectifier will not stay constant. The scattering of Z_{load} values is evaluated using Eq. (5.24). All cases with the calculated values of load are listed and described in Annex A.

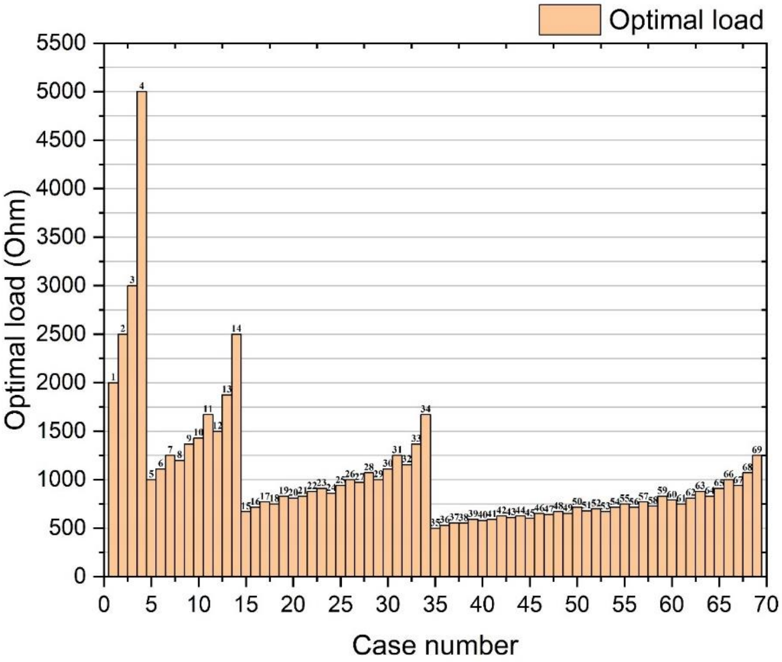

Figure 5.43: Calculated optimal load values of the four-port rectifier according to different cases listed in Annex A.

A trade-off is necessary in the specification of Z_{load}. As our aim is not to optimize the performance of the circuit for a special defined case, but to have an acceptable performance for at many cases as possible, we choose the value of load at which we have less difference between the chosen value with the others. Regarding Fig. 5.43, we see that the values of Z_{load} concentrate around the value of 1 kΩ. Therefore, in this thesis, the output load of the four-series-topology rectifier is selected as 1 kΩ.

5.3.3. Conclusion

In this section, we introduce a study about the electrical interference between the rectifier and the PMU. The Maximum Power Point condition is considered. Two requirements are induced: the input impedance of the PMU is the output load of the rectifier to reduce the impedance mismatch loss between two electrical blocks and this value of impedance is selected as the optimal load of the rectifier.

Cette thèse est accessible à l'adresse : https://theses.insa-lyon.fr/publication/2023ISAL0007/these.pdf
© [X.V.L. NGUYEN], [2023], INSA Lyon, tous droits réservés

A state-of-art of the methods of analyzing the optimal load of the rectifier is presented. These methods are based on investigating the maximum conversion efficiency to deduce the optimal value of the load. According to the state-of-art, the optimal load is not constant at different levels of input power of the rectifier. Literally, this value decreases when the RF input power increases.

After that, two methods for evaluating the optimal load of the rectifier are studied. The principle of the two methods is similar to the state-of-art. In the first method, for each load value, the RF matching circuit is optimized and the conversion efficiency is then determined. The drawback of this method is its experimental complexity. Therefore, the second method based on measuring the reflected power of the RF matching circuit and adjusting the incident power to get the desired transmitted power towards the diode is considered. Unlike the first method, this method uses only one rectifier for its deployment. A simulation of these two methods is performed to verify their precision. Since the simulated results are in good agreement, the second method is chosen from an experimental point of view.

The measurements are then carried out at 2.45 GHz for different input power levels. The optimal load values vary from are 5 kΩ to 2 kΩ with increasing input power. A comparison between our results and the state-of-art shows a fair agreement.

The optimal load for the four-port rectifier is also evaluated. A trade-off value is set to 1 kΩ. Our circuit is desired to work for all possibilities and not optimized for a particular case. Therefore, the value of 1 kΩ is selected to satisfy this requirement.

5.4. Wrap-Up

In this chapter, we introduce rectifier circuits designed for the linear polarization patch antenna and for the system of four circular polarization patch antennas. For the first rectifier, the method of simulating the mixed of lumped components and microstrip lines for the matching circuit is presented. The measurements of reflection coefficient to check the impedance matching condition of the circuit as well as the rectified voltage with the antenna in an anechoic chamber are deployed. The result is comparable to the selected state-of-art and opens a possibility of using Plastronics to create the RF circuits for energy harvesting applications. Since the RF matching circuit of this rectifier employs inductors, the variation of value of lumped components may change the matching in RF bands. Moreover, this requires more soldering pads to complete the circuit. Another study of the microstrip matching circuit is preferred. The rectifier designed for the system of antennas with four inputs is described. The configuration of implanting a RF choke and segmenting the ground planes to improve the capability of blocking the RF signals entering the PMU is also demonstrated. The measurements of the reflection coefficient and the rectified voltage of the rectifier are carried out. The measured results are compared to the selected state-of-art. According to the comparison, the rectifier fabricated applying Plastronics technique has nearly similar performances as the ones in other works, i.e. PCB, flexible circuits, 3D printed circuits.

A Power Management Unit with discrete components is also presented in this chapter. The circuit consists of four electrical blocks: the self-oscillating Armstrong converter for *Cold start phase*, the flyback converter in DCM for *Normal operation* and two UVLO circuits used to separate the different phases. The topology of each block and the reason of choosing the relating components are justified.

Finally, in order to set the Maximum Power Point condition of the rectifier and the PMU, the electrical interference between these blocks is analyzed. Determining the optimal output load of the rectifier is necessary. The method for measuring this parameter and its deployment are described in this chapter. A comparison between our values and the ones in the selected state-of-

Cette thèse est accessible à l'adresse : https://theses.insa-lyon.fr/publication/2023ISAL0007/these.pdf
© [X.V.L. NGUYEN], [2023], INSA Lyon, tous droits réservés

art is done. A good agreement is achieved. The optimal load is 5 kΩ, 3 kΩ, 2.5 kΩ and 2 kΩ at -30 dBm, -20 dBm, -10 dBm and 0 dBm, respectively, for a mono-series diode topology rectifier with SMS7630-079LF Schottky diode. For the rectifier of four-inputs, the optimal load is afterwards calculated and the obtained value is 1 kΩ.

Cette thèse est accessible à l'adresse : https://theses.insa-lyon.fr/publication/2023ISAL0007/these.pdf
© [X.V.L. NGUYEN], [2023], INSA Lyon, tous droits réservés

Cette thèse est accessible à l'adresse : https://theses.insa-lyon.fr/publication/2023ISAL0007/these.pdf
© [X.V.L. NGUYEN], [2023], INSA Lyon, tous droits réservés

CHAPTER 6: EXPERIMENTAL RESULTS

Cette thèse est accessible à l'adresse : https://theses.insa-lyon.fr/publication/2023ISAL0007/these.pdf
© [X.V.L. NGUYEN], [2023], INSA Lyon, tous droits réservés

Cette thèse est accessible à l'adresse : https://theses.insa-lyon.fr/publication/2023ISAL0007/these.pdf
© [X.V.L. NGUYEN], [2023], INSA Lyon, tous droits réservés

6. EXPERIMENTAL RESULTS

The operation of the proposed Power Management Unit will be analyzed. Firstly, the PMU will be tested with the four-port rectifier circuit. The rectifier will be supplied by a RF source CXG N5611B from Keysight. Each operation phase of the PMU and the standby mode of the flyback converter will be studied. After that, the RF source will be replaced by the Flower Pot antennas. The purpose is to evaluate the performances of the RFEH system manufactured using the rapid prototyping Plastronic technique. The cold start voltage, the output voltage under different loads, the global efficiency of the circuit will be concerned by the performance evaluation.

6.1. Load

As a demonstration load, we consider a low-power temperature sensor STTS22H from STMicroelectronic [158] or a low-power microcontroller RF430FRL152H from Texas Instruments [159]. The microcontroller consists of a 16-bit MSP430 and a RF transponder NFC ISO 15693 at the frequency of 13.56 MHz. The characteristics of these components are listed below.

Temperature sensor

- Supply voltage: 1.5 to 3.6 V
- Protocol of communication: I^{2}C
- Ultralow current: 1.75 µA in one-shot mode
- UDFN package dimensions : 2.0 x 2.0 x 0.5 mm

Microcontroller and RF transponder

- Supply voltage: 1.45 to 1.65 V
- Low current: 140 µA/MHz (1.5 V) in Active mode and 16 µA in Standby mode (LPM3)
- Protocol of communication: SPI and I^{2}C.
- VQFN (24) package dimensions : 4.0 x 4.0 mm

The desired supply voltage of the temperature sensor and the microcontroller is 1.5 to 1.6 V.

Considering that the microcontroller is active during the whole cycle with a frequency clock of 2 MHz, the maximum current consumption is 280 µA.

For the sensor, the maximum current consumption in one-shot mode is 2 µA.

Therefore, the total current consumption is 282 µA.

In addition, the temperature sensor is desired to operate for a duration of 120 ms.

The energy consumption of the microcontroller and the sensor (E_{demo}) can be calculated as

$$E_{demo} = U.I.T \tag{6.1}$$

where, U is supply voltage of the microcontroller and the sensor (V), I is current consumption of the microcontroller and the sensor (A), T is the operating duration (s).

The minimum and maximum energy consumption of the microcontroller and the sensor are 51 µJ and 55 µJ respectively.

Cette thèse est accessible à l'adresse : https://theses.insa-lyon.fr/publication/2023ISAL0007/these.pdf
© [X.V.L. NGUYEN], [2023], INSA Lyon, tous droits réservés

6.2. Pre-analysis of the flyback converter performances

As described in Section 5.2.1.3 in Chapter 5, the flyback converter in the PMU is configured in Discontinuous Conduction Mode (DCM). In this mode, the input impedance (R_{in}) of the converter can be defined as

$$R_{in} = 2Lf/d^2 \tag{6.2}$$

Where L is the primary inductance of the coupled inductor (H), f is the switching frequency (Hz) and d is the duty cycle of the oscillator (50%).

From Eq. (6.2), we can extract the following equation as R_{in} has been evaluated as 1 kΩ.

$$Lf = \frac{R_{in}d^2}{2} = \frac{1000\times 0.5^2}{2} = 125 \text{ F.Hz} \tag{6.3}$$

The efficiency of the flyback converter can be analyzed as proposed in [157] and the result is shown in Fig. 6.1. With the selected components, the conversion efficiency of the flyback converter ($\eta_{flyback}$) is estimated as 65%.

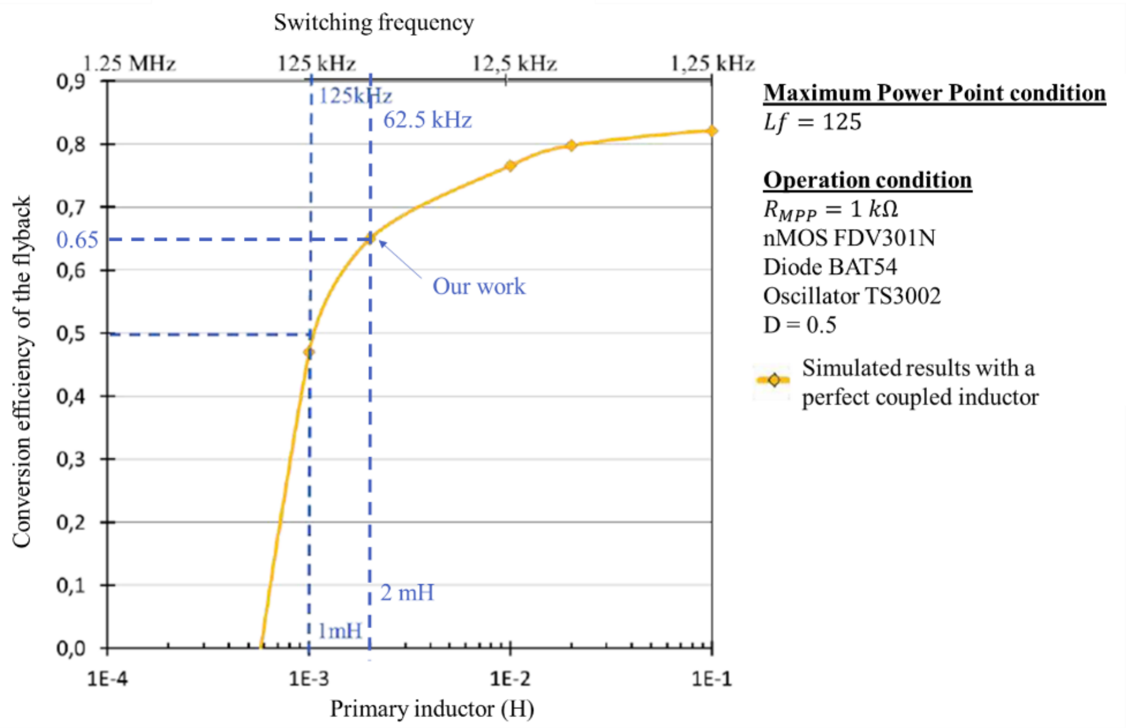

Figure 6.1: Simulated conversion efficiency of the flyback converter adapted from [157]

6.3. Cold start and Normal operation of PMU

The four-port rectifier designed for the system of four circular polarization patch antennas is connected to the discrete PMU in order to verify their operation. In the first test and to ease the deployment, a branch of the rectifier is supplied with an RF input power of -7.5 dBm, where the PMU starts and keeps operating in *Normal operation* phase, at the frequency of 2.45 GHz.

Cette thèse est accessible à l'adresse : https://theses.insa-lyon.fr/publication/2023ISAL0007/these.pdf
© [X.V.L. NGUYEN], [2023], INSA Lyon, tous droits réservés

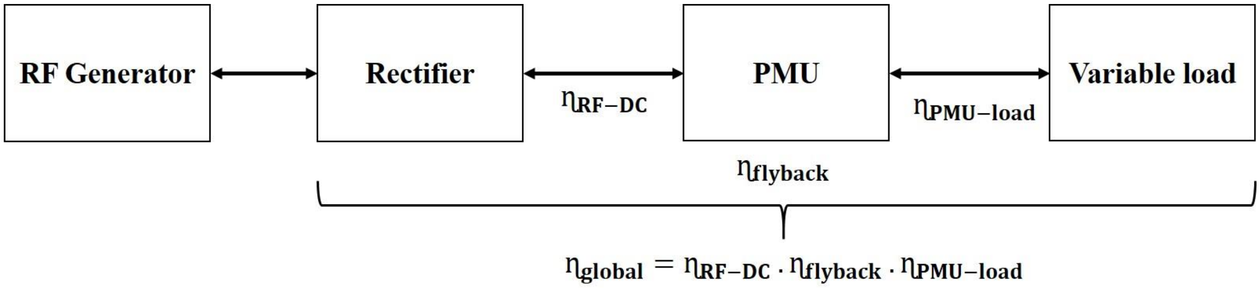

Figure 6.2: Schematic of measurement setup (η_{RF-DC}: RF-DC conversion efficiency of the rectifier; $\eta_{flyback}$: conversion efficiency of the flyback converter in the PMU; $\eta_{PMU-load}$: transmission power efficiency between the PMU and the load; η_{global}: total efficiency of the system of the rectifier and the PMU)

The measured cold start voltage is 0.26 V meanwhile the estimated value is around 0.18 V. The discrepancy of 0.08 V comes from the non-idealities of the discrete components, i.e. the JFET and the transformer.

The main voltage waveforms of each phase of operation of the circuit are illustrated in Fig 6.3.

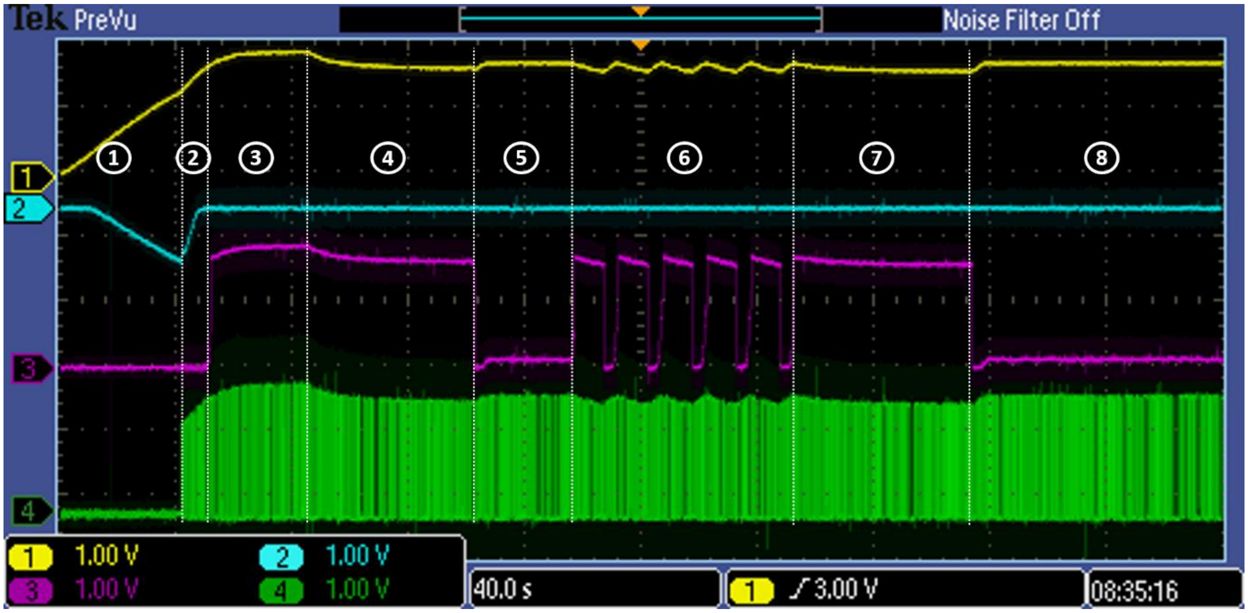

Figure 6.3: Waveforms at each test point of the PMU. These test points are illustrated in Fig. 5.29 (Yellow: V_{store} – voltage across the storage capacitor; Blue: V_{arm} – activation of Armstrong converter; Purple: V_{load} – output voltage of the PMU; Green: V_{osc} – signal generated by the oscillator to control the flyback converter)

The phases in Fig. 6.3 are the following:

1) Firstly, the load is set as 1 MΩ to act as open circuit (or a detection mode of the RF signals). The Armstrong converter operates and the PMU is currently in *Cold start* phase. The voltage V_{store} across the storage capacitor C_s is boosted under the action of the Armstrong converter. Since the latter voltage does not reach the high-level threshold voltage of the UVLO#1 ($V_{high\ 1} = 1.2$ V) thus the flyback converter is not activated and V_{load} is still zero. The high-level threshold voltage of the UVLO#1 is set as 1.2 V to equate the minimum starting voltage of the TS3002 oscillator for the control of the flyback converter.

2) When V_{store} reaches $V_{high\ 1}$, the UVLO#1 is closed and acts as a shorted circuit. The energy stored in C_s is absorbed by the oscillator, which is in turn start-up and activates the flyback

Cette thèse est accessible à l'adresse : https://theses.insa-lyon.fr/publication/2023ISAL0007/these.pdf
© [X.V.L. NGUYEN], [2023], INSA Lyon, tous droits réservés

converter. We observe in Fig. 6.3 the oscillating signal, V_{osc}, generated by the circuit TS3002. Here, we can confirm that an external source is not required for the operation of the oscillator.

Simultaneously, the blocking JFET J177 is also opened under voltage V_{trans} equal to V_{store}. As the flyback converter is in operation, V_{store} keeps increasing due to this converter. The signal of V_{arm} starts to return to zero, which means that the Arsmtrong converter is turned off, because the blocking JFET opened more and more strongly when V_{store} increases. However, V_{store} is still lower than the high-level threshold voltage ($V_{high\ 2}$) of the UVLO#2 (1.57 V). This value of $V_{high\ 2}$ is selected as the operating voltage of common microcontrollers and sensors. There is no energy supplied to the load consequently. The PMU is in *Transition* phase.

3) When the flyback converter is in operation, the input impedance of the PMU is 1 kΩ as indicated in Chapter 5. Verifying experimentally this parameter is an essential step.

The measurement setup is pictured in Fig. 6.4.

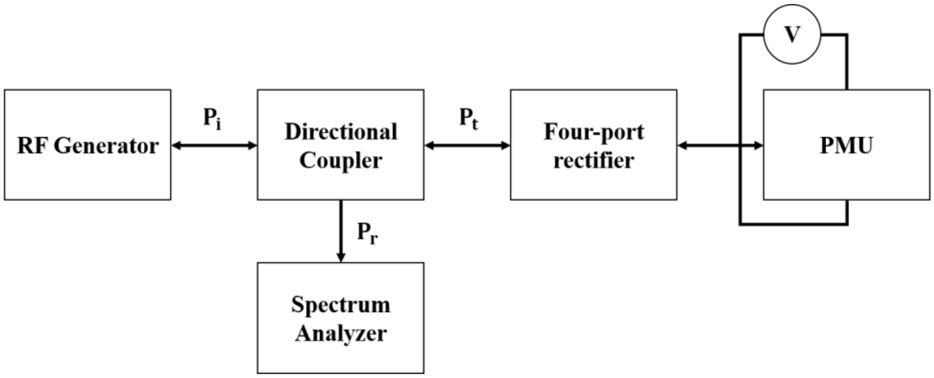

Figure 6.4: Measurement setup of the input voltage of the PMU

We compare the input voltage of the PMU in this operation when supplied by the four-port rectifier and the rectified voltage of this rectifier when connected to a variable load (with 0.1% of error verified with the Multimeter 2000 from Keithley) with different RF input power.

Firstly, the input voltage of the PMU is measured at -10 dBm, -7.5 dBm and -5 dBm of transmitted power to the rectifier (P_t) when the flyback converter is in operation. To obtain the desired values of P_t, the transmitted power of the RF generator (P_i) is adjusted and P_t is calculated as

$$P_t = P_t - P_r \tag{6.4}$$

where, P_r is reflected power from the rectifier measured with the Spectrum Analyzer CXA N9000B (W).

The measured reflected power at P_i values of -10 dBm (100 µW), -7.5 dBm (178 µW) and -5 dBm (316 µW) are 20 nW, 35 nW and 60 nW respectively. These values of reflected power are very small and negligible to P_i. Therefore, we can suppose that the rectifier has a good (RF) impedance matching at these input power levels with the PMU as a load.

The measured input voltages of the PMU are 0.16 V, 0.26 V and 0.33 V respectively. The voltages are measured with the Multimeter 2000 from Keithley (input impedance is higher than 10 GΩ with a resolution of 0.1 µV). Additionally, the reflected power by the PMU and the rectifier at these input power levels (P_r) are also measured using the Spectrum Analyzer CXA N9000B.

Cette thèse est accessible à l'adresse : https://theses.insa-lyon.fr/publication/2023ISAL0007/these.pdf
© [X.V.L. NGUYEN], [2023], INSA Lyon, tous droits réservés

Afterwards, the rectifier is connected to a variable load (0.1 % of error and 0.3 Ω of internal impedance). When the load varies, the (RF) matching conditions of the rectifier are modified, P_t changes consequently. Therefore, to ensure that P_t is always identical and equates to the values of PMU's input voltage measurement for every value of the load, P_r is measured and P_i is adjusted to obtain the desired value of P_t using Eq. (6.4).

The measurements show that at 1 kΩ the input voltage of the flyback is 0.17 V, 0.25 V and 0.35 V at -10 dBm, -7.5 dBm and -5 dBm respectively. Therefore, we can conclude that the input impedance of the PMU in this operation phase is around 1 kΩ. This result respects our previous calculation in Chapter 5.

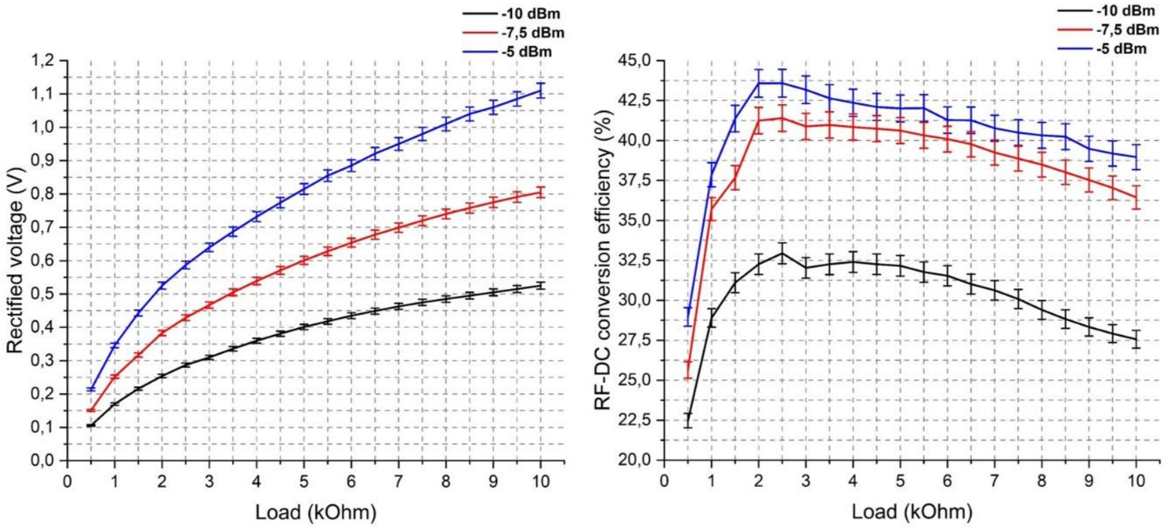

a b

Figure 6.5: (a) Measured rectified voltage and (b) corresponding RF-DC conversion efficiency of the rectifier

The switching frequency generated by the oscillator TS3002 is also measured using the oscilloscope MSO4034B with the probe of 10 MΩ. The result shown in Fig. 6.6 shows a signal of 62.4 kHz. A slight difference between the calculation and the real configuration of the oscillator comes from the variation of the discrete resistances of the circuit.

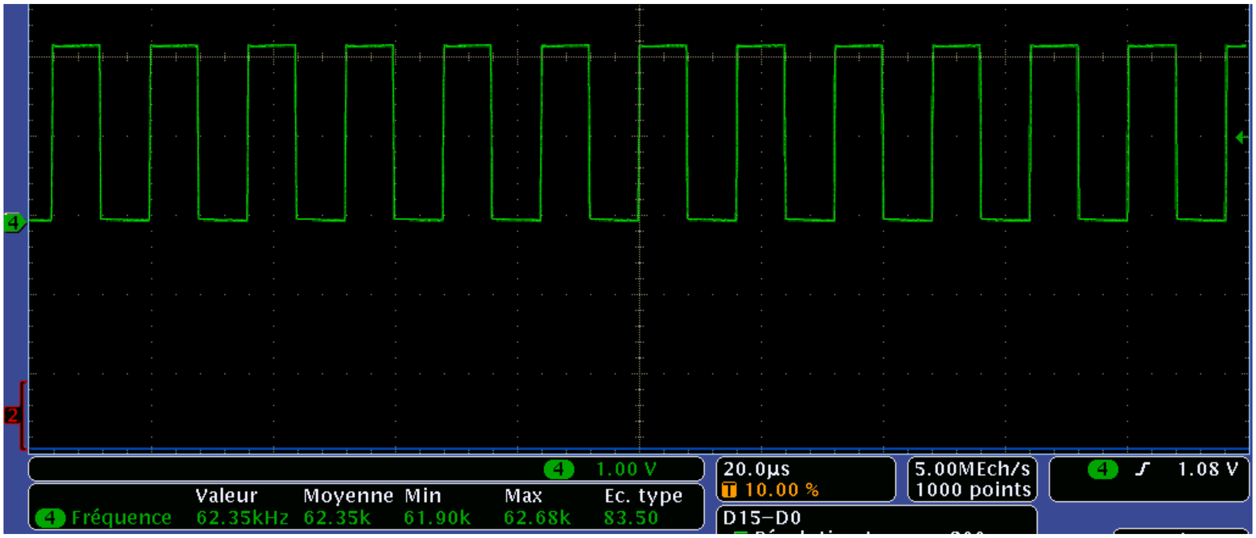

```
                                           4  1.00 V     20.0µs          5.00MEch/s    4  ƒ  1.08 V
                                                         T 10.00 %       1000 points
             Valeur     Moyenne  Min     Max     Ec. type
4 Fréquence  62.35kHz   62.35k   61.90k  62.68k  83.50     D15–D0
```

Figure 6.6: Measured waveform generated by the oscillator TS3002

Cette thèse est accessible à l'adresse : https://theses.insa-lyon.fr/publication/2023ISAL0007/these.pdf
© [X.V.L. NGUYEN], [2023], INSA Lyon, tous droits réservés

Because the input voltage and the input impedance of the flyback converter are (0.26 ± 0.02) V and 1 kΩ, respectively, the input power of the converter is (70 ± 10) µW. As indicated below, the conversion efficiency of the converter is estimated as 65 %, therefore, the output power can be estimated as 45.3 µW.

The flyback converter boosts V_{store}. When V_{store} is higher than $V_{high\ 2}$, the UVLO#2 is closed. The energy stored in C_s will be transmitted to the load. Here, the load is 1 MΩ. V_{load} is identical to V_{store}. In our first test, the value of storage capacitor is 470 µF. The voltage accross C_s is (2.26 ± 0.02) V. The stored energy in this capacitor (E_{stored}) can be calculated as

$$E_{stored} = \frac{1}{2}CU^2 = \frac{1}{2} \times 470\mu \times 2.26^2 = 1.2\ mJ \tag{6.5}$$

The transmission of energy from C_s to the load occurs immediately, but without any voltage drop because of the low-current inrush in the load. The circuit is now in *Normal operation* phase. The PMU output voltage is (2.2 ± 0.02) V, the current consumption of the load is (2.2 ± 0.02) µA.

The input voltage and the current consumption of other electrical parts supplied by C_s, i.e. TS3002, UVLO#1, UVLO#2 and Blocking JFET are also studied. The input voltages are measured with Multimeter 2000 of Keithley and the current consumption is measured with Keithley 6485 Picoammeter. The energy consumption is also calculated for a duration of 120 ms. The results are listed in Table 6.1.

Table 6.1: Measured current consumption and voltage of electrical parts in our PMU with the load 1 MΩ

Electrical parts	**Current consumption (µA)**	**Voltage (V)**	**DC Power consumption (µW)**	**Energy consumption (µJ)**
TS3002	15.2	2.2	33.44	4
UVLO#1	21.8	0.02	0.44	0.05
UVLO#2	2.2	0.04	0.09	0.01
Blocking JFET	0.15	2.2	0.33	0.04
Total loss			34.3	4.10

During this phase, the oscillator TS3002 consumes much more power than the other electrical parts and 6.9 times higher than the consumption of the load (4.8 µW). The consumption of the UVLOs and the Blocking JFET is very small and can be neglected in this case.

4) The load is reduced to 100 kΩ. UVLO#1 is still closed, therefore, the flyback converter is still in operation. V_{load} is reduced to 1.62 V, but still higher than the low-level threshold voltage $V_{low\ 2}$ (1.4 V) of UVLO#2. UVLO#2 is still closed and the output voltage is identical to the stored voltage across C_s. The consumption of each electrical part is listed in Table 6.2.

Cette thèse est accessible à l'adresse : https://theses.insa-lyon.fr/publication/2023ISAL0007/these.pdf
© [X.V.L. NGUYEN], [2023], INSA Lyon, tous droits réservés

*Table 6.2: Measured current consumption and voltage of electrical parts in our PMU with the load 100 k*Ω

Electrical parts	**Current consumption (µA)**	**Voltage (V)**	**DC Power consumption (µW)**	**Energy consumption (µJ)**
TS3002	8	1.66	13.28	1.59
UVLO#1	24.2	0.02	0.48	0.06
UVLO#2	16.2	0.04	0.65	0.08
Blocking JFET	0.15	1.66	0.25	0.03
Total loss			14.66	1.76

In this case, the oscillator TS3002 consumes less energy than in the case of 1 MΩ. This can be explained as the supply voltage of the oscillator is decreased, the current consumption is consequently reduced. The frequency is slightly decreased with a scale of 0.1 kHz, but this decrement is small and can be neglected.

A question arises: is the current consumption of this oscillator dependent on the input voltage or not? A measurement of the current consumption under different values of the input voltage is then carried out. The input voltage is provided by a DC generator and the current is measured by Keithley 6485 Picoammeter and the oscillator TS3002 is set up to achieve the signal of 62.5 kHz at the output. The results are listed in Table 6.3. The input voltage is limited to 2.1 V because the recommended maximum supply voltage of the oscillator is 1.8 V according to the datasheet.

Table 6.3: Measured current consumption and voltage of TS3002

Input voltage (V)	**Current consumption (µA)**	**Equivalent impedance (MΩ)**	**DC Power consumption (µW)**
1.2	4.5	0.27	5.4
1.4	5.3	0.26	7.42
1.7	8	0.21	13.6
2	11	0.18	22
2.1	13	0.16	27.3

According to the measurements, the current consumption and the power consumption of the oscillator increase in variation of the input voltage. This can limit the capability of providing the power and the energy from the PMU to the output load, which are the micro-controller and the sensor.

5) The load is then reduced from 100 kΩ to 10 kΩ. V_{load} drops until it is lower than $V_{low\ 2}$. The calculated time constant of V_{load} drop is 4.7 s while the measured value is 5.7 s. The measurements are deployed with an oscilloscope MSO4034B with the probe of 10 MΩ. The time of discharging of the capacitor from 1.68 V to 1.48 V is measured. As shown in Fig 6.7, the measured duration is 752 ms. The time constant (τ) is then calculated as

$$\tau = \frac{T}{\ln\left(\frac{V_0}{V_c}\right)} \tag{6.6}$$

where, V_0 is voltage of the capacitor at time t = 0 (V), V_c is voltage of the capacitor at time t = T (V), T is the duration (s).

Cette thèse est accessible à l'adresse : https://theses.insa-lyon.fr/publication/2023ISAL0007/these.pdf
© [X.V.L. NGUYEN], [2023], INSA Lyon, tous droits réservés

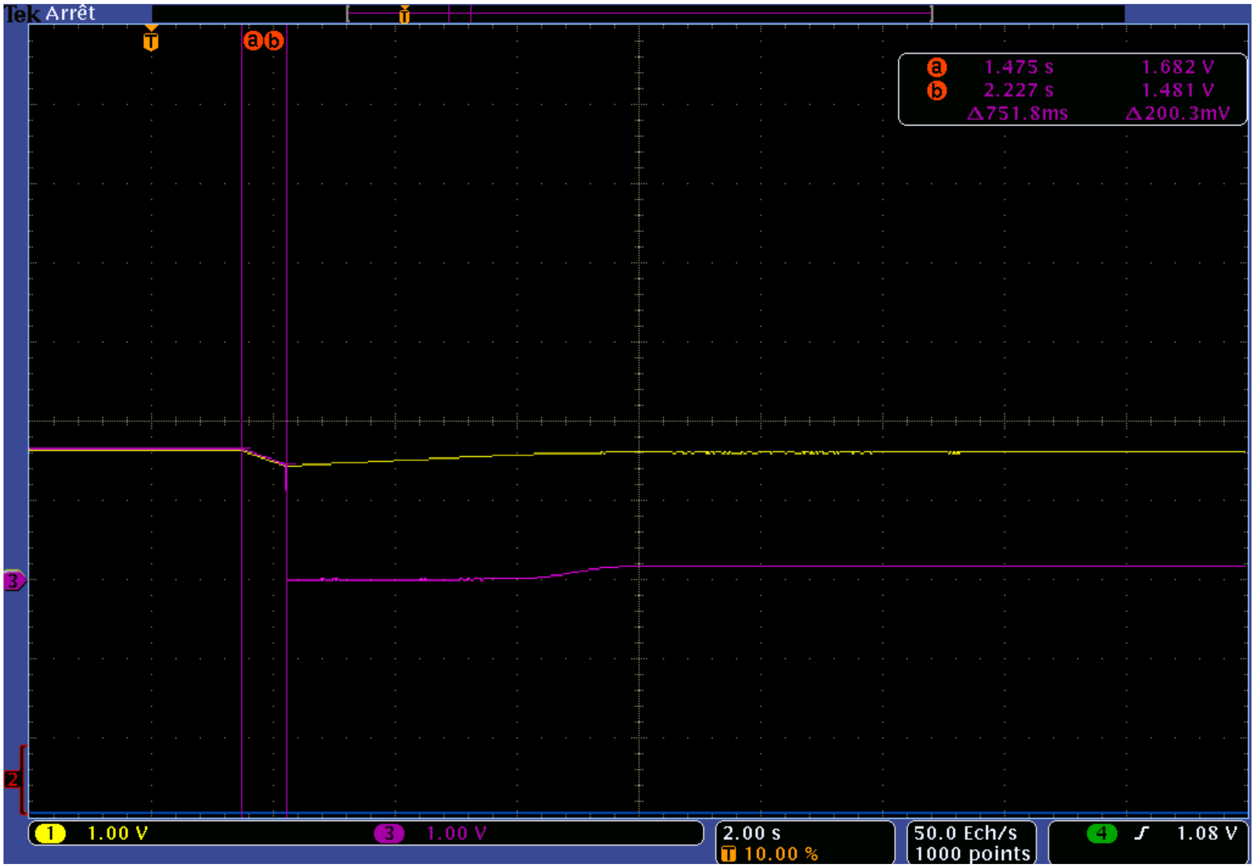

Figure 6.7: Waveforms of discharging of the storage capacitor

V_{load} goes below the low-level threshold voltage of UVLO#2 which then opens and the load is now disconnected from the PMU. In this case, the temporary load of the PMU is the internal impedance of the UVLO#2. The flyback converter is still operating as UVLO#1 is kept closed. The flyback converter helps increasing again V_{store} until it is higher than $V_{high\ 2}$. Since, the load is low, its consumption increases, a slight output voltage is obtained. Table 6.4 summarizes the energy consumption of each electrical part of the PMU over 120 ms of operation.

Table 6.4: Measured current consumption and voltage of electrical parts in our PMU with the load 10 kΩ

Electrical parts	Current consumption (µA)	Voltage (V)	DC Power consumption (µW)	Energy consumption (µJ)
TS3002	7	1.62	11.34	1.36
UVLO#1	200	0.02	4	0.48
UVLO#2	200	0.04	8	0.96
Blocking JFET	0.15	1.62	0.24	0.03
Total loss			23.58	2.83

6) The load is fixed to 80 kΩ,. This load consumes more power and energy, thus, C_s discharges quickly, but the energy storage is recovered also quickly.

7) The load is set to 100 kΩ with a similar operation as in the case 4.

8) The load is set to 10 kΩ with a similar operation as in the case 5.

Cette thèse est accessible à l'adresse : https://theses.insa-lyon.fr/publication/2023ISAL0007/these.pdf
© [X.V.L. NGUYEN], [2023], INSA Lyon, tous droits réservés

The output voltage is 1.62 V for a load of 100 kΩ with a cold start voltage of 0.26 V and a voltage of 0.26 V in *Normal operation phase* when the RF input power is -7.5 dBm. The PMU voltage boost ratio is then 6.1. In *Normal operation phase*, the input power of the flyback ($P_{in\ flyback}$) converter is

$$P_{in\ flyback} = \frac{0.26^2}{1000} = 67.6\ \mu W$$

At the load of 100 kΩ, according to the measurement, the total output power of the flyback converter, which is the sum of the losses of the components and the load consumption, is 40.9 µW. Therefore, the efficiency of the flyback ($\eta_{flyback}$) in this case can be obtained as

$$\eta_{flyback} = \frac{40.9}{P_{in\ flyback}} = \frac{40.9}{67.6} = 60.5\ \%$$

This value of $\eta_{flyback}$ is lower than the estimated value (65 %) as shown in Section 6.2. This makes sense as the loss in the coupled inductor is not included in the estimation.

The global efficiency of the system of the rectifier and the PMU (η_{global}) in *Normal operation* phase can be expressed as

$$\eta_{global} = \frac{V_{load}^2}{R_{load} P_{total\ in\ rectifier}} \tag{6.7}$$

where, R_{load} is the output load (Ω), $P_{total\ in\ rectifier}$ is the total input power of the rectifier (W). It should be reminded that in this measurement, the PMU is tested with a four-port rectifier with one fed port and the others connected to 50 Ω.

Since the total input power of the rectifier is -7.5 dBm, the obtained global efficiency of the system is 14.8 % of the load of 100 kΩ. A comparison between our circuit with the state-of-art is indicated in Table 6.5

Cette thèse est accessible à l'adresse : https://theses.insa-lyon.fr/publication/2023ISAL0007/these.pdf
© [X.V.L. NGUYEN], [2023], INSA Lyon, tous droits réservés

Table 6.5: Comparison between our work with our state-of-art

	Paing [99]	**Hsieh** [100]	**Salah** [95]	**Ahmed** [160]	**Our work**
Frequency	1.93 GHz	830 MHz	2.45 GHz	900 MHz	2.45 GHz
Antenna	Rigid patch antenna	RF source	Flexible patch antenna	RF source	RF source
DC/DC converter	Boost (DCM)	Switched inductor Boost (DCM)	Boost (DCM)	Multi-stage reconfigurable Dickson rectifier	Armstrong and flyback
Oscillator	IC	IC	IC (3-stage oscillator of UB20M)	NI	Discrete (TS3002)
Controller quiescent consumption	200 nA at 1.95 V (0.39 µW)	1.56 µA at 2V (3.12 µW)	150 nA at 3V (0.45 µW)	NI	4.5 µA at 1.2 V (5.4 µW)
					5.3 µA at 1.4 V (7.4 µW)
					8 µA at 1.7 V (13.6 µW)
					11 µA at 2 V (22 µW)
					13 µA at 2.1 V (27.3 µW)
MPPT Scheme	NI	Dynamic	Pre-defined the input impedance of the Boost converter	NI	Pre-defined the input impedance of the flyback converter
Global efficiency	10% at 3.3 dBm	44.1% at -12 dBm	28.7% at -7 dBm	40% at -8 dBm	14.8% at -7.5 dBm
Cold start	A battery voltage of 1.95 V	Rectifier with Boost (CCM) charges the output capacitor (0.3 V)	Precharged supercapacitor of 2 V	NI	0.26 V

NI: Not Indicated in the article
Dynamic: Using other circuits integrated in the PMU to seek the MPP

Our PMU has lower global efficiency than other circuits of the state-of-art at the power scale of -8 to -7 dBm. It should be noticed that our PMU uses a discrete oscillator TS3002 for the operation of the flyback converter and the power loss is originated mainly from this electrical part. If we compare the controller quiescent current, this oscillator consumes more power than other IC oscillators in [95], [99] and [100]. The performance of our PMU might be improved by replacing the oscillator TS3002 by a lower consumption oscillator. As illustrated in Fig. 6.1, the conversion efficiency of the flyback converter can be enhanced by using a higher primary inductor. Furthermore, the switching frequency can be then reduced, this will decrease the consumption of the oscillator. However, a higher primary inductor required a bigger coupled inductor for the

Cette thèse est accessible à l'adresse : https://theses.insa-lyon.fr/publication/2023ISAL0007/these.pdf
© [X.V.L. NGUYEN], [2023], INSA Lyon, tous droits réservés

flyback. This will increase the dimensions of the whole circuit and may also increase the loss in the coupled inductor.

A limitation of our circuit is that there is no Maximum Power Point Tracking scheme. In our configuration, the input impedance of the flyback is fixed at a defined value (1 kΩ for all possibilities) meanwhile the optimal load of the rectifier changes in variation of the RF input power. As shown in Fig. 6.6, the optimal load of the rectifier with one fed branch at -7.5 dBm is 2 kΩ giving an RF-DC conversion efficiency (η_{RF-DC}) of 41.2 % while with an output load of 1 kΩ (input impedance of the PMU), this efficiency is reduced to 35.7 %, which is equivalent to 5.5 % of degradation. This means that 5.5 % of DC power transmitted from the rectifier to the PMU is lost. Therefore, adding a MPPT scheme can improve the global efficiency of the whole circuit. The idea of using an active circuit to modify the switching frequency of the oscillator with the purpose of seeking the Maximum Power Point for each possibility can be considered [100]. However, this active circuit may take a part of the consumption of the whole PMU circuit.

The cold start voltage is also a necessary parameter of the PMU for low power energy harvesting applications. By configuring the Armstrong converter to kick-start the PMU, our circuit has a lower cold start voltage than other commercial circuits. Literally, this cold start voltage level can be reduced by using a transformer with a higher turn ratio between the secondary and the primary inductors. However, this requires a bigger transformer, hence, the losses and the dimensions may be increased. Another idea of reducing the cold start voltage is to operate the circuit with a lower zero-gate voltage drain current and/or lower threshold voltage JFET.

6.4. Standby mode of the flyback converter

In this section, the *Standby mode* of the flyback converter in *Deactivation phase* will be studied. First of all, the PMU is operating in *Normal operation* phase, then, the input power to the rectifier is slowly decreased until V_{store} is 1.1 V, at which value the oscillator stops operating. According to the measurements, with the minimum RF input power to the rectifier of -12 dBm with the corresponding voltage of 0.1 V, the flyback stays in *Standby mode* at the loads of 100 kΩ and 1 MΩ. The measured waveforms are shown in Fig. 6.8.

Cette thèse est accessible à l'adresse : https://theses.insa-lyon.fr/publication/2023ISAL0007/these.pdf
© [X.V.L. NGUYEN], [2023], INSA Lyon, tous droits réservés

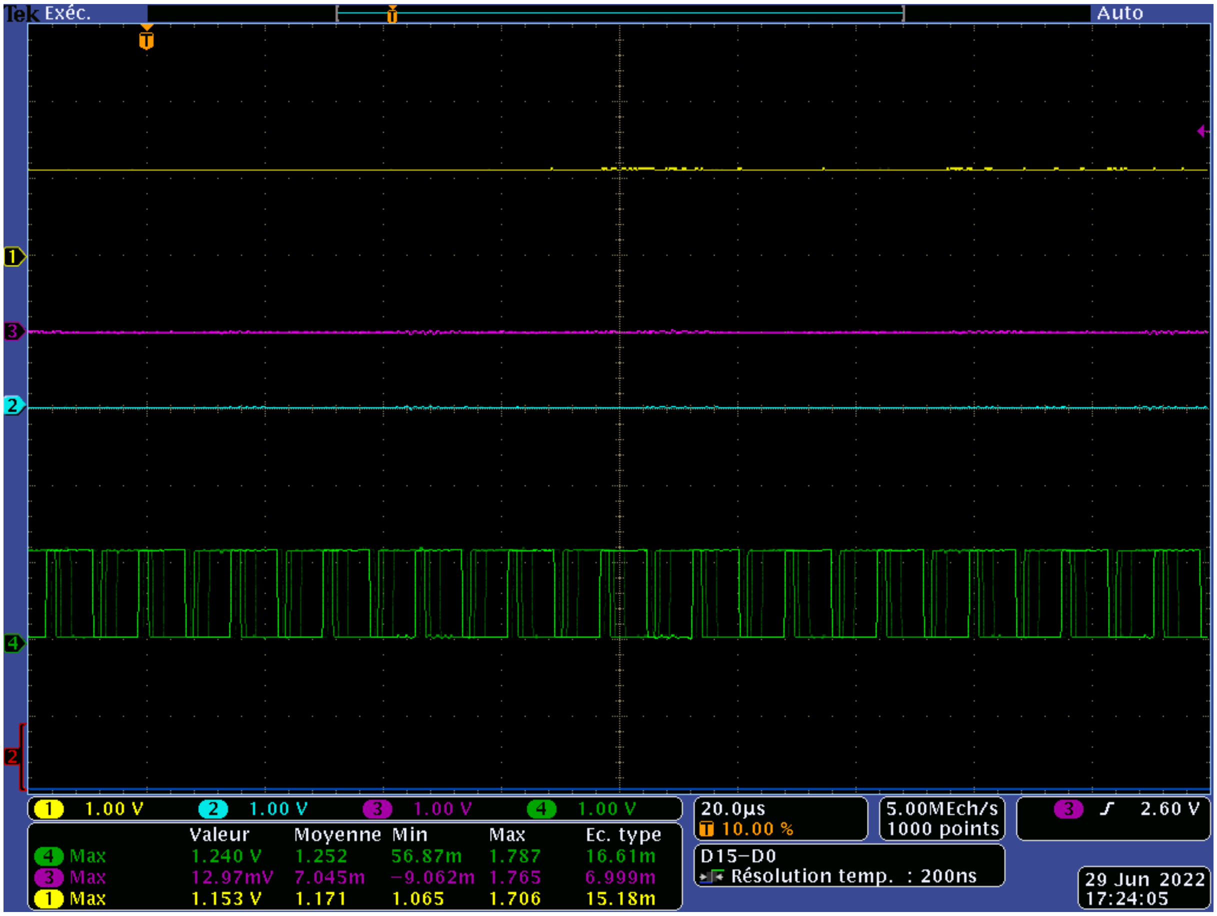

	Valeur	Moyenne	Min	Max	Ec. type
4 Max	1.240 V	1.252	56.87m	1.787	16.61m
3 Max	12.97mV	7.045m	−9.062m	1.765	6.999m
1 Max	1.153 V	1.171	1.065	1.706	15.18m

Figure 6.8: Waveforms at each test point of the PMU in Standby mode of the flyback converter in Deactivation phase. These test points are illustrated in Fig. 5.29 (Yellow: V_{store} – presenting the voltage at the storage capacitor; Blue: V_{arm} – presenting the activation of Armstrong converter; Purple: V_{load} – presenting the output voltage of the PMU; Green: V_{osc} – presenting the signal generated by the oscillator of the flyback converter).

As plotted in Fig. 6.8, the voltage across the storage capacitor V_{store} is still higher than the low-level threshold voltage of the UVLO#1, this UVLO is in closed state. The oscillator TS3002 of the flyback converter is still supplied and the oscillating signal is generated. This keeps the flyback converter staying in operation. Moreover, because V_{store} is higher than the threshold voltage of the Blocking JFET of the Armstrong converter, this converter is deactivated. As a proof, V_{arm} is always zero during this phase.

However, V_{store} is lower than the low-level threshold voltage of UVLO#2, this electrical part is in opened state. Therefore, the output voltage at the load V_{load} is zero in this case.

When the (RF) input power of the PMU is high enough such that V_{store} reaches the high-level threshold voltage of the UVLO#2, the connection between the output load and the PMU will be re-established and the PMU will return to *Normal operation* phase. Nevertheless, if the input power of the PMU becomes lower, the PMU will be deactivated completely.

The standby mode of the flyback converter corresponds to an operation where the DC power extracted from the (RF) input power is dissipated in the losses of the components of the circuit. No energy may be given to the load. This is another way to appreciate the high level of losses in the PMU. This is a question of technology.

Cette thèse est accessible à l'adresse : https://theses.insa-lyon.fr/publication/2023ISAL0007/these.pdf
© [X.V.L. NGUYEN], [2023], INSA Lyon, tous droits réservés

6.5. PMU with rectenna of the Flower Pot

In this section, the operation of the PMU will be analyzed when connected to the rectenna of the Flower Pot. This rectenna is shown in Fig. 6.9. The antenna and the rectifier are manufactured separately in a first step to ease the measurement. Afterwards, the transmission lines of each port of the rectifier are soldered manually to the feeding lines of the antennas respectively. The substrates' dimensions of the antenna and the rectifiers are calculated and managed so that both parts are well fitted with each other during assembly.

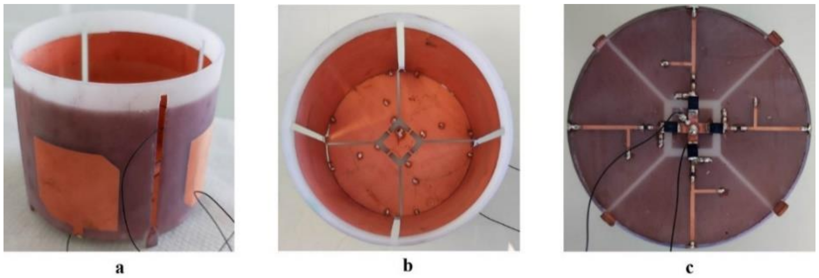

Figure 6.9: Flower Pot (a. Circular polarization patch antenna; b. Inside of the object – Ground planes of antennas and rectifier; c. The four ports rectifier)

The measurement setup is presented in Fig. 6.10. The transmitting antenna is a linear polarization patch antenna realized on Rogers 4003C as described in section 4.3.1 in Chapter 4. This antenna's gain is measured as 5.3 dB. The transmitting antenna is linked to an adjustable RF source. The attenuation of connection cables between this antenna and the source is measured and the obtained value is 1.3 dB at 2.45 GHz. The distance between the transmitting antenna and the rectenna is (0.11 ± 0.001) m. This distance ensures the condition of Fraunhofer Far-field region of the antenna, whose radius is 0.035 m.

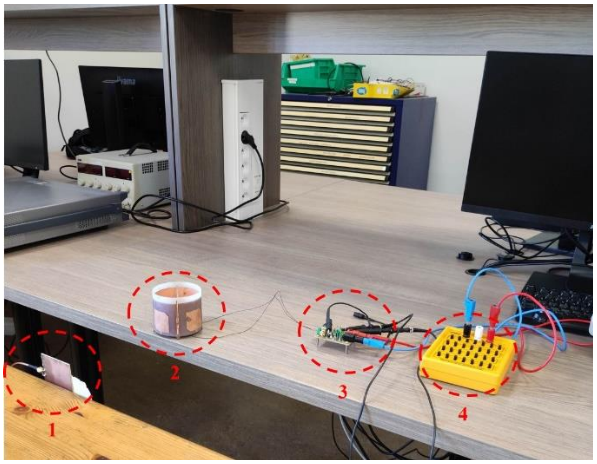

Figure 6.10: Measurement setup to study the performance of the whole circuit (1. Transmitting patch antenna; 2. receiving antennas with the four-port rectifier; 3. Power Management Unit under test; 4. Variable load)

Since the measurements are carried out in a normal environment, the Friis' equation is not applicable. To get the receiving power value of the antenna of the Flower Pot, another identical system of antenna is used. One antenna is linked to a Spectrum Analyzer to measure the receiving power while the three others are connected to 50 Ω in order to avoid the re-radiating phenomenon. As described in Chapter 4, the antenna of the Flower Pot is a circular polarization patch. The whole circuit will be tested in two orthogonal planes: vertical and horizontal.

Cette thèse est accessible à l'adresse : https://theses.insa-lyon.fr/publication/2023ISAL0007/these.pdf
© [X.V.L. NGUYEN], [2023], INSA Lyon, tous droits réservés

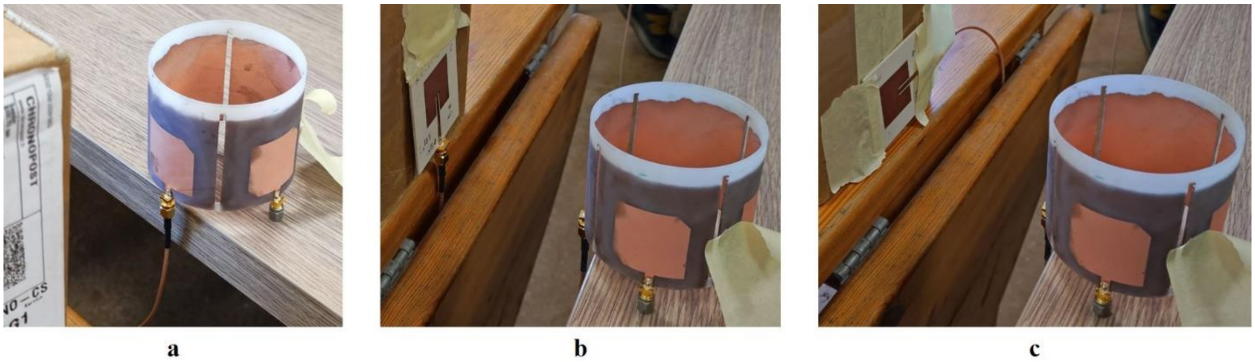

Figure 6.11: Measurement setup to obtain the receiving power of the circular polarization patch antenna of Flower Pot (a. Receiving antenna; b. Transmitting patch antenna in vertical plane; c. Transmitting patch antenna in horizontal plane)

In order to obtain the same results as illustrated in Fig. 6.3, the receiving power of the antenna of Flower Pot should be around -7.2 dBm. We have a slight difference between this value with the one mentioned in Section 6.4 because of the impedance mismatch loss between the antenna and the rectifier. As the impedance of the antennas and the rectifiers are not purely resistive (50 Ω) and they are not identical with each other at 2.45 GHz, this loss will still exist. Besides, the receiving power of the antennas in other positions (side-by-side position and opposite position) is also measured. The measured results are -35 dBm for the side-by-side position and -37 dBm for the opposite position. Due to these results, we observe that the rectifier connected with those antennas will provide very low power to the PMU and they can be neglected compared to the receiving power of the first antenna.

To achieve that the receiving power value, in vertical plane, the transmitting power by the linear polarization patch antenna is around 10.5 dBm meanwhile in the horizontal plane, this parameter should be around 11.3 dBm. The difference between these values is in agreement with the experimental radiation pattern of the antenna in Section 4.3.2.4 of Chapter 4.

The waveform results of the PMU are plotted in Fig. 6.12.

Cette thèse est accessible à l'adresse : https://theses.insa-lyon.fr/publication/2023ISAL0007/these.pdf
© [X.V.L. NGUYEN], [2023], INSA Lyon, tous droits réservés

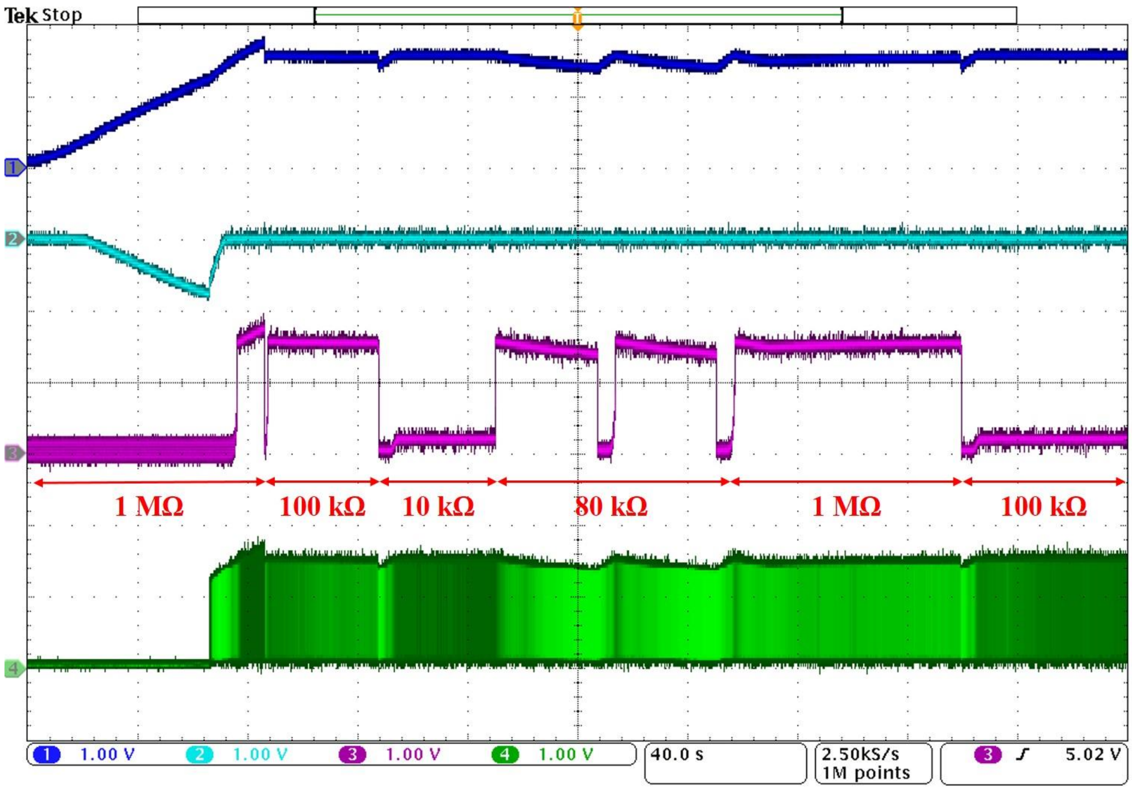

Figure 6.12: Emitting patch in vertical plane configuration (10.5 dBm), main voltage waveforms inside the PMU (Blue curve: V_{store}; Light blue curve:V_{arm}; Purple curve: V_{out}; Green curve: V_{osc}).

At 1 MΩ and 100 kΩ of load, the maximum output voltage is 2.2 V and 1.6 V, respectively, with an input voltage of 0.26 V. The voltage amplification ratio is around 6.15. The global efficiency of the whole circuit (antenna, rectifier and PMU) at this value of load is 13.4 %. We have a lower global efficiency here since a higher RF input power is required to get the same level of input and output voltage at 100 kΩ as the load.

The flyback converter stays in *Standby mode* as long as the receiving power of the antenna is approximately higher than -11.5 dBm.

6.6. Wrap-Up

The operation of the proposed Power Management Unit with discrete components is verified. Three operation phases of the circuit are demonstrated, which are *Cold start, Transition,* and *Normal operation*. The measurements show that the cold start voltage of the circuit is around 0.26 V obtained with an input power of -7.5 dBm (RF) input power to the rectifier with a global efficiency of 14.8 % with a load of 100 kΩ.

A comparison of global efficiency, controller quiescent current, cold start voltage between our work and our state-of-art is realized.

Our circuit has a lower global efficiency than other works in the scale of -8 to -7 dBm (RF) input power. This global efficiency can be improved by using a lower consumption oscillator for the flyback and/or using a higher primary inductor of the coupled inductor in the flyback configuration.

The circuit can start operating by itself as long as the input voltage is higher than 0.26 V. In fact, this value of cold start voltage can be decreased by using a higher turn ratio between the secondary and the primary inductors of the transformer of the Armstrong converter.

Cette thèse est accessible à l'adresse : https://theses.insa-lyon.fr/publication/2023ISAL0007/these.pdf
© [X.V.L. NGUYEN], [2023], INSA Lyon, tous droits réservés

The MPPT scheme is not deployed in our circuit. One solution would be to insert an active circuit to modify the switching frequency of the oscillator in order to seek the Maximum Power Point of the PMU for each different possibility.

In the *Deactivation* phase, *Standby mode* of the PMU is also studied. This mode of the flyback converter is obtained with an RF input power of -12 dBm to the rectifier and the corresponding DC voltage of 0.1 V for an output load of 100 kΩ and 1 MΩ.

Our PMU is afterwards tested with the rectenna of Flower Pot. The measurements show a global efficiency of 13.4 % at a load of 100 kΩ with a receiving power of -7.2 dBm of the antenna.

The studies about the performance of the PMU when the rectifier is fed with two and four ports by a RF source or by antennas simultaneously are not yet carried out because of the time constraint of the thesis. In addition, the question of optimizing the storage capacitor (minimum value, minimum size, technique of fabrication, etc.) of the PMU is not yet solved.

Cette thèse est accessible à l'adresse : https://theses.insa-lyon.fr/publication/2023ISAL0007/these.pdf
© [X.V.L. NGUYEN], [2023], INSA Lyon, tous droits réservés

CHAPTER 7: CONCLUSION AND PERSPECTIVES

Cette thèse est accessible à l'adresse : https://theses.insa-lyon.fr/publication/2023ISAL0007/these.pdf
© [X.V.L. NGUYEN], [2023], INSA Lyon, tous droits réservés

Cette thèse est accessible à l'adresse : https://theses.insa-lyon.fr/publication/2023ISAL0007/these.pdf
© [X.V.L. NGUYEN], [2023], INSA Lyon, tous droits réservés

7. CONCLUSION AND PERSPECTIVES

7.1. Conclusion

This work concentrates on the Radio Frequency Energy Harvester designed on rigid substrates in 2D and 3D forms manufactured applying Rapid Plastronics technology for not only mechanical but also electrical purposes. The main contribution of this thesis is to examine and to verify the possibilities of using this new manufacturing technology, Stereolithography for printing the substrates and ElectroLess Deposition (ELD) method for fabricating the conductive traces, in order to realize the RF circuits used in Energy Harvesting applications on the surface of the plastic objects in 2D and 3D forms.

In the approach of manufacturing, among many low-cost printing methods, i.e. Fused Deposition Modeling, Laser Direct Structuring, etc., Stereolithography is preferred due to its high precision, high resolution and high repeatability. The good surface quality is also a bonus of this method. Additionally, this method allows us to create the 2D and 3D objects with high complexity easily. In this thesis, the chosen resins are High Temp (HT) Resin v1 and High Temp Resin v2 from Formlabs because of their high thermal resistance. This parameter plays an important role to give us a preview about the capability of soldering the electrical components later. Afterwards, ELD method is selected in order to obtain the conductive traces on the surface of the printed objects. The advantage of this method is its compatibility to every polymer and non-conductive substrates. Moreover, this method is able to metallize the surface of the object as long as the liquid can go through, which is useful for metallizing the vias. Another advantage is that the resistivity of ELD copper is close to the value of bulk copper and much lower than the conductive inks used in Printed Electronics. In applications of low power energy harvesting, especially RF energy harvesting, the low resistivity of conductor can reduce the conductive loss in the circuits.

Before designing the antennas and the RF circuits, understanding the electromagnetic properties of the substrate, i.e. relative permittivity, loss tangent, and of the conductor, i.e. the resistivity, is an essential step. Two Transmission Lines method is performed to extract the relative permittivity and the loss tangent of the substrates over a wide band of frequency, 0.5-2.5 GHz. The results show that the relative permittivity of the SLA substrates is (3 ± 0.1) and (2.9 ± 0.1), and their loss tangent is (0.025 ± 0.0025) and (0.04 ± 0.0025) over a band of 0.5-2.5 GHz. For the conductor, the measured thickness is around (7 ± 1) µm with an acceptable surface roughness, which is (1 ± 0.2) µm. Low profile surface roughness is an advantage of Plastronics in RF circuits fabrication. Besides, the resistivity of ELD copper is measured using the four-probe method. The measured value is 0.02-0.025 (µΩ.m), which is very close to the bulk copper conductivity, 0.017 (µΩ.m).

In the concept of RFEH circuit, antennas play the role of capturing the EM waves and of transmitting them towards the rectifier for the conversion from EM waves into DC energy. The 2D linear polarization patch antenna deposited on HT Resin v1 is investigated for our first study. A good impedance matching is obtained at 2.45 GHz with a gain of +2.5 dB. The impact of the conductive loss and the dielectric loss on the gain of the antenna is analyzed with the aid of CST Microwave Studio 2019. The study shows that by replacing the HT Resin v1 by a lower loss substrate, i.e. Rogers 4003C, the gain of the antenna can be enhanced to 2.77 dB. The conductive loss of the ELD copper is 0.03 dB in the gain of the antenna. This loss is supposed as negligible, which is less than 0.1 dB, when the resistivity of the conductor is lower than 0.021 µΩ.m.

Literally, the requirement of capturing all the polarizations existing in the air of the RFEH is necessary. In order to validate that requirement, systems of circularly polarized patch antenna are proposed. Firstly, a 2D planar circular polarization patch antenna is obtained. However, its half

Cette thèse est accessible à l'adresse : https://theses.insa-lyon.fr/publication/2023ISAL0007/these.pdf
© [X.V.L. NGUYEN], [2023], INSA Lyon, tous droits réservés

power beamwidth and its directional radiation pattern cannot ensure the full covering around the objects. A system of patch antennas with common ground surfaces is then considered to eliminate these drawbacks. The antennas are deposited on a cylinder with a curvature radius of 40 mm to broaden the HPBW. In addition, the antennas are placed in quadrature positions. From that, the objects can be immerged in the radiation of the antennas. In order to improve the isolation between the antennas in the system, the ground surface is segmented. Each antenna has its own ground surface. The gain of the antenna is also improved due to this configuration. The antennas of the final proposed system, called Flower Pot, are well-matched over a wide band of frequency, which can cover the Wi-Fi 2.45 GHz band. The isolation between the antennas in side-by-side and opposite position are lower than -35 dB and -45 dB respectively. The measured gain of the antenna is around 1.35 dB. The dimensions of the manufactured cylinder are 80π x 70 mm^3.

Two rectifier circuits are also studied. The first circuit is used for the 2D linear polarization patch antenna and the second one is designed for the systems of four circular polarization patch antennas deposited on the cylinder. Both rectifiers have the impedance interference of 50 Ω with the antennas. The circuits are deposited on 2D planar substrates. Because of the time constraint of the thesis, the performance of these circuits when they are deposited on 3D surfaces is not studied yet. The Power Management Unit is also analyzed. For the operation verification, the PMU is assembled from the discrete components. The electrical interference between the rectifier and the PMU is learnt. The Maximum Power Point condition is considered in this thesis. This condition is established by having the impedance matching at the optimal load of the rectifier. Determining the optimal load of the rectifier is therefore necessary. The method of identifying this parameter is introduced. According to the results, the optimal load of the rectifier in the mono-diode series topology is not constant as variation of input power. At -30 dBm, -20 dBm, -10 dBm and 0 dBm, the values are 5 kΩ, 3 kΩ, 2.5 kΩ and 2 kΩ, respectively. Because the designed rectifier for Flower Pot has four ports operating individually, the output load of the circuit is calculated. The circuit is desired to operate for all possibilities, the output load is hence found out as 1 kΩ.

Thereafter, the operation of the PMU is evaluated. The PMU is connected to the rectifier for Flower Pot for the operational test. Four operation phases of the PMU are demonstrated, which are *Cold start, Transition, Normal operation* and *Deactivation*. The measured cold start voltage is around 0.26 V, which are lower than the existing PMUs in the market. The *Standby mode* of the flyback of our PMU is also studied. The results show that the flyback enters this mode when the input power of the rectifier is around -12 dBm with the corresponding input voltage of the PMU of 0.1 V. At the input power of -7.5 dBm of the rectifier, the output voltage of the PMU is 1.62 V with a PMU boost ratio of 6.14 with a load of 100 kΩ. The global efficiency of the whole circuit is 14.8 %. When the PMU is connected to a rectenna, the global efficiency is 13.4 %.

7.2. Perspectives

In the aspect of polymers, the selected SLA substrates have high loss, which create the lossy impacts on the performance of the antennas and the RF circuits. Another limitation of these materials is their fragility. Other materials can be considered here such as LCP, PEEK, etc., which are high temperature super engineering polymers. The loss tangent of these materials is very low and this can reduce the dielectric loss in the antennas and the RF circuits. In addition, these materials have a very good thermal resistance, therefore, soldering the SMDs on their surface can be easily done. The main drawback here is the technology of manufacturing these materials are not as mature as SLA and is much more expensive and complex. Another drawback is that with a lower loss tangent, the patch antennas might have a narrower band of frequency.

Cette thèse est accessible à l'adresse : https://theses.insa-lyon.fr/publication/2023ISAL0007/these.pdf
© [X.V.L. NGUYEN], [2023], INSA Lyon, tous droits réservés

For the antenna design, the study of curving the antennas in two or multi directions, i.e. the sphere, can be envisaged. The miniaturization of the antennas can be as well considered to reduce their form factor. In addition, the feeding method of our antennas is the transmission line method. To reduce their total size, the idea of using the probe feed method or the coupled line method may be considered. However, manufacturing multi-layer electric circuits and electric vias in Rapid Plastronics is still in research. Once the manufacturing method is well managed, the study of the equivalent electrical model and the impact of the plastronic via in RF domain should also be discussed.

For the rectifier design, modeling the diode used in the rectifier is a necessary process to understand more about the behavior of the diode. In addition, designing a rectifier on a non-planar surface is an interest to follow afterwards.

Our Power Management Unit is tested using the discrete components, i.e. transistors, oscillators, etc. The efficiency of our circuit is lower than our state-of-art. This parameter of our PMU can be improved by

- Replacing the discrete oscillator TS3002 by the lower consumption oscillator in form of IC (i.e. ring oscillators).
- Using a higher primary inductor of the coupled inductor to improve the efficiency of the flyback converter.
- Adding the MPPT scheme in the configuration of our PMU. This idea can be realized by using an active circuit to vary the switching frequency of the flyback converter in order to make the input impedance of the converter equal to the optimal load of the rectifier.

The cold start voltage of our PMU can be reduced more by using a higher turn ratio between the secondary and the primary inductors of the transformer of the Armstrong converter and/or using a lower threshold voltage, lower zero-gate voltage drain current JFET.

The storage capacitor of the PMU is not optimized yet. A study about the value and the dimensions of this component can be mentioned to minimize the total size as well as to ensure the operation of the consumption load, which are the microcontrollers and the sensors.

During the PMU test, only one branch of the four-port rectifier is supplied. The question about the performance of the PMU when the two or four branches of this rectifier are fed simultaneously can be discussed. As estimated, the more branches participate the operation, the more power received by the PMU. This might reduce the charging time of the storage capacitor.

Because of the fabrication and shipment delay of components, the final circuit with the selected microcontroller and sensor cannot be tested at the end of this thesis. A test with the final circuit should be deployed to qualify the operation of the demonstrator.

Cette thèse est accessible à l'adresse : https://theses.insa-lyon.fr/publication/2023ISAL0007/these.pdf
© [X.V.L. NGUYEN], [2023], INSA Lyon, tous droits réservés

Cette thèse est accessible à l'adresse : https://theses.insa-lyon.fr/publication/2023ISAL0007/these.pdf
© [X.V.L. NGUYEN], [2023], INSA Lyon, tous droits réservés

RESUME ETENDU EN FRANCAIS

Cette thèse est accessible à l'adresse : https://theses.insa-lyon.fr/publication/2023ISAL0007/these.pdf
© [X.V.L. NGUYEN], [2023], INSA Lyon, tous droits réservés

Cette thèse est accessible à l'adresse : https://theses.insa-lyon.fr/publication/2023ISAL0007/these.pdf
© [X.V.L. NGUYEN], [2023], INSA Lyon, tous droits réservés

0. Introduction

Nous sommes dans une nouvelle ère de technologie, appelée Internet of Things (IoT) ou Internet des Objets, où les appareils électriques communiquent entre eux sans fil. Les appareils d'IoT trouvent leurs rôles dans de nombreux domaines, tels que les télécommunications, l'éducation, les soins de santé, les domaines industriels, etc. En raison de leur développement rapide, ces appareils apparaissent partout dans notre vie quotidienne sous nombreuses formes, de la petite taille (des capteurs autonomes, des téléphones mobiles, etc.), ou même de grande taille telle que des véhicules, des drones, des appareils ménagers, des installations d'usines, etc.

Selon Cisco, le nombre d'appareils connectés est estimé à atteindre 500 milliards d'ici 2030, soit environ 59 fois plus que la population mondiale à ce moment.

Un obstacle à surmonter dans le développement des appareils IoT est le système d'alimentation en énergie. L'utilisation de piles pour ces appareils n'est pas une solution durable. Le remplacement régulier des batteries est souvent compliqué. En plus, jusqu'à 78 millions de batteries d'appareils IoT devraient être jetées quotidiennement d'ici 2025 si rien n'est fait pour améliorer leur durée de vie. Par ailleurs, la plupart des batteries contiennent des métaux et des produits chimiques causant des impacts nocifs à l'environnement et à la santé humaine. Par conséquent, le remplacement des batteries par d'autres sources qui sont « eco-friendly » avec l'environnement pourrait être considéré comme une solution d'obtenir des appareils à longue durée de vie.

Récupérer l'énergie ambiante disponible dans l'environnement et la convertir en énergie DC semble une solution désirable. De nombreux circuits sont développés en récupérant l'énergie thermique, l'énergie mécanique, la lumière ou les ondes de radiofréquence (RF). Parmi eux, les circuits de récupération d'énergie de radiofréquence (RFEH) peuvent supposer comme des bons candidats quand il n'y a pas de lumière, pas de chaleur ou lorsque les objets ne bougent pas.

Un RFEH consiste de trois blocs principaux. Le premier bloc est dédié à capturer les ondes électromagnétiques ambiantes et à les transférer au redresseur RF-DC pour transformer l'énergie RF en DC. L'unité de gestion de puissance (PMU) du deuxième bloc contient un convertisseur DC/DC, qui contrôle le flux d'énergie vers un dispositif de stockage (un condensateur, une batterie, etc.), et un superviseur de tension (VS), qui transfère l'énergie DC au troisième bloc – la charge de consommation – ou coupe cette liaison lorsque le périphérique de stockage est trop épuisé. La charge de consommation peut être les microcontrôleurs, les capteurs, etc.

Les procédés de fabrication conventionnels pour les circuits électroniques permettent de fabriquer du RFEH en assemblant une carte de circuit imprimé (PCB) rigide en 2D et/ou une carte de circuit imprimé semi-rigide/flexible (également appelée FLEX-PCB). Bien qu'assez efficace en ce qui concerne la capture de l'énergie RF (grâce à l'utilisation d'antennes patch par exemple) et l'électronique (efficacité de la conversion RF-DC), les possibilités permises par la fabrication conventionnelle de RFEH sont limitées au niveau mécanique, même au niveau géométrique le plus élémentaire.

À d'autres égards, un inconvénient du RFEH en général est l'empreinte géométrique, en particulier en ce qui concerne la surface de l'antenne à basse fréquence, qui est difficile à réduire tant pour des raisons théoriques (rapport entre les dimensions de l'antenne et la longueur d'onde) que pour des raisons pratiques (la permittivité relative et la tangente de perte des substrats). Par conséquent, de nouvelles solutions basées sur l'utilisation de multiples rectennas (éventuellement avec des orientations, une polarisation et même une fréquence de travail différente) peuvent être intéressantes.

Cette thèse est accessible à l'adresse : https://theses.insa-lyon.fr/publication/2023ISAL0007/these.pdf
© [X.V.L. NGUYEN], [2023], INSA Lyon, tous droits réservés

Dans ce travail, nous espérons explorer des possibilités de fabriquer RFEH avec une stratégie basée sur une nouvelle technologie appelée Plastronique, qui permet de contourner certaines limitations imposées par l'assemblage conventionnel de PCB et FLEX-PCB.

La Plastronique est la convergence des plastiques et de l'électronique afin de créer les traces conductrices (y compris les antennes) et de monter les Composants Montés en Surface (CMS) sur toute forme de surfaces polymères, de la 2D à la 3D, du simple au complexe.

Par rapport aux techniques de fabrication conventionnelles de PCB et de FLEX-PCB, la Plastronique nous offre des avantages spécifiques afin de

- Intégrer des antennes et des CMS sur le boîtier en polymère des appareils électroniques (comme indiqué ci-dessous, la plupart des téléphones mobiles contiennent déjà des antennes plastroniques pour les télécommunications, etc.)
- Combiner une grande variété de matériaux polymères avec des circuits électroniques (contrairement au PCB et au FLEX-PCB qui sont limités à quelques polymères non utilisables pour former un tel boîtier)
- Simplifier les interconnexions électriques entre les différents blocs d'un appareil
- Simplifier le processus d'assemblage, etc.

La Plastronique permet d'intégrer l'électronique à la surface d'objets polymères, souvent largement inutilisés. Ainsi, au lieu de miniaturiser les rectennas des RFEH, il serait peut-être avantageux d'organiser plusieurs RFEH sur la même surface. Après tout, le nombre de sources de RF ambiantes, leurs distances et leurs orientations par rapport au RFEH sont inconnus.

Il existe différents processus pour élaborer des circuits plastroniques. Cependant, la plupart d'entre eux sont industriels, nécessitant un outillage coûteux et complexe (par exemple, un moule d'injection), ne convenant pas à un travail de recherche. De plus, les méthodes existantes pour le prototypage de dispositifs plastroniques ne sont pas complètement satisfaisantes (par exemple, la section sur le procédé ProtoPaint dans la thèse de S. Kamotesov[5]).

Par conséquent, l'objectif de ce travail est de démontrer la faisabilité du RFEH avec une technologie de la Plastronique et peu coûteuse développée dans notre laboratoire, adaptée au prototypage. Cette technologie, appelée Plastronique Rapide, est basée sur la fabrication du substrat de l'appareil par impression 3D, en utilisant la Stéréolithographie (SLA), et la réalisation des traces conductrices en appliquant la métallisation autocatalytique (ELD). L'objectif n'était pas de développer cette technologie mais de l'appliquer dans le contexte de RF (ce qui n'était pas fait auparavant) et de RFEH.

Les contextes de cette thèse sont :

- Développer d'un RFEH dédié aux capteurs de faible consommation pour l'IoT
- Intégrer d'une rectenna avec une unité de gestion de la puissance (PMU) discrète et un dispositif de stockage.
- Démontrer d'un véhicule d'essai autonome fabriqué à l'aide de la Plastronique Rapide utilisant des charges résistives.

Un point spécifique est qu'en raison du très faible niveau d'énergie ambiante disponible, la fabrication du RFEH ne peut pas être directement dérivée des méthodes utilisées pour obtenir des antennes plastroniques pour les télécommunications. La connexion du redresseur avec l'antenne a

---

[5] Sergkei Kamotesov. Transmission d'énergie par induction électromagnétique en plastronique 3D. Electronique. Université de Lyon, 2019. Français. ⟨NNT : 2019LYSE1353⟩. ⟨tel-02496934⟩

Cette thèse est accessible à l'adresse : https://theses.insa-lyon.fr/publication/2023ISAL0007/these.pdf
© [X.V.L. NGUYEN], [2023], INSA Lyon, tous droits réservés

été soigneusement conçue et réalisée. Afin de réaliser cela, il est nécessaire d'améliorer notre compréhension de nombreuses questions liées à la RF, à l'électronique à faible niveau de puissance, aux propriétés des matériaux et au traitement des matériaux. On m'a demandé de travailler sur les deux premiers points et de coopérer avec des spécialistes des matériaux en ce qui concerne les deux autres points et d'utiliser leurs résultats. Par conséquent, il est intéressant de classer les difficultés en termes de questions scientifiques et techniques comme suit :

Questions scientifiques

- Propriétés électromagnétiques du polymère sur la gamme de RF : la permittivité relative, la tangente de perte.
- Propriétés du conducteur : la conductivité/résistivité, l'épaisseur de dépôt, la rugosité de surface.
- Concept d'antennes et de redresseurs RF-DC pour le RFEH proposé.

Questions technologiques

- Interconnexion électrique des composants et des fonctions dans le circuit :

Quels sont les principaux paramètres ?
Comment réaliser l'interconnexion ?

- Types et formes d'antennes pour le RFEH proposé.
- La méthodologie de simulation des antennes et des redresseurs RF-DC.

Ce manuscrit se compose de sept chapitres.

Dans le premier chapitre, un bref état de l'art sur la Plastronique est rapporté. Des exemples d'antennes 3D fabriquées à l'aide des méthodes d'impression 3D sont également discutés. Plusieurs aspects de la Plastronique Rapide sont rapportés pour motiver ce travail.

Le deuxième chapitre donne une revue des circuits de récupérateurs d'énergie dans la littérature. Les topologies du redresseur seront présentées. L'intérêt des différentes antennes (antenne patch, antenne dipôle, etc.) pour le RFEH est discuté. En outre, l'interaction entre l'antenne, le redresseur et le PMU seront également mentionnés. Quelques exemples de rectennas 2D et de rectennas 3D seront présentés.

Dans le troisième chapitre, la Plastronique Rapide sera décrite. Cela inclut la méthode de fabrication du substrat, le processus de réalisation des traces conductrices et la méthode de connexion des CMS aux traces. Le substrat et le conducteur ont toujours des effets cruciaux sur les performances des antennes et des circuits RF. Par conséquent, les étapes d'extraction des propriétés électromagnétiques du conducteur et du substrat réalisés seront présentées. La méthode de mesure de la permittivité relative, la tangente de perte du substrat déployée dans cette thèse sera également présentée. Une comparaison entre les matériaux sélectionnés et ceux de la littérature sera donnée.

Ensuite, dans le quatrième chapitre, la conception de l'antenne patch est discutée. En effet, il devrait respecter certaines exigences pour les applications de récupération d'énergie. Les exigences les plus importantes sont que la bande passante de fréquence souhaitée de l'antenne, qui est choisie pour couvrir la portée Wi-Fi (2,45 GHz), avec la possibilité de capturer toutes les polarisations autour de l'objet. L'antenne patch est choisie en raison de sa simplicité de conception électrique. La masse complète du patch peut réduire les impacts des éléments placés derrière le plan sur les performances rayonnantes de l'antenne. La configuration des antennes patch sera étudiée pour répondre aux exigences précédentes. Des outils de simulation électromagnétique seront utilisés pour obtenir la conception d'antenne la plus appropriée pour le démonstrateur final.

Cette thèse est accessible à l'adresse : https://theses.insa-lyon.fr/publication/2023ISAL0007/these.pdf
© [X.V.L. NGUYEN], [2023], INSA Lyon, tous droits réservés

Une antenne patch polarisée linéaire fondamentale fonctionnant à 2,45 GHz est mentionnée en premier. L'étude des impacts du substrat et des conducteurs sur les performances rayonnantes de l'antenne patch sera également présentée. Ensuite, pour satisfaire aux exigences de capture de toutes les polarisations dans l'air de l'antenne pour RFEH, la configuration proposée d'antennes patch à polarisation circulaire sera décrite.

Le cinquième chapitre montre la méthode de simulation et de conception du redresseur pour les antennes conçues dans le chapitre précédent. La méthodologie de simulation et de conception de ce circuit pour la bande Wi-Fi sera mentionnée. Le PMU est généralement ajouté après le redresseur dans le but d'augmenter la basse tension rectifiée à la tension de fonctionnement minimale de la charge et de réguler la tension de sortie boostée. L'interconnexion électrique entre l'antenne, le redresseur et le PMU sera étudiée.

La technique de correspondance de l'impédance de 50 Ω entre l'antenne et le redresseur sera présentée. De plus, ce chapitre donne un aperçu de l'identification de la charge optimale du redresseur à différents niveaux de puissance d'entrée. La charge optimale du redresseur conçu pour le démonstrateur sera étudiée. Cela offre une vision de la mise en place de l'interférence d'impédance entre le redresseur conçu et le PMU.

Le sixième chapitre présente les résultats expérimentaux des RFEH fabriqués à l'aide de la technologie Plastronique Rapide. Tout d'abord, le comportement électrique du PMU se connectant au redresseur conçu est étudié en variation de la charge de sortie (1 MΩ, 100 kΩ, 80 kΩ et 10 kΩ). Ensuite, le RFEH plastronique avec l'antenne présentée au chapitre 4 sera testé dans le but de vérifier les performances de l'ensemble du circuit. Une comparaison avec l'état de l'art sera également discutée.

Enfin, en conclusion, nous résumons les travaux déployés dans cette thèse. Les améliorations suggérées et les perspectives concernant les RFEH plastroniques sont présentées.

Cette thèse est accessible à l'adresse : https://theses.insa-lyon.fr/publication/2023ISAL0007/these.pdf
© [X.V.L. NGUYEN], [2023], INSA Lyon, tous droits réservés

1. Etat de l'art sur la Plastronique

Dans ce chapitre, nous rapportons les différentes méthodes de fabrication des circuits électriques de forme 2D et 3D, qui sont PCB et FLEX-PCB, l'électronique imprimée (PE) et la 3D Plastronique.

PCB et FLEX-PCB sont des méthodes conventionnelles, et sont développés et optimisés en grande partie. Cependant, ces méthodes utilisent quelques substrats pour la fabrication tandis que la Plastronique dispose d'une grande variété de substrats qui ne sont généralement pas (encore) optimisés. Cela peut donner de nouvelles possibilités de choisir les substrats à faible perte pour les applications de récupération d'énergie RF.

L'électronique imprimée est une méthode proche de la Plastronique. L'inconvénient principal de cette méthode est la résistivité électrique élevée de l'encre conductrice utilisée dans la fabrication. Cela peut augmenter la perte dans les RFEHs, puis réduire les performances des circuits.

En comparaison avec l'électronique imprimée, pour la Plastronique, le conducteur, appelé cuivre sans électrode, est obtenu en utilisant la méthode ELD, dont la résistivité est proche de celle du cuivre massif. Un autre avantage de cette méthode de métallisation est que la surface des objets peut être métallisée tant que le liquide peut passer.

Afin de fabriquer les substrats polymères, en Plastronique, les méthodes courantes sont le moulage par injection et/ou le thermoformage. Ces méthodes sont très appropriées pour la production de masse. Néanmoins, avec une forme complexe de substrats, les moules utilisés sont très coûteux et le déploiement est compliqué. Par conséquent, les méthodes d'impression 3D, c'est-à-dire la modélisation par dépôt de fusion, le frittage laser, la Stéréolithographie, sont préférées en cas de prototypage de quelques substrats 3D pour la recherche. Parmi les trois méthodes, la Stéréolithographie est une solution pratique en raison de sa bonne finition de surface avant durcissement et de l'absence de porosité. De plus, l'utilisation de polymères à performance thermique acceptables (High Temp Resin v1 et High Temp Resin v2 dans cette thèse) peut nous permettre de souder les CMS à la surface des polymères.

Lors de notre première tentative, les résines SLA sont sélectionnées. Cependant, ces résines ont de mauvaises propriétés RF. Le LCP et le PEEK, qui sont couramment utilisés comme substrats d'antennes téléphoniques, peuvent être envisagés pour remplacer ces résines SLA en raison de leurs bonnes propriétés RF et thermiques.

Cette thèse est accessible à l'adresse : https://theses.insa-lyon.fr/publication/2023ISAL0007/these.pdf
© [X.V.L. NGUYEN], [2023], INSA Lyon, tous droits réservés

2. Etat de l'art sur la récupération d'énergie ambiante

Dans ce chapitre, nous rapportons le principe des différents mécanismes des circuits de récupération d'énergie ambiante, qui sont des énergies thermique, mécanique, solaire et radiofréquence. Leur densité d'énergie mesurée disponible dans l'environnement, leurs avantages et leurs inconvénients sont mentionnés plus loin. Le RFEH est un candidat approprié comme source d'alimentation pour les cas particuliers où aucune autre énergie disponible de potentiel plus élevé et si la charge utile nécessite un très faible niveau d'énergie (ou accepte de fonctionner sporadiquement). Le faible coût et la disponibilité des ondes RF dans la vie quotidienne (environnements intérieurs et extérieurs) sont les avantages. Néanmoins, le faible niveau de densité de puissance des ondes RF est un inconvénient. Le concept de RFEH ne peut répondre qu'à une très faible consommation de production, à moins que les stratégies de stockage à long terme ne soient considérées comme servant des charges d'exploitation sporadiques.

Ensuite, la structure électrique d'une rectenna (RECTifier et anTENNA) est présentée. Différents types de topologies existantes du redresseur ainsi que l'interférence d'impédance entre cette partie et l'antenne sont introduits. L'adaptation d'impédance de 50 Ω est sélectionnée principalement pour des raisons pragmatiques, bien que ce ne soit pas la meilleure option. Puis, l'unité de gestion de la puissance est également concernée. Cette partie électrique optionnelle est proposée essentiellement dans le but d'augmenter et de contrôler la tension de sortie de la rectenna à une valeur souhaitée de la charge de consommation. L'adaptation d'impédance entre le PMU et le RF-DC redresseur est également analysée. La condition Maximum Power Point (MPP) est suggérée pour la correspondance d'impédance afin de maximiser la puissance de sortie de l'ensemble du système.

Les rectennas 2D et 3D développés dans la littérature sont répertoriés comme faisant partie de l'état de l'art. Les techniques courantes pour créer des rectennas 3D sont les suivantes :

- Assemblage des pièces de PCB 2D dans une forme 3D simple.
- Utilisation de matériaux flexibles pour les substrats et la technique d'impression à l'encre ou de textile conducteur pour obtenir les circuits 3D.
- Impression directe des formes 3D pour le substrat et utilisation de la technique d'impression à l'encre. La première technique nous donne les circuits avec une bonne résistance mécanique avec une bonne performance électrique. Néanmoins, la limite de cette technique est sa faible diversité et la complexité de l'assemblage. Il semble par exemple difficile d'intégrer de tels RFEH fabriqués dans la plupart des appareils existants.

Pendant ce temps, les paramètres peuvent être améliorés avec la deuxième technique. Cependant, la rigidité des circuits fabriqués est un inconvénient majeur de cette technique.

Avec l'aide de la fabrication additive, la troisième technique semble un bon choix pour améliorer la complexité et la rigidité des circuits 3D fabriqués. De plus, cette technique peut être appliquée à la fabrication d'appareils 5G émergents.

En effet, la question de la conductivité du conducteur peut être résolue en passant la méthode ELD, ce qui nous donne un bien meilleur conducteur.

Cette thèse est accessible à l'adresse : https://theses.insa-lyon.fr/publication/2023ISAL0007/these.pdf
© [X.V.L. NGUYEN], [2023], INSA Lyon, tous droits réservés

3. Fabrication et Caractérisation des matériaux

3.1. Fabrication

Stéréolithographie – Méthode d'impression des substrats

Dans cette thèse, les objets sont imprimés avec des imprimantes Form2 et Form3 de Formlabs en utilisant le photopolymère High Temp (HT) Resin v1 et HT Resin v2 de Formlabs. Ces résines sont sélectionnées en raison de leur bonne résistance aux hautes températures (environ 289°C à 0,45 MPa pour le HT Resin v1 et 238 °C à 0,45 MPa pour le HT Resin v2) ce qui permet aux composants électriques d'être facilement soudés sur la surface des substrats plus tard.

La Stéréolithographie (SLA) est développée sur la base de la polymérisation de résines photosensibles. Comme cette méthode est additive, l'objet fabriqué est construit couche par couche dans un réservoir de photopolymère sous l'action d'un laser d'une longueur d'onde définie. Une machine SLA contient des pièces matérielles, qui sont une plate-forme construite submergeant le réservoir de résine liquide et la source laser, et une partie logicielle utilisée pour contrôler le processus d'impression. Les objets 3D avec des structures de support, qui sont nécessaires pour soutenir et maintenir la forme des pièces imprimées pendant le processus, sont convertis en assemblage de tranches 2D. Ces tranches 2D correspondent à la trace du laser solidifiant la résine et créant ainsi les couches des objets. Ce processus sera répété jusqu'à ce que les objets soient finis. La durée dépend de la quantité de tranches 2D d'impression, des dimensions, de la surface de ces tranches, du type de résine, etc. Ensuite, les objets imprimés sont retirés de la machine et les restes de résine liquide sur les objets sont nettoyés par l'application d'un solvant, c'est-à-dire l'isopropanol. Les objets produits par la SLA ne sont généralement pas entièrement polymérisés. Par conséquent, des fours UV sont nécessaires pour un durcissement final. Les structures porteuses peuvent être retirées manuellement avant ou après durcissement dans les fours UV. Enfin, les objets sont ensuite poncés pour enlever complètement les restes de structures porteuses sur leurs surfaces.

Métallisation autocatalytique

La métallisation de l'objet est la prochaine étape du processus de fabrication. L'objet est immergé dans un bain de solution catalytique au palladium (Macuplex Activator-D34C, MacDermid), rincé à l'eau et déposé dans un réservoir de cuivre sans électrode (MidCopper 100XB, MacDermid) pendant environ 120-180 min. La surface des objets est entièrement métallisée avec du cuivre de 6-7 µm typique de l'épaisseur.

Méthode de gravure du conducteur

Après avoir déposé une couche conductrice en appliquant la méthode ELD, afin de créer les traces conductrices désirables sur la surface des objets, une étape de gravure est nécessaire. Une méthode soustractive est appliquée pour cette étape. Les masques d'un polyvinyle spécifique sont découpés à l'aide de la fraiseuse CAMM-1 GS-24 de Roland suivant la conception des circuits avec la dimension de coupe minimale de 12,5 µm par coupe. En effet, la précision des traces conductrices gravées dépend de ce paramètre de la machine de découpe. Ces masques couvriront les traces conductrices souhaitées déposées sur les objets. Après cela, les objets masqués seront plongés dans un bain de perchlorure de fer pour éliminer totalement les parties conductrices déposées indésirables. La durée du processus dépend de l'épaisseur du conducteur déposé. Dans notre cas, le temps moyen de gravure est d'environ 1 minute. Une fois le processus de gravure terminé, les objets sont nettoyés à l'eau et les masques sont retirés mécaniquement. Les objets sont ensuite séchés avec l'air comprimé pour éliminer l'eau restante sur la surface des objets.

Cette thèse est accessible à l'adresse : https://theses.insa-lyon.fr/publication/2023ISAL0007/these.pdf
© [X.V.L. NGUYEN], [2023], INSA Lyon, tous droits réservés

Méthode de montage des composants

Le montage des composants électriques sur la surface d'objets métallisés par la méthode ELD est la dernière étape du processus de fabrication. Les composants peuvent être soudés manuellement à l'aide d'un matériau de brasage standard sur la surface de l'objet. Cependant, cette méthode passe du temps à finir, la qualité des soudures n'est pas assurée et n'est pas précise.

Une autre méthode consiste à utiliser un four de refusion afin d'effectuer la soudure. Le four a une forme de long tunnel constitué d'une bande transporteuse pour parcourir les circuits. À l'intérieur du four, il y a plusieurs sources de chaleur. La vitesse de la bande transporteuse et la température du four sont contrôlées par un ordinateur pour respecter le profil de refusion recommandé de la pâte de braser appliquée. Le profil de refusion est un profil de température dans le four en fonction de la variation de température recommandée pour la soudure des pièces.

Etapes de fabrication

Les étapes de fabrication peuvent être résumées comme suit :

- Imprimer des objets en plastique à l'aide de la méthode SLA et enlever des structures porteuses. Les structures porteuses sont poncées pour l'enlèvement total.
- Traiter la surface des objets afin d'améliorer la force d'adhérence entre le conducteur et les surfaces déposées.
- Dépôt de couche sur les surfaces des objets. La couche de Pd est servie de catalyseur pour déclencher la réaction d'oxydo-réduction. Les objets sont profondément immergés dans le bain de Pd.
- Immerger profondément les objets traités dans le bain de Cu^{2+} pour l'ELD après dépôt de la couche de Pd. La réaction entre le Cu^{2+} et le Pd se produit dans le bain.
- Finir le processus de métallisation. Les objets sont ensuite lavés à l'eau et séchés avant de passer le processus de gravure.
- Masquer des objets avec des masques en polyvinyle de la machine de découpe pour le processus de gravure.
- Finir le procédé de gravure pour obtenir les traces conductrices souhaitées. Les objets sont ensuite lavés à l'eau et les masques sont retirés. Les traces conductrices souhaitées se déposent à la surface des objets.
- Souder les composants électriques sur la surface des objets. Ces objets sont prêts pour des tests électriques.

3.2. Caractérisation des matériaux

Pour le conducteur, l'épaisseur mesurée est d'environ (7±1) µm avec une rugosité de surface acceptable, qui est de (1±0,2) µm. Cette valeur de rugosité de surface est comparable à celle du Rogers 4003C commercial, un substrat très connu pour les applications RF, (0,5±0,2) µm. La rugosité de surface à bas profil est un avantage de la Plastronique dans la fabrication de circuits RF. En outre, la résistivité du cuivre d'ELD est mesurée à l'aide de la méthode à quatre sondes. La valeur mesurée est de 0,02-0,025 (µΩ.m), ce qui est très proche de la conductivité du cuivre massif, 0,017 (µΩ.m). La comparaison de la résistivité du conducteur déposé proposé et de celle des encres d'impression utilisées dans la fabrication d'antennes et de circuits RF, donne un meilleur résultat, de 5 à 10 fois inférieur. Cela nous permet de compter sur moins de pertes conductives dans les circuits conçus. C'est un autre avantage de la Plastronique dans la fabrication de circuits RF.

Cette thèse est accessible à l'adresse : https://theses.insa-lyon.fr/publication/2023ISAL0007/these.pdf
© [X.V.L. NGUYEN], [2023], INSA Lyon, tous droits réservés

Une méthode à large bande pour déterminer les propriétés diélectriques des substrats – la méthode à deux lignes de transmission – est étudiée et développée pour caractériser Rogers 4003C pour validation, puis évaluer les substrats de la Stéréolithographie sélectionnés, qui sont le High Temp Resin v1 et le High Temp Resin v2 de Formlabs. Avec la conductivité mesurée et la rugosité de surface mesurée du cuivre d'ELD, la permittivité relative du HT Resin v1 et du HT Resin v2 est obtenue comme (3±0,1) et (2,9±0,1), respectivement, et leur tangente de perte mesurée est (0,025±0,0025) et (0,04 ±0,0025), respectivement. Leur permittivité relative est très proche de celle des substrats dans l'état de l'art, mais leur tangente de perte est plus élevée d'un facteur de 1,5 à 10. C'est un problème car cela augmentera les impacts de perte sur le comportement électrique des antennes et des circuits RF.

Cette thèse est accessible à l'adresse : https://theses.insa-lyon.fr/publication/2023ISAL0007/these.pdf
© [X.V.L. NGUYEN], [2023], INSA Lyon, tous droits réservés

4. Antennes

4.1. Paramètres de rayonnement

Les paramètres de diffraction (paramètres S) sont l'un des paramètres les plus importants pour étudier le comportement électrique d'une antenne.

Le coefficient de réflexion ou perte de retour, noté S_{xx} ou Γ, de l'antenne est une mesure de la quantité de puissance rayonnée/absorbée réfléchie par cette antenne. Le phénomène provient de l'impédance incompatible entre l'antenne et les autres composants électriques, circuits, etc. à une impédance de référence définie. Pour les conditions d'appariement d'impédance des composants RF, la valeur est définie comme étant purement résistive de 50 Ω dans ce travail.

Une fois le coefficient de réflexion de l'antenne mesuré, la bande passante peut être identifiée, c'est-à-dire lorsque le coefficient de réflexion est inférieur à une valeur prédéfinie (normalement -10 dB).

Lorsque deux ou plusieurs antennes sont très proches l'une de l'autre, S_{xy} (avec $x \neq y$) est une mesure de la puissance rayonnée par l'antenne « x », absorbée par l'antenne « y ». En d'autres termes, ce paramètre S décrit le couplage mutuel entre deux antennes proches.

La directivité (D) est le paramètre décrivant théoriquement les performances de capture de l'antenne. La directivité d'une antenne est définie comme le rapport entre l'intensité du rayonnement dans une direction donnée de l'antenne et l'intensité du rayonnement moyennée sur toutes les directions.

Le gain est le paramètre décrivant les performances de capture de l'antenne dans la réalité. Le gain d'une antenne est défini comme le rapport entre la puissance rayonnée réelle par l'antenne dans une direction donnée et la puissance qui serait obtenue si la puissance acceptée par l'antenne était rayonnée isotrope. Généralement, la direction donnée étudiée spécifie la direction principale de l'antenne. Plus le gain de l'antenne est important, plus la quantité de puissance rayonnée ou absorbée par cette antenne est élevée. L'antenne ne rayonne que si son gain est strictement positif. Lorsque le gain est noté en dB, cela signifie que les pertes (perte d'impédance de décalage, perte de conduction et perte diélectrique) de l'antenne sont incluses dans le paramètre.

La polarisation de l'antenne dans une direction donnée est définie comme la polarisation de l'onde rayonnée par l'antenne. La polarisation d'une onde rayonnée est la propriété d'une onde EM décrivant la direction et la magnitude relative du vecteur de champ E variant dans le temps. En d'autres termes, ce paramètre décrit la tendance de rotation des ondes EM rayonnées par l'antenne dans un sens de propagation donné.

Il existe trois types de polarisation d'une onde EM

- Polarisation linéaire
- Polarisation elliptique
- Polarisation circulaire

Afin d'indiquer la polarisation de l'antenne, un rapport axial (AR) est introduit.

- Si $1/2 \leq AR \leq 2$, la polarisation de l'antenne est circulaire.
- Si $AR=0$ ou $AR=\infty$ la polarisation de l'antenne est linéaire.
- Sinon, la polarisation de l'antenne est elliptique.

Cette thèse est accessible à l'adresse : https://theses.insa-lyon.fr/publication/2023ISAL0007/these.pdf
© [X.V.L. NGUYEN], [2023], INSA Lyon, tous droits réservés

Lorsque la polarisation de l'antenne et des ondes EM reçues par cette antenne ne sont pas alignées, il existe une perte provenant de l'inadéquation de polarisation. Ainsi, la polarisation circulaire est préférée pour réduire cette perte.

Le modèle de rayonnement d'une antenne est un motif présentant où la puissance est rayonnée par l'antenne ou où l'antenne peut recevoir les ondes EM. Il existe deux principaux types de modèles de rayonnement.

- Directionnel : une antenne directionnelle présente la propriété de rayonner ou de recevoir des ondes EM plus efficacement dans certaines directions que dans d'autres.

- Omnidirectionnel : une antenne omnidirectionnelle est essentiellement non directionnelle à un endroit donné et présente un motif directionnel dans n'importe quel plan orthogonal. Un motif omnidirectionnel est un type spécial de motif directionnel. Un modèle de rayonnement omnidirectionnel parfait sera sous la forme d'un « donut ».

L'angle d'ouverture du faisceau est un paramètre associé au schéma de rayonnement de l'antenne. La largeur du faisceau est définie comme la séparation angulaire entre deux points identiques du côté opposé des points extremum du motif.

L'angle d'ouverture du faisceau de demi-puissance (HPBW) est défini comme l'angle entre les deux directions dans lequel l'intensité de rayonnement du faisceau est égale à la moitié du maximum d'un faisceau. Dans ce travail, le HPBW de l'antenne est choisi pour indiquer l'espace rayonnant/absorbant de l'antenne dans un plan défini d'une direction donnée.

4.2. Critères prédéfinis

Les bandes de fréquences disponibles que nous pouvons récupérer sont les bandes de GSM 900, GSM 1800, UMTS, 2,45 GHz Wi-Fi. La sélection des bandes et la conception des antennes cohérentes avec ces bandes sont nécessaires pour optimiser les performances du RFEH créé. Dans ce travail, la bande de fréquence étudiée sera la bande Wi-Fi 2,45 GHz.

Des ondes RF ambiantes existent autour des objets. Cependant, ils se propagent dans n'importe quelle direction arbitraire et leur polarisation, c'est-à-dire linéaire, elliptique, circulaire, n'est pas fixe. Par conséquent, la capacité de capturer ces ondes est une étude de cas. L'utilisation d'un système d'antennes peut être favorable pour assurer la couverture du diagramme de rayonnement des antennes sur les objets, mais l'isolation entre les antennes doit également être prise en charge. Un isolement élevé est nécessaire pour réduire le phénomène d'auto-absorption et de re-rayonnement des antennes. De plus, le gain des antennes doit être évalué.

Les critères prédéfinis des antennes conçues peuvent être résumées de haut en bas comme :

- La fréquence de la bande d'opération : bande Wi-Fi 2,45 GHz.
- La possibilité de capturer toutes les polarisations dans l'air autour de l'objet dans toutes les directions.
- L'isolation élevée entre les antennes en cas d'utilisation d'un réseau d'antennes.
- Le gain des antennes doit être aussi élevé que possible.
- Les caractéristiques de l'antenne doivent être relativement immunisées contre la précision réelle de la fabrication.

Cette thèse est accessible à l'adresse : https://theses.insa-lyon.fr/publication/2023ISAL0007/these.pdf
© [X.V.L. NGUYEN], [2023], INSA Lyon, tous droits réservés

4.3. Antennes

Une antenne patch 2D à polarisation linéaire fabriquée avec un substrat de HT Resin v1 fonctionnant à 2,45 GHz est créée. L'antenne a une bande passante de 85 MHz avec un gain mesuré de +2,5 dB à 2,45 GHz.

Une autre antenne patch sur substrat Rogers 4003C, utilisant une méthode de fabrication conventionnelle, est utilisée pour comparer la bande passante et le gain au patch. Le patch de substrat Rogers donne une bande passante de 23 MHz et un gain de +5,3 dB. La bande passante inférieure du patch de substrat Rogers provient de la tangente de perte inférieure de ce substrat. Pendant ce temps, le gain plus élevé bénéficie de la tangente de perte plus faible et de la conductivité plus élevée de la feuille de cuivre. L'étude de la différence de gain est effectuée par simulation car la perte diélectrique représente environ 2,77 dB de la dégradation du gain de l'antenne patch tandis que la perte conductive représente environ 0,03 dB.

Le gain de l'antenne plastronique est plus petit mais suffisamment satisfaisant pour tenir compte du processus de fabrication et du polymère choisi pour le substrat (qui sera également celui de la coque de l'appareil final).

Deuxièmement, des antennes patch de polarisation circulaire sont introduites. Pour simplifier la conception, une seule alimentation avec antenne patch d'angle tronquée est sélectionnée. Une antenne patch circulaire 2D fabriquée avec le HT Resin v2 est concernée pour la première étude. Une bonne antenne patch de polarisation circulaire est obtenue avec le gain de 1,7 dB. Cependant, les impacts sur le diagramme de rayonnement (le directionnel rayonnement, l'angle d'ouverture du faisceau de demi-puissance) sont mis en évidence. Deux objets avec des configurations différentes de la masse (les masses communes et segmentées) de quatre antennes de patch de polarisation circulaire incurvées disposées comme un cylindre sont proposés comme solution pour atténuer ces impacts. Les performances rayonnantes de ces deux configurations sont analysées avec des gains mesurés de 1,26 dB et 1,6 dB. Le système de patchs avec des masses segmentées est sélectionné en raison de l'isolation satisfaisante entre les antennes et d'un gain satisfaisant. Ce système d'antenne sera appelé Flower Pot pour la suite de la thèse.

Cette thèse est accessible à l'adresse : https://theses.insa-lyon.fr/publication/2023ISAL0007/these.pdf
© [X.V.L. NGUYEN], [2023], INSA Lyon, tous droits réservés

5. Redresseurs et Circuit de gestion de la puissance

Les ondes EM capturées par l'antenne seront converties en énergie DC pour d'autres applications dans un circuit RFEH. Le redresseur a un élément important de la conversion des ondes EM en énergie DC. Néanmoins, dans l'aspect de la récupération d'énergie, la tension rectifiée par le redresseur est généralement très faible et loin de la tension de fonctionnement minimale de nombreux appareils électroniques. De plus, cette valeur de tension dépend également de la valeur de la charge. Par conséquent, une unité de gestion de puissance (PMU) est proposée comme la charge de sortie du redresseur afin d'augmenter et de réguler la tension rectifiée du RFEH à la tension requise des charges de consommation, c'est-à-dire les capteurs, les microcontrôleurs, etc. Pour maximiser les performances du RFEH, le redresseur et le PMU doivent être bien étudiés.

5.1. RF-DC redresseurs

Sélection des diodes

Le choix d'une diode appropriée est important dans la conception du redresseur, car les diodes sont la source principale de perte et leurs performances déterminent celles du circuit. L'efficacité de conversion du redresseur dépend de la capacité de jonction à polarisation nulle (C_{j0}), de la résistance série (R_s) et de la tension de claquage (V_{br}). Une diode appropriée doit avoir une faible capacité de jonction à polarisation nulle, une faible résistance en série et une tension de claquage élevée. Cependant, il est très difficile d'avoir ces trois conditions simultanément en raison du mécanisme physique des diodes et de ces paramètres inter-corrélés.

En plus, une diode à basse tension seuil (V_{th}) est souhaitée pour la conception du redresseur. Le courant de saturation inverse (I_s) de la diode est également l'un des paramètres caractéristiques importants. Pour les grandes I_s, la résistance de la diode diminue, par conséquent, la diode permet de démarrer la conduction à de faibles niveaux de puissance d'entrée, la tension d'allumage de la diode devient faible. Ainsi, la diode avec une grande I_s sera plus facile à fonctionner aux faibles niveaux de puissance d'entrée. De plus, la diode à grande I_s offrira une meilleure efficacité de conversion comparativement

Pour conclure, une diode de rectification souhaitable pour la conception du redresseur devrait avoir simultanément la condition suivante

- Petite V_{th}
- Petite R_s
- Petite C_{j0}
- Grande V_{br}
- Grande I_s

La diode Schottky SMS7630 possède la tension de seuil la plus basse et le courant de saturation inverse le plus élevé. En plus, cette diode donne une meilleure performance pour les niveaux de puissance inférieurs à 13 dBm. Alors, pour cette thèse, cette diode de rectification est choisie.

Redresseur de l'antenne patch de polarisation linéaire

Étant donné que la puissance d'entrée ciblée du redresseur est de -20 dBm à 2,45 GHz, la topologie de diode de série est sélectionnée pour obtenir un bon RFoM[6] du circuit. Pour la diode de rectification, la diode Schottky SMS7630-079LF de Skyworks Solutions Inc. est sélectionnée. Ici, le modèle SPICE de la diode de rectification est utilisé car d'autres modèles pratiques ne sont pas

---

[6] RFoM (en anglais) : Rectenna Figure of Merit

Cette thèse est accessible à l'adresse : https://theses.insa-lyon.fr/publication/2023ISAL0007/these.pdf
© [X.V.L. NGUYEN], [2023], INSA Lyon, tous droits réservés

disponibles. Comme la diode est à l'intérieur d'un boîtier 79LF, les éléments intérieurs de ce boîtier peuvent ajouter des impacts parasites sur les performances du circuit à haute fréquence.

Le condensateur de stockage du redresseur est un condensateur CMS de 12 pF utilisé pour les applications de faible puissance de Murata. La charge de sortie est une résistance de 10 kΩ de Yageo Corp, valeur de l'impédance d'entrée de ce PMU.

Le circuit est simulé et optimisé à l'aide de l'Advanced Design System (ADS) 2019, puis validé par la Co-Simulation d'ADS Momentum. Sachant que les ensembles de composants CMS entraînent également des impacts parasites, des modèles ADS des composants de Murata, c'est-à-dire condensateur de stockage, inductance, sont utilisés dans la simulation. Dans ces modèles, les éléments parasites des paquets sont caractérisés et modélisés pour les simulations ADS.

A -20 dBm, on a un décalage de fréquence de résonance entre la simulation et la mesure. Cette divergence peut provenir de la variation de l'inductance utilisée dans le circuit d'appariement et des éléments parasites de l'ensemble de la diode rectificative. En revanche, à ce niveau de puissance, l'impédance du circuit est suffisamment adaptée à 50 Ω car le coefficient de réflexion est d'environ -11,8 dB. Une autre mesure est déployée pour obtenir le niveau de puissance où le pic de fréquence de résonance est à 2,45 GHz. A -24 dBm, le S_{11} mesuré du circuit est minimum, soit -20 dBm. Ceci conclut sur l'adaptation d'impédance satisfaisant du redresseur à -24 dBm et 2,45 GHz. Les mesures de la tension rectifiée et de l'efficacité de conversion seront déployées à -24 dBm.

La tension rectifiée mesurée à 2,45 GHz est de 72 mV sur la charge de 10 kΩ correspondant à un rendement de conversion de 13% tandis que la valeur simulée est de 88 mV. La différence peut provenir de la perte dans les connecteurs SMA utilisés pour connecter le redresseur et l'antenne et de la variation des paramètres du modèle utilisé dans la simulation.

Redresseur des antennes patches de polarisation circulaire – Flower Pot

Chaque branche du redresseur se compose d'un stub de court-circuit pour le circuit correspondant et pour la boucle fermée du courant continu dans le circuit, une diode Schottky SMS7630-079LF de Skyworks Solutions Inc. comme la diode de rectification, un condensateur individuel de 1 nF ($C_{indivual}$) utilisé pour stocker la puissance rectifiée à la cathode de diode. Afin de bloquer tout signal RF entrant dans l'unité de gestion de la puissance, un quasi atténuateur RF, configuré à partir d'un RF choke, est ajouté en série après chaque condensateur individuel. En outre, le plan de masse de chaque branche du redresseur est séparé l'un de l'autre afin d'avoir l'individualité et est connecté au plan DC via une ligne mince et courte pour améliorer la capacité de protection du PMU contre les signaux RF.

À la sortie commune du circuit du redresseur, le condensateur de stockage commun (C_{common}) est sélectionné comme 1 µF et la charge de sortie du circuit est choisie comme 1 kΩ.

Les condensateurs utilisés dans le circuit proviennent de Murata et les RF chokes de Coilcraft. Les modèles ADS des condensateurs ainsi que les modèles SPICE avec des éléments parasites de la diode sont utilisés dans la simulation.

Le coefficient de réflexion d'une entrée du circuit est mesuré à l'aide d'un VNA (Vector Network Analyzer) calibré avec différents niveaux de puissance, qui sont -30 dBm, -20 dBm, -10 dBm et 0 dBm à 2,45 GHz et une charge de sortie de 1 kΩ.

Le redresseur a une adaptation d'impédance satisfaisante sur une large bande de fréquence qui couvre la bande de Wi-Fi 2,45 GHz. Les fréquences de résonance simulées et mesurées du

Cette thèse est accessible à l'adresse : https://theses.insa-lyon.fr/publication/2023ISAL0007/these.pdf
© [X.V.L. NGUYEN], [2023], INSA Lyon, tous droits réservés

redresseur sont presque similaires. La même observation est obtenue avec la bande passante du redresseur aux différentes valeurs de puissance d'entrée. L'écart de valeur du coefficient de réflexion entre la simulation et la mesure peut provenir de la variation des éléments parasites dans le boitier de la diode. Par ailleurs, lorsque la puissance d'entrée du redresseur augmente, le point de fonctionnement de la diode dans la courbe I-V change, ce qui conduit au décalage vers le haut de la fréquence de résonance du circuit.

La charge de sortie du redresseur est un PMU avec des composants discrets. L'impédance de ce PMU varie en fonction de ses différentes phases de fonctionnement. Ainsi, une étude du comportement d'appariement d'impédance du redresseur avec différentes valeurs de charge à est nécessaire afin d'assurer le bon fonctionnement du RFEH. L'étude est réalisée à -30 dBm, -20 dBm, -10 dBm et 0 dBm avec les charges de 0,5 kΩ, 1 kΩ, 4 kΩ, 7 kΩ et 10 kΩ.

À -30 dBm, le circuit a toujours une adaptation d'impédance satisfaisante sur une bande de 2,35-2,53 GHz et les fréquences de résonance du redresseur restent identiques lorsque la charge varie. Le phénomène de décalage des fréquences de résonance ne se produit pas ici puisque la puissance d'entrée du circuit est très faible, de sorte que le déplacement du point de fonctionnement de la diode est faible et négligeable. Lorsque la puissance d'entrée est plus élevée, le phénomène de changement de fréquence peut être observé plus clairement.

À -20 dBm, le circuit est toujours adapté à 50 Ω pour une bande de 2,35-2,55 GHz. À ce niveau de puissance d'entrée, le déplacement des fréquences de résonance peut être observé dans la simulation. Cependant, selon les mesures, il est difficile de déduire ce phénomène. L'écart peut provenir de la non-idéalité de la diode montée dans le circuit.

La puissance d'entrée du redresseur est augmentée à -10 dBm. Le redresseur est adapté à 2,45 GHz à la charge de 0,5 kΩ, 1 kΩ et 4 kΩ respectivement. Néanmoins, le circuit n'est pas adapté à 50 Ω à 7 kΩ et 10 kΩ à 2,45 GHz. À ces valeurs de charge, les fréquences de résonance du circuit sont décalées vers la droite et assez loin de 2,45 GHz, qui sont de 2,55 GHz. Cela peut s'expliquer par le fait qu'avec la puissance d'entrée plus élevée, le déplacement du point de fonctionnement de la diode dans la courbe I-V se produit plus clairement, le décalage de fréquence est plus élevé. De plus, la bande passante correspondant à l'impédance à 7 kΩ et 10 kΩ n'est pas assez large pour couvrir la fréquence de 2,45 GHz. L'écart entre la simulation et la mesure peut provenir des éléments parasites de l'emballage et du modèle de la diode utilisée dans la simulation. À ce niveau de puissance d'entrée élevé, le déplacement des fréquences de résonance peut être observé puisque le point de fonctionnement de la diode se déplace plus efficacement.

À 0 dBm, le modèle SPICE de la diode ne peut pas donner de bons résultats car les modèles sont identifiés pour la simulation de petits signaux tandis que 0 dBm est considéré comme un grand signal. Par conséquent, pour obtenir de bons résultats, un grand modèle de signal de diode doit être étudié. Le circuit est adapté à 2,45 GHz avec la charge de 0,5 kΩ, 1 kΩ et 4 kΩ selon les mesures.

La mesure de la tension rectifiée est effectuée à 2,45 GHz sous les niveaux de puissance d'entrée de -20 dBm, -10 dBm et 0 dBm respectivement. Trois cas différents sont étudiés : un port, deux ports et quatre ports sont alimentés simultanément avec les mêmes niveaux de puissance de -20 dBm, -10 dBm et 0 dBm.

Selon les résultats simulés et mesurés, nous constatons que lorsque le nombre de ports fournis augmente, la tension rectifiée augmente également. En ce qui concerne l'efficacité de conversion, à -20 dBm, la valeur maximale est obtenue lorsque la charge est proche de 1 kΩ. Cela peut s'expliquer par le fait que le redresseur est optimisé pour cette valeur de puissance d'entrée et de charge. Sinon, à -10 dBm, nous avons un décalage du point d'efficacité de conversion maximale

Cette thèse est accessible à l'adresse : https://theses.insa-lyon.fr/publication/2023ISAL0007/these.pdf
© [X.V.L. NGUYEN], [2023], INSA Lyon, tous droits réservés

du redresseur. Avec un port alimenté, cette valeur est d'environ 1 kΩ pendant ce temps avec deux ou quatre ports alimentés, la valeur de la charge optimale diminue, autour de 0,5 kΩ. A 0 dBm, on a le même phénomène que la puissance d'entrée de -10 dBm.

5.2. Unité de gestion de la puissance (PMU)

Le fonctionnement du convertisseur DC/DC exige généralement un signal oscillant pour l'état de transition du MOSFET dans le circuit. En revanche, les fréquences de commutation sont généralement fournies par un oscillateur externe nécessitant une source externe, c'est-à-dire des batteries, etc. pour l'alimentation. Le but de ne pas utiliser les batteries pour les appareils IoT n'est pas garanti. Par conséquent, l'unité de gestion de la puissance auto-fonctionnelle ou auto-autonome devient une faveur dans le concept de RFEH des applications de récupération d'énergie.

Blocs fonctionnement du PMU

Le PMU se compose d'un convertisseur Armstrong agissant comme démarreur de l'ensemble du circuit, d'un convertisseur flyback exécutant la capacité d'amplification de tension et de deux circuits Under-Voltage-Lock-Out (UVLO) gérant les différentes phases de fonctionnement du PMU par rapport à la charge.

Under-Voltage-Lock-Out (UVLO)

Ce circuit est utilisé pour allumer et/ou éteindre les appareils électroniques dans le cas où la tension d'entrée dépasse ou descend en dessous des valeurs de fonctionnement définies.

Circuit d'Armstrong

Armstrong Oscillator (AO), inventé par Edwin Armstrong en 1913, est un oscillateur harmonique qui génère un niveau d'oscillation élevé à partir d'une faible tension d'alimentation. Le signal généré est dans la gamme de l'Ultra Haute Fréquence (UHF), ainsi, ce circuit est appliqué précédemment dans le récepteur RF. Cependant, à cause de la non-linéarité du transistor, des effets parasites du transistor et des transformateurs, de nos jours, ce circuit est rarement utilisé dans les applications RF.

Littéralement, le circuit AO peut être utilisé dans des applications d'électronique de puissance. Grâce au rapport d'amplification élevé du transformateur, ce circuit est capable d'obtenir un signal d'oscillation à haute amplitude à partir de sa faible tension d'entrée. En ajoutant un redresseur à la sortie du circuit AO, nous pouvons obtenir une tension de sortie DC supérieure à la tension d'entrée.

L'avantage d'un convertisseur Armstrong est sa capacité d'auto-autonomie. Le circuit peut générer le signal oscillant par lui-même, de sorte qu'une source externe du signal oscillant n'est pas demandée dans le circuit.

Néanmoins, avec le convertisseur Armstrong, la fonction d'adaptation de l'impédance entre le convertisseur et le redresseur n'est pas introduite afin de maximiser la puissance transférée du redresseur au convertisseur. De plus, un autre inconvénient de ce circuit est que l'efficacité du circuit a tendance à se dégrader lorsque la sensibilité à la tension d'entrée est augmentée.

Pour notre thèse, la configuration du transformateur à trois bobines est sélectionnée car une tension de sortie positive est requise dans le circuit.

Cette thèse est accessible à l'adresse : https://theses.insa-lyon.fr/publication/2023ISAL0007/these.pdf
© [X.V.L. NGUYEN], [2023], INSA Lyon, tous droits réservés

Convertisseur flyback

La structure du convertisseur flyback est assez similaire à la structure de Buck-Boost. La différence entre deux circuits est la partie amplification dans le circuit, seulement une inductance pour Buck-Boost et une inductance couplée pour le flyback. Dans cette thèse, le convertisseur flyback est préféré puisque la tension porte-source du transistor MOSFET (Metal-Oxide-Semiconductor Field-Effect) utilisé dans le circuit est référencée à la terre, la tension de contrôle provenant du circuit de commande sera indépendante de la tension d'entrée du convertisseur.

Le circuit flyback a deux modes de fonctionnement différents : le mode de conduction continue (CCM) et le mode de conduction discontinue (DCM). Pour notre circuit, le mode DCM du convertisseur flyback est sélectionné grâce à la possibilité d'ajuster l'impédance d'entrée du convertisseur à ce mode en définissant la fréquence de commutation, le rapport cycle du signal généré par l'oscillateur et l'inductance primaire de l'inductance couplé.

Implémentation pratique

Le circuit comporte les quatre phases de fonctionnement suivantes : *Démarrage à froid*, *Transition*, *Fonctionnement normal* et *Désactivation*.

Dans notre PMU, le circuit d'Armstrong est utilisé pour déclencher l'opération du PMU. Cette phase est appelée *Démarrage à froid*.

Lorsque la tension amplifiée par le circuit d'Armstrong atteint à la valeur définie (1,2 V), le convertisseur flyback commence à prendre son rôle d'amplification dans le circuit. En parallèle, le circuit d'Armstrong commence à se désactiver. Nous sommes en phase *Transition.*

Une fois le circuit d'Armstrong est arrêté complètement, la phase *Fonctionnement normal* du PMU est acquise. Dans cette phase, le convertisseur flyback prend totalement son rôle d'amplification dans le PMU.

Quand la tension d'entrée ou/et la puissance d'entrée n'est pas suffisamment élevée pour maintenir l'opération du PMU, ce circuit se tombe en phase *Désactivation.*

5.3. Maximum Power Point

Afin d'attirer plus de puissance du redresseur vers le PMU, la condition MPP (Maximum Power Point) doit être créée. L'impédance d'entrée du PMU doit être la charge optimale du redresseur. La charge optimale est celle à laquelle l'efficacité de conversion RF-DC du redresseur atteint son maximum.

Méthode d'estimation de la charge optimale à partir de la puissance réfléchie du redresseur

Dans cette méthode, le circuit correspondant n'a pas besoin d'être optimisé pour une certaine valeur de charge, la puissance d'entrée ou la fréquence. Le principe de cette méthode est de mesurer la puissance réfléchie (P_r), qui provient du circuit d'adaptation d'impédance RF imparfait du redresseur, puis d'ajuster la puissance d'entrée du redresseur (P_i) de telle sorte que la puissance reçue (P_t) par la diode rectificative soit réglée à la valeur souhaitée (-30 dBm, -20 dBm et -10 dBm). L'efficacité de conversion RF-DC est calculée pour différentes valeurs de charge afin d'obtenir la valeur de la charge optimale par la suite. Pour cette méthode, deux coupleurs directionnels sont nécessaires. Un coupleur est utilisé pour mesurer P_i et l'autre est utilisé pour mesurer P_r. Il convient de noter que l'atténuation du coupleur, des connecteurs, des câbles, etc. (P_{loss}) doit être identifiée avec précision pour obtenir des résultats satisfaisants.

Cette thèse est accessible à l'adresse : https://theses.insa-lyon.fr/publication/2023ISAL0007/these.pdf
© [X.V.L. NGUYEN], [2023], INSA Lyon, tous droits réservés

Conclusion

La charge optimale du redresseur ou du ZBR (Zero Bias Resistance) de la diode diminue lorsque le niveau de puissance d'entrée augmente. À -30 dBm, -20 dBm, -10 dBm et 0 dBm, la charge optimale est respectivement de 5 kΩ, 3 kΩ, 2,5 kΩ et 2 kΩ.

De plus, les caractéristiques I-V du redresseur sont également étudiées. Les lignes caractéristiques quasi-parallèles sont obtenues. Le redresseur de topologie de la série mono-diode est suggéré pour modéliser comme une source de tension avec une résistance interne, qui est le ZBR de la diode de rectification.

5.4. Charge optimale du redresseur de quatre entrées

Le concept du redresseur conçu pour le Flower Pot est un redresseur à topologie à quatre séries en parallèle avec une sortie commune à la fin, où le redresseur se connectera au PMU.

Lorsque le niveau de puissance d'entrée est inférieur à -30 dBm, la tension rectifiée ainsi que la puissance de sortie du redresseur sont très faibles donc négligeables, pour simplifier les calculs, une hypothèse est introduite : « *La puissance d'entrée de chaque branche est considérée comme nulle si son niveau est inférieur à -30 dBm. La branche correspondante sera supposée comme un circuit ouvert.* ». En outre, une autre hypothèse dans laquelle toutes les branches sont censées être identiques est également appliquée.

Étant donné que les niveaux de puissance d'entrée des quatre branches ne sont ni identiques ni constants (de -30 dBm à 0 dBm), la charge optimale de chaque branche ne sera pas identique et la charge optimale du redresseur ne restera pas constante. La diffusion des valeurs Z_{load} est évaluée.

Un compromis est nécessaire dans la spécification de Z_{load}. Comme notre objectif n'est pas d'optimiser les performances du circuit pour un cas défini spécial mais d'avoir une performance acceptable pour dans la plupart des cas possibles, nous choisissons la valeur de charge à laquelle nous avons moins de différence entre la valeur choisie et les autres. Nous constatons que les valeurs de Z_{load} se concentrent autour de la valeur de 1 kΩ. Par conséquent, dans cette thèse, la charge de sortie du redresseur de topologie à quatre séries est sélectionnée comme 1 kΩ.

5.5. Conclusion

Dans ce chapitre, nous présentons les circuits de redresseur conçus pour l'antenne patch de polarisation linéaire et pour le système de quatre antennes patch de polarisation circulaire. Pour le premier redresseur, la méthode de simulation du mélange de composants discrets et de lignes de microbandes pour le circuit correspondant est présentée. Les mesures du coefficient de réflexion pour vérifier l'état d'adaptation d'impédance du circuit ainsi que la tension rectifiée avec l'antenne dans une chambre anéchoïque sont déployées. Le résultat est comparable à l'état de l'art sélectionné et ouvre la possibilité d'utiliser la Plastronique pour créer les circuits RF pour les applications de récupération d'énergie. Sachant que le circuit d'adaptation d'impédance de ce redresseur utilise des inductances, la variation de valeur des composants discrets peut modifier l'adaptation d'impédance du circuit dans les bandes RF. De plus, cela nécessite plus de soudure pour fabriquer le circuit. Une autre étude du circuit d'adaptation d'impédance de microbandes est préférable. Le redresseur conçu pour le système d'antennes à quatre entrées est décrit. La configuration de l'implantation d'un RF choke et de la segmentation des plans de masse pour améliorer la capacité de blocage des signaux RF entrant dans le PMU est également démontrée. Les mesures du coefficient de réflexion et de la tension rectifiée du redresseur sont effectuées. Les résultats mesurés sont comparés à l'état de l'art sélectionné. Selon la comparaison, le redresseur

Cette thèse est accessible à l'adresse : https://theses.insa-lyon.fr/publication/2023ISAL0007/these.pdf
© [X.V.L. NGUYEN], [2023], INSA Lyon, tous droits réservés

fabriqué en appliquant la Plastronique possède des performances presque similaires à celles d'autres œuvres, c'est-à-dire les PCBs, les circuits flexibles, les circuits imprimés en 3D.

Une unité de gestion de la puissance avec des composants discrets est également présentée. Le circuit se compose de quatre blocs électriques : le convertisseur Armstrong auto-oscillant pour la phase de démarrage à froid, le convertisseur flyback en DCM pour le fonctionnement normal et deux circuits UVLO utilisés pour séparer les différentes phases. La topologie de chaque bloc et la raison du choix des composants associés sont justifiées.

Enfin, afin de régler la condition Maximum Power Point du redresseur et du PMU, les interférences électriques entre ces blocs sont analysées. Il est nécessaire de déterminer la charge de sortie optimale du redresseur. La méthode de mesure de ce paramètre et son déploiement sont décrits dans ce chapitre. Une comparaison entre nos valeurs et celles de l'état de l'art sélectionné est faite. Un bon accord est obtenu. La charge optimale est de 5 kΩ, 3 kΩ, 2,5 kΩ et 2 kΩ à -30 dBm, -20 dBm, -10 dBm et 0 dBm, respectivement, pour un redresseur de topologie de diode mono-série avec diode Schottky SMS7630-079LF. Pour le redresseur de quatre entrées est ensuite calculé et la valeur obtenue est de 1 kΩ.

Cette thèse est accessible à l'adresse : https://theses.insa-lyon.fr/publication/2023ISAL0007/these.pdf
© [X.V.L. NGUYEN], [2023], INSA Lyon, tous droits réservés

6. Résultats expérimentaux

Dans ce chapitre, le fonctionnement du circuit d'accumulateur d'énergie (PMU) proposé sera analysé. Tout d'abord, le PMU sera testé avec le circuit de redresseur à quatre ports comme source d'alimentation DC. Le redresseur sera alimenté par une source RF CXG N5611B de Keysight. Chaque phase de fonctionnement du PMU et le mode Veille du convertisseur flyback seront étudiés. Après cela, la source RF sera remplacée par les antennes de Flower Pot. Le but est d'évaluer les performances de l'ensemble du système d'un RFEH fabriqué à l'aide de la technique Plastronique. La tension de démarrage à froid, la tension de sortie à différentes charges, l'efficacité globale du circuit seront concernées par l'évaluation des performances.

Le fonctionnement du PMU proposé avec des composants discrets est vérifié. Trois phases de fonctionnement du circuit sont démontrées, à savoir le démarrage à froid, la transition et le fonctionnement normal. Les mesures montrent que la tension de démarrage à froid du circuit est d'environ 0,26 V obtenue avec une puissance d'entrée de -7,5 dBm RF au redresseur avec un rendement global de 14,76 % avec une charge de 100 kΩ.

Une comparaison de l'efficacité globale, du courant de repos du contrôleur, de la tension de démarrage à froid entre notre travail et notre état de l'art est réalisée.

Notre circuit a une efficacité globale inférieure à celle des autres ouvrages à l'échelle de -8 à -7 dBm. Cette efficacité globale peut être améliorée en utilisant un oscillateur à faible consommation pour le flyback et/ou en utilisant une inductance primaire plus élevée de l'inductance couplée dans la configuration flyback.

De plus, notre circuit ne nécessite pas de supercondensateur préchargé ou de batterie pour le démarrage à froid. Le circuit peut commencer à fonctionner seul tant que la tension d'entrée est supérieure à 0,26 V. En fait, cette valeur de tension de démarrage à froid peut être diminuée en utilisant un rapport de rotation plus élevé entre les inductances secondaires et primaires du transformateur du convertisseur Armstrong.

Le schéma MPPT n'est pas déployé dans notre circuit. Une solution consiste à ajouter un circuit actif pour modifier la fréquence de commutation de l'oscillateur afin de rechercher le point de puissance maximale du PMU pour chaque possibilité différente.

Dans la phase de désactivation, le mode veille du PMU est également étudié. Ce mode du convertisseur flyback est obtenu avec une puissance d'entrée RF de -12 dBm au redresseur et la tension continue correspondante de 0,1 V pour une charge de sortie de 100 kΩ et 1 MΩ.

Notre PMU est ensuite testé avec la rectenna de Flower Pot. Les mesures montrent un rendement global de 13,4 % à une charge de 100 kΩ avec une puissance de réception de -7,2 dBm de l'antenne.

Les études sur les performances du PMU lorsque le redresseur est alimenté à deux et quatre ports par une source RF ou par des antennes simultanément ne sont pas encore réalisées en raison de la contrainte de temps de la thèse. De plus, la question de l'optimisation du condensateur de stockage (valeur minimale, taille minimale, technique de fabrication, etc.) du PMU n'est pas encore résolue.

Cette thèse est accessible à l'adresse : https://theses.insa-lyon.fr/publication/2023ISAL0007/these.pdf
© [X.V.L. NGUYEN], [2023], INSA Lyon, tous droits réservés

7. Conclusions et Perspectives

7.1. Conclusion

Ce travail se concentre sur le récupérateur d'énergie par radiofréquence conçu sur des substrats rigides sous forme 2D et 3D fabriqués en appliquant la technologie Plastronique Rapide. La contribution principale de cette thèse est d'examiner et de vérifier les possibilités d'utilisation de cette nouvelle technologie de fabrication, la Stéréolithographie pour l'impression des substrats et la méthode de métallisation autocatalytique pour la fabrication des traces conductrices, afin de réaliser les circuits RF utilisés dans les applications de récupération d'énergie à la surface des objets plastiques sous forme 2D et 3D.

Dans l'approche de la fabrication, parmi de nombreuses méthodes d'impression à faible coût de substrat, c'est-à-dire la modélisation par dépôt fondu, la structuration directe au laser, etc., la Stéréolithographie est préférée en raison de sa haute précision, de sa haute résolution et de sa haute répétabilité. La bonne qualité de surface est également un bonus de cette méthode. De plus, cette méthode nous permet de créer facilement des objets 2D et 3D avec une grande complexité. Dans cette thèse, les résines choisies sont High Temp Resin v1 et High Temp Resin v2 de Formlabs en raison de leur résistance thermique élevée. Ce paramètre joue un rôle important pour nous donner un aperçu de la capacité de souder les composants électriques plus tard. Ensuite, la méthode ELD est sélectionnée afin d'obtenir les traces conductrices sur la surface des objets imprimés. L'avantage de cette méthode est sa compatibilité avec tous les substrats polymères et non conducteurs. De plus, cette méthode est capable de métalliser la surface de l'objet tant que le liquide peut passer. Un autre avantage est que la résistivité du cuivre ELD est proche de la valeur du cuivre massif et beaucoup plus faible que les encres conductrices utilisées dans l'électronique imprimée. Dans les applications de récupération d'énergie à faible puissance, en particulier la récupération d'énergie RF, la faible résistivité du conducteur peut réduire la perte conductive dans les circuits.

Avant de concevoir les antennes et les circuits RF, la compréhension des propriétés électromagnétiques du substrat, c'est-à-dire la permittivité relative, la tangente de perte, et du conducteur, c'est-à-dire la résistivité est une étape essentielle. La méthode des deux lignes de transmission est effectuée pour extraire la permittivité relative et la tangente de perte des substrats sur une large bande de fréquence, 0,5-2,5 GHz. Les résultats montrent que la permittivité relative des substrats SLA est (3±0,1) et (2,9±0,1), et leur tangente de perte est (0,025±0,0025) et (0,04 ±0,0025) sur une bande de 0,5-2,5 GHz. Pour le conducteur, l'épaisseur mesurée est d'environ (7±1) µm avec une rugosité de surface acceptable, qui est de (1±0,2) µm. La rugosité de surface à profil bas est un avantage de la Plastronique dans la fabrication de circuits RF. En outre, la résistivité du cuivre déposé sans électrolyse est mesurée à l'aide de la méthode à quatre sondes. La valeur mesurée est de 0,02-0,025 (µΩ.m), ce qui est très proche de la conductivité du cuivre en vrac, 0,017 (µΩ.m).

Dans le concept de circuit RFEH, les antennes jouent le rôle de capturer les ondes EM et de les transmettre vers le redresseur pour la conversion des ondes EM en énergie DC. L'antenne patch de polarisation linéaire 2D déposée sur le HT Resin v1 est étudiée pour notre première étude. Une bonne correspondance d'impédance est obtenue à 2,45 GHz avec un gain de +2,5 dB. L'impact de la perte de conduction et de la perte diélectrique sur le gain de l'antenne est analysé à l'aide de CST Microwave Studio 2019. L'étude montre qu'en remplaçant le HT Resin v1 par un substrat à faible perte, à savoir Rogers 4003C, le gain de l'antenne peut être augmenté à 2,77 dB. La perte de conduction du cuivre ELD est de 0,03 dB dans le gain de l'antenne. Cette perte est supposée négligeable, ce qui est inférieur à 0,1 dB, lorsque la résistivité du conducteur est inférieure à 0,021 µΩ.m.

Cette thèse est accessible à l'adresse : https://theses.insa-lyon.fr/publication/2023ISAL0007/these.pdf
© [X.V.L. NGUYEN], [2023], INSA Lyon, tous droits réservés

Littéralement, l'exigence de capturer toutes les polarisations existantes dans l'air du RFEH est nécessaire. Afin de valider cette exigence, des systèmes d'antenne patch à polarisation circulaire sont proposés. Tout d'abord, une antenne patch de polarisation circulaire planaire 2D est obtenue. Cependant, sa demi-puissance de largeur de faisceau et son schéma de rayonnement directionnel ne peuvent pas assurer la couverture complète autour des objets. Un système d'antennes patch avec des surfaces de sol communes est alors envisagé pour éliminer ces inconvénients. Les antennes sont déposées sur un cylindre d'un rayon de courbure de 40 mm pour élargir le HPBW. De plus, les antennes sont placées en quadrature. À partir de là, les objets peuvent être immergés dans le rayonnement des antennes. Afin d'améliorer l'isolation entre les antennes du système, la surface du sol est segmentée. Chaque antenne a sa propre surface au sol. Le gain de l'antenne est également amélioré grâce à cette configuration. Les antennes du système final proposé, appelé Flower Pot, sont bien assorties sur une large bande de fréquence, qui peut couvrir la bande Wi-Fi 2,45 GHz. L'isolation entre les antennes en position côte à côte et en position opposée est inférieure à -35 dB et à -45 dB respectivement. Le gain mesuré de l'antenne est d'environ 1,35 dB. Les dimensions du cylindre fabriqué sont de 80π x 70 mm^3.

Deux circuits de redresseur sont également étudiés. Le premier circuit est utilisé pour l'antenne patch de polarisation linéaire 2D et le second est conçu pour les systèmes de quatre antennes patch de polarisation circulaire déposées sur le cylindre. Les deux redresseurs ont l'interférence d'impédance de 50 Ω avec les antennes. Les circuits sont déposés sur des substrats planaires 2D. A cause de la contrainte de temps de la thèse, la performance de ces circuits lorsqu'ils sont déposés sur des surfaces 3D n'est pas encore étudiée. Le circuit d'accumulateur d'énergie est également analysé. Pour la vérification du fonctionnement, le PMU est assemblé à partir des composants discrets. L'interférence électrique entre le redresseur et le PMU est apprise. La condition de suivi du point de puissance maximale est prise en compte dans cette thèse. Cette condition est établie en ayant l'impédance correspondant à la charge optimale du redresseur. Il est donc nécessaire de déterminer la charge optimale du redresseur. La méthode d'identification de ce paramètre est introduite. Selon les résultats, la charge optimale du redresseur dans la topologie de la série mono-diode n'est pas constante en tant que variation de la puissance d'entrée. À -30 dBm, -20 dBm, -10 dBm et 0 dBm, les valeurs sont respectivement de 5 kΩ, 3 kΩ, 2,5 kΩ et 2 kΩ. Étant donné que le redresseur conçu pour Flower Pot dispose de quatre ports fonctionnants individuellement, la charge de sortie du circuit est calculée. Le circuit est souhaité pour fonctionner pour toutes les possibilités, la charge de sortie est donc trouvée comme 1 kΩ.

Par la suite, le fonctionnement de l'PMU est évalué. Le PMU est connecté au redresseur de Flower Pot pour le test de fonctionnement. Quatre phases de fonctionnement du PMU sont démontrées, à savoir le démarrage à froid, la transition, le fonctionnement normal et la désactivation. La tension de démarrage à froid mesurée est d'environ 0,26 V, ce qui est inférieur aux PMU existants sur le marché. Le mode Veille du flyback de notre PMU est également étudié. Les résultats montrent que le flyback entre dans ce mode lorsque la puissance d'entrée du redresseur est d'environ -12 dBm avec la tension d'entrée correspondante du PMU de 0,1 V. À la puissance d'entrée de -7,5 dBm du redresseur, la tension de sortie du PMU est de 1,62 V avec un rapport de suralimentation PMU de 6,14 avec une charge de 100 kΩ. L'efficacité globale de l'ensemble du circuit est de 14,8%. Lorsque le PMU est connecté à une rectenna, l'efficacité globale est de 13,4%.

7.2. Perspectives

Dans l'aspect des polymères, les substrats SLA sélectionnés ont une perte élevée, ce qui crée des impacts avec perte sur les performances des antennes et des circuits RF. Une autre limite de ces matériaux est leur fragilité. D'autres matériaux peuvent être considérés ici tels que le LCP, le

Cette thèse est accessible à l'adresse : https://theses.insa-lyon.fr/publication/2023ISAL0007/these.pdf
© [X.V.L. NGUYEN], [2023], INSA Lyon, tous droits réservés

PEEK, etc., qui sont des polymères super d'ingénierie à haute température. La tangente de perte de ces matériaux est très faible, ce qui peut réduire la perte diélectrique dans les antennes et les circuits RF. De plus, ces matériaux ont une très bonne résistance thermique, par conséquent, la soudure des CMS sur leur surface peut être facilement effectuée. Le principal inconvénient ici est que la technologie de fabrication de ces matériaux n'est pas aussi mature que SLA et est beaucoup plus chère et complexe. Un autre inconvénient est qu'avec une tangente de perte plus faible, les antennes peuvent avoir une bande de fréquence plus étroite.

Pour la conception de l'antenne, l'étude de la courbure des antennes dans deux ou plusieurs directions, c'est-à-dire la sphère, peut être envisagée. La miniaturisation des antennes peut également être envisagée pour réduire leur facteur de forme. De plus, la méthode d'alimentation de nos antennes est la méthode de la ligne de transmission. Pour réduire leur taille totale, l'idée d'utiliser la méthode d'alimentation par sonde ou la méthode de la ligne couplée peut être envisagée. Cependant, la fabrication de circuits électriques multicouches et de vias électriques dans la Plastronique Rapide est encore en recherche. Une fois que la méthode de fabrication est bien gérée, l'étude du modèle électrique équivalent et l'impact de la Plastronique via dans le domaine RF devraient également être discutées.

Pour la conception du redresseur, la modélisation de la diode utilisée dans le redresseur est un processus nécessaire pour mieux comprendre le comportement de la diode. De plus, la conception d'un redresseur sur une surface non plane est un intérêt à suivre par la suite.

Notre unité de gestion de l'alimentation est testée à l'aide de composants discrets, c'est-à-dire des transistors, des oscillateurs, etc. L'efficacité de notre circuit est inférieure à notre état de l'art. Ce paramètre de notre PMU peut être amélioré par

- Remplacer de l'oscillateur discret TS3002 par l'oscillateur à faible consommation sous forme de circuit intégré (c'est-à-dire des oscillateurs en anneau).

- Utiliser d'une inductance primaire plus élevée de l'inductance couplée pour améliorer l'efficacité du convertisseur flyback.

- Ajouter le fonctionnement de suivi la condition de MPPT dans la configuration de notre PMU. Cette idée peut être réalisée en utilisant un circuit actif pour faire varier la fréquence de commutation du convertisseur flyback afin de rendre l'impédance d'entrée du convertisseur égale à la charge optimale du redresseur.

La tension de démarrage à froid de notre PMU peut être davantage réduite en utilisant un rapport de rotation plus élevé entre les inductances secondaires et primaires du transformateur du convertisseur Armstrong et/ou en utilisant une tension de seuil inférieure, un courant de vidange de tension à grille zéro plus faible JFET.

Le condensateur de stockage du PMU n'est pas encore optimisé. Une étude sur la valeur et les dimensions de ce composant peut être mentionnée pour minimiser la taille totale ainsi que pour assurer le fonctionnement de la charge de consommation, qui est les microcontrôleurs et les capteurs.

Lors du test PMU, une seule branche du redresseur à quatre ports est fournie. La question de la performance du PMU lorsque les deux ou quatre branches de ce redresseur sont alimentées simultanément peut être discutée. Selon les estimations, plus il y a de succursales participant à l'opération, plus le PMU reçoit d'énergie. Cela pourrait réduire le temps de charge du condensateur de stockage.

Cette thèse est accessible à l'adresse : https://theses.insa-lyon.fr/publication/2023ISAL0007/these.pdf
© [X.V.L. NGUYEN], [2023], INSA Lyon, tous droits réservés

En raison du retard de fabrication et d’expédition des composants, le circuit final du microcontrôleur et du capteur ne peut pas être testé à la fin de cette thèse. Un test avec le circuit final doit être déployé pour qualifier le fonctionnement du démonstrateur.

Cette thèse est accessible à l'adresse : https://theses.insa-lyon.fr/publication/2023ISAL0007/these.pdf
© [X.V.L. NGUYEN], [2023], INSA Lyon, tous droits réservés

REFERENCES

[1] "Up to 78 million batteries will be discarded daily by 2025, researchers warn | News," *CORDIS | European Commission*. https://cordis.europa.eu/article/id/430457-up-to-78-million-batteries-will-be-discarded-daily-by-2025-researchers-warn (accessed May 06, 2022).

[2] "Cisco and SAS Edge-to-Enterprise IoT Analytics Platform," p. 13.

[3] "The future of the IoT (batteries not required)," *MIT News | Massachusetts Institute of Technology*. https://news.mit.edu/2021/future-iot-batteries-not-required-0521 (accessed May 06, 2022).

[4] D. H. N. Bui, "Printed flexible antenna for energy harvesting," phdthesis, Université Grenoble Alpes, 2017. Accessed: Sep. 21, 2022. [Online]. Available: https://tel.archives-ouvertes.fr/tel-01721461

[5] H. P. Phan, "Design of 2D and 3D antennas on flexible materials," phdthesis, Université Grenoble Alpes, 2018. Accessed: Feb. 27, 2022. [Online]. Available: https://tel.archives-ouvertes.fr/tel-02138893

[6] Wagih, Mahmoud, (2021), Optimal rectenna design for textile, flexible, and printed radio frequency energy harvesting. Doctoral Thesis, 308pp.

[7] Song, C (2017) *Broadband Rectifying-Antennas for Ambient RF Energy Harvesting and Wireless Power Transfer.* PhD thesis, University of Liverpool.

[8] J. Franke, "Three-Dimensional Molded Interconnect Devices (3D-MID)," in *Three-Dimensional Molded Interconnect Devices (3D-MID)*, J. Franke, Ed. Hanser, 2014, p. I–XII. doi: 10.3139/9781569905524.fm.

[9] S. Kamotesov, "Transmission d'énergie par induction électromagnétique en plastronique 3D," phdthesis, Université de Lyon, 2019. Accessed: May 06, 2022. [Online]. Available: https://tel.archives-ouvertes.fr/tel-02496934

[10] "RO4003C^{TM} Laminates - Rogers Corporation." https://www.rogerscorp.com/advanced-electronics-solutions/ro4000-series-laminates/ro4003c-laminates (accessed Aug. 25, 2022).

[11] J. Wiklund *et al.*, "A Review on Printed Electronics: Fabrication Methods, Inks, Substrates, Applications and Environmental Impacts," *Journal of Manufacturing and Materials Processing*, vol. 5, no. 3, Art. no. 3, Sep. 2021, doi: 10.3390/jmmp5030089.

[12] J. J. Adams *et al.*, "Conformal Printing of Electrically Small Antennas on Three-Dimensional Surfaces," *Advanced Materials*, vol. 23, no. 11, pp. 1335–1340, 2011, doi: 10.1002/adma.201003734.

[13] A. Jaafar, S. Schoinas, and P. Passeraub, "Pad-Printing as a Fabrication Process for Flexible and Compact Multilayer Circuits," *Sensors (Basel)*, vol. 21, no. 20, p. 6802, Oct. 2021, doi: 10.3390/s21206802.

[14] C. Goth, S. Putzo, and J. Franke, "Aerosol Jet printing on rapid prototyping materials for fine pitch electronic applications," in *2011 IEEE 61st Electronic Components and Technology Conference (ECTC)*, May 2011, pp. 1211–1216. doi: 10.1109/ECTC.2011.5898664.

[15] S. E. Gordon, J. R. Dorfman, D. Kirk, and K. Adams, "Advances in Conductive Inks across Multiple Applications and Deposition Platforms," p. 43.

[16] R. Venkata Krishna Rao, V. A. K, K. Ps, and S. Singh, "Conductive Silver Inks and its Applications in Printed and Flexible Electronics," *RSC Advances*, vol. 5, pp. 77760–77790, Aug. 2015, doi: 10.1039/C5RA12013F.

[17] "Industrial 3D Printing of Electronics for Manufacturing and AME," *Nano Dimension*. https://www.nano-di.com (accessed Aug. 25, 2022).

[18] D. S. Vorunichev, "Investigation of the Possibilities of Printing Multilayer Printed Circuit Boards on a Dragonfly 3D Printer with Expired Nanoink," in *2021 International Conference on Quality Management, Transport and Information Security, Information Technologies (IT&QM&IS)*, Sep. 2021, pp. 476–479. doi: 10.1109/ITQMIS53292.2021.9642766.

Cette thèse est accessible à l'adresse : https://theses.insa-lyon.fr/publication/2023ISAL0007/these.pdf
© [X.V.L. NGUYEN], [2023], INSA Lyon, tous droits réservés

[19] “Propriétés diélectriques des polymères,” *Techniques de l’Ingénieur*. https://www.techniques-ingenieur.fr/base-documentaire/materiaux-th11/proprietes-generales-des-plastiques-42152210/proprietes-dielectriques-des-polymeres-e1850/ (accessed Aug. 25, 2022).

[20] “Thermoplastics,” *Polymers*. http://polymers.com.au/thermoplastics/ (accessed Aug. 25, 2022).

[21] K. Cheval, “Étude et réalisation de circuits imprimés sur substrats polymères 3D (MID 3D) par microtamponnage,” phdthesis, Université Claude Bernard - Lyon I, 2015. Accessed: Aug. 25, 2022. [Online]. Available: https://tel.archives-ouvertes.fr/tel-01280884

[22] H. Bikas, P. Stavropoulos, and G. Chryssolouris, “Additive manufacturing methods and modelling approaches: a critical review,” *Int J Adv Manuf Technol*, vol. 83, no. 1, pp. 389–405, Mar. 2016, doi: 10.1007/s00170-015-7576-2.

[23] “M. Cabrera, J. Y. Jezequel, J.C. Andre, Three-dimensional machining by laser photopolymerization, in: J. -P. Fouassier, J.F. Rabek (Eds.), Lasers in Polymer Science and Technology: Applications, vol. III, CRC Press, Boca Raton, FL, 1990, pp. 73-95.”

[24] F. Lupone, E. Padovano, F. Casamento, and C. Badini, “Process Phenomena and Material Properties in Selective Laser Sintering of Polymers: A Review,” *Materials*, vol. 15, no. 1, Art. no. 1, Jan. 2022, doi: 10.3390/ma15010183.

[25] V. Dhinakaran, K. P. Manoj Kumar, P. M. Bupathi Ram, M. Ravichandran, and M. Vinayagamoorthy, “A review on recent advancements in fused deposition modeling,” *Materials Today: Proceedings*, vol. 27, pp. 752–756, Jan. 2020, doi: 10.1016/j.matpr.2019.12.036.

[26] T. Gerges, V. Semet, P. Lombard, S. Gaillard, M. Cabrera, and S. A. Lambert, “3D Plastronics for Smartly Integrated Magnetic Resonance Imaging Coils,” *Frontiers in Physics*, vol. 8, 2020, Accessed: Aug. 25, 2022. [Online]. Available: https://www.frontiersin.org/articles/10.3389/fphy.2020.00240

[27] J.-L. Gnanago *et al.*, “Actuators for MRE: New Perspectives With Flexible Electroactive Materials,” *Frontiers in Physics*, vol. 9, Sep. 2021, doi: 10.3389/fphy.2021.633848.

[28] “Modern Electroplating, 5th Edition | Wiley,” *Wiley.com*. https://www.wiley.com/en-us/Modern+Electroplating%2C+5th+Edition-p-9780470167786 (accessed Aug. 25, 2022).

[29] B. D. Barker, “Electroless deposition of metals,” *Surface Technology*, vol. 12, no. 1, pp. 77–88, Jan. 1981, doi: 10.1016/0376-4583(81)90138-2.

[30] “Electroless Plating - Fundamentals And Applications [PDF] [6u2ntjfff380].” https://vdoc.pub/documents/electroless-plating-fundamentals-and-applications-6u2ntjfff380 (accessed Aug. 25, 2022).

[31] P. Njogu, B. Sanz-Izquierdo, A. Elibiary, S. Y. Jun, Z. Chen, and D. Bird, “3D Printed Fingernail Antennas for 5G Applications,” *IEEE Access*, vol. 8, pp. 228711–228719, 2020, doi: 10.1109/ACCESS.2020.3043045.

[32] A. Shastri *et al.*, “3D Printing of Millimetre Wave and Low-Terahertz Frequency Selective Surfaces Using Aerosol Jet Technology,” *IEEE Access*, vol. 8, pp. 177341–177350, 2020, doi: 10.1109/ACCESS.2020.3024584.

[33] T. A. Elwi, Z. A. Abdul Hassain, and O. A. Tawfeeq, “Hilbert metamaterial printed antenna based on organic substrates for energy harvesting,” *IET Microwaves, Antennas & Propagation*, vol. 13, no. 12, pp. 2185–2192, 2019, doi: 10.1049/iet-map.2018.5948.

[34] “Printed Microwave Metamaterial-Antenna Circuitries on Nickel Oxide Polymerized Palm Fiber Substrates | Scientific Reports.” https://www.nature.com/articles/s41598-019-39736-8 (accessed Feb. 27, 2022).

[35] “Sustainable production of highly conductive multilayer graphene ink for wireless connectivity and IoT applications | Nature Communications.” https://www.nature.com/articles/s41467-018-07632-w (accessed Feb. 27, 2022).

[36] T. Leng *et al.*, “Screen-Printed Graphite Nanoplate Conductive Ink for Machine Learning Enabled Wireless Radiofrequency-Identification Sensors,” *ACS Appl. Nano Mater.*, vol. 2, no. 10, pp. 6197–6208, Oct. 2019, doi: 10.1021/acsanm.9b01034.

[37] M. A. Islam, H. N. Hansen, and P. T. Tang, “Micro-MID Manufacturing By Two-Shot Injection Moulding,” *OnBoard Technology*, vol. 9, no. 2, pp. 10–13, 2008.

Cette thèse est accessible à l'adresse : https://theses.insa-lyon.fr/publication/2023ISAL0007/these.pdf
© [X.V.L. NGUYEN], [2023], INSA Lyon, tous droits réservés

[38] A. Islam, H. Hansen, P. Tang, M. Jrgensen, and S. rts, “Two-component microinjection moulding for MID fabrication,” *Plastics, Rubber and Composites*, vol. 39, pp. 300–307, Sep. 2010, doi: 10.1179/174328910X12691245470356.

[39] A. Islam, H. N. Hansen, P. T. Tang, and J. Sun, “Process chains for the manufacturing of molded interconnect devices,” *Int J Adv Manuf Technol*, vol. 42, no. 9, pp. 831–841, Jun. 2009, doi: 10.1007/s00170-008-1660-9.

[40] M. Hüske, J. Kickelhain, J. Müller, and G. Eßer, “LASER SUPPORTED ACTIVATION AND ADDITIVE METALLIZATION OF THERMOPLAS- TICS FOR 3D-MIDS,” p. 12.

[41] A. Friedrich, B. Geck, and M. Fengler, “LDS manufacturing technology for next generation radio frequency applications,” in *2016 12th International Congress Molded Interconnect Devices (MID)*, Sep. 2016, pp. 1–6. doi: 10.1109/ICMID.2016.7738939.

[42] J. Schirmer, M. Reichenberger, S. Neermann, and J. Franke, “Conformable Electronics: Thermoforming and Injection Molding of Electronic Components,” in *2021 44th International Spring Seminar on Electronics Technology (ISSE)*, May 2021, pp. 1–6. doi: 10.1109/ISSE51996.2021.9467588.

[43] O. Rusanen, T. Simula, P. Niskala, V. Lindholm, and M. Heikkinen, “Injection Molded Structural Electronics Brings Surfaces to Life,” in *2019 22nd European Microelectronics and Packaging Conference & Exhibition (EMPC)*, Sep. 2019, pp. 1–7. doi: 10.23919/EMPC44848.2019.8951795.

[44] C. Rowell and E. Y. Lam, “Mobile-Phone Antenna Design,” *IEEE Antennas and Propagation Magazine*, vol. 54, no. 4, pp. 14–34, Aug. 2012, doi: 10.1109/MAP.2012.6309152.

[45] “Thermoplastic Injection Molding: New Packages and 3D - ET,” *studylib.net*. https://studylib.net/doc/18354225/thermoplastic-injection-molding--new-packages-and-3d---et (accessed Sep. 04, 2022).

[46] D. Unnikrishnan, “Mid technology potential for RF passive components and antennas,” *UNIVERSITÉ DE GRENOBLE*, p. 246, 2006.

[47] F. Sonnerat, “Développement d’antennes innovantes pour les terminaux mobiles 4G tenant compte de l’interaction avec l’utilisateur: solutions circuits et antennes envisageables,” p. 191.

[48] Y. Chen, C. Zhang, Y. Lu, W.-W. Yang, and J. Huang, “Compact Dual-Polarized Base Station Antenna Array Using Laser Direct Structuring Technique,” *IEEE Antennas and Wireless Propagation Letters*, vol. 20, no. 1, pp. 78–82, Jan. 2021, doi: 10.1109/LAWP.2020.3040509.

[49] C. Orlob, Q. H. Dao, and D. Kornek, “Dual-polarized log.-periodic antenna on a conical MID substrate,” in *Proceedings of the 5th European Conference on Antennas and Propagation (EUCAP)*, Apr. 2011, pp. 361–364.

[50] A. J. Fenn, D. J. Pippin, C. M. Lamb, F. G. Willwerth, H. M. Aumann, and J. P. Doane, “3D printed conformal array antenna: Simulations and measurements,” in *2016 IEEE International Symposium on Phased Array Systems and Technology (PAST)*, Oct. 2016, pp. 1–4. doi: 10.1109/ARRAY.2016.7832591.

[51] S. Murch, “Technology » RePliForm, Inc.,” *RePliForm, Inc.* https://repliforminc.com/technology/ (accessed Aug. 28, 2022).

[52] J. Heirons *et al.*, “Inkjet printed GPS antenna on a 3D printed substrate using low-cost machines,” in *2016 Loughborough Antennas & Propagation Conference (LAPC)*, Oct. 2016, pp. 1–4. doi: 10.1109/LAPC.2016.7807590.

[53] J. Maas, B. Liu, S. Hajela, Y. Huang, X. Gong, and W. J. Chappell, “Laser-Based Layer-by-Layer Polymer Stereolithography for High-Frequency Applications,” *Proceedings of the IEEE*, vol. 105, no. 4, pp. 645–654, Apr. 2017, doi: 10.1109/JPROC.2016.2629179.

[54] A. H. Wahyudi, J. T. S. Sumantyo, S. Wijaya, and A. Munir, “PLA-based 3D printed circularly polarized X-band horn array antenna for CP-SAR sensor,” in *2018 International Workshop on Antenna Technology (iWAT)*, Mar. 2018, pp. 1–4. doi: 10.1109/IWAT.2018.8379219.

[55] S. Wang, L. Zhu, and W. Wu, “3-D Printed Inhomogeneous Substrate and Superstrate for Application in Dual-Band and Dual-CP Stacked Patch Antenna,” *IEEE Transactions on Antennas and Propagation*, vol. 66, no. 5, pp. 2236–2244, May 2018, doi: 10.1109/TAP.2018.2810330.

Cette thèse est accessible à l'adresse : https://theses.insa-lyon.fr/publication/2023ISAL0007/these.pdf
© [X.V.L. NGUYEN], [2023], INSA Lyon, tous droits réservés

[56] M. F. Farooqui and A. Kishk, “3-D-Printed Tunable Circularly Polarized Microstrip Patch Antenna,” *IEEE Antennas and Wireless Propagation Letters*, vol. 18, no. 7, pp. 1429–1432, Jul. 2019, doi: 10.1109/LAWP.2019.2919255.

[57] M. Shirvanimoghaddam *et al.*, “Towards a Green and Self-Powered Internet of Things Using Piezoelectric Energy Harvesting,” *IEEE Access*, vol. 7, pp. 94533–94556, 2019, doi: 10.1109/ACCESS.2019.2928523.

[58] C. Gould and R. Edwards, “Review on micro-energy harvesting technologies,” in *2016 51st International Universities Power Engineering Conference (UPEC)*, Sep. 2016, pp. 1–5. doi: 10.1109/UPEC.2016.8114023.

[59] L. Mateu and F. Moll, “Review of energy harvesting techniques and applications for microelectronics,” in *VLSI Circuits and Systems II*, Jun. 2005, vol. 5837, pp. 359–373. doi: 10.1117/12.613046.

[60] S. Meninger, J. O. Mur-Miranda, R. Amirtharajah, A. Chandrakasan, and J. H. Lang, “Vibration-to-electric energy conversion,” *IEEE Transactions on Very Large Scale Integration (VLSI) Systems*, vol. 9, no. 1, pp. 64–76, Feb. 2001, doi: 10.1109/92.920820.

[61] X. Yue, J. Kiely, D. Gibson, and E. M. Drakakis, “Charge-Based Supercapacitor Storage Estimation for Indoor Sub-mW Photovoltaic Energy Harvesting Powered Wireless Sensor Nodes,” *IEEE Transactions on Industrial Electronics*, vol. 67, no. 3, pp. 2411–2421, Mar. 2020, doi: 10.1109/TIE.2019.2896321.

[62] L. Li, T. Jia, and Y. Huang, “Compact Dual-Band, Wide-Angle, Polarization-Angle-Independent Rectifying Metasurface for Ambient Energy Harvesting and Wireless Power Transfer,” *IEEE TRANSACTIONS ON MICROWAVE THEORY AND TECHNIQUES*, p. 11.

[63] L. Li, X. Zhang, C. Song, and Y. Huang, “Progress, Challenges and Perspective on Metasurfaces for Ambient Radio Frequency Energy Harvesting,” *Applied Physics Letters*, vol. 116, Jan. 2020, doi: 10.1063/1.5140966.

[64] C. L. Holloway, E. F. Kuester, J. A. Gordon, J. O’Hara, J. Booth, and D. R. Smith, “An Overview of the Theory and Applications of Metasurfaces: The Two-Dimensional Equivalents of Metamaterials,” *IEEE Antennas and Propagation Magazine*, vol. 54, no. 2, pp. 10–35, Apr. 2012, doi: 10.1109/MAP.2012.6230714.

[65] M. Zeng, A. Andrenko, X. Liu, Z. Li, and H.-Z. Tan, “A Compact Fractal Loop Rectenna for RF Energy Harvesting,” *IEEE Antennas and Wireless Propagation Letters*, vol. PP, pp. 1–1, Jul. 2017, doi: 10.1109/LAWP.2017.2722460.

[66] E. Vandelle, D. H. N. Bui, T.-P. Vuong, G. Ardila, K. Wu, and S. Hemour, “Harvesting Ambient RF Energy Efficiently With Optimal Angular Coverage,” *IEEE Transactions on Antennas and Propagation*, vol. 67, no. 3, pp. 1862–1873, Mar. 2019, doi: 10.1109/TAP.2018.2888957.

[67] “Self-Powered Implantable Medical Devices: Photovoltaic Energy Harvesting Review - Zhao - 2020 - Advanced Healthcare Materials - Wiley Online Library.” https://onlinelibrary.wiley.com/doi/full/10.1002/adhm.202000779 (accessed Apr. 28, 2022).

[68] D. Elsheakh, *Microwave Antennas for Energy Harvesting Applications*. IntechOpen, 2017. doi: 10.5772/64918.

[69] Romain Berges, Ludivine Fadel, Laurent Oyhenart, Valérie Vigneras, Thierry Taris. A Flexible printed dual-band antenna dedicated to RF Energy Harvesting Application. Journées Nationales sur la Récupération et le Stockage d'Énergie, May 2016, Bordeaux, France. ⟨hal-01484377⟩.

[70] H. Takhedmit, “Ambient RF Power Harvesting : Application to Remote Supply of a Batteryless Temperature Sensor,” Sep. 2016.

[71] A. Khemar, A. Kacha, H. Takhedmit, and G. Abib, “Design and experiments of a dual-band rectenna for ambient RF energy harvesting in urban environments,” *IET Microwaves, Antennas & Propagation*, vol. 12, no. 1, pp. 49–55, 2018, doi: 10.1049/iet-map.2016.1040.

[72] X. Gu, L. Grauwin, D. Dousset, S. Hemour, and K. Wu, “Dynamic Ambient RF Energy Density Measurements of Montreal for Battery-Free IoT Sensor Network Planning,” *IEEE Internet of Things Journal*, vol. PP, pp. 1–1, Mar. 2021, doi: 10.1109/JIOT.2021.3065683.

Cette thèse est accessible à l'adresse : https://theses.insa-lyon.fr/publication/2023ISAL0007/these.pdf
© [X.V.L. NGUYEN], [2023], INSA Lyon, tous droits réservés

[73] F. Khalid, W. Saeed, N. Shoaib, M. U. Khan, and H. M. Cheema, “Quad-Band 3D Rectenna Array for Ambient RF Energy Harvesting,” *International Journal of Antennas and Propagation*, vol. 2020, p. e7169846, May 2020, doi: 10.1155/2020/7169846.

[74] “bq25504.pdf.” Accessed: Apr. 27, 2022. [Online]. Available: https://www.ti.com/lit/ds/symlink/bq25504.pdf?ts=1650996666495&ref_url=https%253A%252F%252Fwww.google.com%252F

[75] “Datasheet_AEM30330_energy_harvesting_IC_REV1.1.pdf.” Accessed: Sep. 09, 2022. [Online]. Available: https://e-peas.com/wp-content/uploads/2021/08/Datasheet_AEM30330_energy_harvesting_IC_REV1.1.pdf

[76] C. Song, Y. Huang, J. Zhou, J. Zhang, S. Yuan, and P. Carter, “A High-Efficiency Broadband Rectenna for Ambient Wireless Energy Harvesting,” *IEEE Transactions on Antennas and Propagation*, vol. 63, no. 8, pp. 3486–3495, Aug. 2015, doi: 10.1109/TAP.2015.2431719.

[77] A. Eid, J. G. D. Hester, J. Costantine, Y. Tawk, A. H. Ramadan, and M. M. Tentzeris, “A Compact Source–Load Agnostic Flexible Rectenna Topology for IoT Devices,” *IEEE Transactions on Antennas and Propagation*, vol. 68, no. 4, pp. 2621–2629, Apr. 2020, doi: 10.1109/TAP.2019.2955211.

[78] X. Gu, L. Guo, S. Hemour, and K. Wu, “Optimum Temperatures for Enhanced Power Conversion Efficiency (PCE) of Zero-Bias Diode-Based Rectifiers,” *IEEE Transactions on Microwave Theory and Techniques*, vol. 68, no. 9, pp. 4040–4053, Sep. 2020, doi: 10.1109/TMTT.2020.2992024.

[79] “Harvesting Wireless Power: Survey of Energy-Harvester Conversion Efficiency in Far-Field, Wireless Power Transfer Systems.” https://ieeexplore.ieee.org/document/6810996 (accessed Jun. 14, 2022).

[80] H. Mahfoudi, H. Takhedmit, M. Tellache, and S. Boisseau, “Wireless sensor node remote supply using a compact stacked rectenna array with voltage multipliers at 2.45 GHz,” *International Journal of Microwave and Wireless Technologies*, vol. 12, no. 4, pp. 309–315, May 2020, doi: 10.1017/S1759078719001314.

[81] H. Kanaya, S. Tsukamaoto, T. Hirabaru, D. Kanemoto, R. K. Pokharel, and K. Yoshida, “Energy Harvesting Circuit on a One-Sided Directional Flexible Antenna,” *IEEE Microwave and Wireless Components Letters*, vol. 23, no. 3, pp. 164–166, Mar. 2013, doi: 10.1109/LMWC.2013.2246779.

[82] M. K. Hosain, A. Z. Kouzani, M. F. Samad, and S. J. Tye, “A Miniature Energy Harvesting Rectenna for Operating a Head-Mountable Deep Brain Stimulation Device,” *IEEE Access*, vol. 3, pp. 223–234, 2015, doi: 10.1109/ACCESS.2015.2414411.

[83] O. O’Conchubhair, K. Yang, P. McEvoy, and M. J. Ammann, “Amorphous Silicon Solar Vivaldi Antenna,” *IEEE Antennas and Wireless Propagation Letters*, vol. 15, pp. 893–896, 2016, doi: 10.1109/LAWP.2015.2479189.

[84] Vlad Marian. Transmission d'énergie sans fil : Application au réveil à distance de récepteurs en veille zéro consommation. Autre. Ecole Centrale de Lyon, 2012. Français. ⟨NNT : 2012ECDL0045⟩. ⟨tel-00787608⟩.

[85] S. Hemour *et al.*, “Towards Low-Power High-Efficiency RF and Microwave Energy Harvesting,” *IEEE Transactions on Microwave Theory and Techniques*, vol. 62, no. 4, pp. 965–976, Apr. 2014, doi: 10.1109/TMTT.2014.2305134.

[86] H. Takhedmit, L. Cirio, F. Costa, and O. Picon, “Transparent rectenna and rectenna array for RF energy harvesting at 2.45 GHz,” in *The 8th European Conference on Antennas and Propagation (EuCAP 2014)*, Apr. 2014, pp. 2970–2972. doi: 10.1109/EuCAP.2014.6902451.

[87] F. Congedo, G. Monti, L. Tarricone, and V. Bella, “A 2.45-GHz Vivaldi Rectenna for the Remote Activation of an End Device Radio Node,” *IEEE Sensors Journal*, vol. 13, no. 9, pp. 3454–3461, Sep. 2013, doi: 10.1109/JSEN.2013.2265081.

[88] D. De Donno, L. Catarinucci, and L. Tarricone, “An UHF RFID Energy-Harvesting System Enhanced by a DC-DC Charge Pump in Silicon-on-Insulator Technology,” *IEEE Microwave and Wireless Components Letters*, vol. 23, no. 6, pp. 315–317, Jun. 2013, doi: 10.1109/LMWC.2013.2258002.

Cette thèse est accessible à l'adresse : https://theses.insa-lyon.fr/publication/2023ISAL0007/these.pdf
© [X.V.L. NGUYEN], [2023], INSA Lyon, tous droits réservés

[89] H. Sun, Y. Guo, M. He, and Z. Zhong, “A Dual-Band Rectenna Using Broadband Yagi Antenna Array for Ambient RF Power Harvesting,” *IEEE Antennas and Wireless Propagation Letters*, vol. 12, pp. 918–921, 2013, doi: 10.1109/LAWP.2013.2272873.

[90] M.-J. Nie, X.-X. Yang, G.-N. Tan, and B. Han, “A Compact 2.45-GHz Broadband Rectenna Using Grounded Coplanar Waveguide,” *IEEE Antennas and Wireless Propagation Letters*, vol. 14, pp. 986–989, Oct. 2015, doi: 10.1109/LAWP.2015.2388789.

[91] J.-K. Huang, W.-T. Hung, T.-H. Cheng, and S.-Y. Chen, “A 2.45-GHz high-efficiency loop-shaped PIFA rectenna for portable devices and wireless sensors,” in *2015 IEEE International Symposium on Antennas and Propagation USNC/URSI National Radio Science Meeting*, Jul. 2015, pp. 1284–1285. doi: 10.1109/APS.2015.7305031.

[92] S. Shen, C.-Y. Chiu, and R. D. Murch, “A Dual-Port Triple-Band L-Probe Microstrip Patch Rectenna for Ambient RF Energy Harvesting,” *IEEE Antennas and Wireless Propagation Letters*, vol. 16, pp. 3071–3074, 2017, doi: 10.1109/LAWP.2017.2761397.

[93] M. Stoopman, S. Keyrouz, H. J. Visser, K. Philips, and W. A. Serdijn, “Co-Design of a CMOS Rectifier and Small Loop Antenna for Highly Sensitive RF Energy Harvesters,” *IEEE Journal of Solid-State Circuits*, vol. 49, no. 3, pp. 622–634, Mar. 2014, doi: 10.1109/JSSC.2014.2302793.

[94] S.-E. Adami, “Optimisation de la récupération d’énergie dans les applications de rectenna,” phdthesis, Ecole Centrale de Lyon, 2013. Accessed: Jul. 03, 2022. [Online]. Available: https://tel.archives-ouvertes.fr/tel-00967525

[95] S.-E. Adami *et al.*, “A Flexible 2.45-GHz Power Harvesting Wristband With Net System Output From −24.3 dBm of RF Power,” *IEEE Transactions on Microwave Theory and Techniques*, vol. 66, no. 1, pp. 380–395, Jan. 2018, doi: 10.1109/TMTT.2017.2700299.

[96] “bq25570.pdf.” Accessed: Jul. 02, 2022. [Online]. Available: https://www.ti.com/lit/ds/symlink/bq25570.pdf?ts=1656754775956&ref_url=https%253A%252F%252Fwww.ti.com%252Fproduct%252FBQ25570

[97] “LTC3108.pdf.” Accessed: Jul. 02, 2022. [Online]. Available: https://www.analog.com/media/en/technical-documentation/data-sheets/LTC3108.pdf

[98] “LTC3109 - Auto-Polarity, Ultralow Voltage Step-Up Converter and Power Manager,” p. 24.

[99] T. Paing, E. Falkenstein, R. Zane, and Z. Popovic, “Custom IC for Ultra-low Power RF Energy Harvesting,” in *2009 Twenty-Fourth Annual IEEE Applied Power Electronics Conference and Exposition*, Feb. 2009, pp. 1239–1245. doi: 10.1109/APEC.2009.4802822.

[100] P.-H. Hsieh, C.-H. Chou, and T. Chiang, “An RF Energy Harvester With 44.1% PCE at Input Available Power of -12 dBm,” *IEEE Transactions on Circuits and Systems I: Regular Papers*, vol. 62, no. 6, pp. 1528–1537, Jun. 2015, doi: 10.1109/TCSI.2015.2418834.

[101] H. Sun, Y. Guo, M. He, and Z. Zhong, “Design of a High-Efficiency 2.45-GHz Rectenna for Low-Input-Power Energy Harvesting,” *IEEE Antennas and Wireless Propagation Letters*, vol. 11, pp. 929–932, 2012, doi: 10.1109/LAWP.2012.2212232.

[102] “Antenna Theory: Analysis and Design, 4th Edition | Wiley,” *Wiley.com*. https://www.wiley.com/en-us/Antenna+Theory%3A+Analysis+and+Design%2C+4th+Edition-p-9781118642061 (accessed May 18, 2022).

[103] Hakim Takhedmit. Modélisation et conception de circuits de réception complexes pour la transmission d'énergie sans fil à 2.45 GHz. Autre. Ecole Centrale de Lyon, 2010. Français. ⟨NNT : 2010ECDL0025⟩. ⟨tel-00564596⟩.

[104] J. Kimionis, M. Isakov, B. S. Koh, A. Georgiadis, and M. M. Tentzeris, “3D-Printed Origami Packaging With Inkjet-Printed Antennas for RF Harvesting Sensors,” *IEEE Transactions on Microwave Theory and Techniques*, vol. 63, no. 12, pp. 4521–4532, Oct. 2015, doi: 10.1109/TMTT.2015.2494580.

[105] G. Andia Vera, A. Georgiadis, A. Collado, and S. Via, “Design of a 2.45 GHz rectenna for electromagnetic (EM) energy scavenging,” in *2010 IEEE Radio and Wireless Symposium (RWS)*, Jan. 2010, pp. 61–64. doi: 10.1109/RWS.2010.5434266.

Cette thèse est accessible à l'adresse : https://theses.insa-lyon.fr/publication/2023ISAL0007/these.pdf
© [X.V.L. NGUYEN], [2023], INSA Lyon, tous droits réservés

[106] M. Wagih, A. S. Weddell, and S. Beeby, "Meshed High-Impedance Matching Network-Free Rectenna Optimized for Additive Manufacturing," *IEEE Open Journal of Antennas and Propagation*, vol. 1, pp. 615–626, 2020, doi: 10.1109/OJAP.2020.3038001.

[107] D. Vital, S. Bhardwaj, and J. L. Volakis, "A 2.45 GHz RF Power Harvesting System Using Textile-Based Single-Diode Rectennas," in *2019 IEEE MTT-S International Microwave Symposium (IMS)*, Jun. 2019, pp. 1313–1315. doi: 10.1109/MWSYM.2019.8700836.

[108] A. Bakytbekov, T. Nguyen, C. Huynh, K. Salama, and A. Shamim, "Fully Printed 3D Cube-Shaped Multiband Fractal Rectenna for Ambient RF Energy Harvesting," *Nano Energy*, vol. 53, Sep. 2018, doi: 10.1016/j.nanoen.2018.09.022.

[109] A. Eid *et al.*, "Inkjet-/3D-/4D-Printed Perpetual Electronics and Modules: RF and mm-Wave Devices for 5G+, IoT, Smart Agriculture, and Smart Cities Applications," *IEEE Microwave Magazine*, vol. 21, no. 12, pp. 87–103, Oct. 2020, doi: 10.1109/MMM.2020.3023310.

[110] "Formlabs Customer Support," *Formlabs Customer Support*. http://support.formlabs.com/ (accessed Sep. 19, 2022).

[111] "Microwave Engineering, 4th Edition | Wiley," *Wiley.com*, Feb. 27, 2022. https://www.wiley.com/en-us/Microwave+Engineering%2C+4th+Edition-p-9781118298138R120 (accessed Feb. 27, 2022).

[112] "Série M: mesure XRF de l'optique poly-capillaire la plus avancée." https://bowmanxrf.com/fr/bowman-m-series/ (accessed Jun. 19, 2022).

[113] J. C. Rautio and V. Demir, "Microstrip conductor loss models for electromagnetic analysis," *IEEE Transactions on Microwave Theory and Techniques*, vol. 51, no. 3, pp. 915–921, Mar. 2003, doi: 10.1109/TMTT.2003.808693.

[114] J. C. Rautio, "An investigation of microstrip conductor loss," *IEEE Microwave Magazine*, vol. 1, no. 4, pp. 60–67, Oct. 2000, doi: 10.1109/6668.893247.

[115] R. Horton, B. Easter, and A. Gopinath, "Variation of microstrip losses with thickness of strip," *Electronics Letters*, vol. 7, no. 17, pp. 490–491, Aug. 1971, doi: 10.1049/el:19710332.

[116] "RH-2000," *Hirox Europe*. https://hirox-europe.com/fr/products/3d-digital-microscope/rh-2000/ (accessed Jun. 19, 2022).

[117] S. P. Morgan Jr., "Effect of Surface Roughness on Eddy Current Losses at Microwave Frequencies," *Journal of Applied Physics*, vol. 20, pp. 352–362, Apr. 1949, doi: 10.1063/1.1698368.

[118] P. G. Huray, "Impact of Copper Surface Texture on Loss: A Model that Works," p. 22.

[119] A. F. Horn III, J. Reynolds, P. LaFrance, and J. Rautio, "Effect of conductor profile on the insertion loss, phase constant, and dispersion in thin high frequency transmission lines," *DesignCon 2010*, vol. 1, May 2010.

[120] E. J. Denlinger, "Losses of Microstrip Lines," *IEEE Transactions on Microwave Theory and Techniques*, vol. 28, no. 6, pp. 513–522, Jun. 1980, doi: 10.1109/TMTT.1980.1130112.

[121] A. M. Mangan, S. P. Voinigescu, M.-T. Yang, and M. Tazlauanu, "De-embedding transmission line measurements for accurate modeling of IC designs," *IEEE Transactions on Electron Devices*, vol. 53, no. 2, pp. 235–241, Feb. 2006, doi: 10.1109/TED.2005.861726.

[122] P. I. Deffenbaugh, R. C. Rumpf, and K. H. Church, "Broadband Microwave Frequency Characterization of 3-D Printed Materials," *IEEE Transactions on Components, Packaging and Manufacturing Technology*, vol. 3, no. 12, Art. no. 12, Oct. 2013, doi: 10.1109/TCPMT.2013.2273306.

[123] C. Orlob, D. Kornek, S. Preihs, and I. Rolfes, "Characterization of Electromagnetic Properties of Molded Interconnect Device Materials," in *2009 German Microwave Conference*, Mar. 2009, pp. 1–4. doi: 10.1109/GEMIC.2009.4815856.

[124] J. Baker-Jarvis, M. D. Janezic, and D. C. Degroot, "High-frequency dielectric measurements," *IEEE Instrumentation Measurement Magazine*, vol. 13, no. 2, Art. no. 2, Apr. 2010, doi: 10.1109/MIM.2010.5438334.

Cette thèse est accessible à l'adresse : https://theses.insa-lyon.fr/publication/2023ISAL0007/these.pdf
© [X.V.L. NGUYEN], [2023], INSA Lyon, tous droits réservés

[125] V. Palazzi *et al.*, “3-D-Printing-Based Selective-Ink-Deposition Technique Enabling Complex Antenna and RF Structures for 5G Applications up to 6 GHz,” *IEEE Trans. Compon., Packag. Manufact. Technol.*, vol. 9, no. 7, Art. no. 7, Jul. 2019, doi: 10.1109/TCPMT.2019.2919187.

[126] J. A. Byford, C. Oakley, and P. Chahal, “Additively Manufactured Frequency Selective Structures on Curved Surfaces,” in *2018 48th European Microwave Conference (EuMC)*, Sep. 2018, pp. 671–674. doi: 10.23919/EuMC.2018.8541568.

[127] K. Szostak and P. Słobodzian, "Broadband Dielectric Measurement of PCB and Substrate Materials by Means of a Microstrip Line of Adjustable Width," in *IEEE Microwave and Wireless Components Letters*, vol. 28, no. 10, pp. 945-947, Oct. 2018, doi: 10.1109/LMWC.2018.2864196.

[128] “Dielectric properties of 3D-printed materials for anatomy specific 3D-printed MRI coils - ScienceDirect.” https://www.sciencedirect.com/science/article/abs/pii/S1090780718300582 (accessed Feb. 27, 2022).

[129] F. M. Mbango, “Contribution A La Caractérisation des Matériaux Utilisés en Microélectronique RadioFréquence,” phdthesis, Université Joseph-Fourier - Grenoble I, 2008. Accessed: Feb. 27, 2022. [Online]. Available: https://tel.archives-ouvertes.fr/tel-00353177

[130] D. Béchevet, “Contribution au développement de tag RFID UHF et Microondes sur matériaux plastiques,” phdthesis, Institut National Polytechnique de Grenoble - INPG, 2005. Accessed: Feb. 27, 2022. [Online]. Available: https://tel.archives-ouvertes.fr/tel-00119837

[131] D. Unnikrishnan, D. Kaddour, and S. Tedjini, “Molded interconnect devices for RF applications: Transmission lines and low pass filters,” in *2012 International Symposium on Signals, Systems, and Electronics (ISSSE)*, Oct. 2012, pp. 1–5. doi: 10.1109/ISSSE.2012.6374330.

[132] N. Duangrit, B. Hong, A. D. Burnett, P. Akkaraekthalin, I. D. Robertson, and N. Somjit, “Terahertz Dielectric Property Characterization of Photopolymers for Additive Manufacturing,” *IEEE Access*, vol. 7, pp. 12339–12347, 2019, doi: 10.1109/ACCESS.2019.2893196.

[133] J.-L. Coutaz, F. Garet, and V. P. Wallace, *Principles of Terahertz Time-Domain Spectroscopy*. New York: Jenny Stanford Publishing, 2018. doi: 10.1201/b22478.

[134] G. Boussatour, “Caractérisation diélectrique et thermique de films biopolymères pour l’électronique flexible haute fréquence,” These de doctorat, Lille, 2019. Accessed: Feb. 27, 2022. [Online]. Available: http://www.theses.fr/2019LILUI015

[135] T. Hirano, J. Hirokawa, and M. Ando, “Influence of the SMA connector and its modeling on electromagnetic simulation,” *Microwave and Optical Technology Letters*, vol. 57, no. 9, pp. 2168–2171, 2015, doi: 10.1002/mop.29304.

[136] E. Hammerstad and O. Jensen, “Accurate Models for Microstrip Computer-Aided Design,” in *1980 IEEE MTT-S International Microwave symposium Digest*, May 1980, pp. 407–409. doi: 10.1109/MWSYM.1980.1124303.

[137] W. Su, R. Bahr, S. A. Nauroze, and M. M. Tentzeris, “Novel 3D-printed ‘Chinese fan’ bow-tie antennas for origami/shape-changing configurations,” in *2017 IEEE International Symposium on Antennas and Propagation USNC/URSI National Radio Science Meeting*, Jul. 2017, pp. 1245–1246. doi: 10.1109/APUSNCURSINRSM.2017.8072665.

[138] A. Siblini, “Optimization of Antenna ARMA (Agile Matrix Antenna radiating by pixel elaborated with Meta-material) For beam forming for the RFID and Radar Applications,” phdthesis, Université de Limoges ; Université Libanaise, 2017. Accessed: Jul. 03, 2022. [Online]. Available: https://tel.archives-ouvertes.fr/tel-01698830

[139] M. Kara, “A simple technique for the calculation of the bandwidth of rectangular microstrip antenna elements with various substrate thicknesses,” *Microwave and Optical Technology Letters*, vol. 12, no. 1, pp. 16–20, 1996, doi: 10.1002/(SICI)1098-2760(199605)12:1<16::AID-MOP4>3.0.CO;2-R.

[140] L. Paul, M. Hosain, S. Sarker, M. H. Prio, M. Morshed, and A. Sarkar, “The Effect of Changing Substrate Material and Thickness on the Performance of Inset Feed Microstrip Patch Antenna,” *American Journal of Networks and Communications*, vol. 4, pp. 54–58, May 2015, doi: 10.11648/j.ajnc.20150403.16.

Cette thèse est accessible à l'adresse : https://theses.insa-lyon.fr/publication/2023ISAL0007/these.pdf
© [X.V.L. NGUYEN], [2023], INSA Lyon, tous droits réservés

[141] Y. R. Patel, A. K. Sisodia, and N. M. Prabhakar, “The Effect of Substrate Material on Microstrip Patch Antenna,” vol. 7, no. 3, p. 4, 2016.

[142] S. S. Gao, Q. Luo, and F. Zhu, “Introduction to Circularly Polarized Antennas,” in *Circularly Polarized Antennas*, IEEE, 2014, pp. 1–28. doi: 10.1002/9781118790526.ch1.

[143] “Microstrip Antennas: The Analysis and Design of Microstrip Antennas and Arrays | IEEE eBooks | IEEE Xplore.” https://ieeexplore.ieee.org/book/5263382 (accessed May 18, 2022).

[144] P. Sharma and K. Gupta, “Analysis and optimized design of single feed circularly polarized microstrip antennas,” *IEEE Transactions on Antennas and Propagation*, vol. 31, no. 6, pp. 949–955, Nov. 1983, doi: 10.1109/TAP.1983.1143162.

[145] G. Muntoni *et al.*, “A Curved 3-D Printed Microstrip Patch Antenna Layout for Bandwidth Enhancement and Size Reduction,” *IEEE Antennas and Wireless Propagation Letters*, vol. 19, no. 7, pp. 1118–1122, Jul. 2020, doi: 10.1109/LAWP.2020.2990944.

[146] J.-P. Geng, J. Li, R.-H. Jin, S. Ye, X. Liang, and M. Li, “THE DEVELOPMENT OF CURVED MICROSTRIP ANTENNA WITH DEFECTED GROUND STRUCTURE,” *PIER*, vol. 98, pp. 53–73, 2009, doi: 10.2528/PIER09081905.

[147] N. Burum and Z. Sipus, “Radiation properties of spherical and cylindrical rectangular microstrip patch antennas,” *undefined*, 2002, Accessed: Jun. 19, 2022. [Online]. Available: https://www.semanticscholar.org/paper/Radiation-properties-of-spherical-and-cylindrical-Burum-Sipus/b0c42bdb44414631678745a64fb4b0576c6ff8c6

[148] M. Gonzalez, “Analisys of Conformal Antennas for Avionics Applications,” 2007.

[149] S. Yan and G. A. E. Vandenbosch, “Radiation Pattern-Reconfigurable Wearable Antenna Based on Metamaterial Structure,” *IEEE Antennas and Wireless Propagation Letters*, vol. 15, pp. 1715–1718, 2016, doi: 10.1109/LAWP.2016.2528299.

[150] S. Ladan and K. Wu, “Nonlinear Modeling and Harmonic Recycling of Millimeter-Wave Rectifier Circuit,” *IEEE Transactions on Microwave Theory and Techniques*, vol. 63, no. 3, pp. 937–944, Mar. 2015, doi: 10.1109/TMTT.2015.2396043.

[151] D. Surender, T. Khan, F. A. Talukdar, A. De, Y. M. M. Antar, and Al. P. Freundorfer, “Key Components of Rectenna System: A Comprehensive Survey,” *IETE Journal of Research*, vol. 0, no. 0, pp. 1–27, May 2020, doi: 10.1080/03772063.2020.1761268.

[152] A. Mouapi, N. Hakem, and G. Vanessa Kamani, “A Selective Rectifier for RF Energy Harvesting Under Non-Stationary Propagation Conditions,” in *2018 IEEE International Conference on Environment and Electrical Engineering and 2018 IEEE Industrial and Commercial Power Systems Europe (EEEIC / I&CPS Europe)*, Jun. 2018, pp. 1–6. doi: 10.1109/EEEIC.2018.8494509.

[153] “APN1014_200324B.pdf.” Accessed: Jul. 03, 2022. [Online]. Available: https://www.skyworksinc.com/-/media/SkyWorks/Documents/Products/1-100/APN1014_200324B.pdf

[154] M. E. Goldfarb and R. A. Pucel, “Modeling via hole grounds in microstrip,” *IEEE Microwave and Guided Wave Letters*, vol. 1, no. 6, pp. 135–137, Jun. 1991, doi: 10.1109/75.91090.

[155] V. Palazzi *et al.*, “A Novel Ultra-Lightweight Multiband Rectenna on Paper for RF Energy Harvesting in the Next Generation LTE Bands,” *IEEE Transactions on Microwave Theory and Techniques*, vol. 66, no. 1, pp. 366–379, Jan. 2018, doi: 10.1109/TMTT.2017.2721399.

[156] D. H. N. Bui, T.-P. Vuong, J. Verdier, B. Allard, and P. Benech, “Design and Measurement of 3D Flexible Antenna Diversity for Ambient RF Energy Scavenging in Indoor Scenarios,” *IEEE Access*, vol. 7, pp. 17033–17044, 2019, doi: 10.1109/ACCESS.2019.2894327.

[157] A. Capitaine, “Récupération d’énergie à partir de piles à combustible microbiennes benthiques,” phdthesis, Université de Lyon, 2017. Accessed: Jul. 03, 2022. [Online]. Available: https://tel.archives-ouvertes.fr/tel-02090785

[158] “stts22h.pdf.” Accessed: Jul. 05, 2022. [Online]. Available: https://www.st.com/resource/en/datasheet/stts22h.pdf

Cette thèse est accessible à l'adresse : https://theses.insa-lyon.fr/publication/2023ISAL0007/these.pdf
© [X.V.L. NGUYEN], [2023], INSA Lyon, tous droits réservés

[159] "rf430frl153h.pdf." Accessed: Jul. 05, 2022. [Online]. Available: https://www.ti.com/lit/ds/symlink/rf430frl153h.pdf?ts=1657045704464&ref_url=https%253A%252F%252Fwww.google.com%252F

[160] A. R. Aboulsaad, F. Hussien, M. Aboudina, and A. N. Mohieldin, "A wide-range reconfigurable RF energy harvesting system with integrated storage and load regulation controller," *AEU - International Journal of Electronics and Communications*, vol. 156, p. 154396, Nov. 2022, doi: 10.1016/j.aeue.2022.154396.

Cette thèse est accessible à l'adresse : https://theses.insa-lyon.fr/publication/2023ISAL0007/these.pdf
© [X.V.L. NGUYEN], [2023], INSA Lyon, tous droits réservés

List of Publications

Conferences

- X. V. L. Nguyen, T. Gerges, J. M. Duchamp, P. Benech, J. Verdier, P. Lombard, M. Cabrera, B. Allard. Accessing High Temperature Stereolithography Photopolymers Compabilities for Antennas. *10th National Days on Energy Harvesting and Storage (JNRSE)*, Jun 2021, Grenoble, France. ⟨hal-03451946⟩

- X. V. L. Nguyen, T. Gerges, J. M. Duchamp, P. Benech, J. Verdier, P. Lombard, M. Cabrera, B. Allard, "Stereolithography-Based Rectenna for Wireless Energy Harvesting," *2021 IEEE 34th International System-on-Chip Conference (SOCC)*, 2021, pp. 34-39, doi: 10.1109/SOCC52499.2021.9739329

- X. V. L. Nguyen, T. Gerges, J. M. Duchamp, P. Benech, J. Verdier, P. Lombard, M. Cabrera, B. Allard, "Rectenna plastronique pour la recuperation d'énergie de Wi-Fi", *Neuvième Conférence Plénière du GDR ONDES,* Lille, 30 Novembre et 1er Décembre, 2021.

- X. V. L. Nguyen, T. Gerges, J. M. Duchamp, P. Benech, J. Verdier, P. Lombard, M. Cabrera, B. Allard, " Stereolithography-Based Wireless Energy Harvester with Low-power Sensors", *Jeunes Chercheurs en Génie Electrique, GDR Systèmes d'Energie Electrique dans leurs Dimensions Sociétales,* Le Croisic, 14 et 17 Juin 2022.

- X. V. L. Nguyen, T. Gerges, J. M. Duchamp, P. Benech, J. Verdier, P. Lombard, M. Cabrera, B. Allard, "3D Plastronics Radio Frequency Energy Harvester on Stereolithography Parts," *2022 Wireless Power Week (WPW)*, 2022, pp. 156-161, doi: 10.1109/WPW54272.2022.9854010.

- X. V. L. Nguyen, T. Gerges, J. M. Duchamp, P. Benech, J. Verdier, P. Lombard, M. Cabrera, B. Allard, "Ambient Electromagnetic Energy Harvesting Circuit using Rectennas Manufactured with Stereolithography Resin", *EPE ECCE 2022*, Hannover, September 5th – 9th, 2022.

Journal

- X. V. L. Nguyen, T. Gerges, P. Bevilacqua, J. M. Duchamp, P. Benech, J. Verdier, P. Lombard, P. U. Linge, F. Mieyeville, M. Cabrera, B. Allard. "Radio-Frequency Energy Harvesting using Rapid 3D Plastronics Protoyping Approach: a Case Study", MDPI Journal of Low Power Electronics and Applications, Special Issue on Low-Power on Edge Computing, 2022.

Cette thèse est accessible à l'adresse : https://theses.insa-lyon.fr/publication/2023ISAL0007/these.pdf
© [X.V.L. NGUYEN], [2023], INSA Lyon, tous droits réservés

Cette thèse est accessible à l'adresse : https://theses.insa-lyon.fr/publication/2023ISAL0007/these.pdf
© [X.V.L. NGUYEN], [2023], INSA Lyon, tous droits réservés

ANNEX A

List of possible cases of optimal load of the four-port rectifier

Case	Number of ports receiving the power	Description	Z_{load} (Ω)
1	1	1 port receives 0 dBm	2000
2	1	1 port receives -10 dBm	2500
3	1	1 port receives -20 dBm	3000
4	1	1 port receives -30 dBm	5000
5	2	2 ports receive 0 dBm	1000
6	2	1 port receive 0 dBm and 1 port receives -10 dBm	1110
7	2	2 ports receive -10 dBm	1250
8	2	1 port receives -20 dBm and 1 port receives 0 dBm	1200
9	2	1 port receives -10 dBm and 1 port receives -20 dBm	1365
10	2	1 port receives -30 dBm and 1 port receives 0 dBm	1430
11	2	1 port receives -10 dBm and 1 port receives -30 dBm	1670
12	2	2 ports receive -20 dBm	1500
13	2	1 port receives -20 dBm and 1 port receives -30 dBm	1875
14	2	2 ports receive -30 dBm	2500
15	3	3 ports receive 0 dBm	670
16	3	2 ports receive 0 dBm and 1 port receives -10 dBm	715
17	3	1 port receive 0 dBm and 2 ports receive -10 dBm	770
18	3	1 port receives -20 dBm and 2 ports receive 0 dBm	750
19	3	3 ports receive -10 dBm	830
20	3	1 port receives -10 dBm, 1 port receives -20 dBm and 1 port receives 0 dBm	810
21	3	1 port receives -30 dBm and 2 ports receive 0 dBm	830
22	3	2 ports receive -10 dBm, 1 port receives -20 dBm	880
23	3	1 port receives -10 dBm, 1 port receives -30 dBm and 1 port receives 0 dBm	910
24	3	2 ports receive -20 dBm and 1 port receives 0 dBm	860
25	3	1 port receive -10 dBm and 2 ports receives -20 dBm	940
26	3	2 ports receive -10 dBm and 1 port receives -30 dBm	1000
27	3	1 port receives 0 dBm, 1 port receives -20 dBm and 1 port receives -30 dBm	970
28	3	1 port receives -30 dBm, 1 port receives -20 dBm and 1 port receives -10 dBm	1070
29	3	3 ports receive -20 dBm	1000
30	3	2 ports receive -30 dBm and 1 port receives 0 dBm	1110
31	3	1 port receives -10 dBm and 2 ports receive -30 dBm	1250
32	3	2 port receives -20 dBm and 1 port receives -30 dBm	1155
33	3	1 port receives -20 dBm and 2 ports receive -30 dBm	1365
34	3	3 ports receive -30 dBm	1670
35	4	4 ports receive 0 dBm	500
36	4	3 ports receive 0 dBm and 1 port receives -10 dBm	530
37	4	2 ports receive 0 dBm and 2 ports receive -10 dBm	555
38	4	1 port receives -20 dBm and 3 ports receive 0 dBm	550

Cette thèse est accessible à l'adresse : https://theses.insa-lyon.fr/publication/2023ISAL0007/these.pdf
© [X.V.L. NGUYEN], [2023], INSA Lyon, tous droits réservés

39	4	3 ports receive -10 dBm and 1 port receives 0 dBm	590
40	4	1 port receives -10 dBm, 1 port receives -20 dBm and 2 ports receive 0 dBm	580
41	4	1 port receives -30 dBm and 3 ports receive 0 dBm	590
42	4	4 ports receive -10 dBm	625
43	4	2 ports receive -10 dBm, 1 port receives -20 dBm and 1 port receives 0 dBm	610
44	4	1 port receives -10 dBm, 1 port receives -30 dBm and 2 ports receive 0 dBm	625
45	4	2 ports receive -20 dBm and 2 ports receive 0 dBm	600
46	4	3 ports receive -10 dBm and 1 port receives -20 dBm	650
47	4	1 port receive -10 dBm, 2 ports receives -20 dBm and 1 port receives 0 dBm	640
48	4	2 ports receive -10 dBm, 1 port receives -30 dBm and 1 port receives 0 dBm	670
49	4	2 ports receive 0 dBm, 1 port receives -20 dBm and 1 port receives -30 dBm	650
50	4	3 ports receive -10 dBm and 1 port receives -30 dBm	715
51	4	2 ports receive -10 dBm and 2 ports receive -20 dBm	680
52	4	1 port receives -30 dBm, 1 port receives -20 dBm, 1 port receives -10 dBm and 1 port receives 0 dBm	700
53	4	3 ports receive -20 dBm and 1 port receives 0 dBm	670
54	4	2 ports receive -30 dBm and 2 ports receive 0 dBm	715
55	4	2 ports receive -10 dBm and 2 ports receive -20 dBm	750
56	4	1 port receives -10 dBm and 3 ports receive -20 dBm	715
57	4	1 port receives -10 dBm, 2 ports receive -30 dBm and 1 port receives 0 dBm	770
58	4	2 port receives -20 dBm, 1 port receives -30 dBm and 1 port receives 0 dBm	730
59	4	2 ports receive -10 dBm and 2 ports receive -30 dBm	830
60	4	1 port receives -10 dBm, 2 ports receive -20 dBm and 1 port receives -30 dBm	790
61	4	4 ports receive -20 dBm	750
62	4	1 port receives -20 dBm, 2 ports receive -30 dBm and 1 port receives 0 dBm	810
63	4	1 port receives -10 dBm, 2 port receives -20 dBm and 2 ports receive -30 dBm	880
64	4	3 ports receive -20 dBm and 1 port receives -30 dBm	830
65	4	3 ports receive -30 dBm and 1 port receives 0 dBm	910
66	4	1 port receives -10 dBm and 3 ports receive -30 dBm	1000
67	4	2 ports receive -20 dBm and 2 ports receive -30 dBm	940
68	4	1 port receives -20 dBm and 3 ports receive -30 dBm	1070
69	4	4 ports receive -30 dBm	1250

Cette thèse est accessible à l'adresse : https://theses.insa-lyon.fr/publication/2023ISAL0007/these.pdf
© [X.V.L. NGUYEN], [2023], INSA Lyon, tous droits réservés

FOLIO ADMINISTRATIF

THESE DE L'INSA LYON, MEMBRE DE L'UNIVERSITE DE LYON

NOM : NGUYEN DATE de SOUTENANCE : 03/02/2023

Prénoms : Xuan Viet Linh

TITRE : Investigation of Ambient Radio-Frequency Energy Harvesting using a Rapid Prototyping Plastronic Approach

NATURE : Doctorat Numéro d'ordre : 2023ISAL0007

Ecole doctorale n°160 : EEA (ELECTRONIQUE, ELECTROTECHNIQUE et AUTOMATIQUE)

Spécialité : Génie Electrique

RESUME : Internet of Things (IoT) or Internet of Objects is defining a new era of technology, where the electrical devices communicate with each other wirelessly. IoT devices have their applications in many fields in our quotidian life, such as telecommunications, education, health care, industrial domains, etc. A barrier to overcome in the development of these devices is their autonomic energy supply scheme. In the aspect of energy supply scheme, Radio Frequency Energy Harvester (RFEH) is selected among recent energy harvester mechanisms (thermal, mechanical, light, etc.). Another interesting aspect is the possibility of integrating the RFEH onto the surface of polymeric objects, which are often largely unused. This seems impossible with PCB and FLEX-PCB, but Plastronics allows to realize this idea. Therefore, the objective of this work is to demonstrate the feasibility of RFEH with a low cost, versatile Plastronics technology developed in our laboratory, suitable for prototyping. This technology, called Rapid Plastronics, is based on the fabrication of the device substrate by 3D printing, using Stereolithography (SLA), and realizing the conductive traces applying Electroless Deposition (ELD). The objective was not to develop this technology, but to apply it in the RF (which was not done before) and RFEH context.

This thesis is conducted in the following phases

In the first phase, the studies of materials manufacturing process (Stereolithography (SLA) substrate, ELD copper) in Rapid Plastronics, relative permittivity, loss tangent of the substrate, and resistivity of the conductor are carried out. These parameters have a crucial role in designing the antennas and the RF-DC rectifier.

In the second phase, designs of patch antenna for the energy harvesting (EH) applications are discussed. Firstly, a fundamental linearly polarized patch antenna operating at 2.45 GHz is studied, and the impacts of the SLA substrate and the ELD copper on the performance of the antenna are mentioned. Then, the circularly polarized patch antennas being able to capture all the polarizations in the air are studied.

The third phase is about the RF-DC rectifiers, the proposed Power Management Unit (PMU) as well as the electrical interconnection between the designed antennas, the rectifiers and the PMU. The technique of matching the 50 Ω impedance between the antenna and the rectifier is presented. Moreover, the technique of identifying the optimal load of the rectifier that offers a vision of setting up the impedance interference between the designed rectifier and the PMU will be also introduced.

In the last phase, the performance of the assembling of the PMU, the rectifiers and the antennas will be analyzed.

MOTS-CLÉS : Radio Frequency Energy Harvesting, Antennas, Power Management Unit, Plastronics, Rapid Plastronics, Stereolithography, Electroless Deposition.

Cette thèse est accessible à l'adresse : https://theses.insa-lyon.fr/publication/2023ISAL0007/these.pdf
© [X.V.L. NGUYEN], [2023], INSA Lyon, tous droits réservés

Laboratoire(s) de recherche : Laboratoire Ampère – UMR CNRS 5005 – INSA Lyon

Directeur de thèse : ALLARD Bruno

Président de jury : BENECH Philippe

Composition du jury :

Rapporteurs :	VIGNERAS Valérie, PRODIC Aleksandar
Examinateurs :	BENECH Philippe, BECHEVET Delphine, DUCHAMP Jean-Marc
Directeur de thèse :	ALLARD Bruno
Co-encadrant de thèse :	CABRERA Michel

Cette thèse est accessible à l'adresse : https://theses.insa-lyon.fr/publication/2023ISAL0007/these.pdf
© [X.V.L. NGUYEN], [2023], INSA Lyon, tous droits réservés